Development and Optimization of Microbial Fuel Cells

Doctoral Thesis

Submitted to the School of Chemical Engineering
of the National Technical University of Athens

By

Theofilos Kamperidis

Chemical Engineer

Athens 2023

Thanks

This PhD thesis was carried out at the Organic Chemical Technology Laboratory of the School of Chemical Engineering of the National Technical University of Athens under the supervision of the NTUA professor Gerasimos Lyberatos, Director of Organic Chemical Technology Laboratory. I would like to thank him for his scientific guidance and undivided support during my thesis. Additionally, I would like to express my deepest gratitude to Dr. Asimina Tremouli for her kindness, expertise and excellent cooperation. The valuable advice and interventions of prof. Lyberatos and Dr. Tremouli facilitated the process of this work.

I would also like to thank NTUA professor Christos Argirusis and NTUA professor Loucas Zouboulakis, whose contribution and scientific advice have been invaluable throughout the process of my thesis. My deepest gratitude to Dr. Federico Aulenta, Research Director at Water Research Institute – National Research Council, for his participation in the Examining Committee and his valuable suggestions for the best completion of the text.

I deeply thank NTUA assistant professor Diomi Mamma, NTUA assistant professor Anestis Vlysidis, NTUA professor Antonis Karantonis for their kindness and willingness to participate in the Examination Committee.

I thank the undergraduate students Aristeidhs Amygdalaris, Xarhs Psilopoulos, Antonis Peppas, Irene Vlachaki, Konstantinos Lekatsas, Elias Couvas, Giannis Pachakis, Georgios Koukios for their consistency and our excellent cooperation during their diplomatic theses.

I also want to express my deepest gratitude to my colleagues, PhD candidates of the Organic Chemical Technology Laboratory, Xarhs Pavlopoulos, Dimosthenis Tsivas, Gerasimos Kanellos, Axilleas Zarkaliou, Konstantina Filippou and Dimitra Theodosi. Our daily collaboration and the help they offered me selflessly throughout during my PhD were invaluable. In addition, I thank Dr. Konstantina Papadopoulou, Ms Evangelia Panothioka and my colleagues of the research team of the Organic Chemical Technology laboratory, because without their excellent help this work would not be completed.

I would also like to sincerely thank all the people who were there for me during the period of my thesis and for the support they showed me all these years. Finally, I would like to express my love and gratitude to my family, without whom the conduct of this research would not have been possible.

Acknowledgments

This research has been financed by the European Union and Greek national funds through the Operational Program Competitiveness, Entrepreneurship and Innovation, under the call RESEARCH – CREATE – INNOVATE (project code: T1EDK-04249).

This research has been financed by the Hellenic Foundation for Research and Innovation (HFRI) and the General Secretariat for Research and Technology (GSRT), under grant agreement No [862].

H.F.R.I.
Hellenic Foundation for
Research & Innovation

European Union
European Structural
and Investment Fund

EPAnEK 2014-2020
OPERATIONAL PROGRAMME
COMPETITIVENESS
ENTREPRENEURSHIP
INNOVATION

ΕΣΠΑ
2014-2020
ανάπτυξη - εργασία - αλληλεγγύη
Partnership Agreement
2014 - 2020

Co-financed by Greece and the European Union

Abstract

A microbial fuel cell (MFC) is an electrochemical system designed for wastewater treatment, with simultaneous electrical current generation. The chemical energy contained in an organic wastewater is converted to electricity through electrochemically active microorganisms. MFCs consist of an anode where the electron donor (organic wastewater) is oxidized and a cathode where an electron acceptor is being reduced. MFC configurations can be divided based on the presence of a cathode chamber to dual chamber and single chamber MFCs.

In this research, single chamber, four-air cathode, MFCs were constructed and operated using a variety of different cost-efficient materials. Initially, experiments were conducted using synthetic glucose medium as the organic wastewater, in order to compare the performance of the material combinations. The highest power density achieved by a single chamber MFC was 14.2 W/m^3, with graphite granules and a graphite rod as anode and four air cathode electrodes (Plexiglas – Gore-Tex – MnO_2). Notable results were obtained from the MFC operating with ceramic cathode electrodes (Mullite – MnO_2) and graphite granules with a graphite rod as anode, peaking at 5.5 W/m^3 power output.

Afterwards, the MFC assemblies that achieved the best performance in terms of current output and efficient wastewater treatment were operated with different substrates originating from household food waste. The effect of each feedstock on the MFC operation was investigated, using FORBI (Food residue biomass) leachate, condensed vapors from dried household food waste (condensate), anaerobic digestion reactors effluents (digestate) and cheese whey (originating from a dark fermentation process). The single chamber MFCs were operated in both batch and continuous modes.

Additionally, dual chamber MFCs were operated to investigate the recovery of heavy metals. In this work the integration of the MFC technology in the recovery of heavy metals from end of life (EoL) photovoltaic panels (PVP) was examined. Following a proposed EoL PVP recycling process, which included mechanical, thermal and chemical processing of the PVPs, a chemical extract containing the heavy metals of the PVP solar cell / thin film was generated. Initially synthetic cathode solutions containing silver and indium were tested. Afterwards, the chemical extract originating from 2nd generation EoL PVP was used in the MFC cathode, to study the metal recovery. Silver recovery was high in the cases studied (>93%), with silver depositions on the cathode electrode and sediments in the cathode chamber. Additionally, the maximum power density obtained was 0.8 W/m^3 corresponding to a silver reaction rate of 2.65 g Ag/h/m^2. Indium recovery up to 96% was achieved during the synthetic indium wastewater experiments, with a maximum power density of 0.17 W/m^3. On the other hand, during indium recovery from the EoL 2nd generation PVP chemical extract, a higher power output was recorded (3.5 W/m^3), with indium depositions (oxides) on the cathode electrode, corresponding to 87% recovery.

To further examine the MFC performance a 2D model simulating the operation of a dual chamber MFC was developed. The MFC technology was investigated experimentally and computationally in order to optimize the performance of this beneficial and environmentally friendly way to treat wastewater.

Table of Contents

1 Introduction

The development of technology has tremendously improved the quality of human life in the last century. The technology advancements enable an increase in life expectancy and subsequently an increase in the global populace. In 1950 it was estimated that the global human population was 2.5 billion people; 72 years later the projected earth population on November 2022 is 8 billion people [1]. The increase in the global population results in greater demands regarding water, food, electricity, housing and transportation among others. Additionally, to satisfy those needs a great amount of waste (solid, liquid and gas) is being generated. It was estimated that for the year 2019 the global electricity consumption was 24000 TWh (terawatt – hours). In the last forty years electricity consumption has tripled. In 2022, the global electricity demand is expected to increase further by 2% (2021, 6%). The slower increase is attributed to the COVID-19 pandemic as well as the global instability [2].

1.1 Clean electricity generation

Electricity is mainly generated by utilizing fossil fuels (61%), nuclear energy (19%) and renewable power sources (20%) [3]. Fossil fuels include natural gas (38%), coal (22%) and petroleum (0.5%). The majority of electricity is being produced by burning coal and natural gas in power plants. The heat from incineration is used to generate steam, which rotates turbines that produce electrical power. Fossil fuels are acquired by mining (solid) or drilling (liquid and gas). Nuclear energy relies on splitting atoms to generate the heat for the steam turbines and subsequently electricity. The advantage of nuclear energy is that little to no air pollution is caused by the operation of nuclear power plants [4]. However, safety concerns, render nuclear power a great debate issue.

In order to achieve transition to a less carbon-dependent energy system and to avoid the usage of fossil fuels, the renewable energy sources are the option towards a more sustainable development. Renewable energy is the energy produced from sources that are replenished at a faster rate than they are consumed. The renewable energy sources (20% of global electricity production) include wind (9%), hydropower (6%), solar (3%), biomass (1%) and geothermal (0.4%) energy [3].

- Wind energy is utilized through wind turbines, by rotating the blades of the turbine the kinetic energy of the wind is converted into electricity by a generator. This method to produce electricity emits no carbon dioxide, has a high conversion efficiency (40% - 50%, maximum theoretical efficiency 59%) and is cost effective, given that land – based wind turbines provide a low – price energy source [5].
- Hydropower is the generation of electricity through the movement of water, often through a dam. This method demands large amounts of water being stored and allowed to flow through turbines generating electricity. Also, instead of a dam, hydroelectric power plants may be placed near rivers, to utilize their flow [4]. Hydroelectricity offers a renewable, low emission power generation, that is reliable and highly efficient (90%) [6].
- Solar energy is the harnessing of the sun light to generate either heat or electricity. To generate heat, sun light is used to directly to heat water or other fluids, by solar thermal panels. To generate electricity solar PV panels are used. The electricity is generated by a semi – conductor, often silicon, present in the PV panel.
- Geothermal energy is the natural heat of Earth, which is generated by the core of our planet and is transferred to its surface, through convection and conduction. The heat is used to boil water in reservoirs (natural / manmade) beneath the Earth's surface. The steam produced is directed to a generator where electricity is produced [7]. This method of power generation is environmentally friendly, renewable and reliable.
- Biomass energy is the energy contained in living or once – living organisms. Biomass includes wood, woodchip, agricultural residues, industrial or municipal waste etc. The conventional method to generate electricity from biomass is through incineration, similar to the operation of fossil fuel power plants. This way, electricity generation is reliable and contributes to the reduction of waste landfilled. It is also a carbon neutral source, meaning the carbon dioxide produced during the incineration is the same amount that was absorbed by plants during their lifecycle. Biomass energy can be characterized as renewable, since biomass can be generated quickly (within a human lifetime) [8]. Despite, the carbon neutrality, the burning of biomass releases greenhouse gases, such as nitrogen oxides, carbon monoxide and methane, contributing to air pollution and climate change [8]. To provide enough materials to generate sufficient amounts of electricity, biomass requires a lot of energy to grow and transport to power plants. Deforestation and reduced biodiversity are two consequences of biomass plants

production. Intense cultivation of plants for a single purpose, strips the land of nutrients, damages local waters due to overuse of fertilizers and results in a negative impact on the ecosystem, while the initial purpose of using biomass was the opposite. The efficiency of a biomass combustion can reach 45% [9]. Despite, the disadvantages of conventional biomass utilization, developing technologies suggest new pathways to benefit from waste, which do not require incineration. In the following chapters of this thesis, alternative utilization of biomass for electricity generation will be presented.

Various technologies have been developed to generate electricity, as humanity increasingly relies on it. The increase of global population requires intense, efficient and reliable electricity generation. Apart from the energy demand, there is a continuous need for other goods such as clean water and food supply, housing and transportation, which human societies try to satisfy. Some countries have achieved a higher rate of industrialization and individual income, while others present a slow rate of industrialization and low income per capita. The quality of life offered depends on the development of each country, resulting in “developing” and “developed” states. The supplied goods produced by human societies are consumed, while at the same time, materials discarded as no longer useful are characterized as waste.

1.2 Waste generation and treatment

The global waste generated may be linked with the population increase, but the consumerism of the “developed” nations is its primary factor. In 2019, it was estimated that two billion tons of waste were generated by 7.6 billion people [10]. The biggest waste generator is the U.S.A. with each citizen producing 808 kg of waste / year on the average. Additionally, waste generation is combined with waste mismanagement and ultimately uncontrolled disposal. Proper waste valorization and treatment is required in order to avert the negative effects of waste accumulation.

In order to deal with the increasing amount of waste, various techniques are employed. Landfilling is the oldest and most common form of waste disposal; when used correctly it can contribute to the reduction of the waste generated. Landfilling, if not conducted properly, results in the pollution of nearby soil or water bodies. Landfilling includes the covering of solid waste with soil, in order to limit the escape of the landfill gases (carbon monoxide, dioxide and methane) produced. The major advantage of landfilling is the low cost of the process resulting in broad use of this waste disposal method [11]. The uncontrollable landfilling can lead to an increase in the gases produced, which contribute to the greenhouse effect, especially methane. The pollution of underground waters may be caused by a landfill if the membranes surrounding the waste rupture. This affects the health of the population around the landfill, along with the wildlife [11]. On the other hand, incineration includes the combustion of waste, converting the waste to ash and utilizing the heat produced. This results in the reduction of the waste volume, removing any toxic substances [12]. The problem revolving incineration is the emission of gasses such as suspended particles, sulphur oxides, furans and other dangerous compounds as well as the need to landfill the generated fly ash in a hazardous waste landfill. Furthermore, incineration has high capital and maintenance costs. Composting is another method used for organic solid waste treatment; it relies on the aerobic decomposition of organic compounds. It results in the removal of pollutants, homogenization of waste and reduction in the overall waste volume. Composting is an environmentally friendly method, which requires long periods of time until it is complete. Additionally, it depends on the initial amount of organic waste used, requiring large areas. Often during the process of composting, odors are emitted, which make it unpleasant for populations around the composting site. The major advantage of composting is the sustainability of the method, as it reduces greenhouse gasses, since produces large amounts of fertilizer and contributes to the improvement of soil quality [13].

1.2.1 Wastewater treatment

A part of the global waste produced corresponds to waters that have been contaminated, originating from major sources including municipal wastewater (sewage), industrial wastewater agricultural wastewater. Wastewater typically contains significant concentrations of solids, dissolved and particulate (organic) matter, microorganisms (capable of causing health hazards), nutrients (such as nitrogen and phosphorus compounds), heavy metals and micro-pollutants [14]. Wastewater has an adverse effect on the environment when discharged and causes health issues on the human population either directly or indirectly. It is necessary to process the wastewaters in order to remove the pollutants and reuse the valuable components. Additionally, global water scarcity requires the minimization of water discharge and reusage of water streams. An example of wastewater utilization is the material recovery (such as the nutrient recovery) and the use of treated wastewater as irrigation water [15].

Wastewater treatment is the combination of the various techniques used to reduce and eliminate the pollutants present in wastewaters. Moreover, throughout the treatment, wastewater is converted to an effluent that can be returned to the water cycle, resulting in a controlled impact on the environment. The main techniques employed include physical, biological and chemical methods for wastewater clarification.

- Physical techniques include screening, filtering, aeration, sedimentation and thermal processing
- Chemical techniques include neutralization, disinfection, flocculation through the use of chemicals (e.g. chlorine used to eliminate bacteria)
- Biological techniques include anaerobic processes (e.g. anaerobic digestion), aerobic processes

In Figure 1 a flow chart of the multiple processes (mechanical, chemical, biological) incorporated in a typical wastewater treatment plant is presented. Municipal wastewater is introduced to the preliminary processing, which includes screening, sieving and filtering for removal of solids, gravel and coarse sand. Afterwards, the stream of wastewater is sent through a sand collector. The pretreatment aims to protect the mechanical compartments from blockages due to unwanted deposits. Afterwards, the sewage is introduced into a flow equalization tank, where daily fluctuations are neutralized, offering a constant supply to the following processes. Sediments are removed and utilized in production of biogas through anaerobic digestion. In the typical wastewater treatment plant, the removal of suspended solids is carried out through a primary sedimentation tank which is a widespread low-cost option.

After the primary follows the secondary treatment, in which biological and physicochemical processes are used in order to remove the organics left from the previous processes. The biological processes are carried out through the oxidation of organic matter by aerobic microorganisms. The most common method encountered during the secondary treatment is the activated sludge process (or activated sludge). Specifically, the activated sludge process includes an aeration tank where the biological oxidation takes place and a secondary sedimentation tank where the microorganisms settle. Subsequently, the wastewater enters the advanced or otherwise tertiary processing, during which, the quality of the liquid characteristics is improved, mainly by the removal of nitrogen and phosphorus. Then, the wastewater is disinfected destroying the micro-organisms in suspension. The disinfection is usually carried out by the chlorination method. A secondary unit is utilized as well, which aims at the separation and treatment of the activated sludge produced in individual processes of the facility (excavations, sand collection, tanks of primary and secondary sedimentation).

Sludge stabilization aims at the destruction of pathogenic microorganisms and at the neutralization of odors. Anaerobic digestion is one process used by several biological treatment plants for stabilization of the sludge and recovery of the energy it contains in the form of biogas (biomethane). In the final stage, the sludge is dehydrated to facilitate its transport and to improve its handling, also dehydration is carried out with filter presses. The initial stage of wastewater treatment involves mechanical processes, which remove some 20% - 30% of solids in the water. The speed with which the wastewater flows through the screens at each step is carefully controlled to assure the effectiveness of the screening process. Any debris that has been collected on the screens is sent to other process steps where the material gets dewatered and then incinerated.

The electricity demand of the various processes that form the wastewater treatment plant is contributing to 25% - 40% of the total operating cost [16]. Additionally, wastewater treatment plants generate greenhouse gas emissions directly (methane, nitrous oxide) or indirectly (through the electricity consumption, fuel consumption for transportation, chemicals required in the treatment process) [17]. Therefore, the optimization of the treatment process is required in order to achieve carbon neutrality and maximize the benefits of its operation.

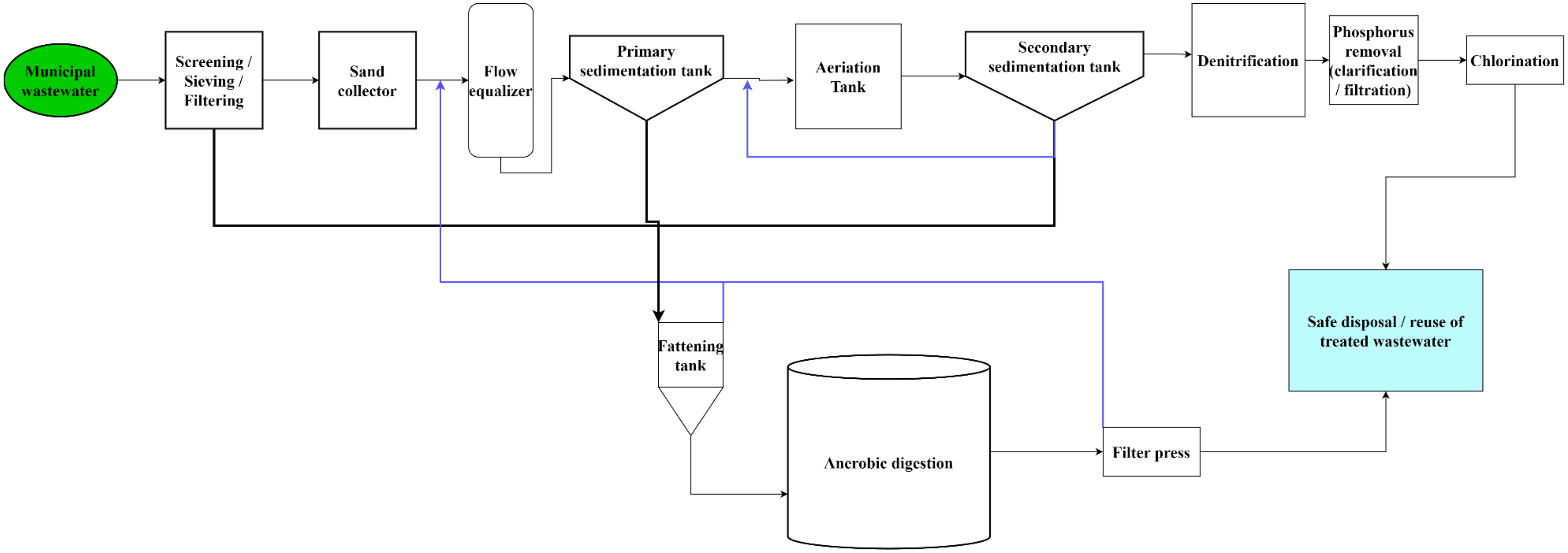

Figure 1. Flow chart of a typical wastewater treatment plant.

1.2.2 Waste utilization for energy production

In order to deal with the increasing energy demand, an environmentally friendly and sustainable approach is needed. Utilizing the waste produced by the population as the “raw material” for energy production, is an efficient way to deal with both problems.

Humanity has managed to store electrical energy in chemical form (batteries) and convert it back to electricity when needed. A similar process can be employed for simultaneous waste treatment with energy production. The technology of bioelectrochemical systems (BESs) has the ability to convert the chemical energy into electricity (and the reverse process if needed). This unique ability is developed by the microorganisms in these systems, as part of their metabolism. It has been the focus of scientific research, resulting in the development of multiple types of bioelectrochemical systems depending on the bioprocesses conducted [18]. Microbial fuel cells (MFCs) are BESs that can be used for the wastewater treatment (primarily) and at the same time electricity production (secondarily).

The advantages that the MFC technology offers, regarding wastewater treatment and energy production, make it a promising method for biomass utilization and waste reduction. This thesis focuses on the optimization of MFCs while examining various wastewaters, as well as materials recovered through reduction. The objective is to enhance the MFC technology with low-cost interventions (cost – effectiveness) under the view of its practical implementation.

2 Theory

2.1 Bioelectrochemical systems

Bioelectrochemical systems take advantage of the microbial metabolism to convert the chemical energy contained in waste into bioelectricity or biofuel (Methane, Hydrogen production) or recovery of valuable products from waste streams (heavy metal recovery) [19]. The operation of these systems is based on the oxidation of an electron donor followed by the reduction of an electron acceptor. The oxidation reaction takes place in the anode chamber and it is catalyzed by electrogenic bacteria which have the ability to transfer the electrons to their exterior (electrochemically active bacteria) [20]. Similarly, the reduction reaction occurs in the cathode chamber and may be catalyzed by microorganisms (biocathode) or catalysts such as platinum, activated carbon etc. (abiotic cathode) [21]. Different types of BES have been developed such as microbial fuel cells (MFCs), microbial electrolysis cells (MECs) microbial solar cells (MSCs) [22], microbial electrosynthesis cells [23], microbial desalination cells (MDCs) [24] and enzymatic fuel cells (EFCs) [25]. These electrochemical cells have been developed for simultaneous wastewater treatment, current generation and production of other substances such as hydrogen in the case of MECs [26]. The most studied BES systems are the Microbial Electrolysis Cells (MECs) and the Microbial Fuel Cells (MFCs). The plethora of bioelectrochemical processes which are catalyzed by microorganisms are exhibited in the multiple BESs that have been developed.

2.1.1 Microbial Fuel Cells

A MFC is a bio-reactor in which the chemical energy that is bound to the organic components of a substrate, is converted into electricity, through catalytic reactions by microorganisms under anaerobic conditions [27]. In general, bacteria gain energy by transferring electrons from a donor, such as glucose, to an electron acceptor, such as oxygen. The greater the potential gradient between the donor (lower potential) and the acceptor (higher potential) of electrons, the greater the energy gain for the bacteria. The microorganisms capable of transferring the electrons from the inside of their cells to an acceptor in their environment, such as an electrode, are characterized as electrochemically active bacteria [20]. In the anode the oxidation of the wastewater takes place and the products of the reaction are dispersed back into the electrolyte. The protons, which were produced by the reaction, diffuse through the anode electrolyte and across a separator in the cathode, where they react with electrons and with the electron acceptor. The anode and the cathode liquids (anolyte – catholyte respectively) come in electrolytic contact through the separator. A separator is a material that allows the passage of charged ions through it, but does not allow the anode and the cathode solutions to mix, while bringing them in electrolytic contact. The usage of a separator between the anode and the cathode also assists to avoid short circuit [28]. The oriented flow of electrons enables the direct conversion of the bacteria's energy into electricity. The operation of the MFCs is summarized in Figure 2.

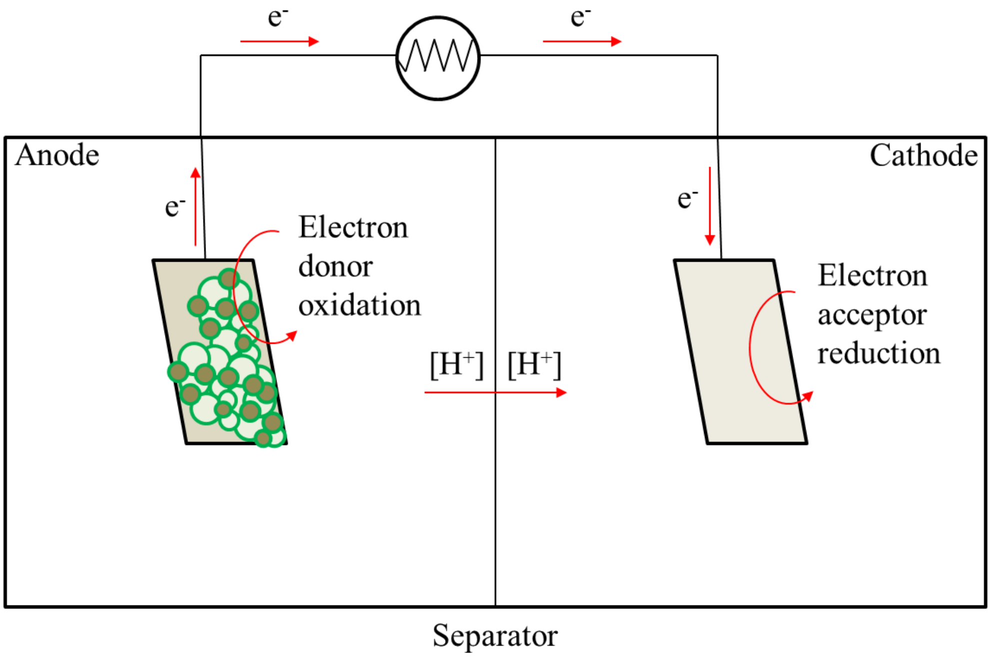

Figure 2. MFC operation schematic

2.1.2 Microbial Electrolysis Cells

Hydrogen is considered a promising energy source and a clean burning fuel, since it does not produce carbon dioxide during its combustion. The production of hydrogen is based on both renewable and non–renewable sources, with the majority being produced by a non-renewable process, steam reforming natural gas (fossil fuel utilization) [29]. The green production of hydrogen includes the electrolysis of water, using renewable energy (wind, solar, geothermal or biomass) [30]. A BES developed to produce hydrogen through the treatment of an organic wastewater is the MEC.

The MEC produces hydrogen gas (H_2), while oxidizing an organic wastewater, through microbial metabolism. Its operation is not spontaneous, and it requires an external voltage application in order for the electrolysis to take place [31]. The cell consists of an anode and a cathode. In the anode, electrochemically active bacteria oxidize the organic substrate, generating carbon dioxide (CO_2), hydrogen cations ($[H^+]$) and electrons. The electrons are transferred through the anode electrode to the cathode, while the protons are diffused into the electrolyte (anode solution). On the cathode surface, hydrogen cations are combined with electrons, through the voltage application and form hydrogen gas. A catalyst is coated on the cathode electrode to reduce the activation energy of the hydrogen evolution reaction and boost the efficiency of the hydrogen MEC production [32]. The most notable hydrogen catalysts are expensive materials like platinum or palladium, while cheaper materials, such as iron or nickel have been used as well. Furthermore, biocathodes have been developed in MECs to catalyze the hydrogen evolution reaction [32]. The hydrogen evolution reaction is considered as follows (adjusted potential for pH=7, 298 K and expressed vs Normal Hydrogen Electrode NHE) [33]:

$$2H^+ + 2e^- \rightarrow H_2, E'^0 = -\ 0.41\ \text{V} \qquad \text{Eq.1}$$

Another advantage of the MEC technology is the ability to convert carbon dioxide to methane, yielding biogas, rich in methane. The conversion of carbon dioxide is achieved through a biocathode in the MEC. The production may be characterized as direct (Eq. 2) or indirect (Eq.3,4) and the respective reactions are presented below [30], [32]:

$$CO_2 + 8H^+ + 8e^- \rightarrow CH_4 + 2H_2O, E'^0 = -\ 2.44\ \text{V} \qquad \text{Eq.2}$$

$$2H^+ + 2e^- \rightarrow H_2, E'^0 = -\ 0.41\ \text{V} \qquad \text{Eq.3}$$

$$CO_2 + 4H_2 \rightarrow CH_4 + 2H_2O \qquad \text{Eq.4}$$

The MEC technology showcases the potential of the BESs, as it can produce hydrogen while degrading organic matter, or it can convert carbon dioxide to methane through the utilization of microbes in the cathode (biocathode).

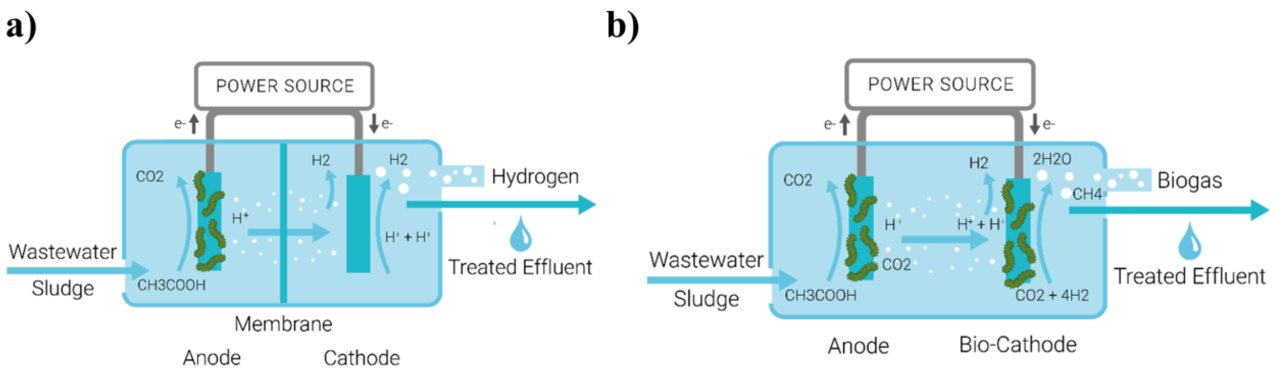

Figure 3. Process of hydrogen production (a) and methane production (b) through the MEC technology, oxidizing acetic acid [34].

2.1.3 Microbial Solar Cells

Microbial solar cells (MSC) are a category of bioelectrochemical systems which utilize photosynthetic / photoautotrophic microorganisms to produce electricity. The photosynthetic microorganisms use the sunlight to produce organic matter, which in turn is oxidized by electrochemically active bacteria, resulting in hydrogen cations [H^+], carbon dioxide CO_2 and electrons e^-. The oxidation takes place in the anode and is followed by the reduction of oxygen in the cathode [35].

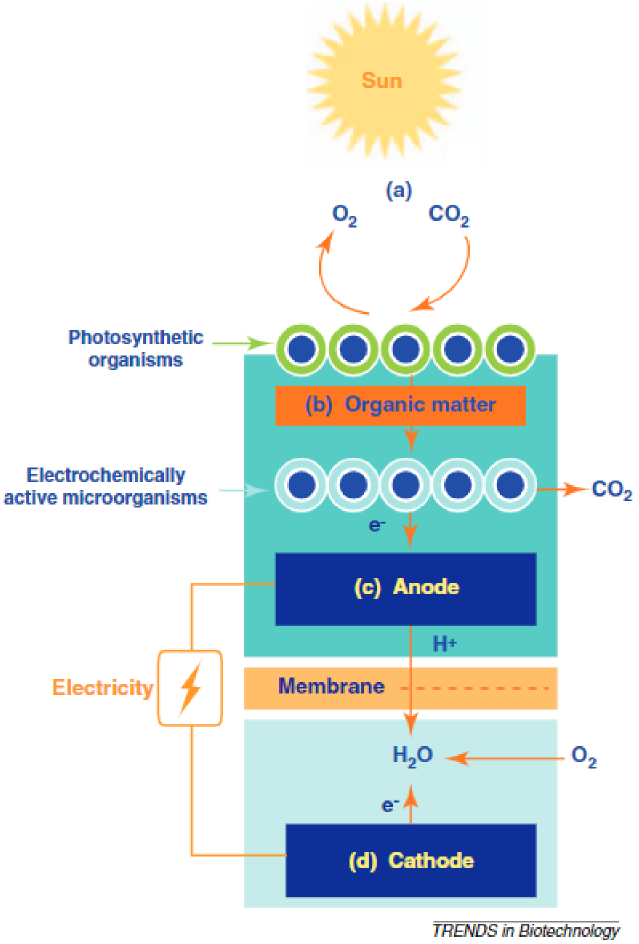

Figure 4. Schematic of a microbial solar cell operation [35].

In Figure 4, the operation principle of a MSC is depicted, as illustrated by [35]. Initially, photosynthesis takes place, which consumes sun energy, carbon dioxide and water to produce glucose and oxygen (Figure 4, (a)). Subsequently, the organic compounds are transferred to the electrochemically active bacteria present in the anode (Figure 4, (b)). There, the oxidation of glucose takes place resulting in electrons, hydrogen cations and carbon dioxide (Figure 4, (c)). Finally, through the transfer of electrons and hydrogen cations to the cathode, oxygen reduction is achieved (Figure 4, (d)). The operation of a MSC is self – sustainable, not requiring addition of an organic substrate. However, the mechanisms regarding electron transfer and photosynthesis are not fully understood [36]. Different MSC configurations have been developed, with observations regarding the reduction of the device size, increasing the mass transfer rate and the performance [36]. Applications of MSC have been described by [35 – 37], presenting the potential of MSC usage to operate low-power devices (such as sensor nodes) in remote and unattended areas.

Miniature MSCs were reported to continuously operate and generate electricity during the day-night cycle, accumulating organic material during its day cycle to produce electricity during the night [35].

2.1.4 Enzymatic Fuel Cells

Enzymatic fuel cells (EFC) operate by oxidizing organic compounds and reduce oxygen or hydrogen peroxide, generating electricity, similar to other BES. The difference lies in the usage of oxidoreductase enzymes to catalyze the transfer of electrons [38]. An EFC consists of two chambers, an anode and a cathode separated by an ion transfer membrane [38], as shown in Figure 5. EFCs offer a sustainable clean energy source, based on the properties of specific isolated enzymes, which present high catalytic activity, while requiring ambient temperature and neutral pH to operate. This reduces the cost of the EFC configuration, when compared to traditional fuel cells. Moreover, the expensive anode – cathode separator may be omitted and the cathode catalyst may be replaced with enzymes, due to the specificity of the enzymes [38]. The EFC is based on the immobilization of these enzymes, either physically or chemically [38].

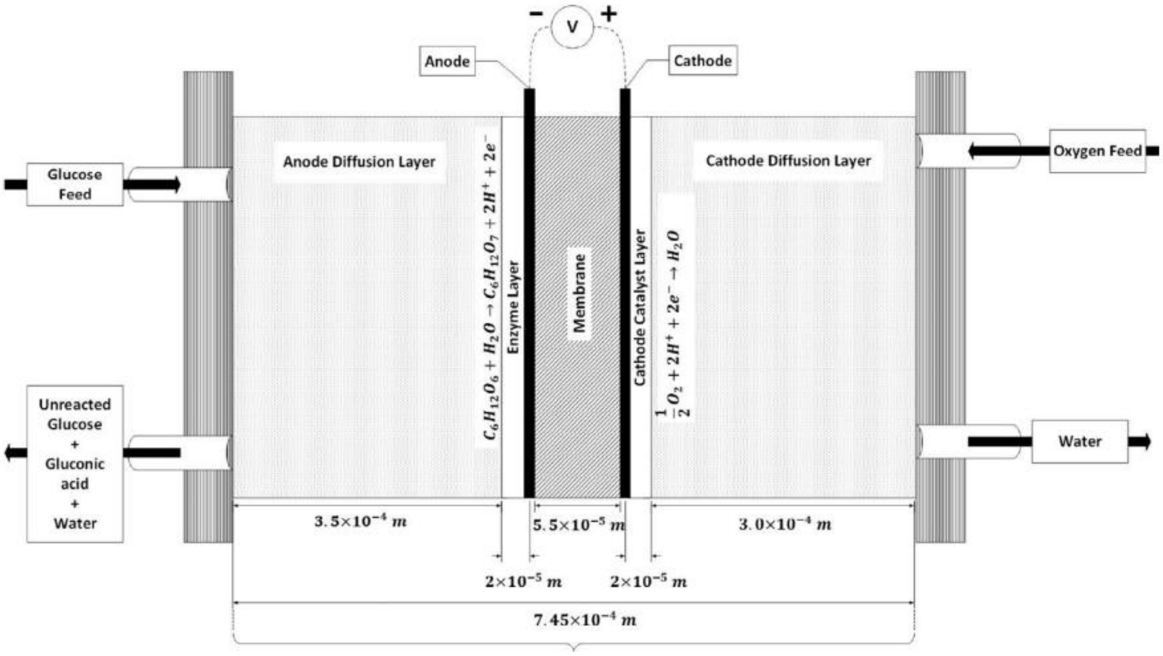

Figure 5. Diagram of a glucose fed enzymatic fuel cell [39].

Applications of EFCs include low power electronic devices, such as biosensors. Implantable and wearable EFCs have been examined, but rejection and immune response of the human body to the device may cause severe health hazards [38].

2.1.5 Electrofermentation

A recently developed aspect of the BESs is the improvement of a fermentation process through bioelectrochemistry. Fermentation is the metabolic process that changes the chemical composition of organic molecules under anaerobic conditions, conducted by microorganisms through enzymes. Fermentation is broadly used to produce a variety of products such as beer, wine, solvents, enzymes and biofuels among others [40]. To improve the traditional fermentative methods, a new technique was developed, which includes the placement of electrodes in the fermentation tank and the regulation of the metabolic processes through voltage application. This technique is called electrofermentation and offers electrochemical control to the metabolic reactions through the electrode implementation [41]. Electrofermentation improves the stability of the fermentation process while it increases the yield of the valuable products [40]. In particular, electrofermentation has been reported as a method to stabilize pH irregularities, while assisting the decomposition of carbon compounds [40], [42]. Additionally, electrofermentation optimizes the yield of products, either through boosting the overall efficiency or by allowing selective production of the required material [43].

The addition of the electrodes in the fermentation and the voltage application convert the process from biochemical to bioelectrochemical. The electrodes may operate as an electron donor (anodic electrofermentation), an electron acceptor (cathodic electrofermentation) or just control the potential to drive the oxidation – reduction reactions [43].

2.2 Microbial Fuel Cell (MFC)

The principles of MFC operation have been described in 2.1.1.

2.2.1 Electron transfer in MFC

Regarding microbial metabolism, based on the electron acceptor, two metabolic pathways are distinguished, respiration and fermentation. During respiration, the electron acceptors are in the exterior of the microbes, while in fermentation the electron acceptors are in the interior of the microbes. Most microorganisms, which are characterized as aerobic, follow respiratory metabolism and use atmospheric oxygen as electron acceptor. The microorganisms that follow a fermentative metabolism do not use oxygen in metabolic reactions and for this reason are characterized as anaerobic [44]. There are many bacteria that are facultative, namely they may grow under both aerobic and anaerobic conditions.

Bacteria try to maximize the energy they will gain by choosing the available electron acceptor with the maximum potential. However, soluble electron acceptors can be depleted in the microbial environment. In this case, the bacteria can choose the metabolic pathway of fermentation, or use no soluble electron acceptors. In the latter case, in order for the reduction to occur, bacteria transfer the electrons out of their cells. This process is known as extracellular electron transfer (EET) [45]. The EET process can be carried out through several mechanisms, which can be classified into two main categories: indirect and direct electron transfer. In indirect electron transfer an organic or inorganic soluble mediator is being reduced or oxidized. Subsequently, the mediator diffuses towards the insoluble acceptor or electron donor, respectively [46]. Direct electron transfer is conducted with the help of enzymes, which are bound to the cellular membrane (e.g. cytochromes) or via conductive capillary diodes (nanowires) [45], [46].

2.2.2 Thermodynamic phenomena in MFCs

In a MFC, an electrochemical reaction pair is taking place, one oxidation (anode) and one reduction (cathode). The reactions take place spontaneously, meaning no external energy supply is needed to initiate them. In order to oxidize the substrate and produce electricity, the electrochemical reaction needs to be favored thermodynamically. The Gibbs free energy is a measure of the maximum work obtained by a reaction.

$$\Delta G_r = \Delta G_r^0 + RTln(\frac{[Products]^p}{[Reactants]^r}) \qquad \text{Eq.5}$$

Where ΔG_r is the Gibbs free energy (J) in particular conditions, ΔG_r^0 is the Gibbs free energy in standard conditions (298 K, 1 bar, 1 M concentration of all species), R is the global gas constant (8.31 J/(mol·K)), T (K) is the temperature and in the logarithm are the activities of the products and the reactants, with their respective stoichiometric coefficients as powers. In MFCs it is more convenient to use the cell's total electromotive force (E_{EMF} [V]), which is defined as the potential difference between the cathode and the anode. The correlation between the Gibbs free energy and the electromotive force is the following:

$$\Delta G_r = -n \cdot F \cdot E_{EMF} \qquad \text{Eq.6}$$

Where n is the number of electrons participating in the reaction and F is Faraday's constant (96485 C/mol). The work (W [J]) that can be produced by the cell is defined as:

$$W = -\Delta G_r \qquad \text{Eq.7}$$

In order to determine whether the reaction pair will take place spontaneously in a MFC, the Gibbs free energy has to be negative (<0), which based on Eq. 6, means that E_{EMF} has to be positive. The E_{EMF} can be calculated by Eq. 6 if solved for it, resulting in the Nernst equation:

$$E_{EMF} = E_{EMF}^0 - \frac{RT}{nF} \cdot \ln (\frac{[Products]^p}{[Reactants]^r}) \qquad \text{Eq.8}$$

where E_{EMF} is the electromotive force in particular conditions and E_{EMF}^0 is the electromotive force in STP conditions. Additionally, in the case of electrochemical reactions, the electromotive force of the two reactions (pair) can be calculated from the following equation:

$$E_{EMF} = E_{Cathode} - E_{Anode} \qquad \text{Eq.9}$$

where $E_{Cathode}$ is the potential of the reduction reaction either in STP or particular conditions and E_{Anode} is the potential of the oxidation reaction in similar conditions.

According to the International Union of Pure and Applied Chemistry (IUPAC), the standard potentials of the half-reactions taking place either at the anode or at the cathode electrode, are defined in reference to the standard hydrogen electrode. The normal hydrogen electrode (NHE) or standard hydrogen electrode (SHE), exhibits a value of its potential equal to zero, in standard conditions (298.15 K, pO_2 =1 bar, $[\frac{[Products]^p}{[Reactants]^r}]$ = 1 M).

The electromotive force and the Nernst equation provide an upper boundary of the reaction potential. This theoretical estimation of the potential is higher than the experimentally achieved one, since there are various ohmic losses present in the system. The difference between the redox potentials of the electron donor and acceptor, respectively, determine whether the electrochemical reaction will be spontaneous. A MFC operation is spontaneous, based on Eq. 6 and the required ΔG has to be negative.

An example of MFC operation is the oxidation of glucose ($C_6H_{12}O_6$) in the anode and the reduction of oxygen in the cathode. Assuming the following equation for the glucose oxidation:

$$C_6H_{12}O_6 + 6H_2O \rightarrow 6CO_2 + 24H^+ + 24e^-, E^0 = -\ 0.014\ \mathrm{V} \qquad \text{Eq.10}$$

On the cathode electrode the oxygen is the electron acceptor and the following reaction is assumed to take place:

$$O_2 + 4H^+ + 4e^- \rightarrow 2H_2O, E^0 = 1.229\ \mathrm{V} \qquad \text{Eq.11}$$

The oxidation potential of glucose in standard conditions is – 0.014 V [33] and the respective reduction potential of oxygen is 1.229 V [33]. Assuming a pH equal to 7 and partial oxygen pressure equal to 0.2 the potentials become, – 0.428 V (Glucose) and 0.805 V (Oxygen) [33]. Calculating the E_{EMF} through Eq. 8, it is equal to 1.23 V, which results in a negative Gibbs free energy when used in Eq. 6, thus indicating the spontaneous operation of a MFC with glucose as electron donor and oxygen as electron acceptor. Additionally, the voltage development of the example MFC will never surpass the 1.23 V.

2.2.3 Overpotential in MFC operation

The electromotive force (E_{EMF}) is a theoretical value calculated by the Nernst equation (Eq. 8). In order to measure the maximum potential developed by a MFC, an infinite resistance needs to be connected between the anode and the cathode electrodes. The Open circuit potential (OCP) is the potential achieved by the MFC when no current flows through the external circuit (infinite external resistance). In theory, the OCP value should be equal to the E_{EMF}, in practice though it is considerably smaller due to internal losses. The overpotential (η [V]) is defined as the difference between the potential of a MFC and the respective maximum theoretical potential (E_{EMF}), calculated by the following equation:

$$\eta = E_{EMF} - U_{Cell} \qquad \text{Eq.12}$$

The overpotential is equal to 0 V, when the E_{EMF} is equal to the U_{Cell}, which is never attained. The highest potential achieved by the MFC is the OCP. The difference between the E_{EMF} and the OCP of the MFC is caused by phenomena such as the diffusion limitation of the electron donor in the anode chamber, or diffusion limitation of the electron acceptor in the cathode chamber. The separator or the membrane employed between the anode and the cathode contributes to the decrease in the output of the MFC.

A MFC consists of an anode, a cathode, the separator between them and the external resistance connected between the electrodes. The overpotential of a cell is calculated by the following equation, which takes into account each distinct overpotential:

$$\eta_{Cell} = \sum \eta_{Anode} + \sum \eta_{Cathode} + \eta_{Ohm} \qquad \text{Eq. 13}$$

Where η_{Cell} is the overpotential of the MFC, $\sum \eta_{Anode}$ and $\sum \eta_{Cathode}$ are the total overpotentials developed in the anode and cathode electrodes, respectively and η_{Ohm} is the ohmic overpotential. The ohmic overpotential is the sum of the ohmic losses caused by the current flow (I) through the ohmic resistance of the MFC (R_Ω):

$$\eta_{Ohm} = I \cdot R_{\Omega} \qquad \text{Eq. 14}$$

To calculate the power output (W) of a MFC at any given moment, the following equation is used:

$$P = U_{Cell} \cdot I \qquad \text{Eq. 15}$$

In order to facilitate the comparison of power output between different MFC configurations, the volumetric power density (W/m^3) is defined, normalizing the power output to the anode chamber volume:

$$p = U_{Cell} \cdot i \qquad \text{Eq.16}$$

where i is the volumetric current density (A/m^3). Furthermore, the power density may be calculated using the total surface area of the electrodes used (W/m^2) using the surface current density (A/m^2).

2.2.4 MFC polarization curve

To examine the various losses in a MFC, a polarization curve needs to be created. The polarization curve is a plot of the potential of a MFC versus corresponding current (or current density). The power curve is the respective plot of the power (or power density) versus the current (or current density) of the MFC. In a polarization curve, it is possible to distinguish the various overpotentials developed by the MFC (Figure 6). A polarization curve is extracted by measuring the potential of a MFC and the current flowing through the external resistance, while altering the value of the external resistance connected to the MFC [0 - ∞).

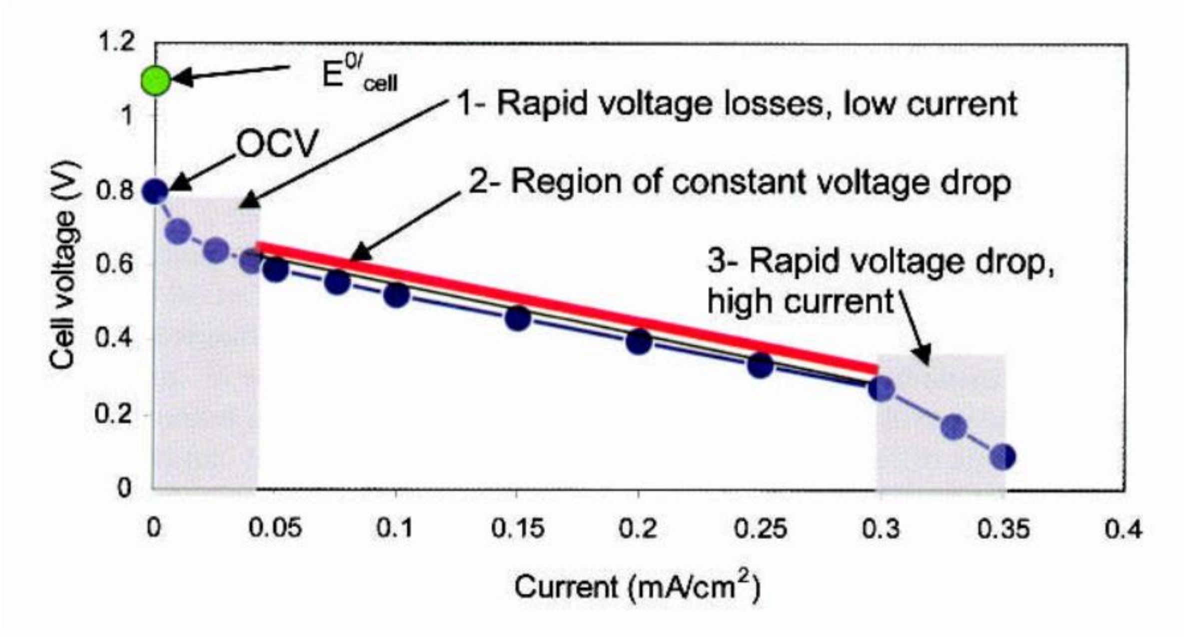

Figure 6. Polarization curve (V – i), highlighting the different types of electrochemical losses and their respective regions [33].

In Figure 6, E^0_{Cell} is the maximum theoretical potential of the MFC (E_{EMF}) and OCV is the same as OCP. If the external resistance is high (→∞), the current is minimal (→0) resulting in a high potential (U_{Cell} → OCP). By inhibiting the current flow, the maximum potential gradient is developed between the MFC electrodes. In that curve area (Figure 6, area 1), where low current and high voltage are observed, the activation overpotential dominates the losses of the MFC. The activation overpotential is caused by the activation energy required by the bacteria in order to start the oxidation of the electron donor. Phenomena such as the transfer of reactants and electrons from the bacteria to the electrolyte and the anode electrode, respectively, contribute to the activation overpotential [27]. To decrease the activation overpotential, heat can be supplied to the system, as long as bacteria can tolerate the temperature. Additionally, the use of catalysts for the electron acceptor reduction and the increase of the electrolyte's conductivity can lower the activation energy required.

If the external resistance is low (→0), the current is maximum (→I_{max}) resulting in a low potential (U_{Cell} → 0). By allowing the maximum electron flow between the MFC electrodes ($R_{External}$ → 0), no potential gradient is able to develop as the charged particles do not accumulate. In that part of the curve (Figure 6, area 3), where high current and low voltage are observed, the concentration overpotential dominates the losses of the MFC. The concentration overpotential is the limitation caused by the mass transfer. In particular, as the electrons are allowed non – stop to flow from the anode to the cathode, the limitation in the power output of the MFC is caused by the diffusion of the electron donor inside the bacteria cells. The concentration overpotential corresponds to the reaction rate being the limiting factor of the MFC operation. To reduce the inhibition of mass transfer, the stirring of the MFC chambers may be employed, allowing continuous supply of electron donor to the microbes. Also, increasing the specific surface of the anode electrode increases the interface between the electrochemically active biofilm and the electrolyte containing the electron donor [45].

In Figure 6, the area 2 (- region of constant voltage drop) the ohmic overpotential dominates the losses of the MFC operation. The ohmic losses of the system are attributed to the resistance of electron flow through the electrolyte, the separator (anode – cathode), the electrodes and generally the connection points of the circuit.

The polarization curve can be used to calculate the internal resistance of the MFC ($R_{Internal}$). In the range of the useful current densities (Figure 6, 2), a linear dependency is observed between the current and the potential.

$$U_{Cell} = OCP - R_{Internal} \cdot I \qquad \text{Eq.17}$$

Where $R_{Internal} \cdot I$ is the sum of the losses due to the internal resistance of the MFC.

Another way to estimate the MFC internal resistance cell is the peak power density method (Jacobi's Law). According to Jacobi's Law: "*At the transfer of maximum power from a source with a fixed internal resistance to a load, the resistance of the load must be the same as that of the source.*" As mentioned, the polarization curve may be extracted by altering the $R_{External}$ of the MFC, recording the voltage and the current of the cell. Using Jacobi's Law and calculating the power output (Eq. 16), it is possible to determine the internal resistance, because when P_{max} is achieved, the $R_{External}$ which is applied to the system is equal to the $R_{Internal}$ of the system. A more accurate method to determine the $R_{Internal}$ of the MFC is through electrochemical impedance spectroscopy (EIS). Additional electrochemical characterization can be conducted by cyclic voltammetry and linear sweep voltammetry.

2.2.5 Electrochemical Impedance Spectroscopy (EIS)

EIS is a powerful tool to study electrochemical phenomena taking place in MFCs. During an EIS experiment, an alternating current of small magnitude is applied to a MFC, studying the response of the system during a perturbation at steady state. The technique can be conducted in a MFC without altering the current – voltage properties of the biological cell [47], meaning it is a non – intrusive experiment.

Impedance (Z) is a complex quantity and represents the inhibition of current flow, caused by an electronic circuit, when subjected to an alternating / direct electric current. The real part of impedance is called resistance (R) and the imaginary reactance (X). Based on Ohm’s law, resistance is defined as the ratio of voltage to current. The electron flow is inhibited by two additional phenomena inductance (L) and capacitance (C), which together form the reactance. As inductance are described the self-induced voltages in a conductor, by the magnetic fields of current [47]. Capacitance is the electrostatic storage of charge induced by voltage between conductors [47]. Impedance is measured in ohm (Ω). By alternating the frequency of an AC signal, it is possible to get DC when the frequency tends to zero. In a DC signal, the resistance and the impedance of a system are the same scalar quantity, the two differentiate when AC is applied to the system. The impedance possesses both magnitude and phase angle as it is a complex number [47].

The EIS method consists of perturbing a system located in equilibrium or steady state by applying a small external disturbance (alternating current) and the simultaneous recording of the response of the system. From the values of the alternating current and the recorded current and voltage, the complex resistance of the system is calculated. Electrochemical properties of the studied system are imprinted in the frequency spectrum of impedance and by proper interpretation it is possible to provide information about various phenomena occurring within it.

EIS measurements are carried out with the help of a potentiostat which is equipped with a frequency response analyzer (FRA). The MFC is connected to the potentiostat in a two or three electrode set – up. In particular, the two-electrode configuration is better applied in the case where the total internal resistance of the MFC is determined for an imposed potential while the three-electrode system is used to analyze each electrode separately. In case of the three-electrode system, one electrode is used as the working electrode, while the second electrode is the so-called auxiliary or counter electrode. The third connection is made with the reference electrode (reference electrode e.g., Ag/AgCl) which is placed in either the anode or cathode chamber, close to the respective electrode under study, reducing the signal noise. In the two-electrode case the counter electrode also functions as the electrode reference without requiring the additional reference electrode. The usage of two – electrode set – up is based on the assumption that the potential of the counter / reference electrode does not vary during measurement, which is not always true [47].

The data collected with the EIS experiment is usually plotted in Bode and Nyquist plots. An ideal resistance possesses only magnitude, while impedance has magnitude and phase angle (complex quantity). The real part of the impedance is the resistance and the imaginary the reactance. In Nyquist plots the real part of the impedance (x – axis) is plotted versus the imaginary part of the impedance (y – axis), with each point in the graph corresponding to a different frequency. In Bode plots the logarithmic frequency (x – axis) is plotted versus the absolute value of impedance and / or the phase angle (y – axis). Furthermore, the analysis of EIS data includes the simulation of the system by an equivalent electrical circuit, called Randle’s circuit (R(RC)). The circuit consists of electrical elements like resistors, capacitors and inductors and is derived by the fitting of the EIS data in the electrical circuit model. The elements of the circuit are corresponded to similar properties of the MFC, such as a resistor to the biofilm resistance, a capacitor to the double – layer capacitance, etc.

The main components to create the equivalent circuit to simulate the MFC are the following:

- R_S (Electrolyte resistance), is the inhibition of current flow by the electrolyte used. The resistance of the electrolyte depends on the type of substances used and their ions, as well as the geometry of the chamber (anode / cathode), where it is placed.
- C_{dl} (Double – layer capacitance), is the perfect capacitor formed by the charge distribution in any interface in a polarized system (e.g., electrode / electrolyte, electrolyte / biofilm in a MFC).
- R_{CT} (Charge transfer resistance), is the resistance caused by the transfer of electrons from a solution to the electrode (e.g., electrolyte – biofilm transfer to anode electrode in a MFC).
- CPE (Constant phase element), is the non – ideal capacitor formed by the charge distribution in any interface in a polarized system. It may be used instead of the C_{dl} and it takes into account an uneven distribution of current flow across the interface studied.

- W (Warburg element), is the equivalent electrical circuit element that corresponds to diffusion impedance, since mass – transfer between the electrolyte and the biofilm affects the electrochemical kinetics greatly. This is observed in low frequencies during the EIS experiment.
- R_B (Biofilm resistance), is the resistance developed by the biofilm, in the MFC case that is the electrochemically active bacteria and possible competing microorganisms, which grow in the anode chamber.
- C_B (Biofilm capacitance), is the capacitor that forms in the interfaces of the biofilm, as charge separation occurs across the biofilm to assist their metabolism (charged ions movement).

However, the MFCs are complex bio-electrochemical systems which cannot be fully interpreted by a single technique. The application of the EIS method combined with cyclic voltammetry alongside biochemical measurements, in combination with the practical implementation of the technology is a solution for the best understanding of the processes that take place in MFCs.

2.3 Factors affecting MFC operation

To maximize the benefits of the MFC technology, the MFC configuration needs to be constructed in a sustainable and economic manner. In this direction, many research groups have examined MFCs either as stand-alone technology or as integrated in existing wastewater treatment processes [48]–[51].

2.3.1 Different MFC geometries

Based on the cathode compartment two different geometries emerge. In the case the cathode compartment is a surface, the MFC is called single – chamber and the electron acceptor is the oxygen in the atmosphere.

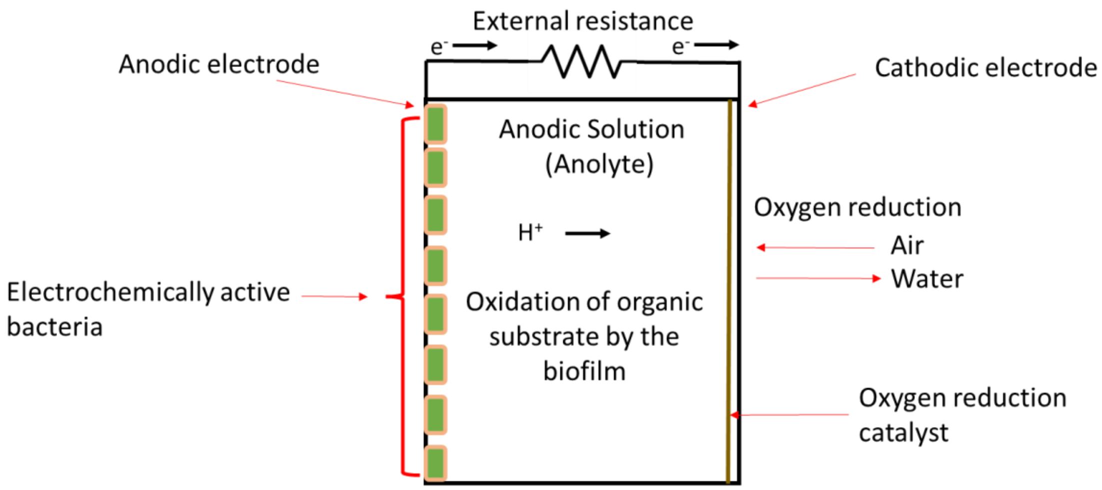

Figure 7. Single – chamber MFC schematic.

In the case of the single – chamber MFC, the electron donor is present in the anolyte. On the internal surface, a separator is placed to allow the products of the oxidation to diffuse through, but prevent the anolyte from spilling. The single chamber MFC geometry does not require electron acceptor supply, because one side of the cathode electrode is exposed to the atmospheric air. This offers continuously oxygen as electron acceptor to the system.

The cathode compartment may be a chamber with a set volume for the cathode electrolyte (catholyte), this is called a dual – chamber MFC (H – type).

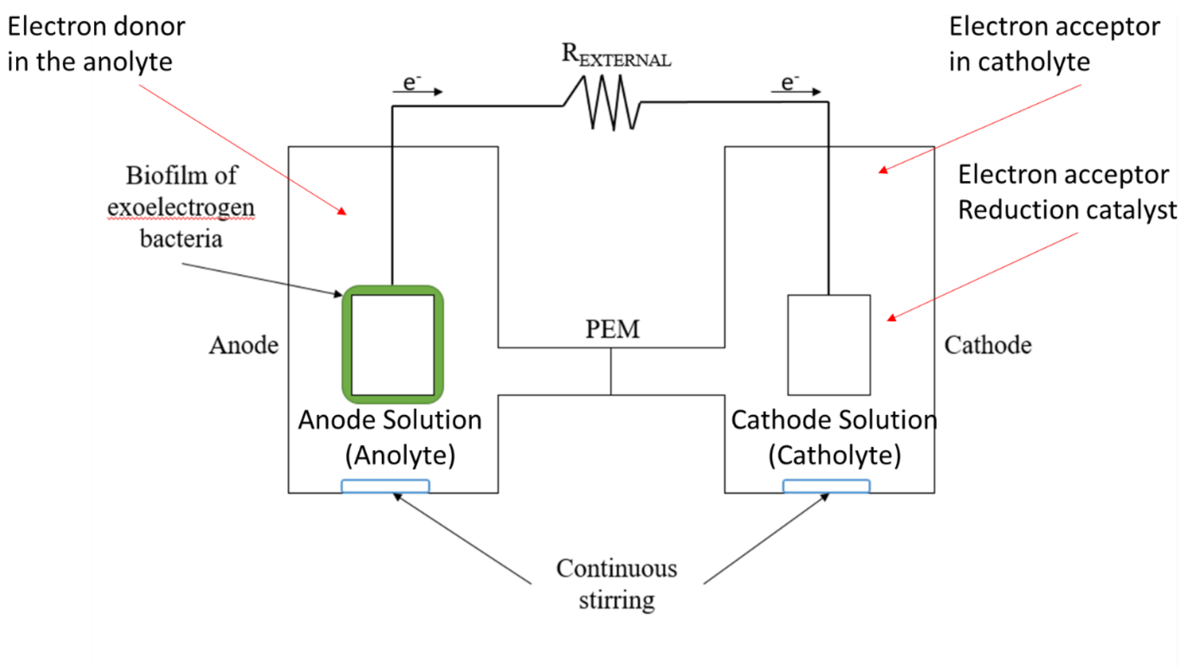

Figure 8. Dual – chamber MFC schematic.

In the case of the dual – chamber MFC, the electron donor is present in the anolyte and the electron acceptor in the catholyte. This configuration requires continuous aeration if oxygen is the electron acceptor, or new cathodic solutions to supply new electron acceptors to the system. Additionally, oxygen reduction requires a catalyst present on the cathode electrode. The dual chamber MFC offers the treatment of two wastewaters, one requiring oxidation and one requiring reduction, while generating electricity.

2.3.2 Microorganisms in the anode

The microorganisms are placed inside the anode chamber, along with the supporting electrolyte. The supporting electrolyte is a solution containing the electron donor (e.g., Glucose) and a buffer solution to assure proper pH, conductivity and feedstock for the microbes. The microorganisms require anaerobic conditions, to perform their metabolism. They may be grown in cultures to be placed inside the MFC or inserted as raw anaerobic sludge. In the latter case, anaerobic sludge inocula are placed in the feedstock. The optimal conditions for microorganisms in MFCs are the mesophilic. Additionally, the bacteria prefer neutral pH and the conductivity of the anolyte must be high enough, so as not to inhibit charge transfer. It has been observed, that the highest current outputs have been achieved by MFC inoculated with raw sludge or wastewater [20].

2.3.3 Electron acceptors

The selection of the electron acceptor depends on the use of the MFC. Oxygen is a typical example of an electron acceptor [52] used in single and dual chamber MFCs, due to its abundance in the atmosphere. In the dual – chamber MFC, oxygen is the usual electron acceptor during acclimation. The supply of oxygen in the cathode chamber is carried out via an air – pump. Furthermore, many alternative acceptors have been studied such as chromium [53], indium [54], copper [55] and silver [56], [57]. The ability of MFCs to reduce heavy metals in the cathode, makes this technology suitable for recovery of these metals from wastewaters.

2.3.4 Materials

Based on the use of the materials in a MFC there are different requirements. The possible uses of the materials are for electrodes, compartments, separators and connections. The selection of all materials should take into consideration the preference of cost – efficient options.

In many cases the materials used for the construction of MFCs have been also used in other fuel – cell technologies. An example is the use of the expensive proton exchange membranes as separators between the anode and cathode. The MFC operation has some restrictions due to the presence of electrochemically active bacteria, which do not appear on common abiotic fuel cells [58]. The development of the MFC technology relies on the usage of low cost but highly efficient materials and the avoidance of expensive catalysts (e.g., platinum), membranes (e.g., PEM) or other chemicals (e.g., potassium permanganate and ferricyanide) [58].

The materials employed in the MFC should be biocompatible when in contact with the electrochemically active biofilm. Additionally, high conductivity materials are used for electrodes in order to reduce the overall resistance of the system [59]. High specific surface area is a characteristic required for the anode electrodes, in order for the biofilm to grow on. The materials in contact with the electrolyte should not be affected by the pH or corroded, in order to achieve uninhibited operation for the maximum possible duration [60].

Apart from the technical characteristics required for the efficient operation of the MFC, the cost of the individual materials needs to be considered [61]. The selection of cost – efficient materials is necessary in order to improve the efficiency of the MFC, while at the same time keeping its construction cost to a minimum. The MFC operation is spontaneous and requires no external intervention, for this reason reducing the expenditure on materials, wastewater treatment and current generation are even more beneficial.

2.3.4.1 Compartments – chambers – structural support

The first material selection in order to assemble a MFC is the container. For the anode chamber the material has to offer structural support, must not inhibit microbial growth (not poisonous) and also should not be conductive. The use of conductive materials as the cell's container may result in a short – circuit and suboptimal operation. For the case of the cathode, similar materials like the anode chamber will be used, since the prerequisites are the same. MFCs are usually made of glass or Plexiglas, or other similar inert materials.

2.3.4.2 Electrodes

In order to optimize the MFCs performance, different electrode assemblies have been tested. Depending on whether it is for the anode or the cathode the electrode should have specific characteristics.

Anode

The anode assembly or the electrode assembly for the anode is used to refer to the electrode, the current collector and the connecting material. It is worth noting that the anode electrode should have high conductivity, in addition to a large specific surface area, resistance to corrosion, a high porosity, resistance to clogging (by the sludge or wastewater used) and finally it should be cheap and easy to manufacture, so that it can be applied on a larger scale. Common electrodes used in the MFC anode are plain or coated graphite/carbon-based materials such as graphite granules [62], felt [63], paper [64] and brush [65]. The preference of scientists for graphite and carbon is due to their large surface area, as well as their low cost [44]. The advantage of these materials is the rapid formation of strong biofilms, where subsequently electrochemically active bacteria dominate. The drawback of carbon and graphite – based materials is the low conductivity, when compared to other materials such as metals. To cope with this problem, researchers have combined graphite or carbon with highly conductive materials such as stainless steel or titanium, resulting in the reduction of ohmic losses in the assembly.

Cathode

On the cathode electrode the reduction reaction takes place, combining the products of the oxidation (anode) and the supplied electron acceptor. The same carbon – based materials are used for the cathode electrode, but a catalyst may be added as well, for the reduction reaction to take place. As mentioned already oxygen is a typical electron acceptor requiring catalysis. When using oxygen as the electron acceptor, although spontaneous, it is a slow reaction, so in order to maximize the rate, a catalyst such as platinum is coated on the cathodic surface [66]. Furthermore, instead of expensive catalysts such as platinum, microbes have been used to catalyze the oxygen reduction in MFC [67]. In this case the oxygen (gas) supplied to the chamber is reacting with the protons (liquid) on the electrode surface (solid), where the electrons are transferred through the anode. The presence of three phases in the cathode chamber has a considerable effect in the development of overpotentials greater than the anode equivalents. This results in the cathode being the limitation to the power production of the MFC.

2.3.4.3 Oxygen reduction catalyst

Oxygen reduction requires a catalyst to take place, however, usage of platinum in MFC has been reduced, due to the high cost of the material [68]. The usage of different catalysts is under research, in many cases developing cathode electrodes sustainably. A commonly used catalyst is manganese dioxide (MnO_2), which is already used in batteries (lithium, alkaline, zinc – carbon).

2.3.4.4 Anode – Cathode Separators

The separator between the anode and the cathode facilitates the transition of protons and helps avoid short circuit. The high internal resistance of dual – chamber MFCs is the result of the high ohmic resistances, high overpotentials and the pH gradients that are generated when using membrane as a separator. Various separators have been studied, especially for the single – chamber MFCs separators may even take structural role in the cathode electrodes. Aiming to decrease the internal resistances along with the cost of MFC configuration, the possible materials qualifying as separators are investigated. The advantage, regarding this matter, of single chamber MFCs is that the expensive separator can be switched with a cheaper one, acting at the same time as the structural material for the cathode electrode [69].

2.3.4.4.1 Membranes

Conventional membrane separators (e.g., Proton Exchange Membranes), have a high cost [70] and increase the ohmic losses [20] limiting the MFC performance efficiency [71]. The most commonly used membrane separators are proton exchange membranes. Less expensive options are cation and anion exchange membranes (CEM, AEM, respectively). Due to the selectivity of these membranes, allowing one type of charged particles to cross through them, their cost increases greatly, even for a few cm^2. Another type of membranes used are the bipolar membranes, which contain both an anion exchange and a cation exchange layer. The disadvantages of membranes, apart from their high cost, include the increase of the MFC's internal resistance, thus reducing its performance and the possibility of back – migration phenomena. Migration is the movement of charged ions due to the presence of a magnetic field. In the MFC a "forward" path may be considered from the anode to the cathode, regarding the proton transfer. In many cases, a gradient forms between the pH of the anode and the cathode due to the continuous flow of protons from the anode to the cathode. This results in the pH increase of the anode and the respective decrease in the cathode. Afterwards, the opposite process may take effect. A proton exchange membrane will allow, for example, the back transfer of protons, due to the pH gradient.

In order to avoid the use of expensive membranes, their removal from the MFC configuration is an approach examined [49]. Materials which have been proven useful to substitute membranes in the MFCs are ceramic based cathode electrodes, which provide a structural support as well. Another assembly is the use of Gore-Tex cloth with a catalytic paste, wrapped around a Plexiglas tube for structural support [72].

2.3.4.4.2 Gore-Tex

The use of cheap and cost – effective materials has been the aim of this research. A material which was adopted from past works [44], is the Gore-Tex cloth. A simple method was used to convert a non – conductive material (GORE-TEX® fabric) in electrically conductive and catalytically active material. GORE-TEX® fabric consists of layers of polytetrafluoroethylene (PTFE), has small pores, is durable and waterproof. In every square inch of fabric there are over 9 x 109 tiny pores, while each pore is 20 times smaller than a drop of water. These properties make Gore-Tex an ideal separator between the anode and the cathode in single chamber MFCs. Based on the water – proof properties of Gore-Tex, the addition of a electrocatalytic paste on it, forms a cathode electrode for air cathode single chamber MFC. The Gore-Tex cloth requires structural support which may be offered by a Plexiglas tube.

2.3.4.4.3 Mullite

Ceramic materials have shown comparable results with ion-exchange membranes at significantly lower cost [58]. Such ceramic materials examples are mullite and terracotta; both have been used as separators in MFCs, with mullite being more effective [73].

The use of ceramic materials in the MFCs is an option that offers advantages, such as resistance to fouling [74], lower cost when compared to other materials used (eg. Platinum coated electrodes) [58], thermal, chemical and mechanical stability [59]. Ceramic separators coated with oxygen reduction catalyst have been successfully used in single chamber MFCs [73], [75][73], [75].

In order for the ceramic materials to be used as a structural component of the electrode, a catalyst needs to be deposited on the surface exposed to air. Various techniques have been employed to accomplish this. Assuming the oxygen reduction catalyst is activated carbon, the following ways of deposition are the most notable. A two-step process was employed to create the activated carbon catalyst, with a phytic acid-doped polyaniline coating and subsequent high-temperature pyrolysis, by[76]. The catalyst was then placed on a stainless-steel mesh with polyfluortetraethylene (PTFE) using a rolling method technique [76]. Another approach of utilizing activated carbon was presented by [77], placing an activated carbon layer on a gravel bed with a copper plate for the electrical connection. This set-up was used as the air-exposed cathode electrode of a single chamber MFC [77]. Activated carbon mixed with carbon black placed on a stainless-steel mesh was used by [78]. The activated carbon mix was prepared by adding carbon black, activated carbon, PTFE and DI water using ultrasonication and afterwards spreading the paste on stainless steel mesh [78].

2.3.5 Temperature, pH & conductivity

The temperature affects the microorganisms and consequently the performance of the MFC. Research has shown that the performance of a single – chamber MFC is inhibited by a temperature below 20 ^{o}C [79]. The optimal conditions for MFC operation are mesophilic. Most MFCs operate under neutral pH conditions to favor the growth of electrochemically active bacteria. However, during the operation of a MFC, the metabolism of the substrate by the microorganisms leads to pH changes in the anode and cathode. More specifically, the production of protons at the anode results in a decrease in pH, while their consumption at the cathode leads to an increase in pH. To combat this phenomenon and maintain the pH at neutral levels, a suitable buffer solution is often added. The performance of a MFC depends to a significant extent on the conductivity of the anode and cathode (if present) solutions.

2.3.6 Substrate / wastewater

The ideal conditions for MFC operation are different for each substrate. For this reason, each different substrate requires separate examination to determine the efficiency of MFC operation, while treating it. The variety of substrates used and their characteristics will be detailed in a separate chapter. The substrate used in the MFC technology is one of the major factors affecting its performance [80]. The MFC technology has exhibited high wastewater treatment efficiency over a range of substrates [50], [69], [80].

2.3.7 External resistance (discharge) & Connecting points

For the operation of the MFC, a resistance is connected externally between the anode and the cathode electrode. In order to monitor the voltage development of the MFC, the anode and cathode electrodes are connected to a voltage recorder. Furthermore, connecting points exist within the cathode electrodes between the current collector and the catalyst layer, where the reduction takes place. In the anode, the respective current collector has to be placed in the electrode containing the electrochemically active biofilm. All of these connections contribute to electrochemical losses, resulting in reduced efficiency in the MFC operation. On the other hand, they are necessary for the operation, as both the external resistance and the current collectors facilitate the electron transfer.

The external resistance is the load connected to the system in order for the converted chemical energy to be utilized as electricity. An external resistance has the role of a lamp connected to an electrical circuit. In the MFC as soon as the wastewater is placed in the anode and the resistance is connected on the electrodes the operation initiates.

2.3.8 Operation mode (Batch / Continuous)

The way a MFC is operated affects the performance during the wastewater treatment. Depending on the continuous, batch or semi-batch operation the power output of the MFC differs.

The continuous operation has achieved higher power outputs, due to the nature of the operation, but requires the addition of a feedstock pump to the system and a feedstock preservation system.

2.4 MFC advances and applications

A MFC possesses the ability to utilize an organic substrate and generate electricity. The organic substrate is oxidized, which makes this technology ideal for the decomposition of organic compounds found in wastewaters. The generation of electricity from wastewater treatment is what makes this technology appealing and research has focused on the scale – up and potential applications of the MFCs.

2.4.1 Configuration design, Scale – up and MFC stacking

In order to improve the overall efficiency and power output of MFCs, multiple cells can be connected in parallel or in series, through external electrode connections. This way MFC stacking can increase the combined current output or improve the overall performance efficiency of the MFC array in comparison to the individual MFC operation. Another approach is the scaling up of a MFC, but the increase in the electrode dimensions and the compartment dimensions does not necessarily lead to an improved performance. Additionally, MFCs have been operated in a cascade, which utilizes the effluent of one MFC as the inlet to the next.

It has been reported that the increase of the MFC scale led to a decreased power output [81]. The increase in the MFC compartment volume leads to increased internal resistances, whether they are caused by the electrode distance or the increased amount of wastewater present between the electrodes. To deal with higher volumes of wastewater requiring treatment, multiple small scale MFCs can be employed, since the power output has been reported to increase with miniaturization and multiplication, as well as stacking (external connections) [82]. The upscaling of MFCs requires the connection of multiple individual cells instead of increasing the dimensions of one cell, which may cause reduced current density output due to the increased electrode surface [81], [82].

Microbial fuel cells have been reported to generate lower energy when compared to traditional fuel cells or batteries [82]. To further optimize the MFC setups ceramic materials have been investigated as cathode electrodes or separators [83]. An example of ceramic materials used in a MFC stack was presented by [73], utilizing mullite and terracotta for the cathode electrodes of the MFCs, creating two arrays. The two arrays consisted of twelve MFCs each and treated the same wastewater (urine), operating continuously. The mullite stack achieved a higher power output (800 μW) when compared to the terracotta stack (520 Mw) [73]. Another MFC array was used by [81], consisting of 5 individual MFC units, treating swine wastewater, in continuous operation and with the wastewater cascading from one MFC to another. The parallel operation resulted in a higher COD removal (83%) and a higher power output (175.7 W/m^2), when compared to the series operation (77% COD removal and 67.5 W/m^2) [81]. The series connection presented greater electrochemical losses due to the cross-conduction effect, which generates parasitic currents inhibiting the MFC operation. Additionally, voltage reversals may be present in the series connection of MFC units. Voltage reversal refers to the reversal of the polarity in the MFC electrodes and the loss of power generation, which is caused by the common current running through the MFC units of the array, when connected in series [81]. An array consisting of six MFC units was developed by [82], operated continuously and in a cascade treating a synthetic wastewater and achieving high COD removal (>95%). It was reported that the array presented a more stable operation during the parallel connection, achieving higher power and current output than the individual MFCs [82]. Another example of MFC optimization was presented by [84], creating a MFC array consisting of four microfluidic MFCs. In particular, (microfluidic) channels establish microscale laminar flow of the anode and cathode solution and no separator is required, as a discreet liquid (anode) – liquid (cathode) interface is formed. The maximum power density of the MFC array was 60.5 $\mu W/cm^2$, described as four times higher than the power output of the individual MFCs [84]. Larger number of MFCs have been also investigated in a stack configuration. As reported by [85], two MFC stacks were created, each consisting of 32 individual cells. The cells were made of a ceramic tube (terracotta) acting as the structural support and the anode – cathode separator. The stacks were operated with urine as the feedstock, each achieving a maximum power density output of 24 mW/m^2. Lower power density output was obtained after the two stacks were connected in parallel (9 mW/m^2) and in series (19 mW/m^2) [85]. Another work was reported to utilize 560 MFC units connected in an array, that generated a power output of 245 mW [83].

2.4.2 MFC in dye degradation

A valuable use of the MFC technology is the treatment of synthetic dyes. Dyes have been reported as major cause of water pollution and pose a danger to human health and the environment

[86]. Azo dyes are synthetic colorants found in the waste of textile industry. The treatment of the wastewater containing these dyes requires a combination of anaerobic and aerobic treatment, due to the resistance these substances present to degradation [87], [88]. The advantage the MFC offers is the possibility of oxidizing or reducing the synthetic dye wastewater in the anode or cathode, respectively, depending on the required process [89].

The MFC technology has been utilized, both the anode and cathode, for the successful decolorization and degradation of an azo dye (Acid Orange 7) [87], [88]. The MFC technology was reported by [87] to decolorize the Acid Orange 7 solution over the period of four days, whether it was placed in the anode or the cathode chamber. A higher COD removal (80%) was reported for the cathode solution containing the dye, than the respective COD removal (60%) of the anode solution containing the dye [87]. Another work focused on the treatment of a synthetic wastewater containing anthraquinone dye, achieving 80% - 90% decolorization over a period of four days [86].

2.4.3 Biosensors and bioremediation for environmental pollution

Biosensors are devices that produce a measurable signal, proportional to the measurable value (concentration, temperature), using bacteria. Bioremediation refers to the destruction, detoxification or immobilization of harmful components with the help of microorganisms [90]. The MFC technology has been effectively used to detoxify Cr(VI) wastewater withing acceptable discharge limits [90]. MFCs have been used as biosensors for a number of different substances, such as organic toxins, heavy metals, BOD and VFAs among others [91].

2.4.4 Metal recovery from wastewater

Another use of the MFC technology is based on the cathode reduction, to electrochemically recover materials present in the cathode solution. A variety of metal and heavy metal ions are present as pollutants in wastewaters, which can be used as electron acceptors in MFCs, due to their redox potential [92]. MFCs have been used to reduce and if needed recover a variety of heavy metals including chromium (Cr(VI)) [53], [93], silver (Ag) [56], [57], copper (Cu) [55], [94], indium (In) [54], selenium (Se) [95] and Gold (Au) among others [92]. The heavy metals have been recovered from synthetic or real wastewaters with MFC configurations utilizing abiotic or bio-cathodes [96]. The majority of the heavy metal reduction experiments are conducted in a dual chamber MFC where the electron acceptor is supplied in the electrolyte.

An application of the MFC technology for material recovery was studied in this work, as a part of a proposed PV panel recycling process.

2.4.5 Power management system for optimized MFC performance

In order to implement the MFC technology in every day applications, the voltage development has to be further increased. So far, the recorded voltage produced in a single MFC does suffice for the requirement of electronic devices [97]. This issue has been partially addressed with the stacking of multiple MFCs, creating MFC arrays. Connecting multiple MFCs in parallel or series connection can enhance the overall voltage output of the system [98]. However, it still does not fulfil the requirements in terms of voltage development of an electronic device, unless a large number of MFC units is used. This leads to the disproportionate area of the MFC array compared to the voltage development of the MFC array. Another proposal is to increase the voltage output of the MFC technology through the use of power management systems.

Power management systems consist of electrical components such as a boost converter, a charge pump, a super capacitor, solid state relays and a charge pump. These components have been used in order to increase the voltage of MFC units to the requirement of specific electronic devices. An example of a power management system was developed for a MFC, which powered successfully a submersible ultrasonic receiver and a real time clock [99]. The type of cell used was a sediment microbial fuel cell, deployed in Palouse River, Pullman, Washington. The MFC set – up consisted of an anode (0.2 m^2) and a cathode (2.4 m^2) connected to the power management system, as shown in Figure 9. The operation of the MFC powers the real time clock and excess energy is stored for the submersible ultrasonic receiver. Once enough power is stored the receiver performs a scan, detecting ultrasonic frequencies and recording the time from the clock. Afterwards, the receiver is set idle and the process repeats. It was also highlighted that sediment MFCs were used to operate temperature sensors [99].

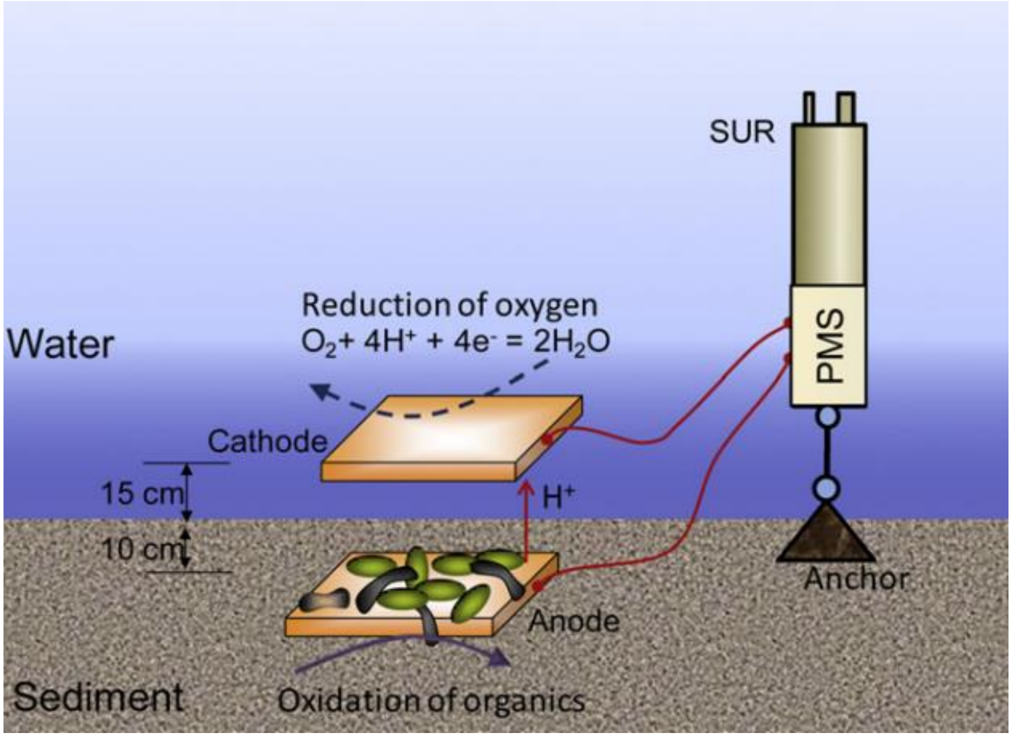

Figure 9. Schematic diagram of the sediment microbial fuel cell connected to the submersible ultrasonic receiver (SUR) and the real time clock (RTC) [99].

3 Microbial Fuel Cell modeling

The different processes that occur within BES such as MFCs can be broken down into the following phenomena: i) microbial metabolism on the anode electrode, ii) diffusion of the organic substrate from the bulk into the biofilm of the anode chamber initiating the oxidation reaction of the electron donor iii) transport of the organic substrate by diffusion and by stirring (convection) in the bulk of the anolyte, iv) oxidation reaction and production of protons and electrons, v) transfer of electrons through the wiring connection (external resistance) from the anodic electrode to the cathodic electrode [100]. In the case of a MEC, instead of simply connecting an external resistance, a voltage is applied between the anode and the cathode. The protons are diffused into the anode and then are transported with convection and diffusion through the separator to the cathode chamber (vi), to either participate in the reduction reaction or to balance out their concentration gradient between the anode and the cathode. Other substances produced by the oxidation are diffused into the bulk of the anolyte. In the cathode chamber the electron acceptor comes in contact with the cathodic electrode and, combined with the electrons, starts the reduction reaction (vii). The products of the reduction are deposited on the cathode electrode, settled in the cathode chamber or mixed with the bulk of the catholyte (viii). Moreover, in the case of a bio-cathode, microbial metabolism is also studied in the cathode. Overall, charge transfer and balance are examined in the BES, along with losses regarding the developed voltage [100].

Modeling is a powerful tool, in order to understand the complex processes occurring within MFC systems. Several models have been proposed in this direction. Because of the various MFC set-ups (single chamber, dual chamber) and the variety of materials used for the electrodes and the catalysts in combination with the different phenomena during the MFC operation, many models have been developed [101], [102]. One of the first models describing MFC operation was created by Zhang and Halme 1995 [103]. Zhang and Halme [103] simulated the operation of a dual-chamber MFC by using Monod kinetics to describe the bacterial growth and substrate consumption, coupling it with Faraday’s law to calculate the current generation. The model was based on the assumption that mass transport and the cathodic reaction are faster than the biochemical and oxidation reactions, thus focusing on the latter. As one of the first attempts in MFC modeling, they highlighted the importance of control over the process by simulation [103]. An example of a model combining bioelectrochemical kinetics along with mass and charge balances in a dual-chamber MFC was developed by Zeng et al. 2009 [104]. The developed model aimed to describe an acetate fed dual chamber MFC. In order to describe the electrochemical phenomena, the combination of the Butler-Volmer expression with Monod kinetics was utilized. Some of the parameter values were extracted from experimental data and some were estimated by the model. Zeng et al 2009 concluded that the cathodic reaction is the limiting factor for the current generation in a MFC. Furthermore, their results indicated that an increase in the electron donor concentration was effective in boosting the MFC performance [104].

Various approaches have been presented in the literature, with different focus points. A study on the biofilm of electrochemically active bacteria during the operation of a MFC was conducted by Belleville et al. 2019 [105]. A 2D model was developed, examining the microorganisms on the anodic electrode at a cellular level. Taking into account microbial growth and segregation, their model aimed to predict the different types of bacteria (methanogens, electrogens) that grow, perish or detach from the electrode during the operation of a glucose fed MFC [105]. Serra et al 2019 focused on the power output of MFCs through polarization curves and created a steady-state electrical model to simulate them [106]. The polarization experiments were conducted by varying the external resistance on six different MFCs from 1000 Ω to 20 Ω, with a simultaneous refreshment of the synthetic wastewater. The model had different kinetics for the different power losses (activation, ohmic, concentration) which may be present during the MFC operation [106].

Furthermore, the various operation modes of MFCs have been examined. A 2D model for simulating the operation of a continuously fed, single-chamber MFC was developed by Day et al 2021 [107]. Different parameters, such as the variation of the hydraulic retention time (HRT) and the alteration of MFC geometry were examined, in order to determine the optimal conditions for simultaneous maximum current generation and substrate consumption. Matsena et al. 2021 created a model simulating the operation of a MFC with hexavalent chromium as the electron acceptor [108]. To describe the growth of the biofilm, Monod kinetics were used, taking into account inhibition by the substrate and the intracellular mediator. Moreover, two types of microorganisms were considered; one that contributes to electricity generation and one that consumes the substrate without releasing electrons. For the description of the electrochemistry, the Butler-Volmer expression was utilized and for the coupling of electrochemistry with microbial activity Faraday’s law was used. In order to simulate the reduction of hexavalent chromium they combined Faraday’s law with Bulter - Volmer and the mass balance equation was derived from the reaction of dichromate (Cr_2O^{-7}) to Cr(III) [108].

Apart from simulation describing MFC operation, models have been developed to support experiments. Sindhuja et al 2016 conducted electrochemical impedance spectroscopy (EIS) experiments in a dual chamber MFC and developed a model to extract the equivalent circuit [109]. The model was developed for a MFC with charcoal electrodes and was used along with a fitting model of Nyquist plot for graphite electrodes. Their aim was the determination of internal resistances in both experimental configurations (charcoal, graphite-based electrodes respectively) and the estimation of the rate determining step in their MFC operation, with glucose as the organic substrate [109]. Oliveira et al 2013 published a study presenting a 1D MFC model [110]. This particular model incorporated heat, charge and mass transfer phenomena at steady state across a MFC configuration, consisting of an anodic electrode, a biofilm, the anolyte solution, the separator (proton exchange membrane), the catholyte and the cathodic electrode. They successfully compared their computational data to the respective results presented by Zeng et al. 2009 [104], [110]. By briefly presenting these models it is easy to understand that MFC modeling is applied over different focus points (i.e., cellular level, spatial and time dependent or dimensionless) resulting in a plethora of publications describing different aspects of this technology.

4 Materials and Methods

In this chapter the set-up of each experiment is described. First, the construction of the electrodes is presented along with the assembly of the MFCs. Then, the analytical techniques are detailed. Finally, the acquisition, preparation and characterization of the effluents used is described and the chapter closes with a table summarizing the various experiments with the different parameters studied.

4.1 Single – chamber Microbial Fuel Cells assembly

The materials used for the single – chamber MFC construction were Plexiglas and Ertalon®. For the anode electrodes, the materials studied were graphite granules, rods and paper, carbon veil and felt and stainless-steel sponges. For the cathode electrodes different catalysts of the oxygen reduction were examined including manganese dioxide, biochar, activated carbon, fly ash. Additionally, Gore-Tex and mullite were tested as cathode electrode materials.

4.1.1 Single – chamber MFC geometry

For the single-chamber MFCs two different geometries were employed, one rectangular and one cylindrical.

The rectangular single-chamber MFCs were made of Plexiglas. The Plexiglas compartment had a height of 15 cm and the same width for all four sides at 9.5 cm. The thickness of the material was 0.8 cm. The total volume of the Plexiglas single-chamber MFC was 0.6 L. The bottom and the lid of the Plexiglas MFC had four 2 cm holes in order for the tubular cathode electrodes to run through the compartment. Furthermore, the lid contained three holes, each 0.8 cm, two of these were used for the inlet and outlet tubes and one for the graphite rod placed for the electron collection. Finally, two holes (diameter 4 mm) were present in the lid for the tubes which were used to circulate Nitrogen (N_2) inside the Plexiglas MFCs to ensure anaerobic conditions.

Figure 10. Rectangular Plexiglas single chamber air cathode MFC. a) Disassembled cell and b) Assembled cell with Gore-Tex electrodes during leakage test.

The cylindrical single-chamber MFCs were made of Ertalon® with a total volume of 0.6 L. The height of the cell was 11.5 cm whereas the “active height” (anode chamber) was 8 cm long. The internal diameter of the unit was 11 cm. One circular Ertalon® lid seals the top of the chamber. The lid is constructed to fit up to four tubes with external diameter 2 cm. The cylindrical lid contained the same holes (0.8 cm) as the rectangular lid, in order to fit the graphite rod as well as inlet and outlet tubes.

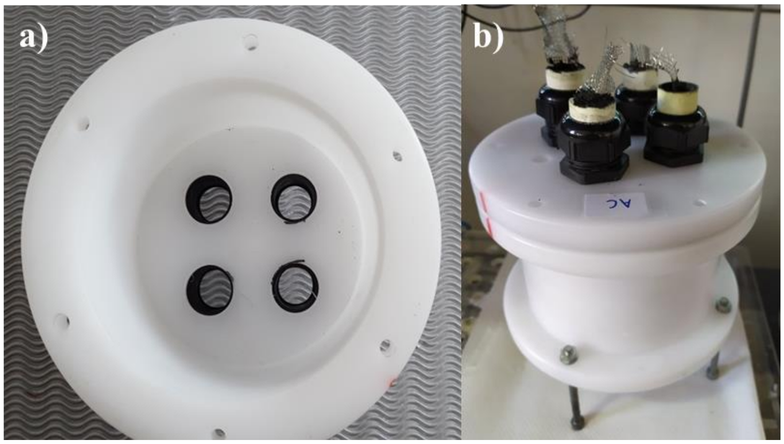

Figure 11. Cylindrical Ertalon® single chamber air cathode MFC. a) Disassembled, top-down view of the interior and b) Assembled cell with mullite electrodes.

An additional cylindrical single-chamber MFC was constructed of Ertalon® (top and bottom) and Plexiglas (cylinder), in order for the anode chamber to be visible. This was different from the other cylindrical MFCs due to the larger size, with a volume of 1.4 L. The height of the cell is 13 cm whereas the “active height” (anode chamber) is 9 cm long. The internal diameter of the unit is

14 cm with 2 mm wall thickness. Two circular Ertalon® lids seal the top and the bottom of the chamber. The lids are constructed to fit up to six tubes with external diameter 2 cm. Specifically due to its relatively big internal diameter this MFC was selected for testing different number (up to six) of cathode electrodes.

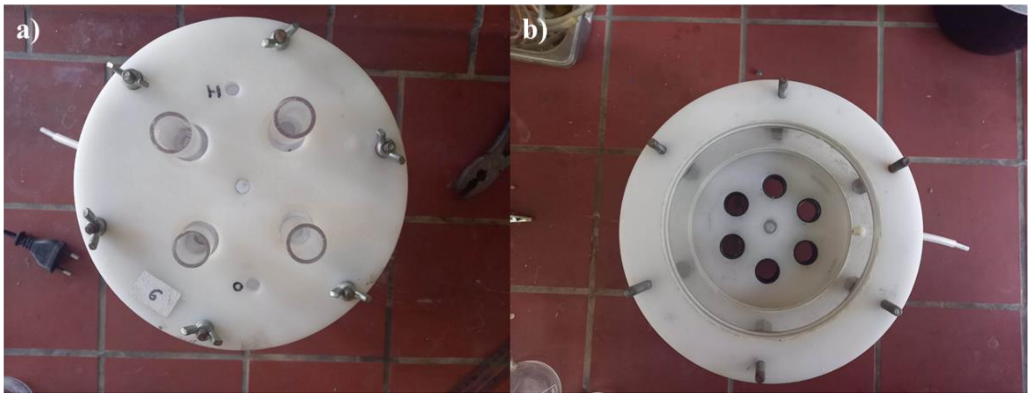

Figure 12. Cylindrical Ertalon® single chamber MFC with modifiable lid and bottom to fit 4 and 6 electrodes. a) Top-down view of the 4 electrode set – up and b) top down view of the 6 electrode set – up.

In all cases the inlet is at the top, with the feedstock flowing towards the bottom of the anodic chamber, for better fluid percolation. The outlet is placed on the side of the anodic chamber, relying on overflow to remove excess liquid from the anode chamber.

4.1.2 Anode electrode preparation

The anode materials studied were carbon-based electrodes. In each MFC a support for the electrochemically active biofilm to grow on, is required and also a current collector to facilitate the electron transfer from the anode to the cathode. The anode configurations used, are presented below:

- Graphite granules with a graphite rod

Graphite granules (type 00514, Le Carbone, Belgium), with diameters ranging between 1.5 and 5 mm, were used as the anodic biofilm support and conducting material, conveying electrons to a graphite rod (13 cm long by 7 mm diameter) inserted into the packed bed of granules. The graphite rod acts as the electron collector, allowing the voltage recording of the anode and the connection of the external resistance on the anode electrode. The specific surface of the graphite granules was 817 – 2720 m^2/m^3. Prior to use the graphite granules were washed with HCl (0.1 M) to remove residues and other substances, maximizing the specific surface area. The washing process was repeated four times and was similar to [111].

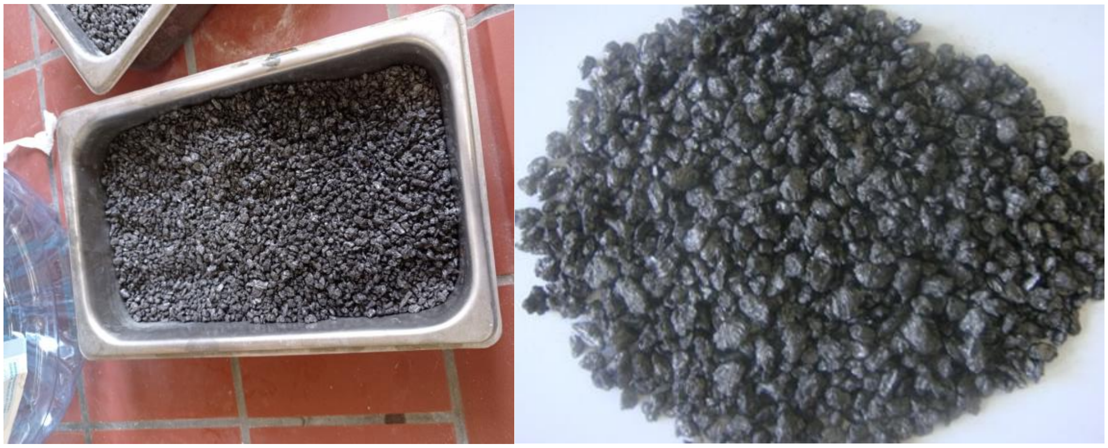

Figure 13. Graphite granules as the biofilm growth medium.

Figure 14. Graphite rods used to facilitate the current collection from the graphite granule bed.

- Graphite felt

Plain graphite felt (Alfa Aesar, 6.35 mm thick, 99%) was used as an anode electrode, with a titanium wire woven through it as the electron collector.

- Stainless steel sponge

Another material studied for its performance as anode electrode was the stainless-steel sponge. Two cases of commercially available sponges were examined, one with plain stainless-steel sponge and one with a stainless-steel sponge heated at 550 ^{o}C for 8 h. In both cases a stainless-steel wire was woven around the sponges as the current collector, on which the voltage recording wires were connected.

Figure 15. Stainless steel sponges placed in a cylindrical single chamber air cathode MFC with 4 mullite electrodes.

4.1.3 Cathode electrode preparation

The cathode electrode assemblies consisted of the following parts:

a) Structural support
b) Anode – Cathode separator
c) Oxygen reduction catalyst
d) Current collector

4.1.3.1 Oxygen Reduction Catalytic paste

Various oxygen reduction catalysts have been studied for their effect on the MFC performance. To incorporate the catalyst in the cathode electrodes, each catalyst examined was placed in a catalytic paste. The oxygen reduction catalytic paste was prepared similarly for all cathode electrodes. In particular, graphite paint (12 g, YSHIELD HSF54), xylene (3 ml), ethanol (3 ml) and 3 g of the selected catalyst were mixed and subsequently sonicated for 0.5 h, in a 5510 Branson ultrasonic bath. The catalytic paste produced this way was used for each cathode electrode. Specifically, the catalysts examined were manganese dioxide (MnO_2, EMD Tosoh Hellas), activated carbon (AC, Sigma-Aldrich, CAS 7440-44-0), fly ash (FA, acquired from Megalopoli Power Plant in Arcadia, Greece), wood biochar (15-150μm). The catalysts selected for each set of experiments are specified in the corresponding sections.

Figure 16. Oxygen reduction catalytic paste spread on a Gore-Tex cloth with a copper wire inserted for electron collection.

4.1.3.2 Plexiglass – Gore-Tex electrodes

Two types of electrode configurations were tested, one with Plexiglas tubes as the structural support and one with mullite. The process to create the Plexiglas – Gore-Tex electrodes is described below.

Commercially available Plexiglas tubes (2 cm diameter, 2mm thickness) were used as the structural support. Plexiglas tubes were uniformly perforated with circular holes (2 mm diameter) which offer surface area available for proton transport from the anode to the cathode. Gore-Tex cloth was used as separator and as support of the cathode oxygen reduction catalyst. The oxygen reduction catalyst was contained in the catalytic paste which was spread on the Gore-Tex cloth, inserting the current collector in the paste and leaving the mix to dry. Afterwards, the cloth is tightly bound on the outside wall of each perforated tube, the side covered with the catalyst coating being the air-facing side (cathode). In Figure 17, the stages of the preparation process of Gore-Tex electrodes are presented.

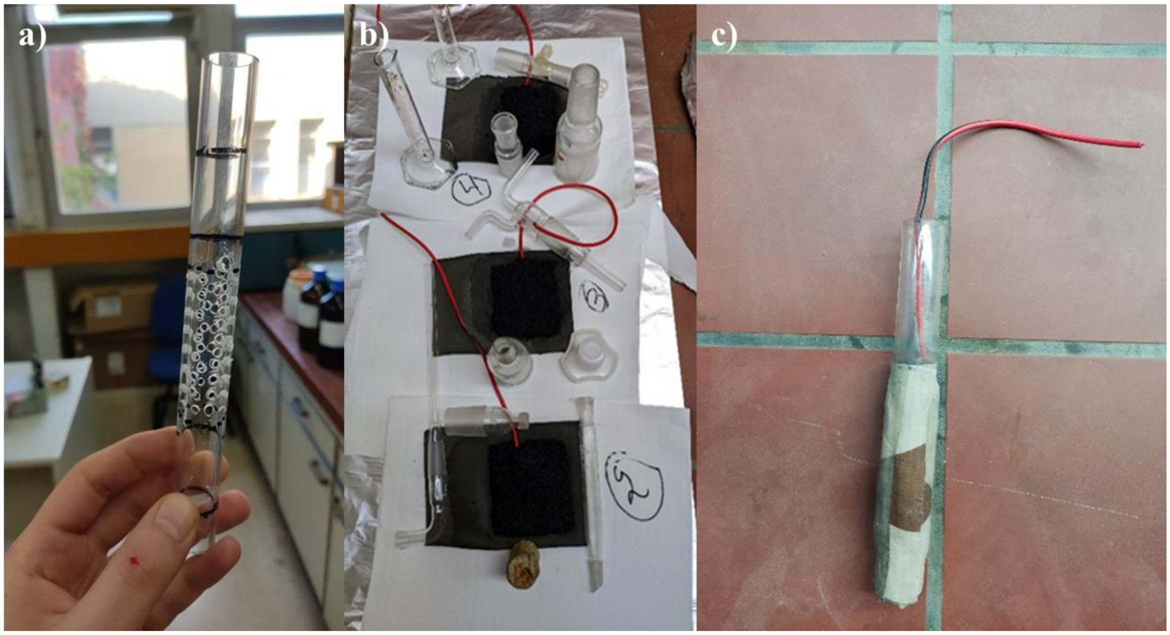

Figure 17. Gore-Tex cathode electrode assembly process, a) perforated Plexiglas tube and wounded thumb, b) oxygen reduction catalytic paste spread on Gore-Tex cloth with copper wire and c) ready Gore-Tex cathode electrode, by wrapping (b) around the tube (a).

4.1.3.3 Mullite electrodes

The process to create the mullite electrodes is described below.

The production of structural ceramic from mullite was achieved through a gel-casting method. Specifically, the reactive organic monomers used in experiments were monofunctional acrylamide, $C_2H_3CONH_2$ (AM) and difunctional N, N-methylene-bisacrylamide $(C_2H_3CONH_2)_2CH_2$ (MBAM). The initiator was ammonium persulfate $(NH_4)S_2O_8$ and the reaction was accelerated using the catalyst N, N, N, N, tetra-methyl-ethylenediamine (TEMED). An aqueous premix solution of water-soluble monomer acrylamide and crosslinker methylene bisacrylamide (MBAM) in 4:1 ratio was used to prepare the slurries. Darvan C was used as a dispersant in the premix solution. For the suspensions of mullite, powders were prepared with solids loading 60%wt, 70%wt, 80%wt respectively. All suspensions were mixed by ball milling using zirconia spheres. The amounts of 1μL of ammonium persulfate (APS) and 0.5 μL of tetra methyl ethylenediamine (TEMED) per gram of slurry were added in each suspension. The formed slurries were casted in tubular molds of variable dimensions till gelation. Prior casting de-airing was performed using a mechanical vacuum pump. The thermal behavior of the gelled system (methacrylate based polymer matrix ceramic composite precursor) and its volatiles removal was followed by TGA measurements under air from 20^oC to 950^oC with a 5K min-1 rate using a Setaram TGA 92 system. Viscosity of the casting slurries was measured using a Brookfield DV-II Pro viscometer at 20 ^oC. Final sintering temperature of the tubes were at 1200^oC/2h providing the ceramic tubes of 18-20% open porosity. The dimensions of these electrodes were: Φ 25 x 180 mm with inner diameter Φ 20 mm and useful internal catalyst surface of 0.44 m^2.

4.1.3.3.1 Coating of the catalyst inside the mullite tubes

Three different techniques were applied in order to coat the oxygen reduction catalytic paste on the inside of the mullite tubes:

Manually brushed (Brush-Coat – BC): The catalytic paste was allowed to dry until a thick slurry was formed, which was afterwards applied inside the specimens using a brush (size 4 – Germany) in 2 layers with natural drying in between. The produced specimens were left to dry naturally for one day.

Using ultrasound (Sono-Coat – SC): The specimens were placed on the ultrasound device (Vibra cell 750 – SONICS, USA) so that the tip was put at a depth of 1 cm from their upper surface. A quantity of the suspension (under stirring) was placed inside the specimens with the help of a pipette, after they were sealed from below with a plastic cap, so that there were no leaks. The sounding process lasted 20 min at 19% of the range, during which suspension refills were needed, so as its level in the test tubes remained the same. At the end of the process, the remained amount of suspension was removed, the cap was taken away and the specimens were allowed to dry naturally for one day.

Wash-coat (WC): during this technique, the slurry was poured into the inner surface of the tube and left to dry physically (up to 24h). Four repetitions were enough for the deposition.

In Figure 18 the stages of mullite electrode production are presented. Starting from the construction from scratch or using commercially available mullite tubes, preparing the oxygen reduction catalytic paste and then employing the techniques to deposit the paste in the interior of the mullite tubes, with the current collector inserted in the paste. The resulting mullite tube is shown in Figure 18 d and e, with different current collectors used (copper wire and stainless steel mesh, respectively).

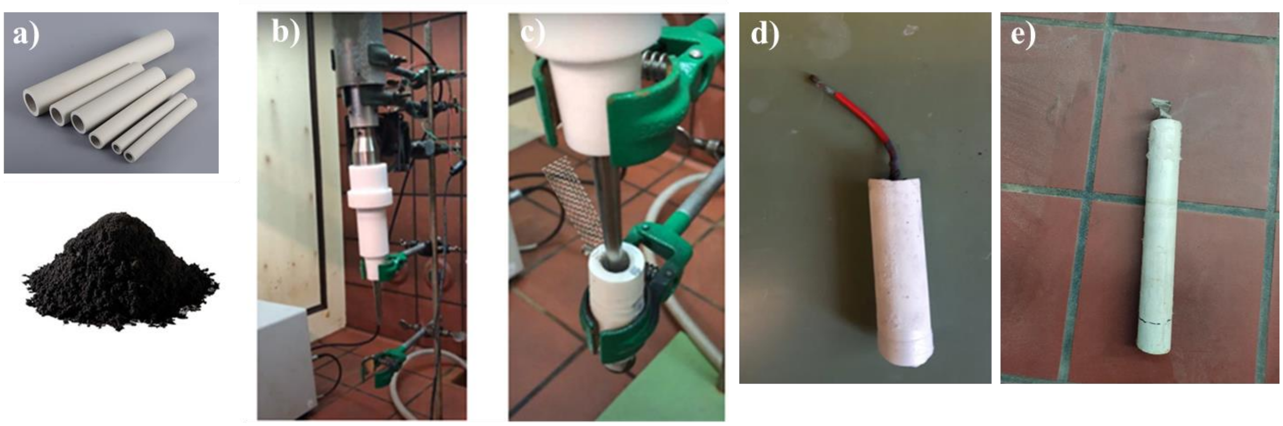

Figure 18. Production process of mullite cathode electrodes, a) mullite tubes and oxygen reduction catalyst, b and c) sono-coating of mullite with the catalytic paste, d and e) mullite cathode electrode with copper wire and stainless-steel mesh as electron collectors, respectively.

After the construction of the cathode electrodes, they were inserted in each MFC. The anode was placed as well in the MFC and leakage tests were conducted. Inlet and outlet tubes along with gas sparging tubes were placed on the lid of the MFC and the assembly was completed. After this process the cell was ready for use.

4.2 Dual – chamber Microbial Fuel Cell assembly

The ability of the dual–chamber MFC to treat two wastewaters simultaneously was investigated, using glucose synthetic wastewater in the anode to be oxidized and a chemical extract containing heavy metals in the cathode to be reduced. Two H – type MFCs were employed for these experiments.

The first was a glass dual–chamber MFC consisting of two 310 mL bottles, connected through a glass bridge where the anode – cathode separator was placed. The anode electrode (2.5 cm x 3.8 cm) was made of plain carbon paper (10 wt.% wet proofing, E-Tek), while the cathode electrode was made of carbon cloth, containing 0.5 mg/cm^2 of Pt catalyst (E-Tek). A proton-exchange membrane (PEM, Nafion™ 117, DuPont) was used to separate the anode and cathode compartments, with a total surface area of 3.8 cm^2. The system was placed inside a temperature-controlled box, set at 32 ^{o}C.

Figure 19. Glass dual chamber MFC, operating with oxygen (air pump – black tube) as the electron acceptor, during acclimation.

A second PTFE dual chamber MFC was used as well, which consisted of a 70 mL anode and 140 mL cathode. As anode electrode carbon felt (5 cm x 5 cm) woven with titanium wire was selected. During the acclimation the cathode was the same Pt coated carbon cloth as in the glass dual chamber MFC. For the heavy metal recovery experiments carbon paper (2.5 cm x 3.8 cm) was used in the cathode. The anode cathode separator was a PEM (5 cm x 5 cm). The system was operated in a temperature-controlled room (27 ^{o}C).

Figure 20. PTFE dual chamber MFC, operating with oxygen (air pump – blue tube) as the electron acceptor, during acclimation.

4.2.1 Cathode electrode preparation

Titanium wire (Sigma Aldritch, 0.8 mm diameter) was connected to the carbon paper and carbon cloth using an epoxy resin (Conductive Epoxy, Circuit Works), for electron collection.

4.2.2 Membrane – Separator

The proton exchange membrane (PEM) was activated before the use in the MFC. The activation process included two steps. Initially, the membrane was placed inside 0.2 M hydrogen peroxide (H_2O_2) for 1.5 h, inside a bath to maintain 80 ^{o}C. Afterwards, the membrane was placed in 0.2 M sulfuric acid (H_2SO_4) for 0.5 h at room temperature. The membrane was rinsed with DI water and stored in DI water until use. The same process is used to clean the membrane.

4.2.3 External Resistance – Assembly

The external load of the MFC was regulated using a resistance decade box. The external resistance was determined by the use of Multimeter (Mastech, MY 61), set at 100 Ω connected between the anode and the cathode electrodes.

4.3 Measurements and analytical methods

In this chapter are presented the measurement techniques, instruments and analytical methods used for the characterization of wastewaters. Afterwards, the electrochemical techniques are presented, used for the performance assessment of the MFC operation.

4.3.1 pH and Conductivity

The measurements of pH and conductivity were conducted using digital instruments WTW INOLAB PH720 and WTW INOLAB, respectively.

4.3.2 Chemical Oxygen Demand (COD)

Chemical oxygen demand is an indicative measure of the pollutants in a liquid solution. It is defined as the amount of oxygen required to fully oxidize the compounds found in waters and wastewaters. For this reason, it used to quantify the pollutants present in a solution as well as to determine the quality of a liquid. The measurements of COD were conducted according to "Standard Methods for the Examination of Water and Wastewater," 2012 [112]. The method used to determine the COD was the "closed-reflux" for the soluble COD.

To measure the soluble COD, the samples were filtered initially, to remove solids which would affect the measurement. The oxidation of the sample took place with excess of potassium dichromate ($K_2Cr_2O_7$) under heat (150 ^oC) in the presence of highly acidic conditions (H_2SO_4 with dissolved Ag_2SO_4). In order to avoid obstruction due to the presence of chloride, silver and bromide ions, mercury sulfide ($HgSO_4$) was added. The general oxidation of an assumed organic compound ($C_nH_aO_bN_c$) by the dichromate ions is the following:

$$C_nH_aO_bN_c + dCr_2O_7^{2-} + (8d+c)H^+ \rightarrow nCO_2 + fH_2O + cNH_4^+ + 2dCr^{3+}$$

$$d = \frac{2n}{3} + \frac{a}{6} - \frac{b}{3} - \frac{c}{2}, \qquad f = \frac{a+8d-3c}{2}$$

After the heating of the reactants for two hours, the measurement of the soluble chemical oxygen demand (sCOD) was done photometrically at 600nm in electronic photometer (Hach DR 2800). The calculation of the concentration of the COD was done by corresponding the absorbance to a concentration, by means of a "standard calibration curve". This curve is obtained by photometry of standard samples of known COD.

4.3.3 Volatile fatty acids (VFAs)

The volatile fatty acids (VFAs) were determined using a gas chromatograph (SHIMADZU GC 2010 plus). For the quantification of VFAs, 1 ml of sample acidified with 30 μL of 20% H2SO4 was analyzed via a gas chromatograph (SHIMADZU GC-2010 plus) equipped with a flame ionization detector and a capillary column (Agilent technologies, 30 m x0.53 mm ID x1 μm film, HP-FFAP) using an autosampler (SHIMADZU AOC-20 s). The oven was programmed from 105 °C to 160 °C at a rate of 15 $°C \cdot min^{-1}$ and subsequently to 225 °C (held for 3 min) at a rate of 20 $°C \cdot min^{-1}$. Helium was used as the carrier gas at 30 $ml \cdot min^{-1}$, the injector temperature was set at 230 °C and the detector at 230 °C [113].

4.3.4 Total organic carbon (TOC) and total nitrogen (TN)

The total organic carbon (TOC) and total nitrogen (TN) of the samples were measured using a TOC-L analyzer (SHIMADZU) with an auto sampler. The method of analysis relied on the catalytic oxidation (680 ^{o}C) of the sample and the subsequent measurement of the carbon dioxide produced. The carrier gas was a mixture of 80% oxygen and 20% nitrogen. The samples were filtered using glass microfiber filters (Whatman GF/A, diameter 55 mm), in order to remove solids that can block the sampling tubes.

4.3.5 Ammonium determination

To measure the ammonium a direct distillation method was followed, using KjelFlex K – 360 distillation device (Buchi). The samples were filtered before analysis (Whatman GF/A, diameter 55 mm) and 10 mL of the filtered sample were mixed with DI water until 50 mL. As the standard solution, ammonium chloride (1 g/L) solution was mixed with DI water (1:20 ratio) and as the blank solution DI water was used.

The following solutions were required for the operation of the KjelFlex K – 360 and in all cases DI water was used (required conductivity < 50 μS/cm):

- Boric acid (H_3BO_3) solution, 20 g H_3BO_3 and 3 g of KCl were dissolved in 1 L of DI water. After the dissolution of boric acid and potassium chloride, the pH of the solution was set at 4.65 with the addition of sodium hydroxide (0.1 M).

- Sodium hydroxide (NaOH) solution, 320 g of NaOH were dissolved in 1 L of DI water and stirred for 45 min and placed in a cold bath.

After the distillation, Bromocresol Green/Methyl Red indicator was added to the sample and it was titrated with sulfuric acid (H_2SO_4, 0.01M).

$$recovery = \frac{[mL(H2SO4_{sample}) - mL(H2SO4_{blank})] \times N_{H2SO4} \times Ar_N}{mL(standard)} \times 1000\ (\frac{mg}{L}) \quad \text{Eq. 18}$$

$$NH3 - N = \frac{\frac{[mL(H2SO4_{sample}) - mL(H2SO4_{blank})] \times N_{H2SO4} \times Ar_N}{mL(standard)}}{recovery} \times 1000\ (\frac{mg}{L}) \quad \text{Eq. 19}$$

4.3.6 Voltage recording

The voltage of the two cells was recorded at 2 min intervals by a Keysight LXI Data Acquisition / Switch Unit (34792A), equipped with an Armature Multiplexer Module (20-channels). Copper wires were used for the connection between the channels and the MFCs' anodes and cathodes. The voltage recorder was connected to a computer, where the data was stored.

4.3.7 Linear Sweep Voltammetry (LSV) & Electrochemical Impedance Spectroscopy (EIS) experiments

Linear sweep voltammetry (LSV) and electrochemical impedance spectroscopy (EIS) experiments were carried out using a Potentiostat – Galvanostat (PGSTAT128N – AUTOLAB) with an Ag/AgCl reference electrode. The electrochemical experiments were conducted at the beginning of each operation cycle, after the feeding of the cells. Before the electrochemical experiments, each cell achieved open-circuit voltage (OCV), by removing the external resistance. LSV was conducted from OCV to short circuit with a negative step (0.005 mV/s), in order to estimate the maximum power output of each cell. EIS measurements estimated the internal resistance of each cell with a frequency range of 2 MHz – 1 mHz using a stimulus of 10 mV amplitude. The overall performance of the cell was estimated using the anode as the working electrode, the cathode as the counter electrode and the three-electrode set-up was completed with a reference (Ag/AgCl) electrode in connection with the counter.

The values of internal resistances of the cell were calculated through Nova software fit analysis considering a model equivalent circuit. The experimental fitting was applied considering the solution resistance of the cell (R_S) in series with two parallel R_Q components. As R_{CT} was defined the charge transfer resistance, R_{BF} the biofilm resistance, Q_{CT} and Q_{BF} the capacitance of charge transfer and biofilm respectively and Warburg element (W) as the diffusion impedance.

The applied electrical equivalent was considered as depicted in Figure 21**.**

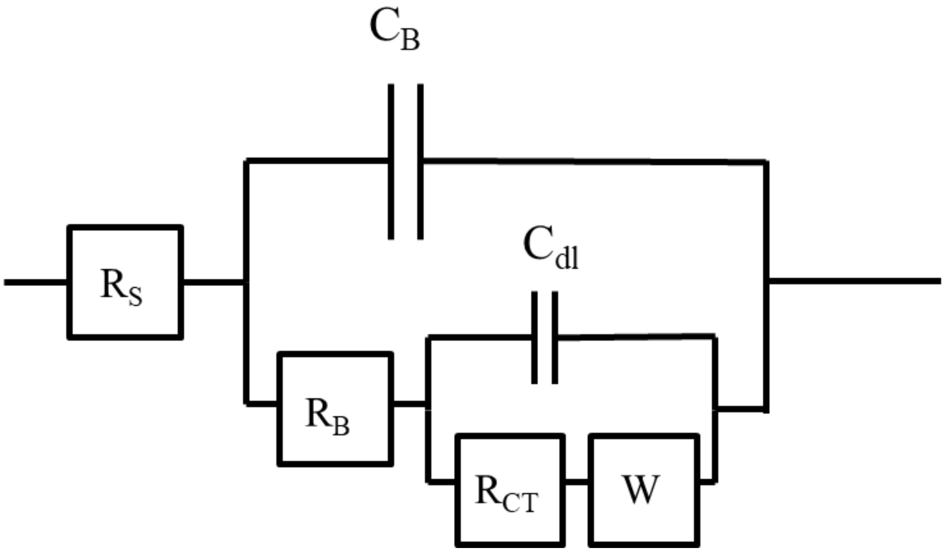

Figure 21. Electrical equivalent for EIS fitting

Where, R_S is the solution resistance, R_{BF} corresponds to the biofilm resistance, R_{CT} is reported as charge transfer resistance related to the nature of the wastewater, Q_{BF} depicts the capacitance of the biofilm, Q_{CT} corresponds to the capacitance of mass transfer and W (Warburg element) depicts the diffusion impedance. Together the R_S, R_{BF} and R_{CT} form the internal resistance of the MFC.

4.3.8 Coulombic efficiency

In order to further assess the performance of the MFCs, the coulombic efficiency (CE) of the cells was calculated. CE is defined as the fraction of the charge produced to the total charge contained in the substrate and is calculated by Equation 20:

$$CE = \frac{M_{O2} \int_0^t I dt}{F \cdot b \cdot V \cdot \Delta COD} \qquad \text{Eq.20}$$

Where MO_2 is the molecular weight of Oxygen (32 g/mol), I is the current generated during the operation cycle (A), F is the Faraday constant (46985 C/mol), b is the number of electrons participating in the reaction (4), V is the working volume of the cells (150 mL) and ΔCOD is the consumed COD ($C_{Initial} – C_{Final}$, g COD/L).

4.3.9 Electricity yield

In order to calculate the total amount of energy per operation cycle of the MFCs the E_{yield} (mJ/g COD/L) was calculated by Equation 21:

$$E_{yield} = \frac{\int_0^t Pdt}{COD_{condensate}} \qquad \text{Eq.21}$$

Where P is the power generated (in W) during each cycle and COD is the initial COD concentration of each cycle (in mg COD/L).

4.3.10 Scanning electron microscopy (SEM) and energy dispersive X-ray Spectrometry (EDS-EDX)

To study the depositions on the electrodes during the heavy metal recovery experiments Scanning Electron Microscopy (SEM) was employed along with Energy Dispersive X-ray Spectrometry (EDS-EDX). After each experiment cycle in the dual-chamber MFC the cathode electrode was stored in a desiccator, until the examination with SEM. Furthermore, the cathode liquid was filtered using glass microfiber filters (Whatman GF/A, diameter 55 mm) which were then studied using SEM and EDS in order to examine the solids which formed and sedimented, not deposition on the cathode electrode.

4.3.11 Atomic Absorption Spectrometry (AAS)

During the experiments of silver reduction and recovery in the dual-chamber MFC, the dissolved silver concentration was measured with Atomic Absorption Spectrometry (AAS).

4.3.12 Inductively coupled plasma - optical emission spectrometry (ICP-OES)

During the experiments of indium reduction and recovery in the dual-chamber MFC, the dissolved indium concentration was measured with Inductively coupled plasma - optical emission spectrometry (ICP-OES).

4.4 Experiments conducted in single chamber MFCs

In this chapter are described the experiments conducted in single chamber air cathode MFCs.

4.4.1 MFC material comparison

The primary set of experiments consisted of material testing using different anode and cathode configurations. In this sub – chapter the sets of the experiments conducted on the different materials used are presented.

4.4.1.1 Glucose synthetic wastewater and MFC acclimation

In order to compare the results of the acclimation and the early operation of each MFC, the same synthetic glucose wastewater was used across all experiments. The synthetic glucose wastewater consisted of a phosphate buffer, potassium chloride, sodium bicarbonate, glucose (as the electron donor) and trace elements of substances necessary for the microbial metabolism. In detail the amounts used are presented in Table 1.

Table 1. Glucose synthetic wastewater composition

Component	Concentration
Monosodium phosphate ($NaH_2PO_4 \cdot 2H_2O$)	5.29 g / L
Disodium phosphate ($Na_2HPO_4 \cdot 2H_2O$)	3.45 g / L
Potassium chloride (KCl)	0.16 g / L
Sodium bicarbonate ($NaHCO_3$)	5 g / L
Glucose ($C_6O_{12}H_6$)	Detailed in each experiment separately
Trace element solutions (A, B, C)	1% v/v of each solution

Table 2. Composition of trace elements solutions used in the synthetic glucose feed.

Component	Concentration
Solution A	
Calcium chloride dihydrate ($CaCl_2 \cdot 2H_2O$)	22.5 g / L
Ammonium chloride (NH_4Cl)	35.9 g / L
Magnesium dichloride dihydrate ($MgCl_2 \cdot 2H_2O$)	16.2 g / L
Potassium Chloride (KCl)	117 g / L
Manganese (II) Chloride $MnCl_2 \cdot 4H_2O$	1.8 g / L
Cobalt (II) chloride ($CoCl_2 \cdot 6H_2O$)	2.7 g / L
Boric acid (H_3BO_3)	0.51 g / L
Copper (II) Chloride ($CuCl_2 \cdot 2H_2O$)	0.24 g / L
Sodium molybdate dihydrate ($Na_2MoO_4 \cdot 2H_2O$)	0.23 g / L
Zinc chloride ($ZnCl_2$)	0.19 g / L
Nickel (II) chloride hexahydrate ($NiCl_2 \cdot 6H_2O$)	0.2 g / L
Tungstic acid (H_2WO_4)	0.01 g / L
Solution B	
Iron (II) sulfate ($FeSO_4$)	0.7 g / L
Solution C	
Diammonium hydrogen phosphate ($(NH_4)_2PO_4$)	7.21 g / L

For each operation cycle the MFC was emptied and refilled with fresh wastewater. Sampling took place during the operation of the MFCs.

The characteristics of the synthetic glucose wastewater did not present variations, the pH was 7, due to the phosphate buffer presence, the conductivity was 11.5 mS/cm and the sCOD was adjusted for the needs of each experiment. For the acclimation of the MFCs the initial glucose amount of the feed was 1 g / L.

The first step in the MFC start–up is the acclimation of the biofilm. During this period, anaerobic sludge inoculums 10% v/v were added to the MFC feed. This process was carried out for the first three operation cycles of each MFC (unless stated otherwise). The anaerobic sludge was obtained from the Wastewater Treatment Plant in Likovrisi, Athens, Greece. The anaerobic sludge characteristics were measured before the use in the MFC and presented in the following Table 3:

Table 3. Indicative characteristics of the anaerobic sludge used in the acclimation of the MFCs.

Anaerobic sludge	pH	Conductivity (mS / cm)	soluble COD (g / L)	total COD (g / L)	TSS (g / L)	VSS (g / L)
	7.3	4.4	0.47	21.9	49	21

4.4.1.2 Oxygen reduction catalyst comparison

Three different catalysts were selected for comparison: manganese dioxide, activated carbon and fly ash. Three rectangular single-chamber MFCs were constructed for this work. The cells were made of Plexiglas and four ceramic tubes run through the anode chamber of each unit. The anodic setup was similar for all three cells, consisting of graphite granules (250 g) and a graphite rod embedded for the electron collection. The mullite tubes were internally coated with the oxygen reduction catalyst. Three different catalysts were tested, one for each cell manganese dioxide MnO_2, activated carbon (AC) and fly ash (FA). Stainless steel mesh was placed on the catalyst paste for better electron collection. An external resistance set 100 Ω was connected to each cell, except when electrochemical experiments were conducted.

The effective volume of each MFC was 150 mL, all cells were operated in batch mode and inside a temperature-controlled room at 27^oC. Glucose synthetic wastewater (1.5 g COD/L) was used as the feedstock.

4.4.1.3 Cathode configuration comparison

Five similar single chamber air cathode MFCs were employed for this experiment. All five cells had graphite granules (250 g) and a graphite rod as the anode. Four cathode electrodes were placed in each cell. Four MFCs contained mullite electrodes with different oxygen reduction catalysts, specifically: MnO2 (M-MnO2), activated carbon (AC) wood biochar (BC) and coal fly ash (CFA). One MFC contained Plexiglas wrapped with Gore-Tex electrodes with MnO_2 as the catalyst. An external resistance set 100 Ω was connected to each cell, except when electrochemical experiments were conducted.

The effective volume of each MFC was 150 mL, all cells were operated in batch mode and inside a temperature-controlled room at 27^oC. Glucose synthetic wastewater (1 g COD/L) was used as the feedstock.

4.4.1.4 Cathode electrode number examination

One cylindrical single – chamber MFC was used for this study, with the characteristic to alter the number of cathode electrodes. As the anode graphite granules (250 g) with a graphite rod embedded in them were used. For the cathode Plexiglas – Gore-Tex electrodes with MnO_2 as oxygen reduction catalyst were selected. Copper wire was used in the cathode for electron transfer.

The MFC was operated with four and then 6 cathode electrodes, while the anode remained the same. An external resistance set 100 Ω was connected to the cell, except when electrochemical experiments were conducted.

The effective volume of the MFC was 300 mL. The cell was operated in batch mode and inside a temperature-controlled room at 27^{o}C. Glucose synthetic wastewater (1 g COD/L) was used as the feedstock.

4.4.1.5 Anode electrode comparison

Three rectangular Plexiglas single chamber air cathode MFCs were constructed. One MFC (SRCF) consisted of carbon felt anode, woven with titanium wire for current collection and three mullite electrodes with MnO_2 as catalyst containing copper wire for electron transfer. One MFC (SRGM1) consisted of graphite granules (250 g) and a graphite rod as anode and four Plexiglas Gore-Tex electrodes with MnO_2 and copper wire, as cathode. One MFC (SRCV) used a carbon veil anode, woven with titanium wire and four mullite electrodes with CFA and stainless steel mesh.

The effective volume of each cell was 150 mL and all cells were operated in batch mode, inside a temperature-controlled room at 27^{o}C. Glucose synthetic wastewater (1 g COD/L) was used as feedstock. An external resistance set 100 Ω was connected to each cell, except when electrochemical experiments were conducted.

4.4.2 MFC integration in a household food waste (HFW) valorization process

In this chapter the use of MFC in various stages of a HFW valorization process is investigated. In particular, HFW was collected, shredded and dried, at municipality level in Halandri, Greece. The drying and shredding process was conducted by the shredder in Figure 22. The products were a soil – like material called FORBI (Food Residue Biomass) and a liquid originating from the condensed vapors, during the drying of HFW, called condensate. FORBI and condensate were used as feedstock for anaerobic digesters, which generated biogas. The generated biogas was then refined and used as the fuel of the truck collecting the municipality HFW, presenting a circular economy applied example. The MFCs were introduced in three stages, at first FORBI leachate was used as feedstock, secondly condensate was used as feedstock and finally, the effluent of the anaerobic digesters was used as feedstock.

FORBI and condensate were produced by a Dryer-shredder GAIA GC-300 (Figure 22). The dryer/shredder was loaded with 120 kg of pre-sorted HFW. The drying took place at 172 ^{o}C for 9 h, with simultaneous shredding of the HFW. Two products were generated from the drying process, the solid homogenous biomass product called FORBI (Food Residue Biomass) [114] and vapors. By condensing the vapors, liquid condensate was produced [113].

The HFW feed in all cases was cooled at 4^{o}C to avoid conditions favorable to the degradation of its organic load and alteration of its characteristics. Also, the HFW feed was stirred continuously to avoid sedimentation of suspended solids.

Figure 22. Shredder, dryer and condenser used for the exploitation of HFW in Halandri, Athens, Greece.

4.4.2.1 FORBI leachate treatment in MFC continuous and batch mode operation

Four rectangular single – chamber MFCs were used to treat wastewater originating from organic food biomass (FORBI). Graphite granules (250 g) with a graphite rod embedded in them were the anode electrode, in each MFC. Each cell had four Plexiglas tubes run through the anode chamber, utilizing four Plexiglas Gore-Tex cathode electrodes, with MnO_2 as the oxygen reduction catalyst and copper wire for the electron transfer.

The effective volume of each cell was approximately 120 mL The cells were operated in batch mode, with synthetic glucose wastewater (0.8 g COD/L). An external resistance set at 100 Ω was connected to each cell during batch mode. The cells were placed in a temperature-controlled room, at 27 ^{o}C.

Afterwards, the synthetic feed was replaced with food residue biomass (FORBI) extract and the units were operated in batch mode for approximately 1000 h. Specifically, FORBI was mixed with water and then filtered using a cloth filter. The produced solution was initially filtered with Whatman filters (pore sizes 1.2 μm to 0.7 μm) and then it was diluted to a final concentration of 1.6 g COD/L. Phosphate buffer was added to the solution (PBS; pH 7) in order to adjust its pH from 3.6 to 7.

During continuous operation the feedstock flowed from the top to the bottom of each unit and went out by overflow, through a constant-level outlet tube, which was placed in the anode chamber. The units were operated at a flow rate 48 mL/h. Each unit was fed individually from a common feeding tank using a peristaltic pump (Masterflex, Cole- Parmer Instrument Company, Vernon Hills, IL, USA). The individual external resistive loads (100 Ω) of the units were removed and the four units were successively connected in series and in parallel connection under a common external load of 100 Ω (Figure 23).

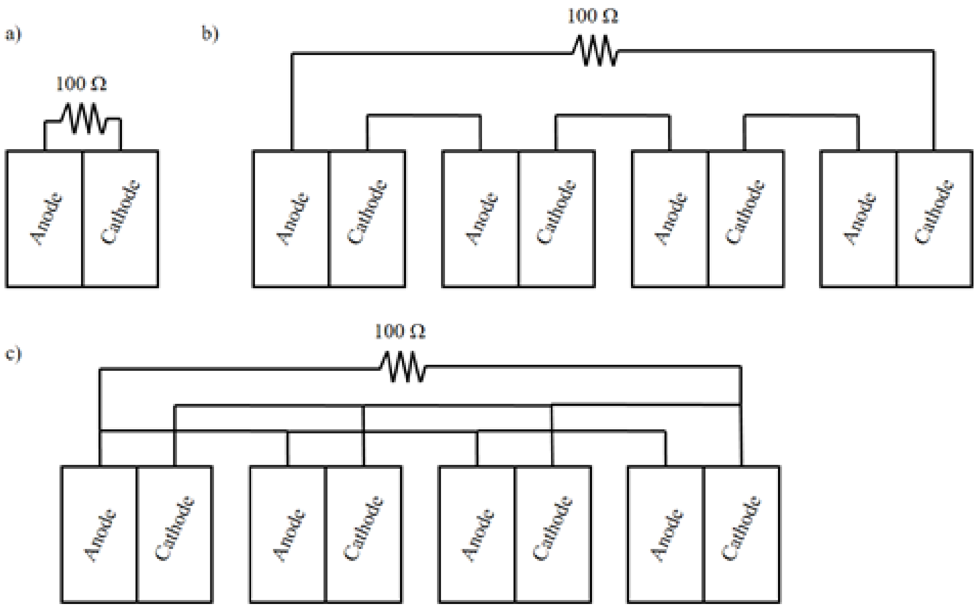

Figure 23. External resistance connections for: a) 2 MFCs, b) 4 MFCs connected in series and c) four MFCs connected in parallel

4.4.2.2 Digestate originating from anaerobic digesters (mesophilic and thermophilic) as MFC feedstock

During the experiments, four identical Plexiglas single chamber air cathode MFC units were operated. The anode compartment was filled with graphite granules (250 g) (anodic liquid volume: 120 ml) while a graphite rod was inserted into the center of the chamber. Each MFC had four Plexiglas Gore-Tex cathode electrodes with MnO_2 as catalyst and copper wire for electron transfer. The cells were operated in batch mode, at 22 ± 2 °C. An external resistance set at 100 Ω was connected to each cell.

As already mentioned, HFW was dried and shredded producing FORBI and condensate. FORBI mixed with tap water (18 g/L) was used as the feedstock for two anaerobic digesters. One AD reactor operating in thermophilic conditions (~50^{o}C) with a volume of 0.5 m^3 and one AD reactor operating in mesophilic conditions (~35^{o}C) with a volume of 4 m^3. Both AD reactors were CSTRs and the effluent of each reactor was used as the feedstock for the MFCs. Each feeding was tested in duplicate (Cells 1, 2: mesophilic digestate, Cells 3, 4 thermophilic digestate).

The digestate was filtered using a 5 μm filter sludge bag and it was then inserted in the MFCs. The characteristics of the mesophilic digestate are presented in Table 4 and the characteristics of the thermophilic digestate are presented in Table 5. The COD concentration of the digested, varied, due to the continuous operation and the alteration of the feed organic load.

Table 4. Mesophilic Digestate Feeding Characteristics (after sludge bag filter).

Cycle	COD (g/L)		pH		Conductivity (mS/cm)		TSS (mg/L)		VSS (mg/L)		VFAs (mg/L)	
Number	Cell 1	Cell 2	Cell 1	Cell 2	Cell 1	Cell 2	Cell 1	Cell 2	Cell 1	Cell 2	Cell 1	Cell 2
1	5.6	5.6	6.9	6.9	2.4	2.4	17.8	17.8	4.8	4.8	305	305
2	6.3	6.6	7.2	7.2	2.4	2.4	4	3.7	3.4	3.1	385	-
3	7.2	6.3	6.8	7.2	2.4	2.4	4.7	4	3.9	3.4	32	385
4	8.1	7.2	6.9	6.8	2.4	2.4	4.5	4.7	4	3.9	800	32
5	6.3	9.7	6.7	7.3	2.4	2.4	2.9	1.3	2.4	1	510	88
6	3.7	11.0	7	6.8	2.4	2.5	4.1	4.9	3.5	4.2	325	779
7	-	3.7	-	7	-	2.4	-	4.1	-	3.5	-	325

Table 5. Thermophilic Digestate Feeding Characteristics (after sludge bag filter).

Cycle	COD (g/L)		pH		Conductivity (mS/cm)		TSS (mg/L)		VSS (mg/L)		VFAs (mg/L)	
Number	Cell 3	Cell 4	Cell 3	Cell 4	Cell 3	Cell 4	Cell 3	Cell 4	Cell 3	Cell 4	Cell 3	Cell 4
1	6.1	6.1	6.9	6.9	2.6	2.6	13.3	13.3	1.4	1.4	842	842
2	4.4	10.0	6.9	7.4	3.9	2.7	3.5	3.5	0.9	3.1	-	-
3	10.0	8.8	7.4	6.7	2.7	3.9	3.5	5	3.1	4.4	1526	1526
4	8.8	8.6	6.7	7.4	3.9	4.6	5	3.4	4.4	2.9	-	-
5	9.8	7.4	7.1	7	4.5	5.2	2.5	4.2	2.2	3.5	-	-
6	7.4	8.1	7	7	5.2	1.8	4.2	1.1	3.5	0.9	-	3052
7	8.1	6.2	7	7.2	1.8	4.8	1.1	1.7	0.9	1.5	3052	2776
8	6.2	-	7.2	-	4.8	-	1.7	-	1.5	-	2776	-

4.4.2.3 Condensate originating from HFW as feedstock

Condensate was co-produced with FORBI during the drying and shredding of HFW waste. The characteristics of condensate are presented in Table 6. The VFAs concentrations are the average values of four different feed samples. Initially, different condensate concentrations were tested in the MFC feedstock, in order to examine the effect on the MFC performance of the different concentrations. Afterwards, “raw” condensate was used as the MFC feedstock. An external resistance set 100 Ω was connected to each cell, except when electrochemical experiments were conducted.

Table 6. Characteristics of condensate from HFW drying.

COD concentration	pH	Conductivity (μS/cm)	VFAs (mg/L)				
			Acetic acid	Butyric acid	Propionic acid	Iso-butyric acid	Iso-valeric acid
13	3.5 ± 0.4	262 ± 100	1008 ± 720	144 ± 68	75 ± 25	40 ± 28	13 ± 4

4.4.2.3.1 Different initial condensate concentrations in the MFC feedstock

Mullite was compared to Gore-Tex as a separator and to Plexiglas as structural support of the cathode electrode. Two rectangular Plexiglas single chamber MFCs were constructed. Each cell had four tubes running through the anodic compartment. The same anode electrode setup was used for both cells, graphite granules (250 g) and an embedded graphite rod. Different cathode electrodes were used for the two cells. For the first cell, four cathodic electrodes with Gore-Tex cloth were assembled as already specified. For the second cell, the four cathodic mullite electrodes were internally coated with the oxygen reduction catalyst paste, MnO_2. The synthetic glucose wastewater was used as feedstock. An external resistance set 100 Ω was connected to each cell, except when electrochemical experiments were conducted.

Following the acclimation period, the synthetic wastewater was switched with condensate originating during the drying process of HFW.

Before feeding the condensate to the anode chamber, it was mixed with phosphate buffer (5.29 g/L $NaH_2PO_4 \cdot 2H_2O$, 3.45 g/L $Na_2HPO_4 \cdot 2H_2O$) and potassium chloride (0.16 g/L). Following the addition of the phosphate buffer and potassium chloride, the pH of the average pH of the anolyte was 6.2 ± 0.7 and the average conductivity 5 ± 0.6 mS/cm (Table 7). The same initial condensate concentrations were examined in both cells, in order to compare the cell's operation performance with different separators. The condensate initial concentration (400 – 4000 mg COD/L) was increased in consecutive operation cycles. For each initial condensate concentration two operation cycles were carried out. The characteristics of the condensate feed are presented in detail in Table 7:

Table 7. Characteristics of the condensate feed after it was mixed with the buffer solution.

Cycle Nr.	COD (g / L)	pH	Conductivity (mS / cm)
1st	0.4	6.7	5.9
2nd	0.5	6.9	5.0
3rd	0.6	6.6	5.0
4th	0.8	6.5	4.9
5th	1.2	6.6	4.9
6th	1.4	6.6	5.2
7th	3	5.1	5.4
8th	4	4.8	3.8

4.4.2.3.2 “Raw” condensate in the MFC feedstock

Following the operation with different initial condensate concentrations in the MFC feed, the impact of “raw” condensate feed on the MFC performance was examined.

For this work, two rectangular single – chamber MFCs were used, the same as chpt. 4.4.2.3.1. Each cell had four tubes running through the anodic compartment. The same anode electrode setup was used for both cells, graphite granules (250 g) and an embedded graphite rod. Different cathode electrodes were used for the two cells. For the first cell, four cathodic electrodes with Gore-Tex cloth and MnO_2 as the catalyst were assembled. For the second cell, the four cathodic mullite electrodes were internally coated with the same oxygen reduction catalyst, MnO_2. An external resistance set 100 Ω was connected to each cell, except when electrochemical experiments were conducted.

Following the acclimation period, synthetic glucose wastewater was replaced with condensate. In order to improve the low conductivity and pH, phosphate buffer was added in the raw condensate. After the mixing the improved pH and conductivity were 4.9 and 6.6 mS/cm, respectively. The condensate feeding presented fluctuations because it originated from gathered HFW, which varied each batch.

4.4.2.4 Condensate fed PABR outlet as MFC inlet

In order to "polish" the effluent of a condensate fed PABR a single chamber air cathode MFC was employed. The anode consisted of graphite granules with a graphite rod embedded in them. The cathode consisted of four mullite tubes coated internally with MnO_2 catalytic paste with a copper wire as current collector.

Condensate was used as the feedstock for anaerobic digestion in a periodic anaerobic baffled reactor (PABR), with an active volume of 77 L. When designing the PABR, the water bath was placed on the inner cylinder, while the outer concentric cylinder is the active volume. The temperature of the reactor was maintained in mesophilic (~35°C) conditions, via the hot water circulating in the closed water bath-water heater system. The volume of the PABR gas phase was equal to 20 L. The reactor was made of stainless steel and the external piping consisted of hard PVC sections (3/4"), connected to 12 automatic solenoid valves. The solenoid valves were connected electronically PLC control panel.

The PABR effluent was collected and used without any pretreatment in the MFC anode, with an effective volume of 150 mL. An external resistance (100 Ω) was connected to the MFC at all times, except when electrochemical experiments were performed. The characteristics of the PABR effluent are presented in Table 8.

Table 8. Condensate fed PABR effluent characteristics, used as MFC feedstock.

COD (g/L)	pH	Conductivity (mS/cm)	TSS (mg/L)	VSS (mg/L)

0.36 ± 0.1	7.9 ± 0.1	3 ± 0.7	0.4 ± 0.1	0.2 ± 0.1

4.4.2.5 MFC technology combined with dark fermentation to efficiently treat cheese whey

The MFC technology was used in a two-stage system with a dark fermentation reactor. The DF process took place in an integrated bio-electrochemical hydrogen (H_2) production system (IBH_2S). The IBH_2S operated with cheese whey (CW) as feedstock [115].

A rectangular single chamber air cathode MFC was used for the IBH_2S effluent treatment. The anode consisted of graphite granules (250 g) with a graphite rod embedded in them for current collection. The cathode consisted of four mullite tubes coated internally with fly ash (FA) catalytic paste, using stainless steel mesh for electron transfer. The effective volume of the FA was 150 mL. The MFC was operated in batch mode and in a temperature-controlled room (~27^{o}C). An external resistance set 100 Ω was connected to the cell, except when electrochemical experiments were conducted.

A synthetic dark fermentation (SDF) wastewater was created, containing similar concentrations of acetic acid, butyric acid and ethanol as the IBH_2S effluent. The SDF consisted of: 1.2 g/L acetic acid, 3.5 g/L butyric acid and 2.5 g/L ethanol in mixed with DI water. The pH of the SDF was adjusted to 6.5 by 2 M NaOH addition. The SDF was fed to the FAMFC to examine the effect on the MFC performance.

The IBH_2S effluent was filtered-sterilized through a 5 μm sludge bag filter. The real dark fermentation (RDF) wastewater was then diluted at 10% and 50% and used as feedstock in the MFC, after the SDF feed. Three different cases were studied of RDF mixed with DI water, 10% RDF, 50% RDF and 10% RDF effluent with increased conductivity by KCl addition. In all cases, the pH of the RDF solutions was adjusted to 6.5, by 2 M NaOH.

Table 9. Characteristics of SDF and RDF wastewaters used as feedstock in FA.

Wastewater	pH	Conductivity (mS/cm)	COD concentration (g/L)
SDF	6.2 ± 0.1	1.6 ± 0.2	4.8 ± 0.2

10% RDF	6.4	3.9 ± 0.1	6.2 ± 0.1
50% RDF	6.5 ± 0.4	14 ± 0.4	32.2 ± 0.1
10% RDF + KCl	7.4 ± 0.8	14 ± 0.6	6.4 ± 0.4

4.5 Experiments conducted in dual chamber MFCs

4.5.1 Silver recovery experiments

The aim of this work is to examine the feasibility of using MFC technology to recover silver from a synthetic wastewater simulating PV hydrometallurgical process extract. The synthetic wastewater simulated the characteristics of pH, conductivity and silver concentration of the chemical extract that was generated from the hydrometallurgical process of 1st generation PV panels in the framework of the PHOTOREC project [116]. In particular this process includes the dismantling of 1st generation PV panel, thermal treatment of the solar cell at 550 °C and acidic extraction of the Si, Ag and Cu, contained in the decomposed solar cell [117].

A dual chamber MFC (300 mL each chamber) was used for the experiments. Both chambers were continuously stirred. Plain graphite paper was used as the anode. For the acclimation the MFC operated with oxygen as the electron acceptor and the cathode electrode was graphite cloth with Pt coating (ETek - 0.5 mg/cm^2), as the oxygen reduction catalyst. For the silver recovery experiments, plain graphite paper was used as the cathode electrode, connected to a titanium wire using a silver conductive epoxy (Conductive Epoxy, Circuit Works). The dimensions of all electrodes used were 2.5 cm x 3.8 cm. The anode solution consisted of synthetic glucose medium (1.5 gCOD/L)

The synthetic wastewater simulated the characteristics (pH, conductivity, concentration) of the chemical extract that was generated from the hydrometallurgical process of 1st generation PV panels. The process to obtain the PV panel extract was the following: dismantling of a 1st generation PV panel to remove the metallic frame, thermal treatment at 550 °C to remove the EVA, sieving to separate the glass from the solar cell and the electrodes and collection of the solar cell parts and electrodes. Afterwards, acidic extraction was employed using 5 N nitric acid (HNO_3) for 3 h, at 25 °C of the PV panel's solar cell [117]. Table 10 presents the characteristics of the real PV panel chemical extract and the characteristics of the subsequent diluted solution.

Table 10. Concentration of silver, pH and conductivity of chemical extract originating from 1st generation polycrystalline silicon PV panel.

	Ag (mg/L)	pH	Conductivity (mS/cm)
PV panel chemical extract	5110	ODL	ODL
1:100 Diluted PV panel chemical extract	51	2	20

Four different recovery cases were examined (R1, R2, R3, R4) in order to examine the influence of pH and conductivity. The initial silver concentration was kept the same for all experiments (approx. 50 mg/L) similar to the concentration of the real chemical extract. The initial concentration value was determined based on the liquid volume of the cell and the amount of PV panel extract available. The corresponding dilution of the PV panel extract led to the aforementioned silver concentration, as well as pH 2 and conductivity of ~20 mS/cm Table 10). The effect of catholyte's pH and conductivity on the silver reduction was studied. The experiments were conducted at pH 7 and pH 2. Moreover, different supporting electrolytes ($NaClO_4$ and KCl) were used to increase the conductivity of the synthetic solution, simulating the high conductivity of the extract (Table 10). In the first experiment (R1) silver nitrate ($AgNO_3$) was dissolved in DI water at the desired concentration and sodium perchlorate ($NaClO_4$) was added, to increase the conductivity of the catholyte (18.9 mS/cm). In the second experiment (R2), silver nitrate was dissolved in DI water and potassium chloride (KCl), was added in order to increase the conductivity (19.5 mS/cm). For the third experiment (R3), silver nitrate was dissolved in DI water with no supporting electrolyte, leading to a considerably lower initial conductivity (0.006 mS/cm) when compared with the other cases (Table 10). The fourth experiment (R4) was carried out with silver nitrate ($AgNO_3$) dissolved in DI water, sodium perchlorate ($NaClO_4$) at pH 2, which was adjusted using nitric acid (0.1 M HNO_3). The sodium perchlorate concentration (0.2 M) was kept constant. At the beginning of each batch cycle the cathode was sparged with nitrogen (N_2) in order to remove the oxygen from the chamber and this process was repeated after every sampling. Table 11 presents the characteristics of the catholyte for each case (R1, R2, R3 and R4). Each experiment was carried out for six consecutive batch cycles, in order to acquire repeatable results.

Table 11. pH and conductivity of the synthetic silver wastewater for the R1, R2, R3 and R4 experiments.

Experiment	Initial pH	Supporting electrolyte	Initial conductivity (mS/cm)
R1	7	$NaClO_4$	18.9
R2	7	KCl	19.5
R3	7	-	0.06
R4	2	$NaClO_4$	18

In order to calculate the maximum silver reduction rate (g Ag/h/m^2) Faraday's law was used:

$$R_{Silver} = \frac{i \cdot Mr}{n \cdot F} \qquad \text{Eq. 22}$$

Where i is the maximum current density (A/m^2) as obtained from electrochemical experiments, Mr is the molar weight of the reacting substance, n is the number of the participating electrons in the reaction and F is Faraday's constant. By determining the maximum power output of the cell through LSV experiments, the maximum rate may also be estimated. Also, in order to extract the rate of the silver reduction, the experimental data were fitted with a linear curve, in order to compare the two rates.

4.5.2 Indium recovery experiments

The aim of this work is to examine the feasibility of using MFC technology to recover indium from a synthetic wastewater simulating PV hydrometallurgical process extract and afterwards indium recovery from a 2nd generation PV (CIGS) chemical extract. The synthetic wastewater simulated the characteristics of the chemical extract that was generated from the hydrometallurgical process of 2nd generation PV panels (CIGS) in the framework of the PHOTOREC project [116]. In particular the process of dismantling the 2nd generation PV panel included the mechanical processing (via a cryogenic mill) of the panel followed by the chemical extraction using nitric acid (HNO_3 70% w/v).

A dual chamber MFC (70 mL anode / 140 mL cathode) made of PTFE (polytetrafluoroethylene) was used for the indium recovery experiments. The anode consisted of graphite felt (5 cm x 5 cm), woven with titanium wire. During the acclimation, oxygen was used as electron acceptor and the cathode electrode was a graphite cloth coated on one side by Pt as the oxygen reduction catalyst (2.5 cm x 3.8 cm). For the indium recovery experiments plain graphite paper was used as the cathode electrode (2.5 cm x 3.8 cm), connected to a titanium wire using a silver conductive epoxy (Conductive Epoxy, Circuit Works).

The anode solution used in all cases was the synthetic glucose wastewater (1.5 g COD/L). During the indium recovery experiments the cathode solution was initially a synthetic wastewater containing indium ($InCl_3$ – 180 ppm) and afterwards the real 2nd gen. PV panel chemical extract was used. In particular the synthetic indium wastewater contained 180 mg/L indium, with a pH of 2, adjusted by adding hydrochloric acid (0.2 M). The MFC operation with synthetic indium wastewater was carried out for 6 operation cycles. Afterwards, the cathode solution was switched with the 2nd generation PV panel chemical extract. Due to the pH of the extract being off detection limits (ODL) the 2nd generation PV panel chemical extract was diluted with DI water (10%) and 3 operation cycles were performed.

The characteristics of the chemical extract originating from the processing of 2nd gen. PV panel (CIGS) are presented in Table 12.

Table 12. Characteristics of the 2nd generation PV panel chemical extract and the diluted chemical extract used in the MFC cathode

	Concentration (mg/L)						
	In	Cu	Mo	Ga	Zn	pH	Conductivity (mS/cm)
Chemical extract	40	26	195	19	107	ODL	ODL
Synth	165	-	-	-	-	~2	2.5
Synth + KCl	130	-	-	-	-	~2	15
Diluted (10%) chemical extract	4	2.6	19.5	1.9	10.7	~1.2	84

4.6 Table of Experiments conducted

In this chapter each experiment is summarized in Table 13, describing the experimental configuration along with the substrate used in each case.

Table 13. Summary of experiments conducted in single and dual chamber MFCs.

Experiment described in chapter	Cell	Anode	Cathode			Feedstock (Anode Substrate)	Operation mode
			# Electrodes	Separator	Catalyst		
4.4.1.2	MnO_2	Graphite granules (250 g) + Graphite rod	4	Mullite	MnO_2	S.G.W. (1.5 g COD/L)	Batch
	FA				Fly ash		
	AC				Activated carbon		
4.4.1.3	M - MnO_2	Graphite granules (250 g) + Graphite rod	4	Gore-Tex Plexiglas	MnO_2	S.G.W. (1.5 g COD/L)	Batch
	P - MnO_2						
	BC			Mullite	Biochar		
	FA				Fly ash		
	AC				Activated carbon		
4.4.1.4	SCH	Graphite granules (300 g) + Graphite rod	4 / 6	Gore-Tex Plexiglas	MnO_2	S.G.W. (1.5 g COD/L)	Batch
4.4.1.5	SRCF	Carbon Felt +Ti wire	3	Mullite	MnO_2	S.G.W. (1.5 g COD/L)	Batch
	SRCV	Carbon Veil +Ti wire	4				
	SMul	Graphite granules (250 g) + Graphite rod					
	SRGM			Gore-Tex Plexiglas			
4.4.2.1	Cell 1		4		MnO_2		

	Cell 2 Cell 3 Cell 4	Graphite granules (250 g) + Graphite rod		Gore-Tex Plexiglas		Forbi leachate (0.8 – 1.6 g COD/L)	Batch & Continuous
4.4.2.2	Cell 1 Cell 2	Graphite granules (250 g) + Graphite rod	4	Gore-Tex Plexiglas	MnO_2	Mesophilic digestate (4 – 11 g COD/L)	Batch
	Cell 3 Cell 4					Thermophilic digestate (4.4 – 11 g COD/L)	
4.4.2.3	Gore-Tex cell	Graphite granules (250 g) + Graphite rod	4	Mullite	MnO_2	Condensate (0.4 – 4 g COD/L)	Batch
	Mullite cell			Gore-Tex Plexiglas		“Raw” condensate (6 – 13 g COD/L)	
4.5.2.4	SMul	Graphite granules (250 g) + Graphite rod	4	Mullite	MnO_2	PABR effluent (0.4 g COD/L)	Batch
4.4.2.5	SRFA	Graphite granules (250 g) + Graphite rod	4	Mullite	Fly ash	SDF (5 g COD/L)	Batch
						RDF (6 – 30 g COD/L)	
4.5.1	Dual glass	Graphite paper (2.5 cm x 3.8 cm)	1	Graphite paper (2.5 cm x 3.8 cm)	-	S.G.W. (1.5 g COD/L)	Batch
4.5.2	Dual PTFE	Carbon Felt (5 cm x 5 cm)	1	Graphite paper (2.5 cm x 3.8 cm)	-	S.G.W. (1.5 g COD/L)	Batch

4.7 Model development

The aim of this work was to develop a time-dependent 2D MFC model, containing mass and charge conservation and transfer phenomena along with a combined Butler-Volmer-Monod kinetics. The model was developed with minimal computational requirements in order to extract quick and accurate results taking into account the geometry of the cell and the materials that comprise it. This model examines glucose consumption in an H-type MFC, calculating the voltage output, substrate consumption and polarization curves. The model proposed an approach to quickly predict and validate optimal conditions for MFC operation. This was accomplished by the use of electrochemical kinetics along with parameters determined by experimental data fitting. The focus of this work was the creation of an improved model to quickly predict accurate conditions, in order to improve the performance of the particular MFC setup.

4.7.1 Experimental set-up

The model was based upon a dual-chamber MFC, in order to validate the computational results with experimental data. Specifically, an H-type MFC was operated in batch mode, consisting of an anode (0.3 L) and a cathode (0.3 L). The solutions in both chambers were continuously stirred. Plain graphite paper (3.8 cm x 2.5 cm) and graphite cloth (3.8 cm x 2.5 cm) coated with Pt as the oxygen reduction catalyst, were used as the anodic electrode and the cathodic electrode, respectively. Titanium wire and a silver conductive epoxy (Conductive Epoxy, Circuit Works) were used for the electrode connection. Between the two chambers a proton exchange membrane (Nafion ™ 117, DuPont - PEM) was placed. Both chambers were under continuous stirring and operated in a temperature control environment set at 30 ^{o}C. A resistance box set at 100 Ω was connected to the cell. The cell was operated with a synthetic glucose wastewater (1 g COD/L) in the anode. For the cathode phosphate buffer (3.67 g/L NaH_2PO_4 and 3.45 g/L Na_2HPO_4) and potassium chloride (0.16 g/L KCl) were used. The cathode chamber was continuously sparged with air, supplying the electron acceptor (O_2).

The cell's potential was recorded at set intervals (2 min) using an Agilent Keysight 34972A LXI Data Acquisition/Switch Unit. The pH and conductivity were measured by digital instruments (WTW INOLAB PH720) and (WTW INOLAB) respectively. Soluble COD was measured according to the standard methods [112]. Polarization experiments were conducted by altering the resistance on the resistance box. Initially, the system achieved open circuit voltage (OCV) by removing the external resistance for 3 h, thus resulting in infinite resistance between the two electrodes. Then the resistance box was connected to the cell and different consecutive resistances were applied (1 MΩ – 0 Ω). Each external resistance was applied for 6 min recording the voltage and the current every 2 min. The current was measured using a multimeter.

4.7.2 Model description

The model was developed in the finite element software (FEM) Comsol Multiphysics® Version 5.2. The model focused on the description of the voltage output, the organic substrate (glucose) consumption and the estimation of the maximum power through polarization curves. Experimentally the glucose concentration was measured in g COD/L, but in the model the corresponding glucose concentration (mol/m^3) was determined. For this reason, the organic substrate results were normalized with the initial value (C/C_0).

The geometry was a vertical section (2D) of the MFC, depicted in Figure 24a. It consisted of an anode, a cathode, the separator (PEM membrane [118]) and the two electrodes (2.5 cm x 3.8 cm). The third dimension (z – axis) was considered equal to the width of the electrodes (2.5 cm). The distance between the two electrodes was 15 cm. The cell was considered to operate in batch mode and at a set temperature (32 ^{o}C). As the electron donor, to be oxidized by the electrogen biofilm, glucose was chosen. The reaction assumed to take place in the biofilm was presented in Eq. 10 (Glucose oxidation) [33].

The biofilm was considered to be on the surface of the anodic electrode and glucose reacted as it came in contact with it. Despite the porosity of graphite paper and the presence of microorganisms, the reaction was assumed to take place homogeneously on the electrode. In the anode chamber the carbon dioxide was considered dissolved in the liquid, thus taking into account only the liquid phase. Furthermore, due to the presence of a phosphate buffer the changes in the anodic pH were considered negligible. The concentration of microorganisms was considered constant, as the assumption was made that the growth rate was equal to the decline rate. This assumption led to a constant biofilm present on the anodic electrode. Moreover, the biofilm was assumed to consist only of electrogenic bacteria and no competing biomass was considered present. The description of the electrochemical reaction rate (mol/m^2/s) taking place in the biofilm was done by the Monod - Butler - Volmer expression. This equation combines the organic substrate consumption rate and the effect of electrochemical phenomena on it, taking into account the overpotential.

$$R_1 = k_1 \frac{C_{Glucose}}{K_{Glucose} + C_{Glucose}} \exp\left(\frac{a_a F}{RT} \eta_a\right) \qquad \text{Eq. 23}$$

Where k_1 (mol/(m^2h)) is the maximum specific growth rate multiplied by the biomass concentration ($k_1 = k_1^0 \cdot X_{bio}$), $C_{Glucose}$ (mol/m^3) is the concentration of glucose in the anode chamber, $K_{Glucose}$ (mol/m^3) is the half velocity rate constant for glucose, a_a is the anodic transfer coefficient, F (C/mol) is the Faraday's constant, R (J/(molK)) is the gas constant, T (K) is the temperature and η_a (V) is the anode overpotential. No inhibition of the microbial activity by the organic substrate was considered.

It was assumed that no diffusion of oxygen from the cathode to the anode takes place. To describe the rate of the reaction in Eq. 11, a Monod-Butler-Volmer kinetic was employed, assuming a Monod-type dependence on dissolved oxygen concentration [119].

$$R_2 = k_2 \frac{C_{Oxygen}}{K_{Oxygen} + C_{Oxygen}} \exp\left(\frac{a_C F}{RT} \eta_c\right) \qquad \text{Eq. 24}$$

where k_2 (m^{12}/(m^4h)) is the forward rate constant of cathode reaction, C_{Oxygen} (mol/m^3) is the concentration of dissolved oxygen in the cathode chamber, K_{Oxygen} (mol/m^3) is the half velocity rate constant for oxygen, a_C is the cathode transfer coefficient and η_c (V) is the cathode overpotential.

The correlation between reaction and rate and current development was done using Faraday's law:

$$R_i = \frac{\nu_i i_{A\,/\,C}}{n_i F} \qquad \text{Eq. 25}$$

Where ν_i is the stoichiometric coefficient (i = glucose or oxygen), i_A (A/m^2) is the current density (anode or cathode) and n_i the number of electrons that take part in the reaction.

In Figure 24b, the algorithm of the model is presented. An initial glucose concentration was selected and as the simulation is initiated, the reaction rate is calculated by the Monod – Butler – Volmer kinetics on the anode electrode surface. The initial value for the voltage between the two electrodes is 0 V. By the use of Faraday's law, the current density on the anode is calculated based on the reaction rate. Through the external resistance the current brings electrons to the cathode electrode, where oxygen reduction takes place. The respective current density is calculated by Faraday's law based on oxygen reduction reaction rate. The charge balance equations calculate the total transfer of charge throughout the cell and the voltage developed between the two electrodes. The overpotential is determined based on the voltage and the standard potentials of the reactions. Simultaneously, the decrease in the glucose concentration and the respective glucose distribution is determined. As a new glucose concentration on the electrode surface is calculated, a new reaction rate is determined, taking into account the new overpotential value.

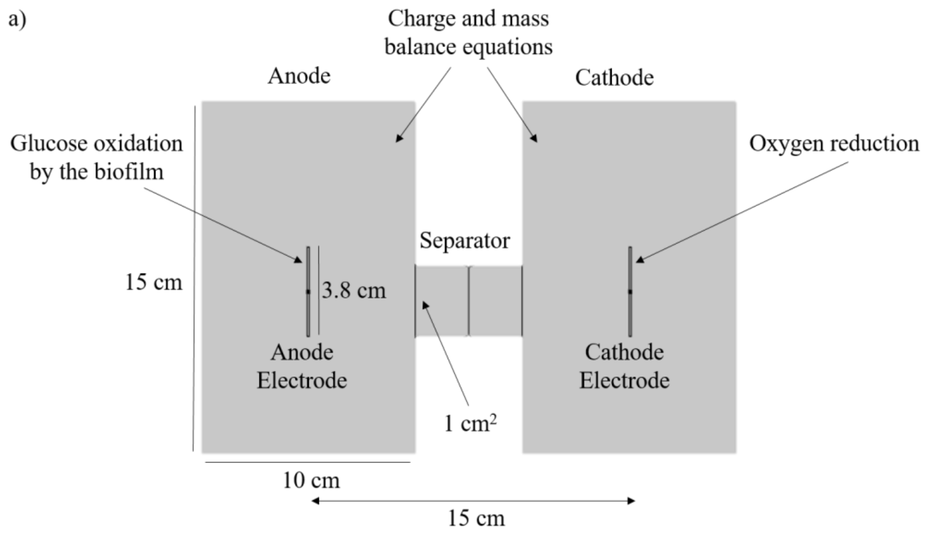

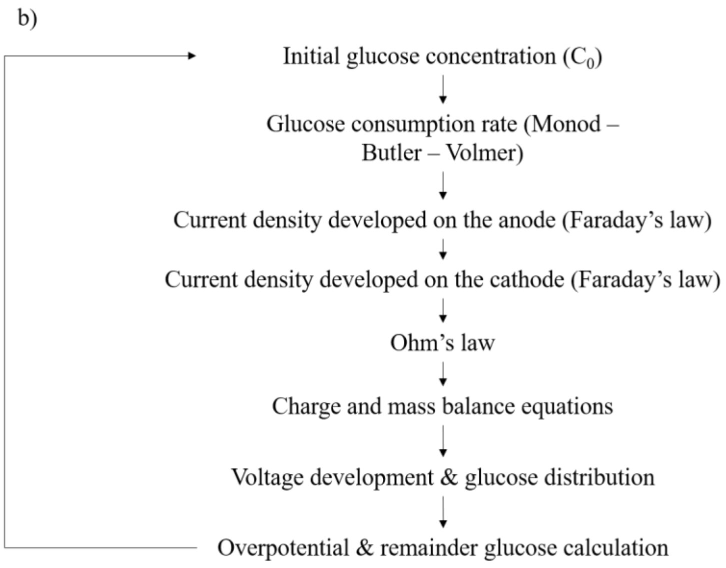

Figure 24. a) Schematic of the MFC domain in the model and b) concise algorithm of the model

4.7.3 Mass and charge transfer equations

The anode and the cathode chambers were considered to be full of the aforementioned synthetic solutions. For the transfer of mass through the anode and the cathode the Nernst – Planck equation was used. This equation takes into account the change of concentration in time and the transport of chemical species by diffusion, convection and migration. This equation takes into account the transport of species due to the concentration gradient (diffusion), by the movement of the bulk of the fluid (convection) and due to the presence of an electric field (migration).

$$\frac{\partial \mathrm{c}}{\partial \mathrm{t}} - \nabla \cdot \left[D \nabla \mathrm{c} - \mathbf{u}\mathrm{c} + \frac{DzF}{RT} c(\nabla \varphi) \right] = \begin{cases} 0, in\ the\ bulk \\ R, on\ the\ electrode\ surface \end{cases} \qquad \text{Eq. 26}$$

Where D (m^2/s) is the diffusion coefficient of the species, **u** (m/**s)** is the velocity vector of the liquid, z is the valence of the ionic species, φ (V) is the potential and R ($mol/(m^2h)$) is the reaction rate. On the walls, a no flux condition was applied and similarly no flux was applied on the separator. Inside the cell, an incompressible Newtonian fluid was assumed.

For the charge transfer in the cell, Ohm's law was used along with charge balance equations. More specifically, a uniform electrolyte medium was assumed for the transfer of charged ions and activation overpotentials were also taken into account:

$$\nabla \cdot \mathrm{i_i} = \begin{cases} 0, in\ the\ bulk \\ Q_i, on\ the\ electrode\ surface \end{cases} \qquad \text{Eq. 27}$$

$$\mathrm{i_i} = \sigma_\mathrm{i} \nabla \varphi_\mathrm{i} \qquad \text{Eq. 28}$$

Where i_i (A/m^2) is the current density (i = electrode / electrolyte), Q (C) is the total charge, σ (S/m) is the conductivity and φ (V) is the potential. Ohmic changes in the electrical connections were considered negligible. For the calculation of the cell's voltage, the open circuit voltage, the anode and cathode overpotential and the ohmic losses in the electrolyte were considered, using the following equation:

$$\mathrm{V}_{cell} = V_{OCV} + \eta_\mathrm{anode} + \eta_\mathrm{cathode} + R_{cell} i_{cell} \qquad \text{Eq. 29}$$

Where V_{OCV} (V) is the open circuit voltage and R_{cell} (Ω) is the internal resistance of the cell, consisting of the separator and the electrolyte resistances. Furthermore, Ohm's law was used to calculate the voltage between the anode and cathode electrodes.

$$\mathrm{V}_{cell} = I R_{ext} \qquad \text{Eq. 30}$$

Where I (A) is the current of the closed circuit, R_{ext} (Ω) is the external resistance connected in the MFC. After the initial simulation runs, the capacitance of the electrodes was incorporated in the model to further examine its effect. The following equation was added to take into account the changes in the potential in the electrode electrolyte interface, as well as the capacitance.

$$\mathrm{i} = \left(\frac{\partial (\varphi_\mathrm{electrode})}{\partial \mathrm{t}} \right) \mathrm{C_{electrode}} \qquad \text{Eq. 31}$$

Where $C_{electrode}$ (F/m) is the capacitance of the electrode. In the anode, the capacitance takes into account the biofilm existence and is different for every acclimation, namely every biofilm. The capacitance also depends on the type of the electrode.

The parameters of the aforementioned equations have been extracted by a fitting model developed using the Aquasim software [16]. This model was a modified version of the respective one by Zeng et al. 2009 [104]. The model contained altered mass balance equations, in order to simulate a batch reactor instead of a CSTR. Glucose was assumed as the electron donor and Andrews kinetics were used instead of the Monod. The resulting Andrews – Butler – Volmer equation is the following:

$$R_i = k_i \frac{C_{Glucose}}{K_{Glucose} + C_{Glucose} + \frac{C_{Glucose}{}^2}{K_i}} \exp\left(\frac{a_a F}{RT} \eta_a\right) \qquad \text{Eq. 32}$$

Where K_i (mol/m^3) is the inhibition of the glucose concentration. Experimental data of the operation of the previously described dual chamber MFC were used as input values for the estimation of the parameters. The results and more details of the Aquasim model were presented elsewhere [44]. The values of the parameters used are presented in the following table:

Table 14. List of model parameters, presented in the order their equations were presented (23 - 32).

Symbol	Description	Unit	Value	Source
k_1	Maximum specific growth rate	mol m^{-2} h^{-1}	$6 \cdot 10^{-3}$	Calculated by Aquasim model [44]
$K_{Glucose}$	Half – velocity rate constant for glucose	mol m^{-3}	$3 \cdot 10^{-4}$	
a_a	Anode transfer coefficient	–	0.05	

k_2	Forward rate constant of cathode reaction	m^{12} mol^{-4} h^{-1}	$9.19\cdot10^{-5}$	
K_{Oxygen}	Half – velocity rate constant for oxygen	mol m^{-3}	$4\cdot10^{-3}$	
a_C	Cathode transfer coefficient	–	0.7	
C_{anode}	Anode Capacitance	F m^{-2}	13721	
$C_{cathode}$	Cathode Capacitance	F m^{-2}	500	
K_S	Glucose inhibition constant	mol m^{-3}	$37\cdot10^{-3}$	
F	Faraday's constant	Coulombs mol^{-1}	96485	[120]
R	Gas constant	J mol^{-1} K^{-1}	8.31	
C_{Oxygen}	Dissolved oxygen concentration in the cathode chamber	mol m^{-3}	0.3125	[121]
D	Glucose diffusion coefficient	m^2 s^{-1}	$0.5\cdot10^{-9}$	
σ_i	Electrolyte conductivity	S m^{-1}	1.2	Experimental values
σ_i	Electrode conductivity	S m^{-1}	10	
E^0	Open Circuit Voltage	V	0.75	
$S_{electrode}$	Electrode surface	cm^2	19	

$S_{separator}$	Separator surface	cm^2	1
$d_{electrode}$	Electrode distance	cm	17

5 Results of single chamber MFC material comparison

The presentation of the results will take place in three parts one for the single – chamber MFCs, one for the dual – chamber MFCs and one for the simulation results. In each section, the objective is stated and the experimental configuration is briefly described.

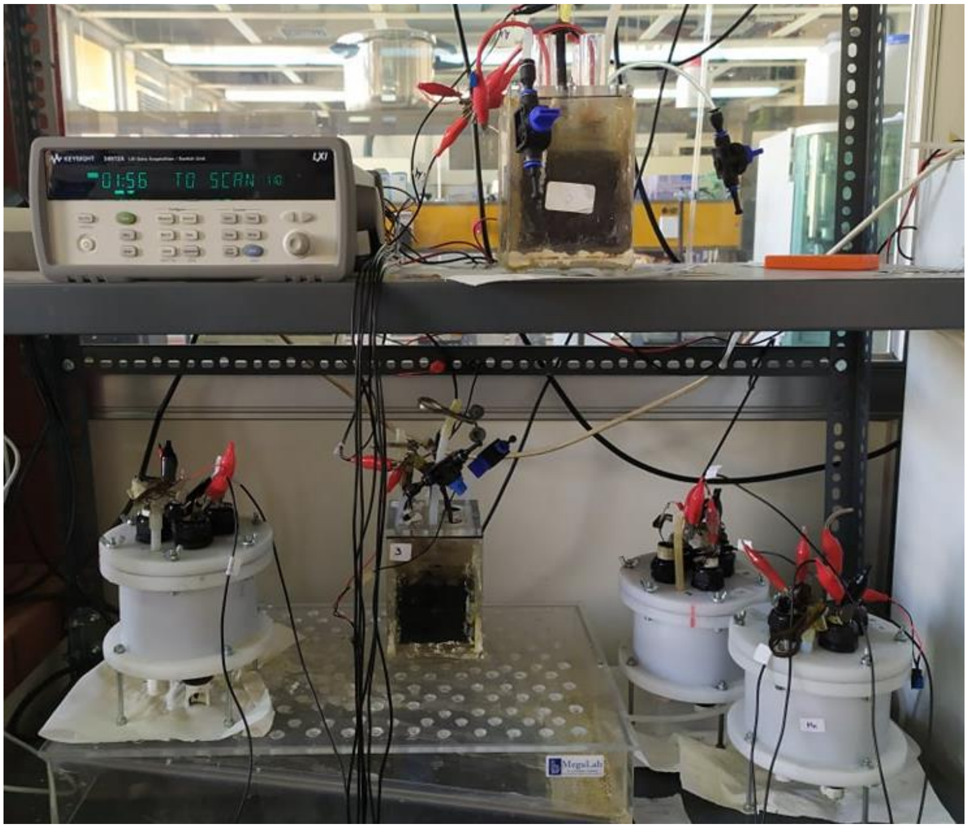

5.1 Oxygen reduction catalyst comparison

5.1.1 Introduction

Utilizing by-products or waste as materials for MFC construction increases the sustainability of the technology. Fly ash FA is generated during the combustion of coal or municipal solid waste for energy production [122]. It is an industrial by-product and is recognized as an environmental pollutant. In the past it was released in the atmosphere contributing to the air pollution, but strict laws have greatly reduced the emissions. The reuse of FA has led to the reduction of it reaching landfills. The main uses of FA are concrete and other structural material production as well as agricultural uses (soil amendment, fertilizer ao.). Considerable research is being carried out worldwide on the use of waste materials in order to avoid an increasing toxic threat to the environment, or to develop more efficient waste disposal techniques [122]. Fly ash can be a useful additive for electrode fabrication, since it has ion – exchange properties [123].

Activated carbon (AC) is a material originating from carbon – based source (wood, lignite, coal) using either a physical or a chemical activation. The basic characteristic of AC is the high surface area, which make it ideal for clearing water and air from pollutants. AC has been studied as an oxygen reduction catalyst in the MFCs, presenting notable results, when compared with different materials for cathode electrodes [124]. There are various ways to incorporate AC in the cathode electrode, either as a packed bed on the electron collector [124], or more complex techniques. AC was used a catalyst, initially subjected to coating and high – temperature pyrolysis, followed by the placement on a stainless – steel mesh using a rolling method [76]. For an air cathode single chamber MFC, an AC layer was placed on a gravel bed with a copper plate for the electrical connection [77].

This work examines different materials as cathode catalysts in order to maximize oxygen reduction occurring in single-chamber MFCs, while at the same time the effect of using mullite as a cathode electrode on the cell's performance is also examined. Specifically, MnO_2, fly ash and activated carbon have been selected as catalysts and mullite as the structural material of the cathodes. MnO_2 is a common catalyst used to accelerate the oxygen reduction rate, while fly ash and activated carbon are potential cheap alternatives, the performance of which is assessed in comparison with MnO_2.

Experimental set – up: 4.4.1.2

Experiments conducted: The MFCs were operated in batch mode and were fed with a synthetic glucose medium (1.5 g COD/L). During the first three batch cycles, the MFCs were inoculated with anaerobic sludge, in order to start the adaptation of the electrochemically active biofilm.

5.1.2 MFC current output and wastewater treatment efficiency for each catalyst

Figure 25 presents the current output versus time for the acclimation and operation of the three cells distinguished by color depending on the catalyst used (Green = MnO_2, Red = AC, Blue =FA). The arrows indicate the point when no further sludge is added in the feed.

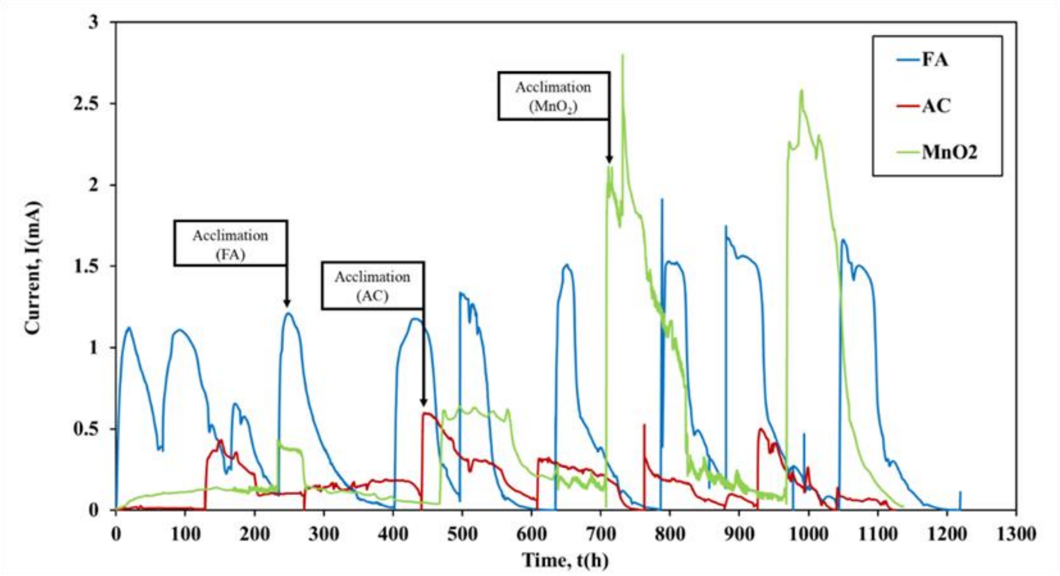

Figure 25. Current output versus time during acclimation and operation of the three cells (Green = MnO_2, Red = AC, Blue = FA). Arrows indicate the points in time where acclimation for each cell was considered complete

Following sludge inoculation, the current peaks during each successive cycle continue to increase, due to the adapting bacteria. The acclimation is finished once the maximum current is repeatable. The acclimation period for MnO2 cell was 700 h, for the FA cell 240 h and for the AC cell 440h, respectively. The FA cell acclimated faster than the other 2 cells, as it presented first repeatable current peaks. Following the acclimation, the maximum current (I_{max}) for the MnO_2 was recorded at the 4th cycle and was equal to 2.79 mA. The FA cell achieved I_{max} equal to 1.9 mA at the 6th cycle. The AC cell peaked at 0.6 mA, though the maximum current produced in each cycle was unstable, as can be observed in Figure 25. The average COD removal of the MnO_2 and FA cells was 81% and of the AC cell 78%. The CE was 12% – 14 % for the MnO_2 cell, while for the FA cell ranged between 6% – 18% and for the AC cell ranged between 2% – 7%. The increase in the maximum current corresponded to the increase in the CE for the MnO_2 and FA cells. The AC cell due to the low current output did not achieve similar CEs, indicating that the organic matter was mainly consumed by antagonistic microorganisms, which did not contribute to the current production.

Table 15 presents the average measurements of pH and conductivity at the end of the operation cycles. In comparison with the feed, all cells presented an increase in the pH. This increase is thought to have been caused by two factors. First, the continuous reduction of air's O_2 in the surface of the cathodic electrodes, as this process consumes the $[H^+]$ and secondly, anaerobic microbial reactions happening because of both electrogenic and other bacteria. Conductivity measurements presented an increase in two cells (MnO_2 and AC), while the FA cell presented a small decrease. The increase of the conductivity is presumably caused by the microbial activity; breaking down substances and increasing the dissolved ions in the anode, similar to

Table 15. Average pH and conductivity values of the effluent of the three cells (MnO_2, FA, AC).

Oxygen reduction catalyst	MnO_2	FA	AC
pH	7.5±0.9	7.7±0.1	8±0.3
Conductivity (mS/cm)	15.2 ±2.4	10.8±0. 1	13.8 ±1.6

5.1.3 Electrochemical characterization of the different MFC operations

Figure 26 presents the results of Linear Sweep Voltammetry experiments on the three cells. The maximum power was achieved by the MnO_2 cell (2.32 W/m^3) whereas the FA cell (1.21 W/m^3) and the AC cell (0.35 W/m^3) produced lower power output. The OCVs (open circuit voltages) obtained were 0.489 V for the MnO_2 cell, 0.419 V for the FA cell and 0.54 V for the AC cell, respectively. The AC cell reached the highest voltage in open-circuit conditions, although it yielded the lowest power production in comparison with the other cells. The MnO_2 cell produced both the highest current and power. The linear polarization curves indicate that ohmic losses dominate in all units. The FA cell achieved the highest CE among the three cells, but its maximum volumetric power density was 1.2 W/m^3.

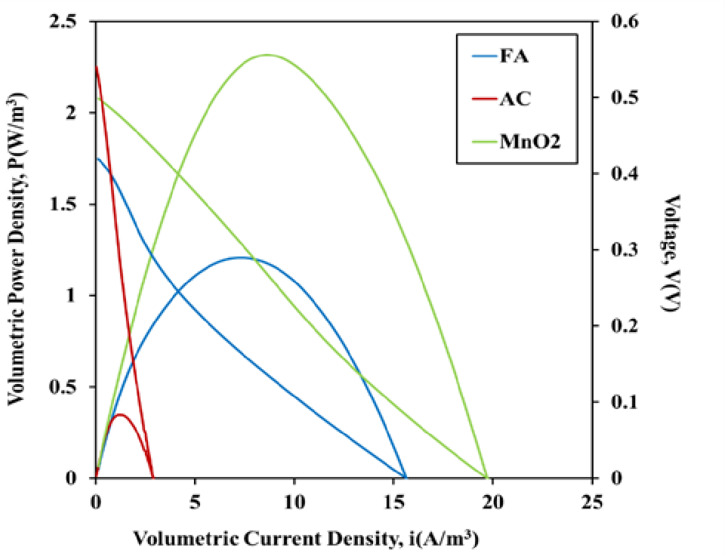

Figure 26. Volumetric power density versus volumetric current density versus voltage as extracted by LSV experiment on all three cells. (Green = MnO_2, Red = AC, Blue = FA)

The results from EIS also explained the lower maximum power output for all the cells. Although MnO_2 and FA depicted similar results in solution resistance (R_S), FA cell presented larger values of charge transfer resistance, thus leading to lower power curves, as shown in Figure 27. AC cell depicted lower resistances in biofilm (R_{BF}), and charge transfer (R_{CT}) leading to Warburg resistance thus explaining the low power output.

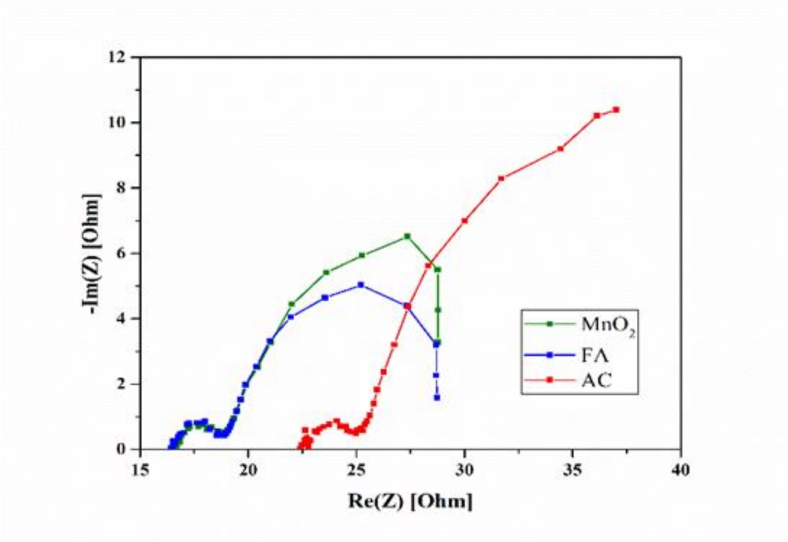

Figure 27. Nyquist plots of the 3 cells with different oxygen reduction catalyst. (Green = MnO$_2$, Red = AC, Blue = FA)

Table 16. EIS fitted results for all the different oxygen reduction catalyst cases.

Fitted Parameters	MnO2	FA	AC
R_S (Ω)	16.1	16.5	22.1
R_{BF} (Ω)	2.1	2.7	11.2
C_{BF} (F)	$0.4 \cdot 10^{-3}$	$0.3 \cdot 10^{-3}$	$12.1 \cdot 10^{-6}$
C_{CT} (F)	$7.2 \cdot 10^{-3}$	$7.9 \cdot 10^{-1}$	0.04
R_{CT} (Ω)	9.9	34.6	56.4

5.1.4 Conclusions

In this work, three MFCs were operated in order to compare MnO$_2$, AC and FA as oxygen reduction catalysts. Mullite was selected as the material for the cathode and graphite for the anode electrodes. The cell with the MnO$_2$ achieved a higher power output and COD removal efficiency (2.32 W/m^3) when compared with the FA cell (1.21 W/m^3) and AC cell (0.35 W/m^3). Further study is needed in order to identify the factors contributing to these results as well as to examine the long-term operation stability of these catalysts.

5.2 Cathode configuration comparison

5.2.1 Introduction

Although many efforts have been made towards the practical implementation of the MFC technology in the field of wastewater treatment, there are still practical barriers to overcome before the utilization of these systems. The main obstacles are the low power output obtained, due to high internal resistance, current instability as well as the high costs of the materials [125]. In this context, the practical implementation of the technology can be achieved through a MFC system that has the appropriate design for scaling up and can be conveniently combined with the existing wastewater treatment facilities, while ensuring high performance using cost effective construction materials.

In this direction, several air-cathode, membrane-less, single-chamber configurations have been examined since these designs increase the power production and reduce the capital cost of MFCs [62], [98]. In such systems, various inexpensive and sustainable materials have been tested as separators and as cathode catalysts [126], [127]. In this view, ceramics are very promising materials to be used as separators in MFCs due to their wide availability, low cost, structural stability, durability and environment-friendliness when compared to other materials [128]. Several studies can be found in the literature using different types of ceramics as separators while treating wastewater [73], [129]–[132]. In addition, in order to overcome the low performance of the air-cathode systems because of the poor cathode oxygen reduction reaction (ORR) [133], the use of platinum has been widely examined [68]. However, since the use of Pt hinders the practical implementation of the MFC technology due to its high -cost and low availability, platinum cathode catalysts have been replaced by carbon-based metal-free, transition metal oxide-based catalysts as well as met-al-nitrogen-carbon catalysts [134].

Beyond the cost effectiveness of the carbon metal-free catalysts, these materials have recently gained significant attention because they do not suffer from crossover effects and have long-term operational stability [135]. In particular activated carbon has high specific surface area, rich porous structure, high mechanical strength and stable properties, as well as excellent acid/alkali resistance [136]. In the same context, biomass-derived black carbon (biochar) has recently gained attention as an electrode material in the MFC technology, since it is a cost- effective and environmentally friendly material [137], [138]. In addition, manganese dioxide is a transition metal oxide that has been extensively used as a cathode catalyst in the MFC systems due to its environmentally-friendly property, good electrocatalytic activity and chemical stability [62], [139], [140].

In this study, five different MFC configurations were developed to improve the cathode performance of a single-chamber four-air cathode MFC under the view of using cost-effective and environmentally friendly materials [141].

Experimental set – up: 4.4.1.3

Experiments conducted: The MFCs were operated in batch mode and were fed with a synthetic glucose medium (1 g COD/L). During the first three batch cycles, the MFCs were inoculated with anaerobic sludge (10% v/v), in order to start the adaptation of the electrochemically active biofilm.

5.2.2 Different MFC cathode configurations comparison

In order to assess the different cathode assemblies, following the acclimation of the units, the MFCs operated in batch mode for approximately 480 h. Figure 28 presents the current output profiles produced from the five units, while CE and COD removal efficiency, from MFCs equipped with the different cathode materials (P-MnO_2, M-MnO_2, CFA, BC, AC), are summarized in Figure 29 and Figure 30.

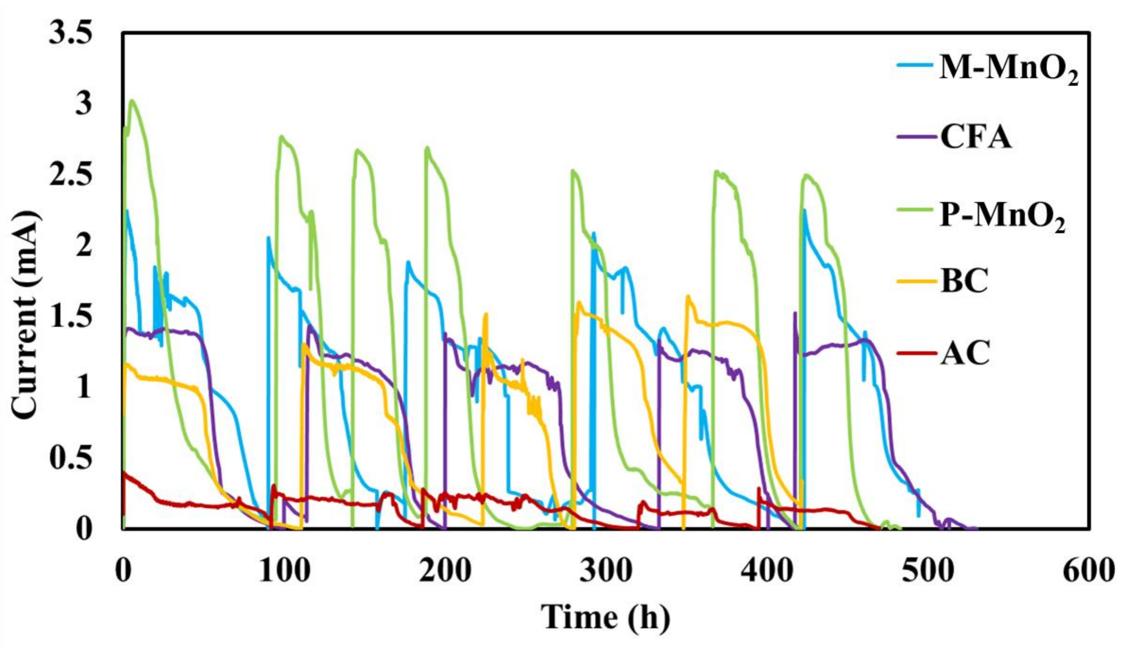

Figure 28. Current output during consecutive batch experiments of the five units with the different cathode assemblies (P-MnO_2, M-MnO_2, CFA, BC, AC) versus time.

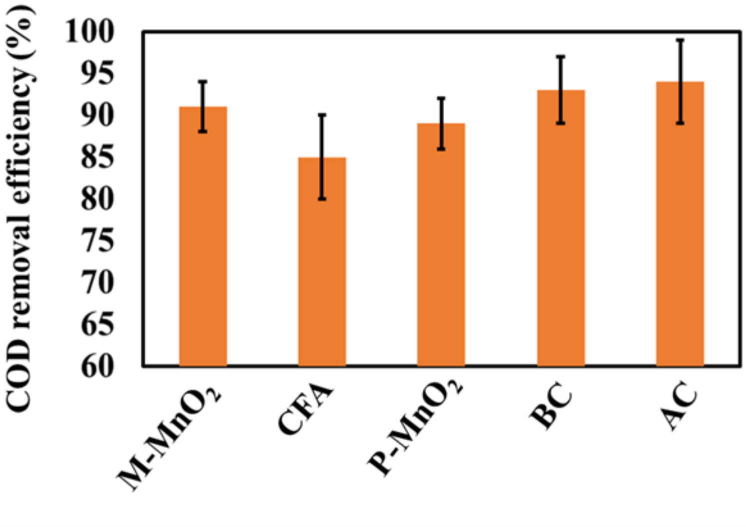

Figure 29. Average COD removal efficiency values with deviations of the five units with the different cathode assemblies (P-MnO$_2$, M-MnO$_2$, CFA, BC, AC) versus time.

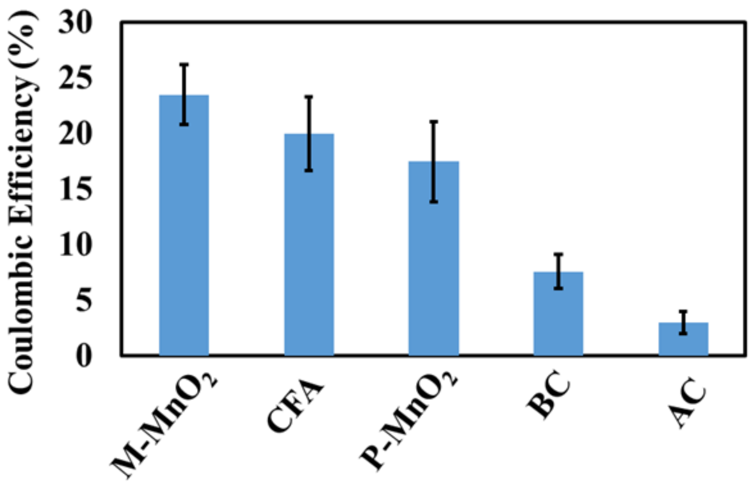

Figure 30. Average CE efficiency values with deviations of the five units with the different cathode assemblies (P-MnO$_2$, M-MnO$_2$, CFA, BC, AC) versus time.

Results showed that the P-MnO$_2$ assembly achieved the highest I_{max} of 2.7 ± 0.2 mA, followed by M-MnO$_2$ with 2.1 ± 0.1 mA, BC with 1.5 ± 0.1 mA, CFA 1.5 ± 0.2 mA and AC 0.3 ± 0.1 mA. Although the maximum current output was obtained from the P-MnO$_2$ assembly, the M-MnO$_2$ unit outperformed in terms of CE, with the second highest CE value achieved from CFA unit. In particular, CE values were 23.5 ± 2.7%, 20 ± 3.3%, 17.5 ± 3.6%, 7.6 ± 1.5%, 3 ± 1%, for the M-MnO$_2$, CFA, P-MnO$_2$, BC and AC units, respectively. Regardless of the performance of the MFCs in terms of current output and CE, all the systems successfully removed the organic substrate of the synthetic wastewater. Specifically, the following COD removal efficiencies were obtained: 94 ± 5% (AC), 93 ± 4% (BC), 91 ± 3% (M-MnO_2), 89 ± 3% (P-MnO_2), 85 ± 5% (CFA). Despite the different cathode assemblies used, the high COD removal efficiency values verify the presence of non - electrogenic bacteria in the anode chamber which also consume the organic matter of the wastewater along with the electrogenic bacteria [142].

5.2.3 Effect of the different cathode assemblies on the MFC power output

Figure 31a and Figure 31b show the dependence of the MFC voltage and the produced power volumetric density, on the current density passing through the units with the different cathode assemblies.

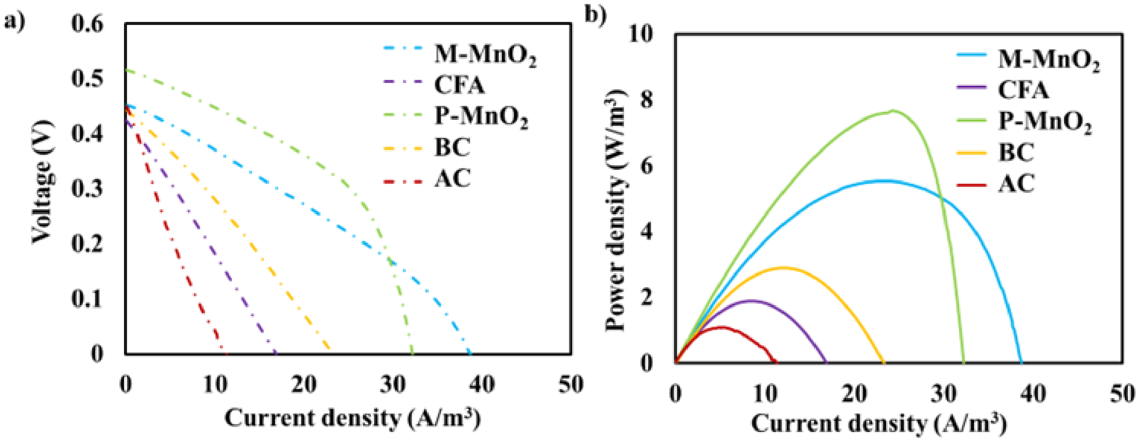

Figure 31. MFC voltage (a) and power density (b) versus current density for the different cathode configurations (P-MnO_2, M-MnO_2, CFA, BC, AC).

As shown in Figure 31a, the open circuit voltage (OCV) was ~ 0.44 V for the assemblies M-MnO_2, CFA, BC and AC, whereas the OCV value for the P-MnO_2 configuration was 0.52 V. The P-MnO_2 configuration achieved the highest maximum power volumetric density 7.7 W/m^3, followed by M-MnO_2 with 5.5 W/m^3, CFA with 2.9 W/m^3, BC with 1.9 W/m^3 and AC with 1.1 W/m^3 (Figure 31b).

In addition, the internal resistance (R_{in}) of the CFA, BC and AC assemblies, as determined by the power density peak method was 133 Ω, 177 Ω and 298 Ω, respectively. Moreover, the almost constant slope of the polarization curves of these units (Figure 31a) indicates the very significant contribution of ohmic losses (ohmic overpotential) for the CFA, BC and AC assemblies. The internal resistance for the MnO_2 catalyst was lower when compared to other catalysts, regardless of the structural support used (Rin was 64 Ω and 70 Ω for P-MnO2 and M-MnO2 respectively). On the other hand, when MnO_2 catalyst is used, in addition to the ohmic losses that occur, a rapid voltage drop is also observed at high current densities, indicating mass transport limitations (Figure 31a).

5.2.4 Conclusions

The operation of five different MFC cathode assemblies was assessed and compared in terms of organic matter removal and electricity generation. Although the wastewater treatment was satisfactory for all cases (COD removal efficiency ≥ 85%), the MnO_2 catalyst outperformed in terms of power generation coal fly ash (2.9 W/m^3), biochar (1.9 W/m^3) and activated carbon (1.1 W/m^3). In particular the P-MnO_2 configuration achieved the highest maximum power volumetric density (7.7 W/m^3) in comparison to M-MnO_2 (5.5 W/m^3). Although the MnO_2 configurations obtained the best performance, the results indicated that the exploitation of coal fly ash and biochar as cathode catalysts in the MFC technology is promising.

5.3 Effect of cathode electrode number

5.3.1 Introduction

The aim of this work was to investigate the effect on MFC performance of the number of cathode electrodes.

Experimental set – up: 4.4.1.4

Experiments conducted: The MFC was operated in batch mode and was fed with a synthetic glucose medium (1 g COD/L). The effective volume of the cylindrical cell was 300 mL.

5.3.2 Comparative operation with 4 versus 6 air – cathode electrodes in single – chamber MFC

The MFC (SCH) with the modifiable lid and bottom, to fit 4 and 6 cathode electrodes, was operated, using the already acclimated graphite granules originating from SRMul. The current output and COD concentration, of the SCH operation, are presented in Figure 32.

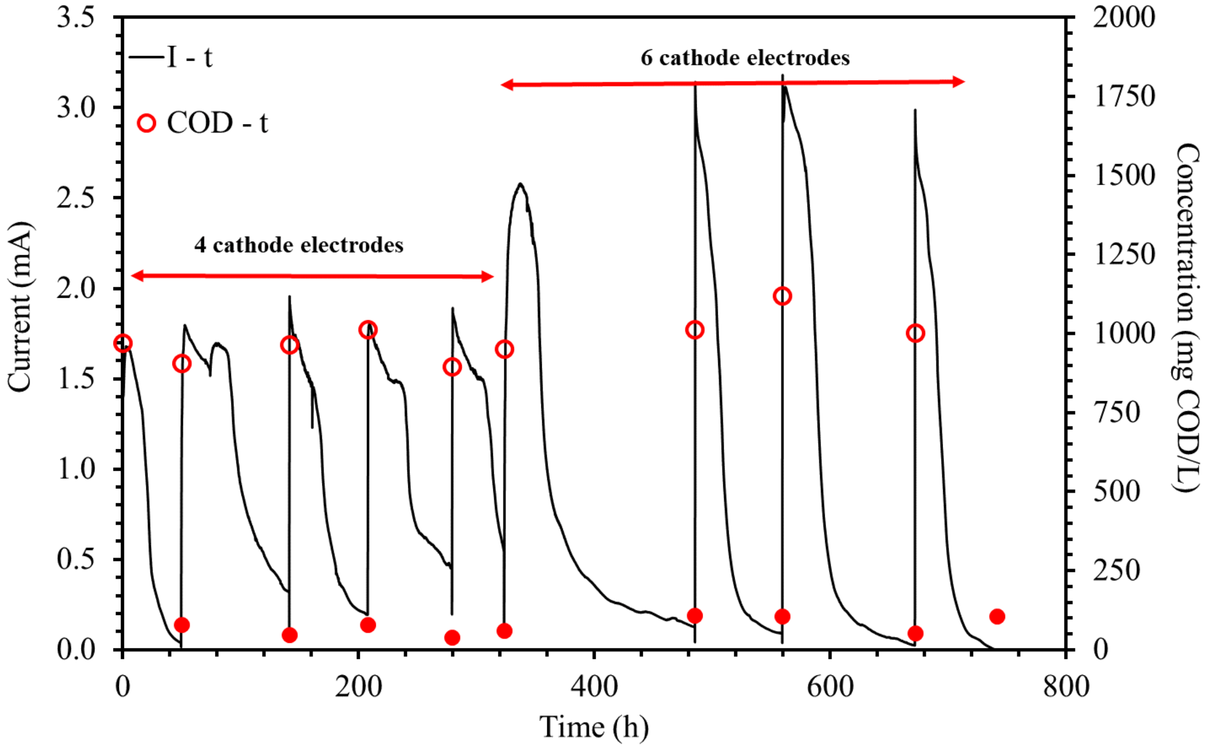

Figure 32. Current output and COD concentration versus time, during batch operation of MFC with 4 and 6 cathode electrodes, respectively.

During the operation with 4 cathode electrodes, the SCH cell achieved a repeatable maximum current output equal to 1.8 ± 0.1 mA (Figure 32). The average COD removal efficiency for the corresponding operation cycles was 94% (Figure 32). The CE of the SCH operation achieved a maximum value of 36% during the 2nd cycle, along with the maximum E_{yield} for 2nd cycle 23.5 mJ/gCOD/L. The CEs were relatively high during the two first cycles (31% - 1st cycle and 36% - 2nd cycle), whereas it decreased during the following three cycles (13% - 3rd cycle, 15% - 4th cycle and 14% - 5th cycle). The E_{yield} of SCH during the operation with 4 cathode electrodes varied (5 mJ/gCOD/L - 1st cycle, 24 mJ/gCOD/L - 2nd cycle, 18 mJ/gCOD/L - 3rd cycle, 10 mJ/gCOD/L - 4th cycle and 12 mJ/gCOD/L - 5th cycle).

Afterwards, the lid and bottom of the SCH were replaced by new ones in order to fit six cathode electrodes in the unit, keeping the acclimated graphite granules in synthetic glucose wastewater in the meantime (1 gCOD/L). The SCH was reassembled using 6 cathode electrodes (Gore-Tex Plexiglas MnO_2) and the same anode, as the operation with 4 cathode electrodes. Then it was filled (effective volume 300 mL) with fresh glucose wastewater (1 gCOD/L).

The SCH operation with 6 cathode electrodes produced a current output of 2.6 mA initially, followed by repeatable peaks at 3.1 ± 0.1 mA, (Figure 32). The COD removal efficiency averaged 91% ± 4% (Figure 32). The CEs presented a similar trend for the different number of cathode electrodes. During the 6 cathode electrode operation the SCH achieved CE 28% in the 6th cycle (Figure 32), followed by reduced CEs in the subsequent cycles (15% - 7th cycle, 18% - 8th cycle and 13% 9th cycle). The maximum E_{yield} was equal to 20 mJ/gCOD/L (6th and 8th operation cycle, Figure 32). The minimum E_{yield} was observed during the 7th and 9th operation cycle and was equal to 13 mJ/gCOD/L and 12 mJ/gCOD/L, respectively.

The pH of SCH effluent presented a small increase when compared to the initial pH of the synthetic glucose wastewater (pH 8 vs pH 7, respectively). The conductivity of the SCH effluent was similar to the initial feedstock value (~11.5 mS/cm).

Overall, the highest current output (3.2 mA) was achieved with the 6 electrodes whereas CE was higher in the case of 4 electrodes (CE 36%). Additionally, the CE during the 4 electrodes operation was higher 36%, when compared to the maximum CE during 6 electrodes, 28%. In both cases similar trends were presented by the respective CEs, as the maximum values were achieved during the first operation cycles, followed by a drop in the subsequent cycles.

5.3.3 Electrochemical characterization of MFC operation with 4 versus 6 air – cathode electrodes

The results of the LSV experiments are presented in Figure 33 for the SCH operation with 4 and 6 cathodes. The power density versus current density is depicted by continuous lines, while the voltage versus current density is depicted by dashed lines. The maximum power density was achieved during the operation with 6 electrodes equal to 3.9 W/m^3 – 7th cycle and 3.4 – 8th cycle, Figure 33. The power density during the 4 cathode electrodes peaked at 1.7 W/m^3, Figure 33. The internal resistances are calculated by the maximum power theorem and the lowest values were achieved during the operation with 6 electrodes, 82 Ω – 7th cycle and 66 Ω – 8th cycle. The 4 cathodes configuration had a higher internal resistance across all operation cycles studied (120 Ω – 3rd cycle , 148 Ω – 4th cycle and 161 Ω – 5th cycle). The difference in the maximum current output (2 mA – 4 cathodes, 3.2 mA – 6 cathodes, Figure 32) and maximum power density achieved (3.9 W/m^3 – 6 cathodes, 1.7 W/m^3 – 4 cathodes, Figure 33) can be attributed to the difference in the internal resistances (66 Ω – 6 electrodes, 120 Ω – 4 electrodes), between the configuration with 4 and 6 cathode electrodes.

The voltage versus current density dashed lines (Figure 33) indicate the domination of ohmic losses during the SCH operation. However, for the 6 cathode electrodes at high current densities (~20 A/m^3, 7th and 8th cycles, Figure 33), the angle of the lines changed, hinting the electrochemical losses due to mass transfer (substrate diffusion in the biofilm). The 4 cathode electrodes did not present this pattern at the respective high current densities (~10 A/m^3 4th cycle, ~11 A/m^3 5th cycle and ~ 14 A/m^3 3rd cycle, Figure 33), resulting in ohmic losses being visible in the voltage versus current density.

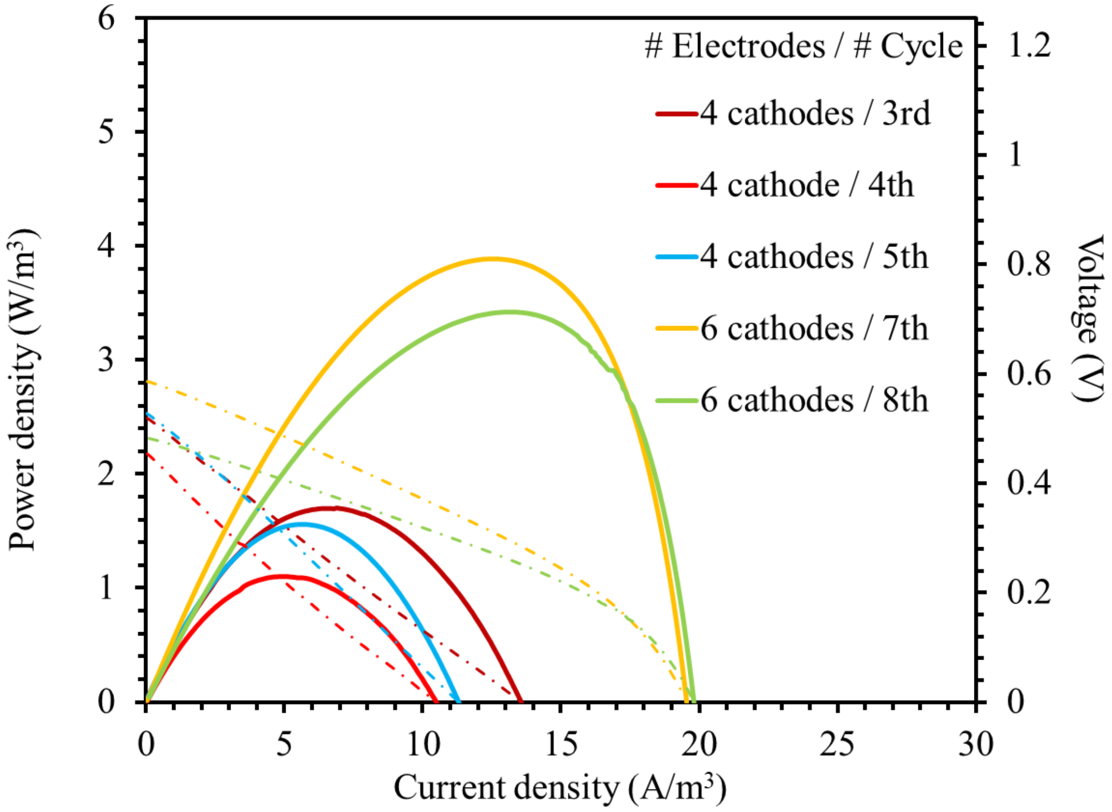

Figure 33. SCH power density and voltage versus current density for the different cathode configurations (4 Gore-Tex and 6 Gore-Tex cathode electrodes, with MnO_2 oxygen reduction catalyst).

5.3.4 Conclusions

The SCH cell operated with 4 and 6 Gore-Tex cathode electrodes, with MnO_2 as cathode catalyst., with the same anode in both cases. The same synthetic glucose wastewater (1 gCOD/L) was used across all operation cycles. The use of 4 cathodes achieved a maximum current output of 2 mA and a maximum power density of 1.7 W/m^3, with a minimum MFC internal resistance of 120 Ω. By increasing the cathode electrodes to 6 and keeping the same anode and feedstock, the MFC performance improved, achieving a maximum current output of 3.2 mA and power density of 3.9 W/m^3. The switch from 4 to 6 electrodes resulted in a lower internal resistance of the SCH (66 Ω), which increased the power output of the cell. High COD removal efficiency was achieved (>89%) across all cases.

5.4 Anode configuration comparison

5.4.1 Introduction

In this chapter four anode materials are compared, with cathode electrodes containing MnO_2 as oxygen reduction catalyst. The aim is to examine the performance of the MFC utilizing carbon felt, graphite granules and carbon veil as anode materials.

Experimental set – up: 4.4.1.5

Experiments conducted: Four MFCs (SRCF, SRCV, Smul and SRGM) were operated in batch mode and were fed with a synthetic glucose medium (1 g COD/L).

5.4.2 MFC operation with different anode electrodes

SRCF MFC operation

The results of the SRCF cell are presented in Figure 34. The maximum current output during the SRCF operation was 2.5 ± 0.2 mA. The cell presented high COD removal efficiency across all operation cycles (~92%, Figure 34). The strength of the carbon felt as an anode material was presented from the average CE achieved ~40%, throughout the SRCF operation (Table 17). The CE values in combination with the COD removal efficiency indicate that a well acclimated biofilm had developed in the carbon felt anode. The pH of the anode was constant, due to the presence of the phosphate buffer ($pH_{Initial} = 7$, $pH_{Effluent} \sim 7.1$). On the other hand, the conductivity of the SRCF (8.5 ± 1.7 mS/cm) presented a decrease compared to the initial value of the synthetic glucose wastewater (11.5 mS/cm, Table 1).

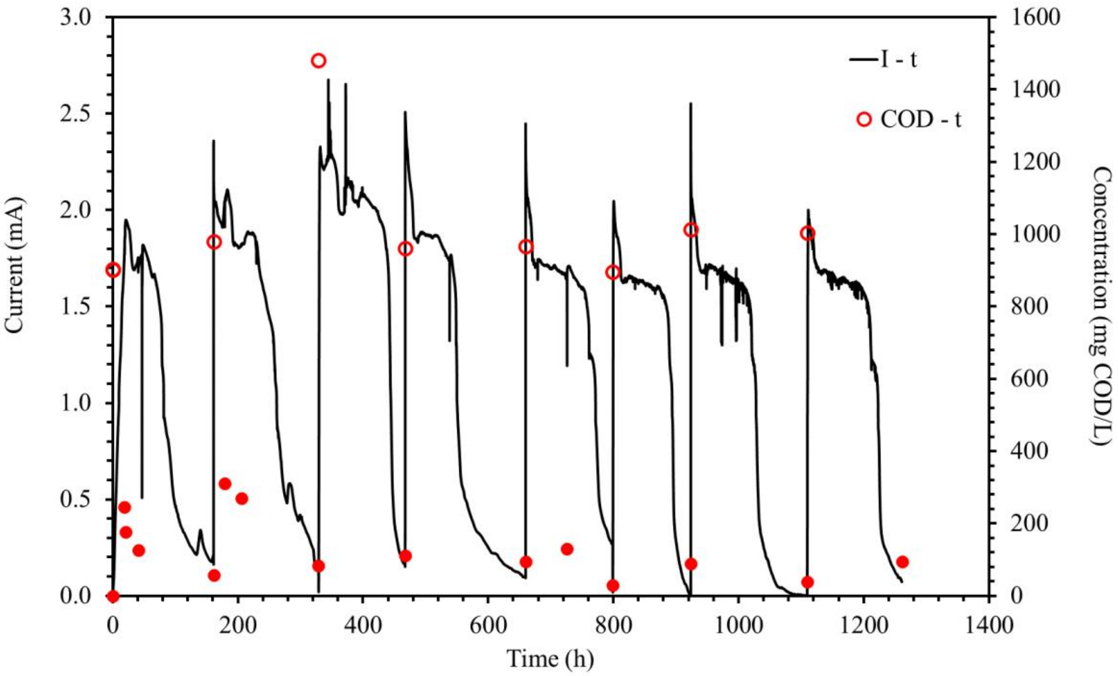

Figure 34. Current output and COD concentration versus time for the single chamber MFC with carbon felt as anode and 3 mullite MnO_2 electrodes as cathode.

The maximum E_{yield} achieved was 34.8 mJ/gCOD/L (Table 17), during the 2nd operation cycle (Figure 34). Overall, the SRCF presented a stable and efficient performance during the synthetic glucose wastewater treatment.

Table 17. Results of the SRCF operation with synthetic glucose wastewater (1 g COD/L) as feedstock.

Cycle #	I_{max} (mA)	Δt cycle (h)	CE (%)	E_{yield} (mJ/gCOD/L)
1	2.3	161	36	24.3
2	2.7	168	46	34.8
3	2.7	138	35	33.3
4	2.5	192	42	31.7
5	2.4	139	42	32.9

6	2.5	125	39	28.1
7	2.5	186	37	28.6
8	2.0	152	41	29.6

SRCV MFC operation

Figure 35 presents the results of the SRCV cell. In particular this cell consisted of an anode with carbon veil and a cathode with four mullite electrodes with MnO_2. The cell did not produce notable current during its operation. However, the concentration of the COD was decreased in each cycle (~80%, Figure 35). The current generation was inhibited by the anode material combination, the electron collector used was a titanium wire woven around the carbon veil. No material was used to glue together the titanium wire with carbon veil, which caused the low current output (~3 pA, Figure 35). The pH in the anode presented an increase (~8.8), compared to the initial value (7, Table 1) of the synthetic glucose wastewater. This anode material combination with the cell's rectangular geometry and four cathode electrodes, did not operate as expected. As highlighted in Figure 35, OCV acquisition experiments were conducted on the marked cycles. No OCV was measured, which adds to the fact that the system short-circuited and malfunctioned due to the connecting points of the titanium wire and the carbon veil. Carbon veil is a material which has been used in the MFC technology [147], without any modifications or pretreatment required, reportedly producing up to 11.9 W/m^3 [147].

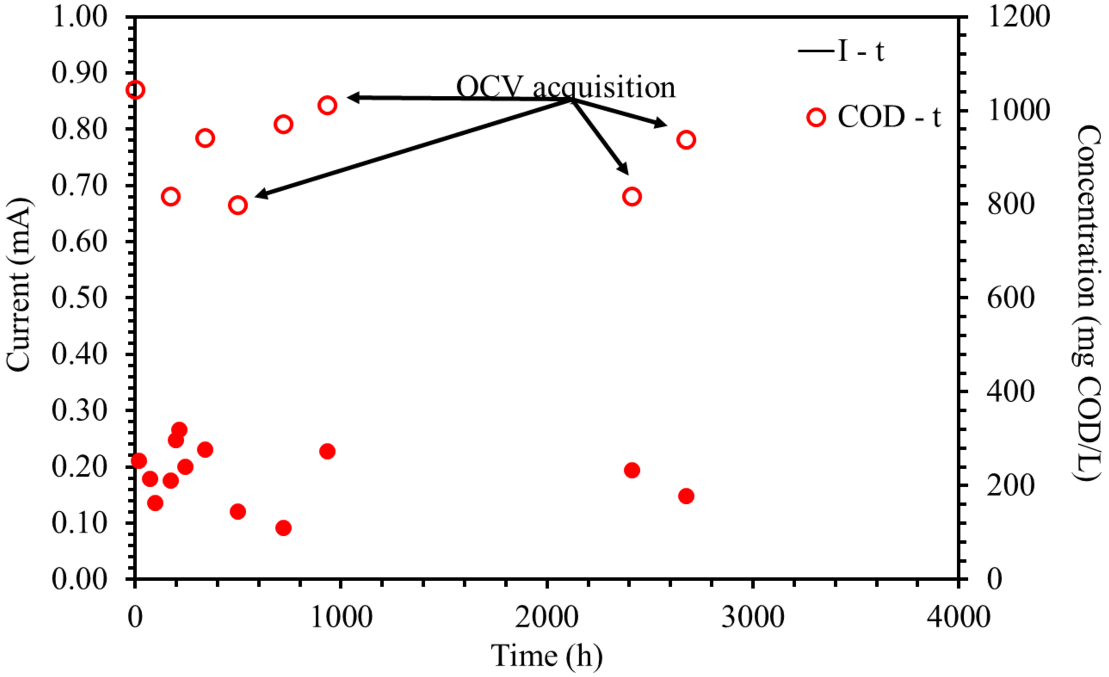

Figure 35. Current output and COD concentration versus time of the single chamber MFC with carbon veil as anode and mullite MnO_2 electrodes as cathode.

SRGM MFC operation

In Figure 36 the results of the SRGM acclimation are presented, with synthetic glucose wastewater (1 g COD/L) and sludge inoculums. This cell consisted of a graphite granule and graphite rod anode and four Gore-Tex cathode electrodes with MnO_2. Initially, the current output was low (0.6 mA 1st cycle and 0.5 mA 2nd cycle, Figure 36). After the third cycle a notable increase in the current output was detected peaking at 3.1 mA, Figure 36. The COD removal efficiency on the first operation cycle was low (38%), due to the partially acclimated biofilm. The subsequent cycles presented higher COD removal efficiency (>71%, Figure 36). The maximum CE achieved was 43% (Table 18), indicating an efficient wastewater treatment. The maximum E_{yield} was 27.8 mJ/gCOD/L, (Table 18), during the synthetic glucose wastewater operation (1 g COD/L). The increase in the current output after the 2nd operation cycle was attributed to the fully acclimated biofilm and the dominance of the electrochemically active bacteria.

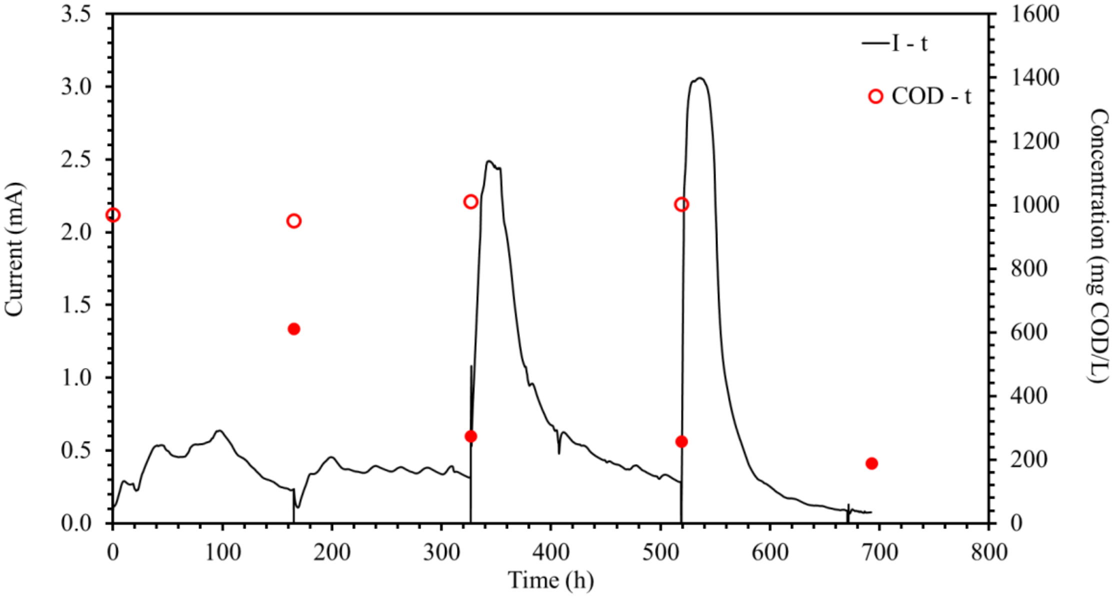

Figure 36. Current output and COD concentration versus time for the single chamber MFC with graphite granules as anode and 4 Gore-Tex Plexiglas electrodes with MnO_2 as cathode (SRGM).

Table 18. Results of the SRGM operation with synthetic glucose wastewater (1 g COD/L) as feedstock.

Cycle #	I_{max} (mA)	Δt cycle (h)	CE (%)	E_{yield} (mJ/gCOD/L)
1	0.6	165	37	3.2
2	0.5	162	16	2.2
3	2.5	192	43	22.5
4	3.1	174	31	27.8

Smul MFC operation

In Figure 37 the results of the Smul MFC operation are presented, with synthetic glucose wastewater (1 g COD/L) as feedstock. This cell consisted of a graphite granule and graphite rod anode and a cathode of four mullite electrodes with MnO_2. Smul achieved repeatable maximum current output peaks (2.3 ± 0.1 mA, Table 19), indicating a well acclimated electrochemically active biofilm. The COD removal efficiency achieved was high (> 94% ± 3%) across all cycles. Moreover, the maximum CE achieved was 38% (2nd cycle, Table 19), with the CE of the rest cycles ranging from 13% to 30% (1st, 3rd – 10th cycle, Table 19). The maximum E_{yield} was 45.7 mJ/gCOD/L (3rd cycle, Table 19).

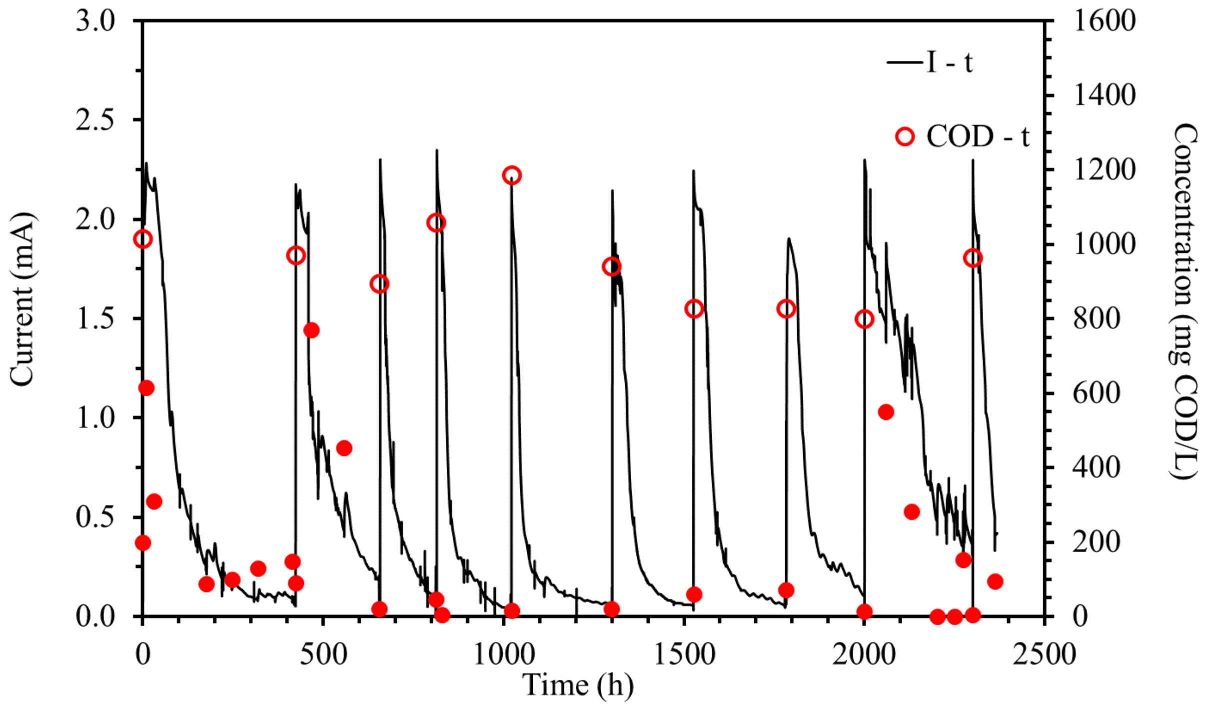

Figure 37. Current output and COD concentration versus time for the single chamber MFC with graphite granules as anode and 4 mullite electrodes with MnO_2 as cathode (Smul).

Table 19. Results of the Smul operation with synthetic glucose wastewater (1 g COD/L) as feedstock

Cycle #	I_{max} (mA)	Δt cycle (h)	CE (%)	E_{yield} (mJ/gCOD/L)
1	2.3	423	30	31.6
2	2.2	231	38	36.3
3	2.3	158	20	45.7

4	2.3	209	16	37.0
5	2.2	278	13	24.0
6	2.2	227	18	21.9
7	2.2	257	24	23.6
8	2.3	217	30	18.3
9	2.3	300	26	32.2
10	2.3	67	19	14.3

5.4.3 Electrochemical characterization of MFCs operating with different anode configurations

To further assess the performance of the cells, LSV experiments were conducted and the results are presented in Figure 38. The SRCV did not present current generation and no notable results were obtained from the LSV experiments. The highest power density during each MFC's operation is compared. The SRGM power density was 14.2 W/m^3, which was greater than the respective maximum power densities achieved by the Smul cell 6.9 W/m^3 and SRCF cell 4.6 W/m^3. The lowest internal resistance was detected in the Smul cell equal to 57 Ω. The SRGM cell internal resistance was 72 Ω, while the SRCF was 87 Ω.

The voltage versus current density lines in Figure 38 indicate the different electrochemical losses present. The SRCF (dashed red line) line indicates that in this case ohmic losses dominated in the system. In the case of the Smul (dashed green line) and SRGM (dashed blue line), apart from the line observed in the low and medium current densities (Figure 38), a curve formed at higher current densities (Figure 38). The mass transfer losses are electrochemical losses due to substrate diffusion in the biofilm. The fast decomposition of the substrate (glucose) is restricted by the slow diffusion of glucose towards the biofilm and the oxidation products outwards from the biofilm. The electrochemical losses due to mass transfer were visible in the two better performing cells (SRGM, Smul), with higher power densities (14.2 W/m^3 and 6.9 W/m^3, Figure 38). The cells which presented the highest power density output (SRGM, Smul), also presented the lowest internal resistances.

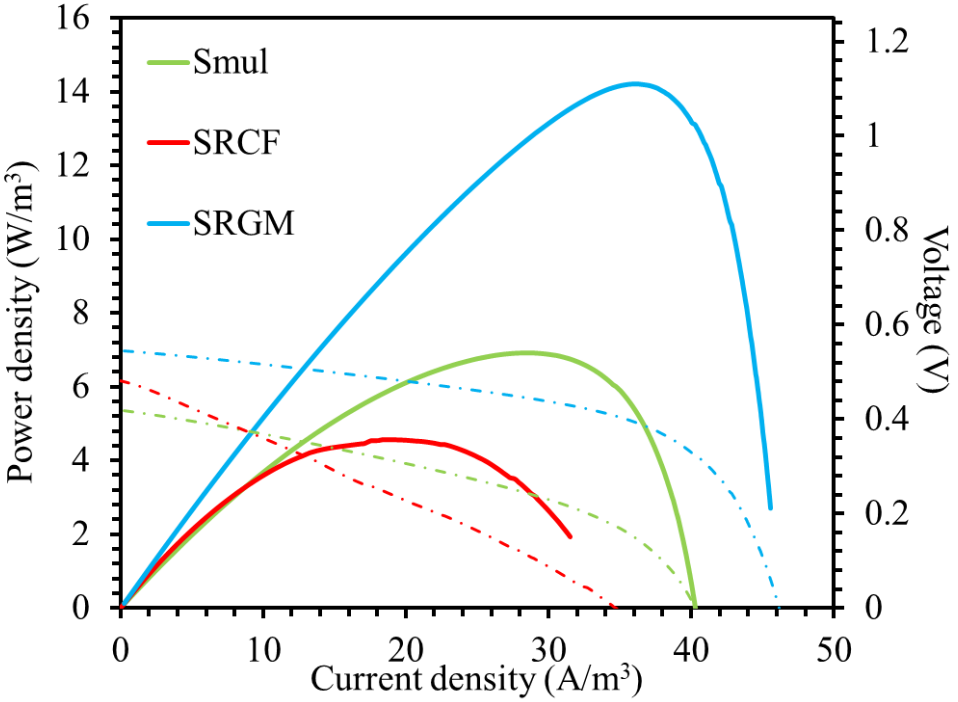

Figure 38. Power density and voltage versus current density for the three MFCs (Smul, SRCF, SRGM), during operation with synthetic glucose wastewater (1 gCOD/L).

5.4.4 Conclusions

In this work different anode configurations were compared. Four MFCs were constructed and operated with synthetic glucose wastewater (1 g COD/L). The different anode used were graphite granules (SRGM, Smul), carbon felt (SRCF) and carbon veil (SRCV). The cathodes were mullite electrodes (Smul, SRCF, SRCV) and Gore-Tex electrodes (SRGM), with MnO_2 as the oxygen reduction catalyst. The highest current output was achieved by the SRGM cell (3.1 mA) along with the maximum power density (14.2 W/m^3). Graphite granules with a graphite rod outperformed the other anode assemblies (carbon felt + titanium wire, carbon veil + titanium wire). On the other hand, the SRCF presented a high average CE (~40%), which corresponds to a well acclimated biofilm in the pores of the carbon felt used. The combination of carbon veil with titanium wire did not yield adequate results, due to the multiple connecting points of the titanium wire and the thin carbon veil.

6 Results of single chamber MFC (household) food waste treatment

Biowaste mainly consists of food waste (60%) and garden waste and corresponds to a share of 34% of the total municipal waste in the EU. Only in the EU-28, 88 million tons of food are wasted every year [148]. Given the consequences of biowaste disposal as well as its potential for valorization, biowaste has to be considered more as a valuable resource stream than as a waste to dispose of. Usually, disposal of bio-waste, such as food waste, includes landfilling or incineration. However, these approaches have a severe impact on the environment. Landfills cause leachate formation and subsequent groundwater pollution, as well as greenhouse gas emissions [149]. On the other hand, incineration consumes high amounts of energy and produces high amounts of carbon dioxide emissions [150]. Given the fact that almost 53% of the total food waste produced in the European Union corresponds to household food waste (HFW), along with the fact that HFW is a material rich in carbon and nitrogen different approaches have emerged using HFW as a feedstock [62], [151], for the production of energy and value added products such as biogas, biosurfactants, bioplastics and organic fertilizers [62], [152], adsorbents for the removal of dye effluents from water streams[149] and plat-form chemicals such as lactic acid [153], [154].

In order to fully exploit HFW, sorting at the source need to be carried out before its use as a feedstock. Separate collection from households secures that plastic, metal, glass and other inorganic materials are not mixed with HFW [155]. Moreover, HFW due to its high-water content and its complex organic matter, has the tendency to be spontaneously biodegraded by aerobic and/or anaerobic microorganisms emitting odors and raising health and environmental [156]. Under the view of confronting these drawbacks and valorize the valuable material of HFW, an alternative approach has been recently developed within the framework of the Horizon 2020 Waste4Think Project [157]. During this Project, in the Municipality of Chalandri, Greece volunteering households along with local food markets sorted their food waste, from the rest of their waste streams. Moreover, in order to overcome the major issue of the HFW spontaneous biodegradation, the collected HFW was dried and shredded thus producing a homogenized solid biomass with low moisture content so that it may be stored for prolonged periods of time. The main product from the drying process, named Food Residue Biomass (FORBI), is rich in carbon and nitrogen, making it an ideal substrate for anaerobic processes [113]. FORBI combines several advantages since it is homogenous, it does not emit odors, it has low –moisture, it can be long term stored without deterioration and it has 1/4 to 1/5 the weight of biowaste, implying reduced transportation costs. Consequently, FORBI has been examined in different bioprocesses. Specifically, it was used as a substrate for dark fermentation [158], as a feedstock in a periodic anaerobic baffled reactor (PABR) [159] and as a substrate for electricity production in MFCs [160]. FORBI was also examined for biofuel production (biohydrogen, bioethanol and methane) [156].

However, along with FORBI production, during the drying process, approximately 75-80% of the moisture contained in HFW is removed and the vapors are collected in the condenser [113]. The produced liquid, named condensate is a material with high organic and low nitrogen content making it a potential feedstock for different processes [113]. Under the scope of fully exploiting all the by-products from the drying process, Lytras et al. 2020 examined the approach of co-digesting the condensate with waste-activated sludge (WAS). In particular, the condensate, due to its low nitrogen content, was co-digested with WAS in a CSTR with 100 L of working volume [113]. The condensate to WAS ratio was 1:5, resulting in an average methane percentage of 74.3% in the produced biogas while the overall methane production was 343 mL methane/g COD [113].

6.1 FORBI leachate treatment in continuous and batch mode

6.1.1 Introduction

In this chapter are presented the results of the MFC operation with FORBI leachate. The aim of this work, is to exploit a four-air cathode single chamber MFC design, which is constructed with relatively low-cost materials, for bioelectricity production and HFW treatment.

Experimental set – up: 4.4.2.1

Experiments conducted: The MFCs were fed with FORBI leachate, created by mixing FORBI and DI water and then filtering it. The FORBI leachate was then diluted to the desired COD concentration (1.6 g COD/L). Phosphate buffer was added in the solution (PBS; pH 7) in order to adjust its pH from 3.6 to 7. The four systems were operated in batch mode initially and then were switched to continuous mode. During the continuous operation two different external connections were examined between the four MFCs, parallel and in series.

6.1.2 MFC batch operation

Following the inoculation period, the units operated individually in batch mode for approximately 1000 h. Figure 39, Figure 40, Figure 41 and Figure 42 show the current output and the COD consumption versus time for the Cell 1, Cell 2, Cell 3 and Cell 4, respectively.

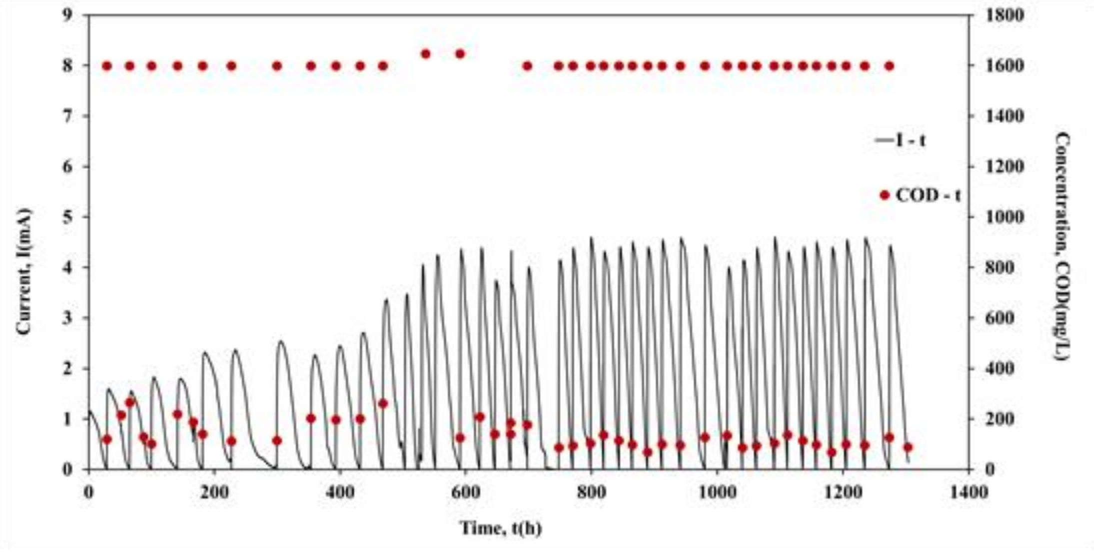

Figure 39. Current output (mA) and COD concentration (mg/L) versus time of Cell 1, during batch operation.

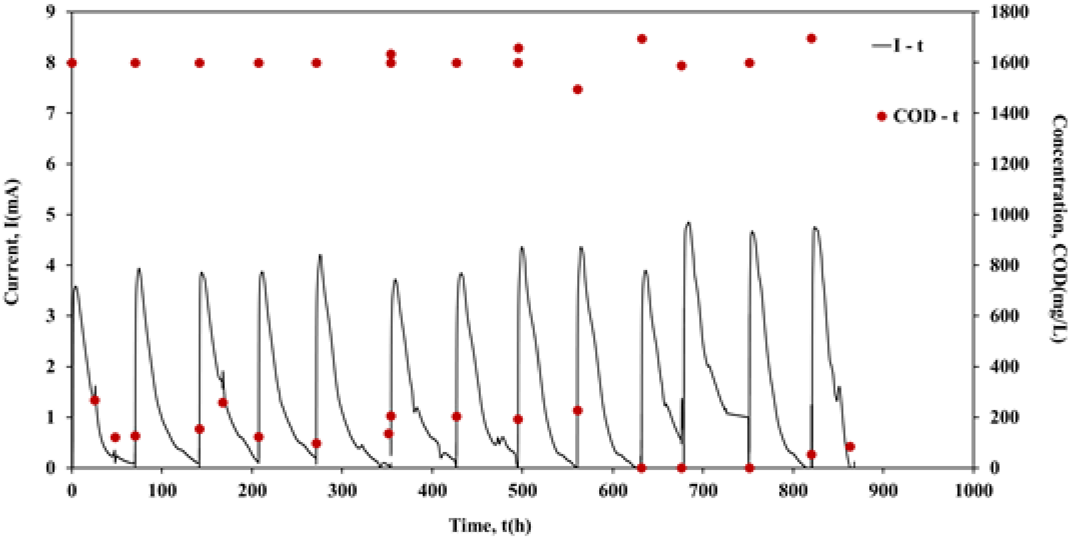

Figure 40. Current output (mA) and COD concentration (mg/L) versus time of Cell 2, during batch operation.

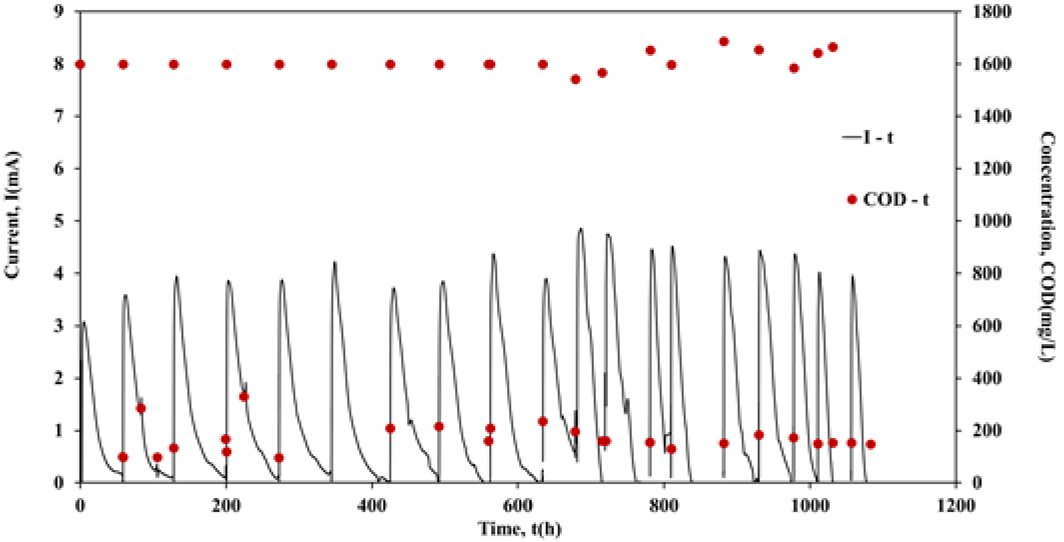

Figure 41. Current output (mA) and COD concentration (mg/L) versus time of Cell 3, during batch operation.

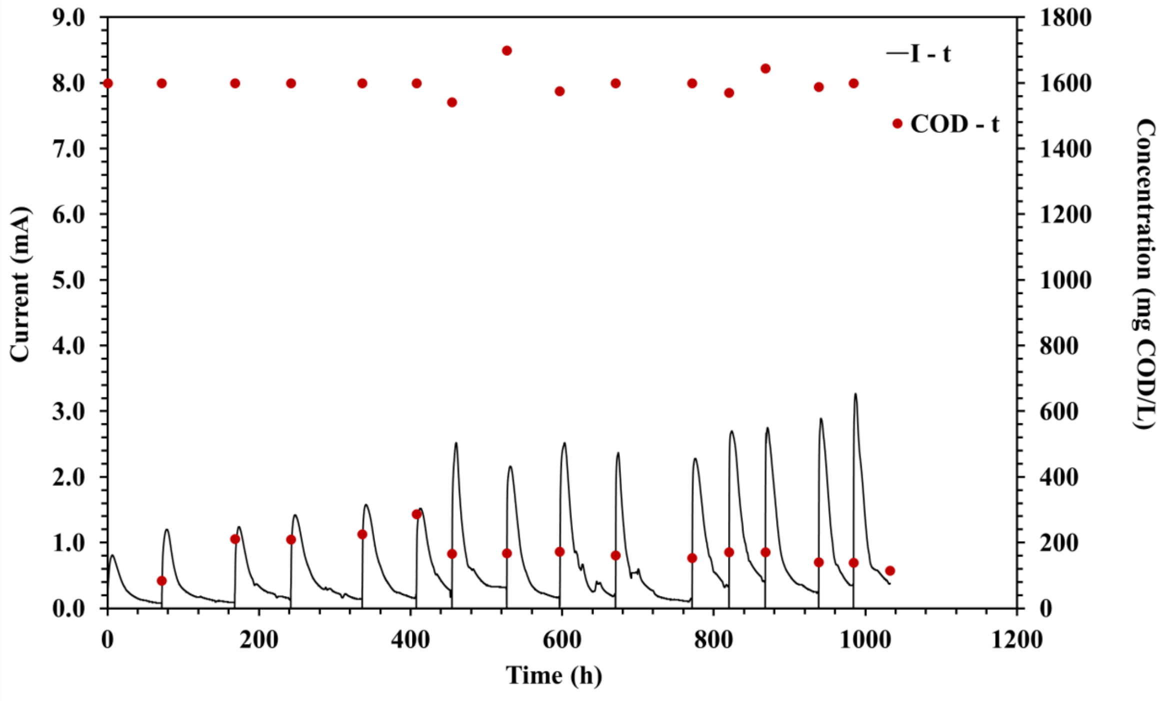

Figure 42. Current output (mA) and COD concentration (mg/L) versus time of Cell 4, during batch operation.

As shown in Figure 39, the COD is efficiently removed in all cases (> 85%). Moreover, during the first 440 h of Cell 1 operation, the maximum current output (I_{max}) was in the range of 1.5 mA to 2.5 mA, while the duration of the batch cycles was ~ 45 h (Figure 39). However, gradual increase of I_{max} was observed in the next 150 h of Cell 1 operation. The maximum current output values remained relatively high (4.2 mA to 4.6 mA) for the following ~ 703 h of Cell 1 operation, while the cycles duration decreased to ~25 h. The cycle duration remained almost constant (~ 70 h) during Cell 2 batch operation, while I_{max} was in the range 3.6 mA to 4.8 mA, with repeated higher maximum current output values after 685 h of Cell 2 operation (Figure 40). Cell 3 performed similarly to Cell 2, since I_{max} was in the range of 3.5 mA to 4.8 mA and the duration of the cycles was ~ 70 h in most of the cycles (Figure 41). On the contrary, although the same conditions and the same handling for the Cell 4 occurred, Cell 4 underperformed in comparison with Cells 1, 2 and 3. In particular, even though I_{max} was gradually increased during operation, it remained relatively low within the range of 0.8 mA to 3.3 mA. The duration presented variations among cycles, between the values 50 h to 100 h (Figure 42). The operation of Cell 4, indicates the difficulty to maintain similar performance among microbial fuel cells. The units cannot be identical since microbial communities are involved in the process. This is a crucial drawback to overcome, particularly when stacks are constructed and a series connection is used [161].

6.1.3 MFC continuous operation with series connection

Following the batch operation of the cells, the operation was shifted to continuous mode (48 ml / h). The individual external resistive loads of the units were removed and the four units were connected in series under a common external load of 100 Ω. Figure 43 shows the current and the power output of the stack during time, as well as the current output of the individual units connected in series.

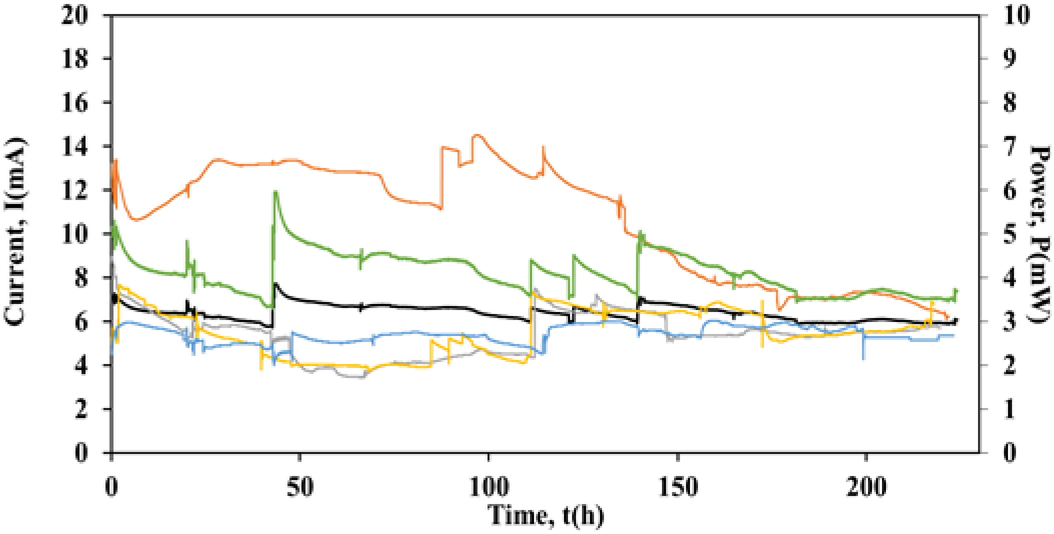

Figure 43. Current output versus time of a) Cell Stack ⬛ , b) Cell 1 🟧 , c) Cell 2 ⬜ , d) Cell 3 🟨 , e) Cell 4 🟦 and power versus time of f) Cell stack 🟩 , during series connection.

As it can be seen from Figure 43, the stack operated for ~222 h under series connection. For the first 154 h of operation, the current output of Cell 1 was I = 12.61 ± 0.96 mA followed by a gradual decrease to 6.24 mA at t = 222 h. The average current output for the Cells 2 and 3 and Cell 4 was I = 5.34 ± 0.95 mA, I = 5.50 ± 1.04 mA and I = 5.42 ± 0.38 mA, respectively. Although, different cell performances were observed during their batch operation and even though some fluctuations of the current output were observed, when the units were serially connected, the stack performance was stable and the voltage reversal phenomenon did not occur. In particular, the average current output of the stack was I = 6.41 ± 0.35 mA, while the average power output was P = 4.1 mW. It is worth mentioning that the higher current output value of the Cell 1, was gradually decreased close to the respective values of Cells 2, 3 and 4.

Moreover, the COD removal for the flow rate 48 ml / h, was ~ 67% for Cell 3 and ~ 58% for the Cells 1, 2 and 4, respectively. The high organic consumption during batch operation (COD consumption > 85%) indicates that higher organic removal could be achieved at flow rates lower than 48 ml / h. Lower flow rates increase the residence time τ of the anolyte within the anode chamber, thus possibly enhancing the COD consumption efficiency from FORBI extract.

6.1.4 MFC continuous operation with parallel connection

Following the series electrical configuration, the units were connected in parallel (Rext = 100 Ω) and the stack operated for ~322 h with this connection. Figure 44 shows the current output of the units and the stack, as well as the power output of the stack in parallel connection.

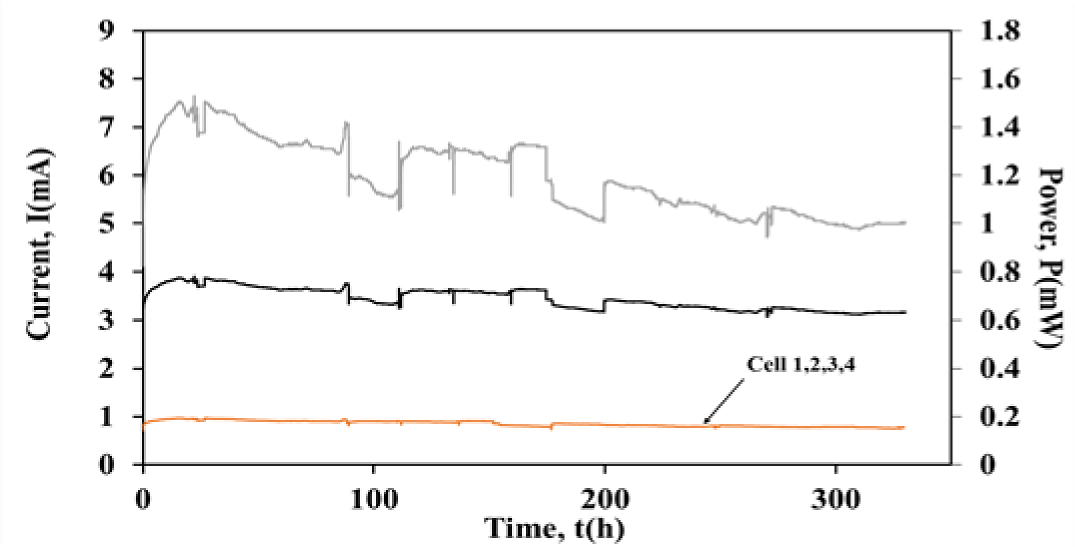

Figure 44. Current output versus time of a) Cell Stack ▬ , b) Individual cells ▬ and power versus time of c) Cell stack ▬ , during parallel connection.

During the parallel connection no fluctuations were observed on the current output and on the power produced from the stack. Specifically, the average current output was I = 3.43 ± 0.23 mA while the power was equal to P = 1.2 mW, respectively. The current output of the units was the same (I = 0.86 ± 0.06 mA), while the COD removal was ~ 62% for Cells 1, 2 and 4 and ~ 72% for the Cell 3.

6.1.5 Electricity yield during batch and continuous operation

Table 20 presents the different E_{yield} (mJ / gCOD / L) for the cells and the cell-arrays. During batch operation Cells 1, 2 and 3 achieved similar yields, ~20 mJ / gCOD / L, respectively.

However, similar to the current output (Figure 43) Cell 4 produced the lowest E_{yield} (6 mJ / gCOD / L), when compared to the other three cells. The highest E_{yield} (2.6 mJ / gCOD / L) was observed for the stack in continuous operation and series connection. Additionally, the E_{yield} for the individual units in series connection was calculated at the 150 h mark (Figure 44), where the current of the individual cells converged to a similar value (~6 mA). The values of the E_{yield} were 2 mJ / gCOD / L for Cell 1 and 0.5 mJ / gCOD / L for Cell 2, 3 and 4.

Furthermore, the E_{yield} of the stack in parallel connection was 0.7 mJ / gCOD / L and the E_{yield} of the units connected in parallel configuration was ~0.2 mJ / gCOD / L), while in series the yields varied. `

Table 20. The E_{yield} (mJ / gCOD / L) of the individual cells and the stacks and the units within the stack during batch and continuous operation.

	Batch	Continuous	
E_{yield} (mJ / gCOD / L)		Series Connection	Parallel Connection
Cell 1	19	2	0.2
Cell 2	20	0.5	0.2
Cell 3	22	0.5	0.2
Cell 4	6	0.5	0.2
Stack		2.6	0.7

It is worth mentioning that although the external resistance of the units and the stacks during batch and continuous mode operation was common (100 Ω), the external resistance of the units within the stack varied. According to Kirchhoff’s law, the Rext for the individual units in series connection was 25 Ω while for the individual units in parallel connection was 400 Ω. Thus, higher current output for the individual units in series connection was observed in comparison with the units in parallel connection (Ohm’s law).

6.1.6 Conclusions

The work demonstrated that although high COD removals (> 85%) were achieved during batch operation, the power output maintained its maximum value (~1.6 mW) per cycle only for ~ 5 h for each cell. On the other hand, when the units operated continuously, the COD removal was lower (67% to 58% and 62% to 72% for series and parallel connection, respectively) in comparison with batch operation, but a constant power output was obtained (P = 4.1 mW, and P = 1.2 mW for series and parallel connection, respectively). The highest E_{yield} (2.6 mJ / gCOD /L) was obtained from the stack connected in series. In addition, although Cell 4 underperformed prior to its series connection, the voltage reversal phenomenon did not occur. This result highlighted the difficulty to set up identical MFC units, which is an optimal condition before the units are connected in series. However, this was not an issue when the units were electrically connected, indicating the feasibility to further increase the number of units within a stack thus treating higher volumes of food residue biomass and enhancing the power production.

6.2 Digestate originating from anaerobic digesters (mesophilic and thermophilic)

6.2.1 Introduction

The process of anaerobic digestion (AD) is promising for food waste treatment with simultaneous production of biogas, namely methane and carbon dioxide [162], [163]. Although AD technology is used extensively for industrial applications, such as FW treatment, it still faces several technical challenges. Examples of the difficulties AD faces include of VFA accumulation in the AD reactor, process instability, foaming, low buffer capacity and need for feedstock pretreatment [164]. Another major issue is the potential use and treatment of its major by-product, the so-called "digestate". Digestate which originates from food waste is mainly used as a biofertilizer, [165], [166]. However, there are environmental and economic constraints that limit the use of this application [165]. In order to overcome these limitations and to exploit the relatively high content of organic molecules and nutrients within the digestate, new technologies are proposed in order to exploit AD effluents [167], [168].

Recently, an alternative exploitation of digestate using microbial fuel cell (MFC) technology has been suggested [169], [170]. In particular, Kim et al [170] investigated the MFC performance for use in removing total ammonia nitrogen (TAN) and residual COD using the effluent from an AD fed with actual swine wastewater. Martinez and Lorenzo [169] reported the development of a floating air-cathode microbial fuel cell using fresh digestate, directly collected from an AD effluent and they suggested that the simplicity of such a system can pave the way for a sustainable environmentally-friendly food waste treatment. Palma et al [171] studied the nitrogen removal from the effluent of an AD, fed with livestock manure and agricultural waste with the MFC technology. The volatile solids removal in the anode chamber was about 60 % while in the aerobic chamber, a good nitrogen removal was observed (up to 60 %). Moreover, Domenico et al [172] treated the digestate originating from an AD fed with agricultural by-products and cow manure. The carbon content was reduced by up to 60%, while anaerobic ammonium oxidation (anammox) bacteria contributed to nitrogen removal from the digestate.

In this chapter the results of MFC operation with AD reactors effluents (digestate), as feedstock, are presented. One digestate originating from a thermophilic AD reactor and one from a mesophilic AD reactor.

<u>Experimental set – up:</u> 4.4.2.2

<u>Experiments conducted:</u> The MFCs were fed with AD effluents. Cells 1 and 2 were fed with mesophilic digestate originating from a 4000 L CSTR anaerobic digester. Cells 3 and 4 were fed with thermophilic digestate originating from a 500 L CSTR anaerobic digester. Both reactors were fed with FORBI slurry. Solid liquid separation was employed on both effluents with 5 μm filter sludge bags, to avoid clogging inside the MFCs. Subsequently, the effluents were fed to the respective MFCs (Mesophilic effl. Cells 1, 2 – Thermophilic effl. Cells 3, 4). The cells were evaluated in terms of electricity production and digestate treatment. In order to characterize electrochemically the MFCs and the effect of the two types of AD effluents on the performance of the cells, their impedance characteristics were also investigated.

6.2.2 MFC operation with AD effluent as feedstock

Figure 45 and Figure 46 show the changes in the current output and the COD removal versus time for the mesophilic and the thermophilic digestate, respectively. As shown in Figure 45, Figure 46, Table 21 and Table 22, the Cells 3 and 4 which were fed with the thermophilic digestate obtained higher values of current output (maximum current output 2.979 ± 0.643 mA and 2.264 ± 0.611 mA, respectively) in comparison to the Cells 1 and 2 which were fed with the mesophilic digestate (maximum current output 1.322 ± 0.605 mA and 1.253 ± 0.387 mA, respectively).

Table 21. Operation characteristics of the mesophilic fed MFCs.

Mesophilic operation										
Cycle Number	Duration (h)		I_{max} (mA)		COD removal (%)		TSS removal (%)		VSS removal (%)	
	Cell 1	Cell 2	Cell1	Cell 2	Cell 1	Cell 2	Cell 1	Cell 2	Cell 1	Cell 2
1	550	441	2.34	1.99	85.3	82.4	98.0	-	95.4	-
2	255	157	1.53	1.23	76.1	85.0	-	-	99.9	-

3	199	255	0.87	1.25	87.5	84.3	89.1	88.9	87.0	89.2
4	141	109	0.94	0.75	82.1	89.5	69.2	92.1	72.2	90.6
5	137	167	0.65	1.35	73.1	91.2	43.5	58.8	40.0	65.4
6	255	143	0.72	1.35	46.1	91.4	-	82.9	99.9	84.6
7	-	157	-	0.95	-	56.3	-	65.1	-	70.1

Table 22. Operation characteristics of the thermophilic fed MFCs.

Thermophilic operation										
Cycle Number	Duration (h)		I_{max} (mA)		COD removal (%)		TSS removal (%)		VSS removal (%)	
	Cell 3	Cell 4	Cell 3	Cell 4	Cell 3	Cell 4	Cell 3	Cell 4	Cell 3	Cell 4
1	116	417	3.71	2.94	83.9	84.5	90.5	95.0	75.7	75.0
2	228	188	3.41	2.63	77.3	90.5	79.3	84.7	35.6	89.4
3	186	253	3.57	2.66	90.3	89.1	88.4	87.1	88.5	87.7
4	234	109	3.34	2.69	84.6	89.3	95.2	77.4	96.1	74.6
5	129	167	3.1	1.48	96.9	87.3	88.2	90.9	98.1	95.1
6	220	144	2.68	1.89	88.1	81.0	92.1	51.8	96.0	48.3
7	148	173	2.27	1.48	82.0	69.2	62.3	-	59.6	-
8	174	-	1.97	-	80	-	-	-	-	-

Moreover, the COD removal ranged from 80 – 90% and was achieved within the first 24 to 48 hours of each cycle operation. Although after the first 24 – 48 hour period, the COD value remained constant, electricity was still produced for more than 190 h. Digestates originating from food waste anaerobic digestion have a low ratio of carbon to nitrogen [173], [174]. Thus, for both the mesophilic and thermophilic digestates, this result can probably be attributed to the relatively fast uptake and storage of the soluble COD in the biofilm of the anode electrode. Then, the organic matter could be slowly used as substrate from the electroactive bacteria generating electricity. It is known that bacteria grown under excess carbon and nitrogen deficiency, can accumulate PHB and poly B-hydroxybutyrate [173], [174] which are considered as energy storage polymers.

Moreover, as can be seen from Figure 45 and Figure 46, the current output curves are smoother for Cells 3 and 4, whereas for the mesophilic fed cells the current curves present a fluctuation among consecutive values (Figure 46). Thermophilic anaerobic digesters have higher rates of hydrolysis and acidification, thus complex organic material is faster converted to basic monomers producing more VFAs than mesophilic anaerobic digesters (Table 21 and Table 22) [175].

Large organic molecules cannot be directly consumed for electricity generation [176], [177]. Consequently, in the case of the mesophilic digestate, the complex organic molecules, which are accumulated within the microorganisms, are more difficult to decompose and be consumed from electrogenic bacteria, compared to respective organic molecules of the thermophilic digestate. This leads to lower current output values, as well as to not smooth current curves in comparison with the respective curves originated from the thermophilic digestate.

Additionally, the VFAs degradation profile followed the same trend as the COD removal. Particularly, VFAs were completely consumed by the biomass within the first 24 to 48 hours of each cycle operation, for both digestates. In the case of the mesophilic feedstock, the VFAs consumption was accompanied with a slight pH increase (from pH~7 to pH ~7.6) which remained constant until the end of each cycle. Moreover, the conductivity did not change during cycle operation for the mesophilic feeding. On the contrary, the thermophilic digestate fed cells presented a small decrease of the pH value (from pH~ 7 to pH ~ 6.3) during cycle operation. Similarly, the conductivity decreased (from~3.6 mS/cm to~2 mS/cm). The origin of this decrease is unclear but it may be related to the relatively big temperature difference between the inlet (~55 ^{o}C) and the operation temperature (~ 22 ^{o}C) of the systems [175]. Each batch cycle lasted approximately 200 h for both digestates, whereas the TSS and VSS were reduced by ~83% and ~ 86% respectively, in each cycle. The ammonium removal which was achieved from the mesophilic fed MFCs was in the range of 46% – 79%, whereas for the thermophilic digestate fed MFCs it was in the range of 85% – 95%.

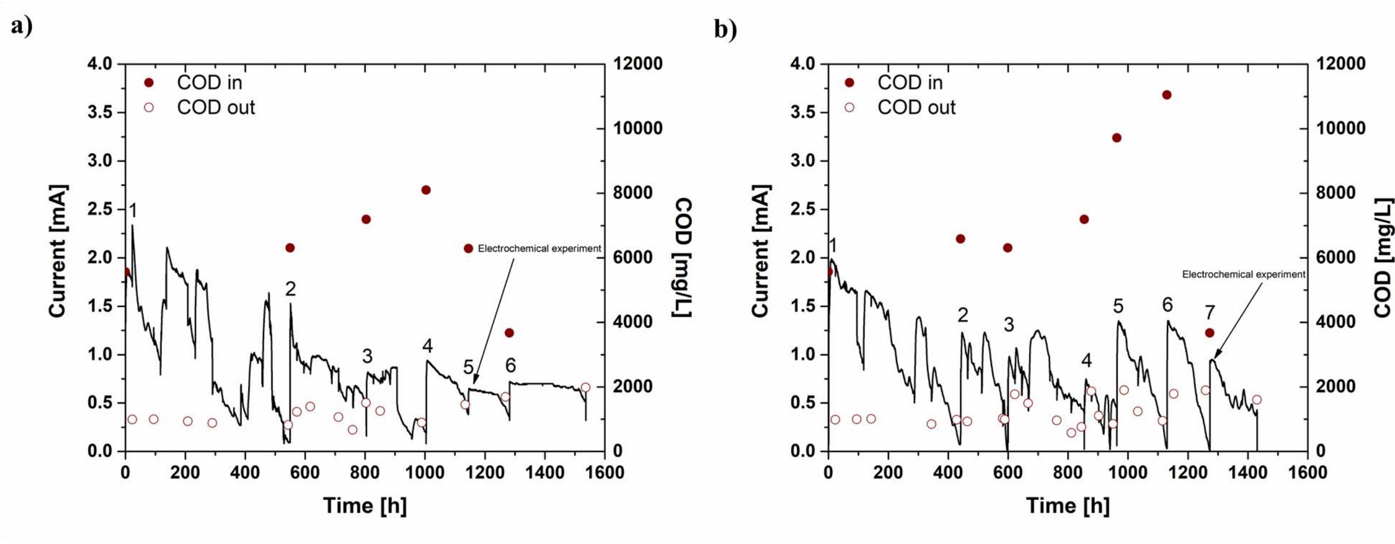

Figure 45. Current output and COD concentration of the (a) Cell 1 and (b) Cell 2 fed with mesophilic digestate versus time. Black arrows indicate the times when electrochemical experiments were carried out. The numbers in graph indicate the consecutive batch cycles.

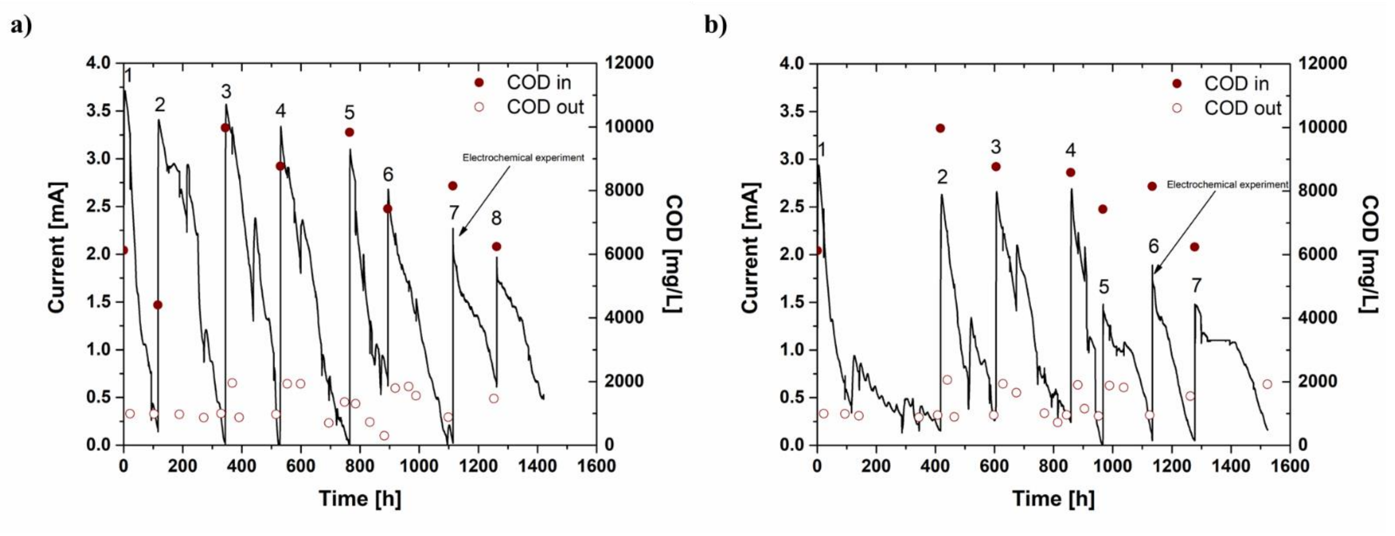

Figure 46. Current output and COD concentration of the (a) Cell 3 and (b) Cell 4 fed with thermophilic digestate versus time. Black arrows indicate the times when electrochemical experiments were carried out. The numbers in graph indicate the consecutive batch cycles.

6.2.3 Effect of the mesophilic and the thermophilic digestate on the polarization performance of the cells

The maximum power output of the cells was determined with polarization experiments. Particularly, LSV measurements were conducted when the batch cycles reached the maximum voltage output at times t = 1134 h, 1277h, 1113 h and 1133 h for the Cell 1 Cell 2, Cell 3 and Cell

4, respectively (Figure 45 and Figure 46). Figure 47 shows the polarization and power output curves of the microbial fuel cells. As can be seen in Figure 47, similarly to the current output curves, the thermophilic digestate fed cells produced higher maximum output (Cell 3: P_{max} = 0.428 mW, Cell 4 P_{max} = 0.421 mW) than the respective maximum power output obtained from the mesophilic digestate fed cells Cell 1: P_{max} = 0.344 mW, Cell 2: P_{max} = 0.347 mW). In addition, the open-circuit voltage (OCV) was 0.191 V, 0.287 V, 0.432 V, 0.295 V for Cells 1, 2, 3 and 4, respectively. Moreover, from the polarization curves, it is evident that low activation losses occur in all cases, while at high current the contribution of mass transport losses is higher for the mesophilic digestate fed cells. This result corroborates the assumption previously made, that the mesophilic digestate is more difficult to consume by electrogenic bacteria, compared to the thermophilic digestate.

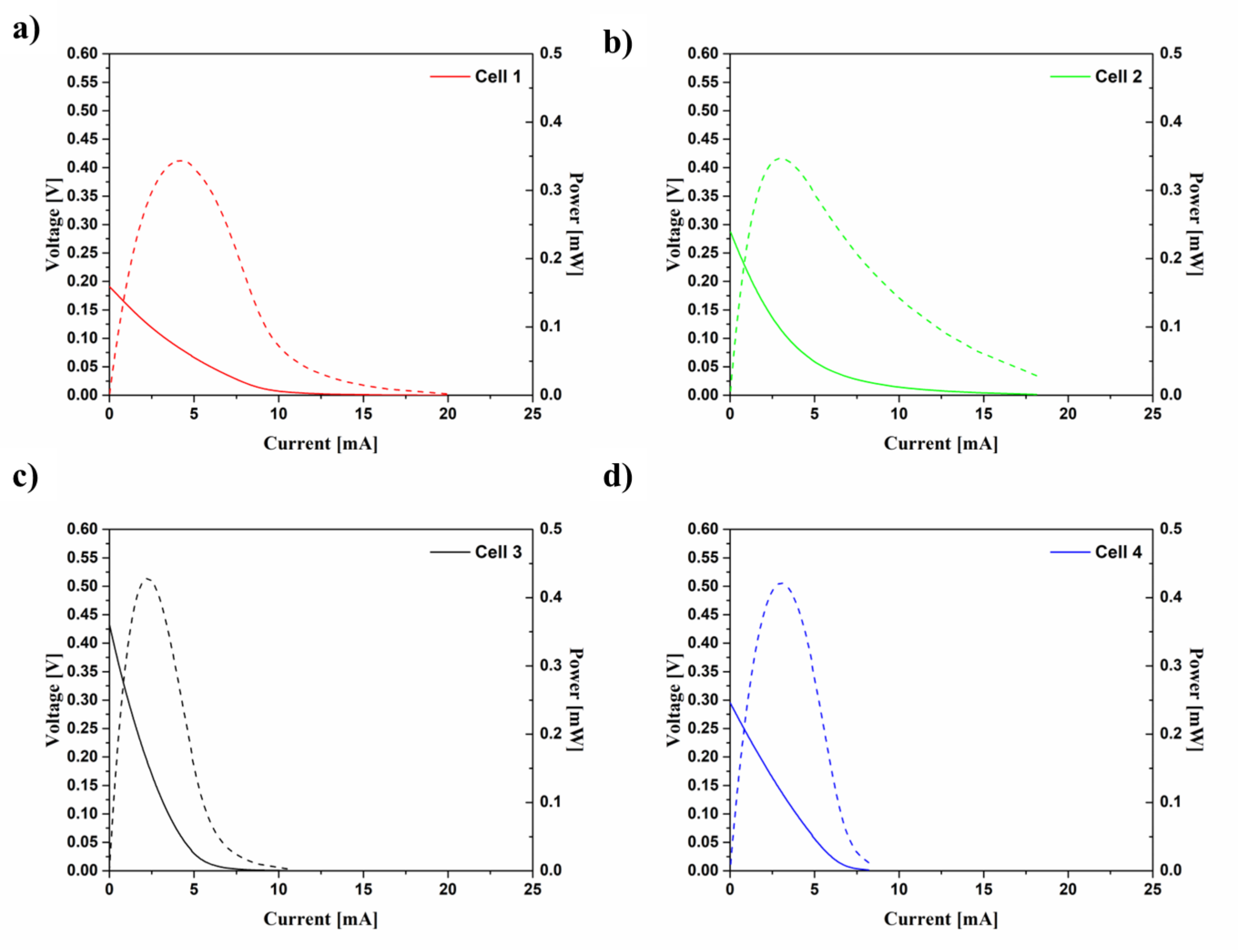

Figure 47. Polarization and power output curves of microbial fuel cells fed by mesophilic ((a),(b) for Cells 1 and 2, respectively) and thermophilic ((c), (d) for Cells 3 and 4, respectively) digestate under batch operation (dashed lines represent the power output curves)

6.2.4 Electrochemical characterization

In order to perform a detailed electrochemical characterization of the cells, EIS experiments were conducted. Figure 48 depicts the Nyquist plots and the impedance characteristics of the four cells under open-circuit conditions.

From the Nyquist diagrams, two arcs are observed followed by a Warburg element as previously reported [139]. Our proposed EIS fitting model fits the experimental data (R^2 = 99.98%) considering that the nature of digestates further contributes to the charge transfer resistance of the cell. Table 23 presents the numerical values of R_S, R_{BF}, R_{CT}, as well as the capacitances of the biofilm and the charge transfer (C_{BF} and C_{CT} respectively).

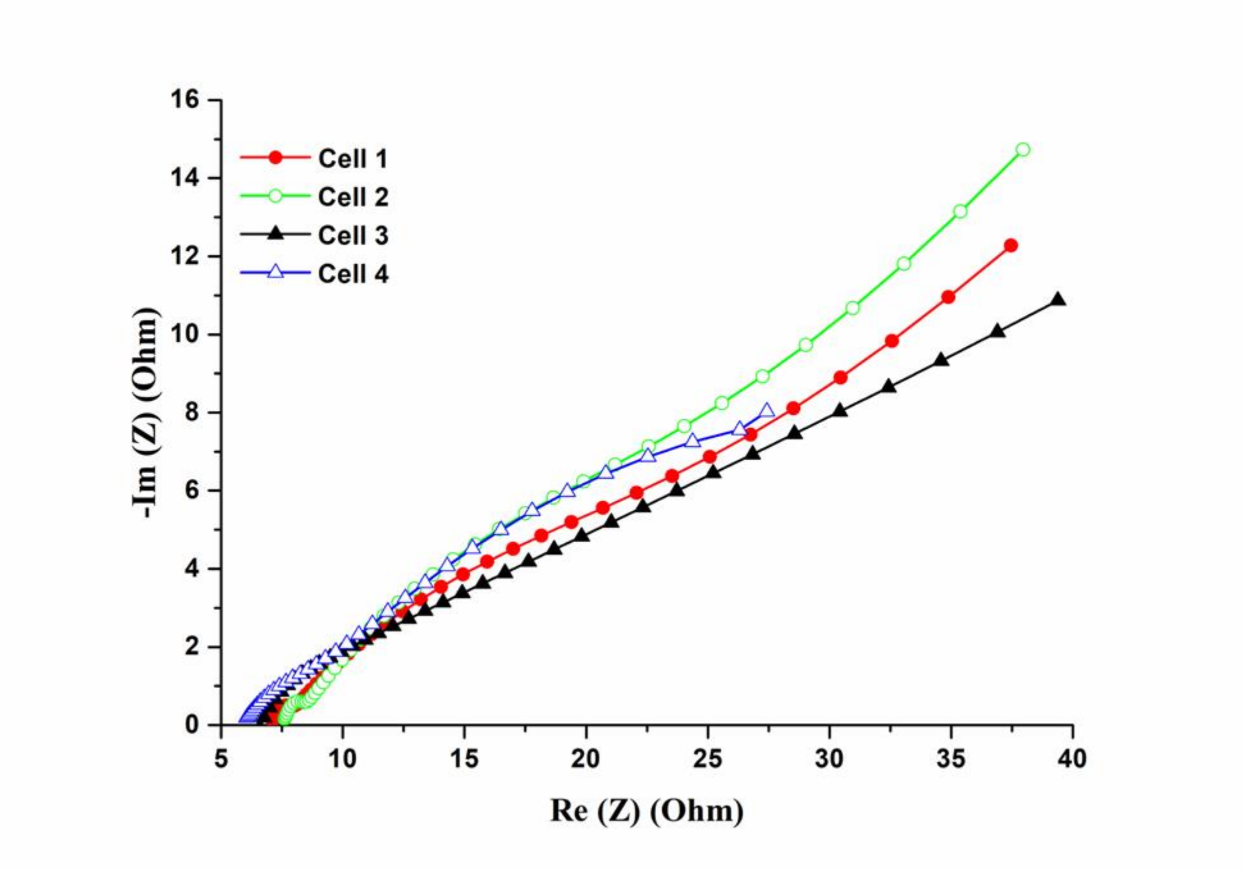

Figure 48. Nyquist diagrams of mesophilic (Cells 1 and 2) and thermophilic (Cells 3 and 4) under open-circuit conditions

Table 23. EIS fitted results for all cells at zero applied potential, during MFC operation with digestate as feedstock, originating from mesophilic (Cell 1, 2) and thermophilic (Cell 3, 4) conditions.

Fitted Parameters	Cell 1	Cell 2	Cell 3	Cell 4
R_S (Ω)	5.1	5.5	10.1	10.5
R_{BF} (Ω)	2.2	2.6	10.3	11.1
C_{BF} (F)	$0.4\cdot10^{-3}$	$0.3\cdot10^{-3}$	$12.1\cdot10^{-6}$	$11.1\cdot10^{-6}$
C_{CT} (F)	$8.2\cdot10^{-3}$	$7.9\cdot10^{-3}$	0.02	0.02

R_{CT} (Ω)	11.9	11.6	26.4	23.2

The first arc of Figure 48 is attributed to biofilm formation. The second capacitive loop corresponds to charge transfer resistance [47]. The equivalent resistances (R_{BF}) are higher in the thermophilic cells indicating larger voltage drops but smaller formation periods as suggested by the values of C_{BF}. This phenomenon is obvious in Figure 47 as the thermophilic digestate fed cells start with higher OCV values than the mesophilic digestate fed ones. Also, the type of digestate used has an impact on the values of the solution resistances. The solution resistances of thermophilic digestate are higher for the cells fed with it than those fed with mesophilic digestate, contributing to more favorable electron pathways. High charge transfer resistance values of (26.4 Ω and 23.2 Ω) are practically increased, in comparison with mesophilic cells (11.9 Ω and 11.6 Ω), and the total attributed to the increased anodic reaction rates of the cells. As biofilm resistances are increasing, microbial consortia are using enhanced direct electron transfer pathways according to the literature [139], [178]. Regarding the fast drop in COD for both types of cells, the biomass in both cases is capable of up taking the organic content. The fast consumption of the COD is correlated with the values of R_{CT} which implies that the thermophilic cells may accumulate relatively more organic matter, slowly releasing it afterward producing higher power outputs. The value of charge transfer capacitance also verifies the former statement in which the thermophilic digestate promotes evident more electrogene pathways, thus enhancing the power output and COD removal.

Regarding the stability of the cells, experimental EIS measurements were held at applied constant values of OCV and half-OCV voltage. The experimental fitted data are represented in Figure 49.

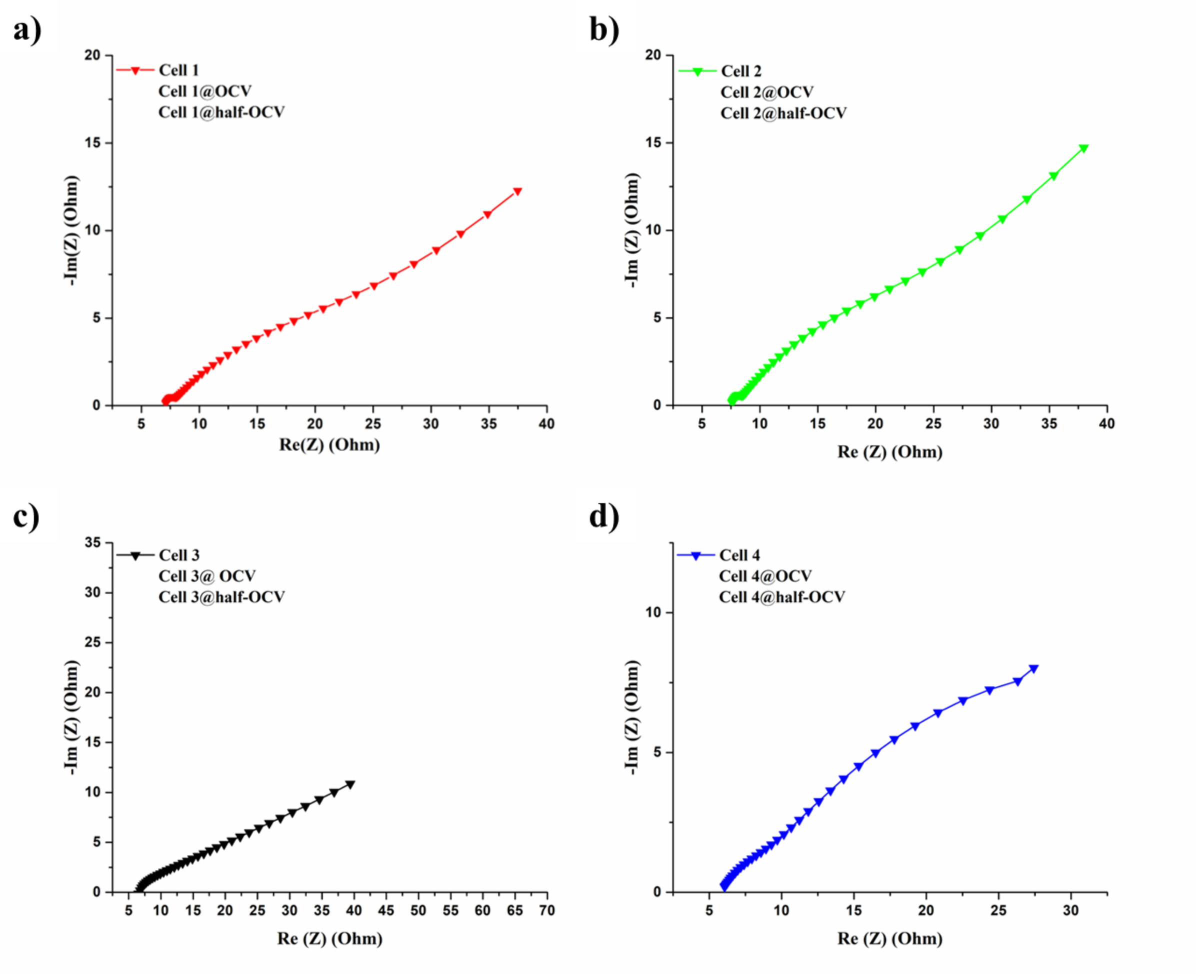

Figure 49. Comparative Nyquist diagrams of mesophilic ((a),(b) for Cells 1 and 2, respectively) and thermophilic ((c), (d) for Cells 3 and 4, respectively) under open current, OCV and half-OCV applied potential

It is clear that the operation of the above cells differs from the data extracted at open current. More specifically, the EIS model used was the one reported in [47] and was used in other similar MFCs. The reverse operation of these cells by applying direct current is evident to the electrochemical reactions that occur within the cells. According to Figure 49, for each cell, after voltage application, the effect of the nature of the digestate is negligible to the operation. This is proved by the different Nyquist plots of the cells in comparison with open current conditions. The two distinguishable arcs followed by a Warburg element implies the operational stability of the cells under reverse operating conditions [47], [139], [178].

6.2.5 Conclusions

The work demonstrated that digestate from fermentable household food waste (FORBI) can be successfully treated using the microbial fuel cell (MFC) technology. The easily biodegradable organic matter was removed by 80 – 90 % within the first 24 – 48 h. The experiments indicated that the MFCs performed better with the thermophilic digestate in comparison with the mesophilic digestate. Moreover, a fast uptake and storage of the soluble COD within the biofilm possibly occurred for both types of digestate. This assumption is corroborated from EIS measurements.

6.3 Condensate at different initial concentrations

6.3.1 Introduction

In order to examine the effect of condensate concentration in the MFC feed, different initial concentrations of condensate were tested ranging from 0.4 – 4 gCOD/L. The aim of the study was to determine the effect of the initial condensate concentration in the MFC performance.

<u>Experimental set – up:</u> 4.4.2.3.1

<u>Experiments conducted:</u> Condensate originating from HFW was used as a MFC feedstock. Condensate was mixed with phosphate buffer and potassium chloride and then it was diluted to the desired initial concentration [400 – 4000 mg COD/L]. The condensate initial concentration was increased in consecutive operation cycles.

6.3.2 MFC operation with different initial condensate concentrations in the feedstock

Following the operation period using synthetic wastewater with glucose, condensate was used as substrate. Different condensate concentrations were examined in the range of 400 mg COD/L to 4000 mg COD/L. The current output and the COD concentration versus time for the different initial condensate concentrations for the Gore-Tex and Mullite cell, are shown in Figure 50 and Figure 51, respectively.

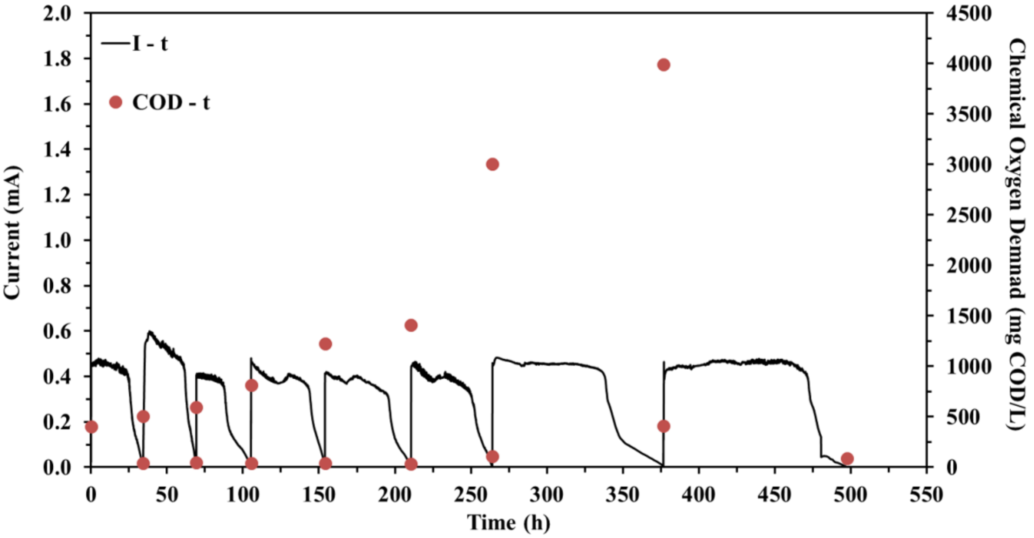

Figure 50. Current output (left) and COD concentration (right) versus time of the Gore-Tex cell.

As can be seen from Figure 50 and Figure 51, the COD removal efficiency was high for all initial concentrations (>86%). In the case of Gore-Tex cell, the maximum current output (I_{max}) for all cycles was approximately 0.5 mA except the case of 500 mg COD/L where the maximum current output was somewhat higher (0.6 mA) (Figure 52). Although the COD removal efficiency and the current output remained relatively stable increasing the initial condensate concentration, the duration of cycles, the CE and the E_{yield} were affected by the initial organic load. The duration of the cycles was increased as the initial condensate concentration increased (Figure 50 and Figure 51). A similar observation was made by [179], increasing the initial COD in a two chamber MFC. The E_{yield} for all cycles, as calculated by Eq. 21 are presented in detail in Table 24 and the coulombic efficiencies (CE) as calculated by Eq. 20 are presented in Figure 52. In particular, the duration of each cycle increased from 34 h to 121 h, as the initial condensate concentration increased from 400 mg COD/L to 4000 mg COD/L. On the contrary, CE and E_{yield} were decreased by 67% and 60% respectively when the initial condensate concentration gradually increased from 400 mg COD/L to 4000 mg COD/L, (Figure 52). Specifically, the maximum CE (4.3%) was obtained at 400 mg COD/L, indicating that the Gore-Tex cell operated better at lower initial condensate concentrations. Similarly, the maximum E_{yield} was achieved at 400 and 500 mg COD/L and was equal to 1.25 and 1.54 mJ/g COD/L, respectively (Table 24 and Figure 52). This behavior may be attributed to the decrease of the anolyte's pH and conductivity as the initial condensate concentrations increased (400 mg COD/L: pH 6.7, 5.9 mS /cm to 4000 mg COD/L: pH 4.8, 3.8 mS /cm) (Table 7). It is known that electrogenic bacteria perform better at an environment close to neutral pH [180], whereas low conductivity values also limit the performance of the cells [50]. Additionally, although relatively low CE values were achieved, high COD removal efficiency was obtained indicating that antagonistic microorganisms consumed a high portion of the organic material [33].

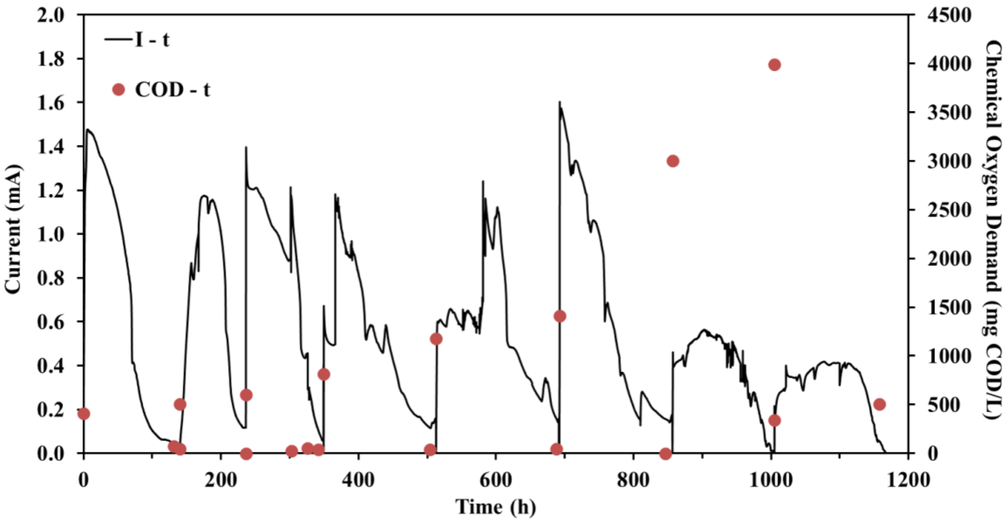

Figure 51. Current output (left) and COD concentration (right) versus time of the Mullite cell.

In the case of the Mullite cell, the maximum current output values that were achieved were 2- to 3- fold higher when compared with Gore-Tex cell. In particular, I_{max} ranged between 1.2 and 1.6 mA for the initial condensate concentrations 400 to 1400 mg COD/L, whereas I_{max} was 0.6 mA and 0.4 mA for the 3000 and 4000 mg COD/L initial concentrations, respectively (Figure 52). Additionally, the duration of each cycle was approximately 3- to 4- fold longer than the corresponding Gore-Tex cell cycles, except in the case of the higher initial condensate concentrations (3000 and 4000 mg COD/L), where similar cycle durations were observed for both cells (Table 24). The duration of the cycles ranged between 96 h and 179 h and on the contrary with Gore-Tex cell, the duration of each cycle did not increase with the initial COD concentration increase. Similarly to the Gore-Tex cell, CE and E_{yield} (calculated by Eq. 20 and Eq. 21) were decreased by 96% and 98% when the initial condensate concentration gradually increased from 400 mg COD/L to 4000 mg COD/L, respectively (Table 24 and Figure 52). In particular, the maximum CE (51%) was obtained at 400 mg COD/L. Similarly, the maximum E_{yield} was achieved at 400 mg COD/L and was 26.5 mJ/g COD/L. Although both cells achieved high COD removal efficiency values, it is clear in both cases that the decrease of the anolyte's pH and conductivity with the initial condensate concentration increase deteriorates the cell's performance. Moreover, the performance of the cells in terms of electricity production is more efficient using the mullite separator instead of the Gore-Tex cloth.

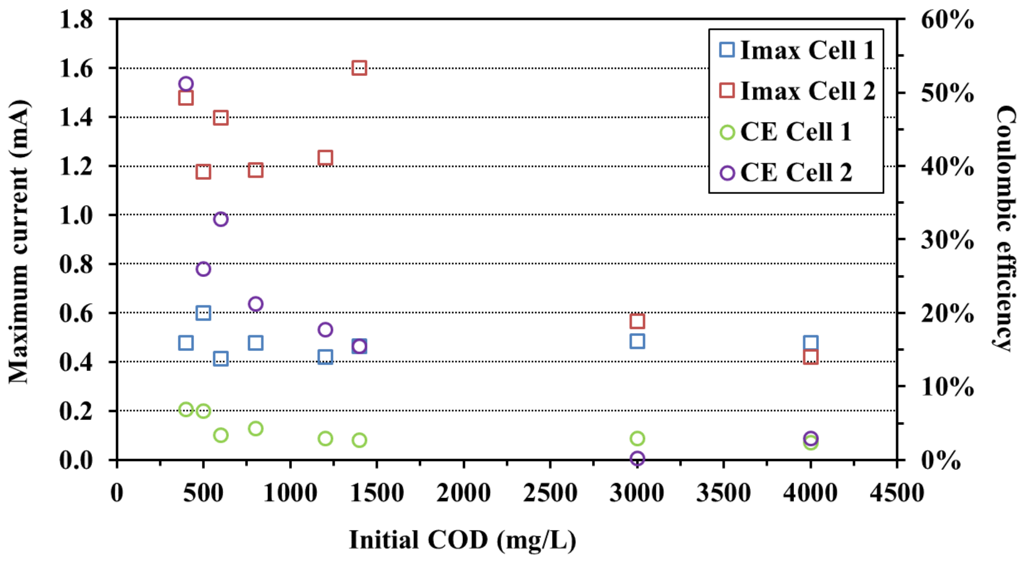

Figure 52. Maximum current (left) and CE (right) versus the initial COD concentrations of condensate fed to the two cells.

Table 24. Operational characteristics (maximum current output, cycle duration, COD removal efficiency, CE and E_{yield}) were achieved for Cell 1 and Cell 2 at different initial condensate concentrations.

Initial condensate concentration (mg COD/L)	Δt Cycle (h)		COD Removal		E_{yield} (mJ/g COD/L)	
	Cell 1	Cell 2	Cell 1	Cell 2	Cell 1	Cell 2
400	34	140	90%	89%	1.31	25.9
500	35	96	91%	99%	1.51	12.2
600	36	113	93%	93%	0.53	15.3
800	49	164	95%	95%	0.77	6.8
1200	57	179	97%	96%	0.51	5.8
1400	54	164	92%	99%	0.46	7.9

3000	113	148	86%	89%	0.53	0.9
4000	121	152	98%	87%	0.50	0.5

6.3.3 Linear Sweep Voltammetry experiments at different initial condensate concentrations

Linear sweep voltammetry (LSV) experiments were conducted in order to examine the effect of condensate concentration on the polarization performance of the cells. Polarization curves were obtained for initial concentrations of 600, 800, 1400 and 3000 mg COD/L. Figure 53 and Figure 54 present the results of the LSV experiments, voltage and power density versus current density for the Gore-Tex and Mullite cell, respectively.

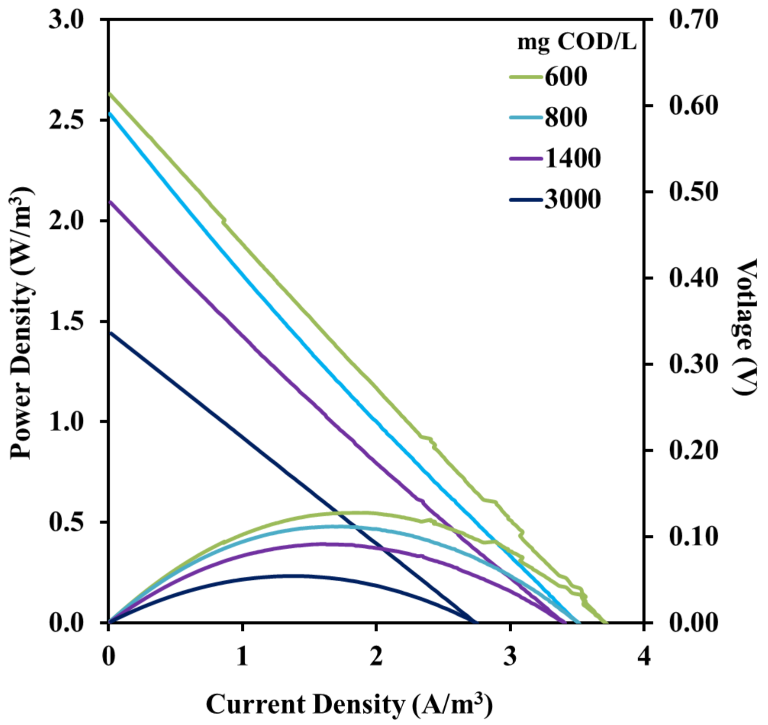

Figure 53. Power density versus current density as extracted by LSV experiments on the Gore-Tex cell, for the following initial condensate concentrations (mg COD/L) a) 600 🟩 , b) 800 🟦 , c) 1400 🟪 and d) 3000 ⬛ .

As can be seen from Figure 53, the maximum power density (P_{max} 0.55 W/m^3) was achieved at 600 mg COD/L. Additionally the increase of the initial condensate concentration led to a gradual decrease of P_{max} values (600 mg COD/L: 0.55 W/m^3, 800 mg COD/L: 0.48 W/m^3, 1400 mg COD/L: 0.4 W/m^3, 3000 mg COD/L: 0.23 W/m^3). The lowest maximum power output (0.23 W/m^3) was obtained at 3000 mg COD/L. Based on the voltage versus current density lines (Figure 53), in all cases, ohmic losses dominated in the Gore-Tex cell. The slope of the voltage versus current density lines indicates the internal resistances, which are greater the steeper the slope. The internal resistances of the Gore-Tex cell which are calculated using the power density peak method also increased with increasing initial condensate concentration (600 mg COD/L: 848 Ω, 800 mg COD/L:956, 1400 mg COD/L: 1016 Ω, 3000 mg COD/L: 1365 Ω).

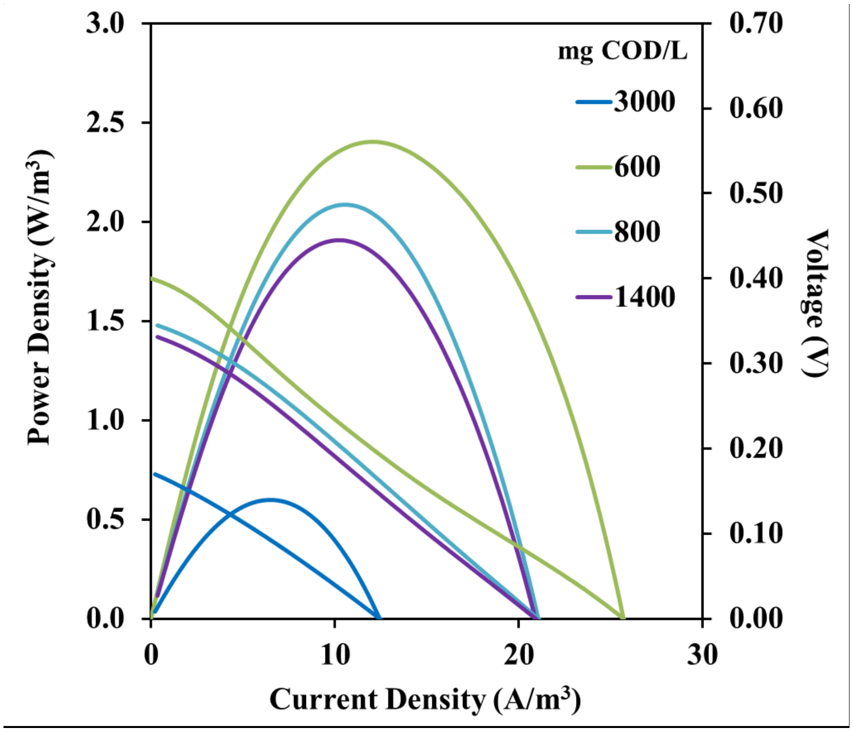

Figure 54. Power density versus current density as extracted by LSV experiments on the Mullite cell, for the initial condensate concentrations (mg COD/L) a) 600 🟩 , b) 800 🟦 , c) 1400 🟪 and d) 3000 ■ , respectively.

The highest maximum power output (2.4 W/m^3) for the Mullite cell, was achieved at 600 mg COD/L. Moreover, the lowest power density (0.6 W/m^3) was obtained for the 3000 mg COD/L initial concentration. For 800 mg COD/L and 1400 mg COD/L the corresponding maximum power densities obtained were 2.1 W/m^3 and 1.9 W/m^3, respectively. Similarly, to the Gore-Tex cell, ohmic losses were exhibited in all cases for the Mullite cell. Using the power density peak method, the internal resistances were calculated for the corresponding initial condensate concentrations

(600 mg COD/L: 91 Ω, 800 mg COD/L: 110 Ω, 1400 mg COD/L: 113 Ω, 3000 mg COD/L: 115 Ω). The internal resistances of the Mullite cell presented a similar pattern as for the Gore-Tex cell. Specifically, by increasing the condensate concentration, the internal resistances increased whereas the maximum power was decreased. Overall, in terms of power output, the Mullite cell outperformed the Gore-Tex cell, indicating the potential of the ceramic material to be effectively used as a separator. In all cases, at low initial condensate concentrations (600 mg COD/L) the maximum power output was high in comparison with the maximum power output values which were obtained at higher initial condensate concentrations (800 – 3000 mg COD/L). Similar results have been previously observed in [181]; by increasing the initial condensate concentration the maximum power output did not present an increase beyond a certain value.

6.3.4 Electrochemical impedance spectroscopy characterization

The results from the LSV experiments indicated that increasing the initial condensate concentration the internal resistance of the cells also increased. In order to define the contribution of the different resistances to the total internal resistance a detailed electrochemical characterization using Electrochemical Impedance Spectroscopy (EIS) measurements was carried out. Figure 55 and Figure 56 present the Nyquist diagrams of the Gore-Tex and Mullite cell, respectively. In both Figures, two distinguishable arcs are presented followed by a Warburg element. The first arc is combined with the biofilm resistance (RBF), while the second arc is attributed to the charge transfer resistance (RCT) as explained by [182], for single-chambered MFCs. RS is calculated by the intersection of the left side of the first arc with the x-axis of the Nyquist diagrams.

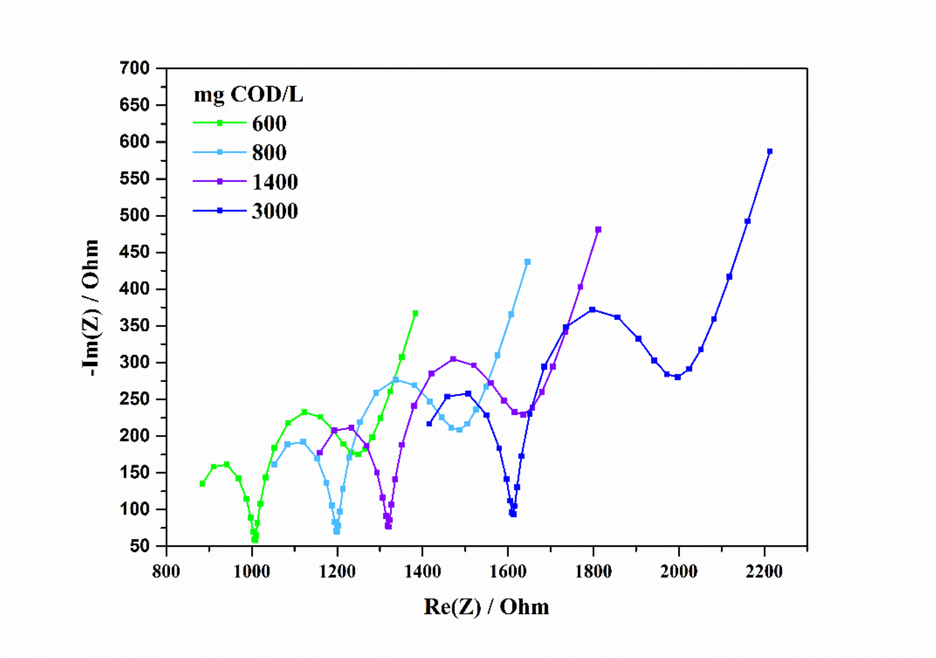

Figure 55. Nyquist diagrams of Cell 1 for different initial condensate concentrations (600 – 3000 mg COD/L).

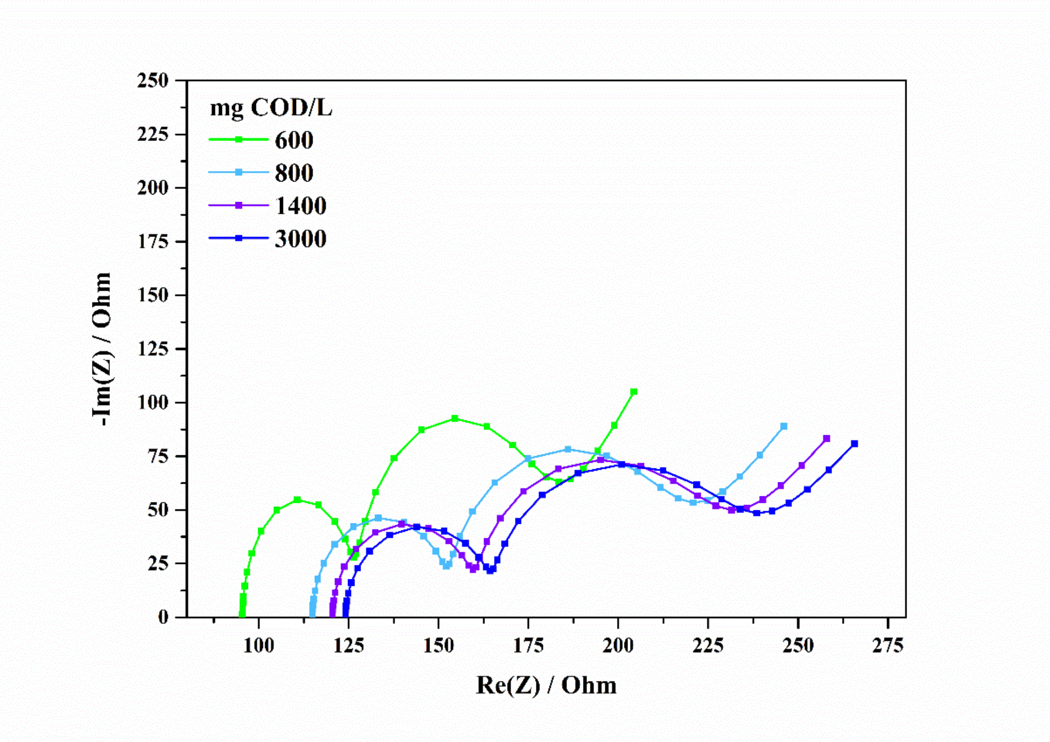

Figure 56. Nyquist diagrams of Cell 2 for different initial condensate concentrations (600 – 3000 mg COD/L).

By applying the fitting model described in earlier publications [62], [72] the internal resistances from each EIS experiment are calculated and presented in Table 25 and Table 26 for the Gore-Tex and Mullite cell, respectively.

Table 25. Gore-Tex cell EIS fitted parameters for different initial condensate concentrations

Fitted Parameters	mg COD/L			
	600	800	1400	3000
R_S (Ω)	330	488	551	741
R_{BF} (Ω)	349	347	354	349
R_{CT} (Ω)	119	150	173	293
Rint (Ω)	798	985	1078	1383

Table 26. Mullite cell EIS fitted parameters for different initial condensate concentrations

Fitted Parameters	mg COD/L			
	600	800	1400	3000
R_S (Ω)	19	24	27	30
R_{BF} (Ω)	31	33	35	34
R_{CT} (Ω)	45	49	52	56
Rint (Ω)	95	106	114	120

As can be seen from Table 25 and Table 26, by increasing the initial condensate concentration the total internal resistance (R_{in}) increases for both cells. These results are in accordance with the previous observation that the decrease of the anolyte's pH and conductivity which occur with an initial condensate concentration increase, deteriorates the cells' performance. This is reflected on the solution resistance (R_s) and the charge transfer resistance (R_{CT}) increase for the Gore-Tex and

Mullite cell, respectively. On the other hand, the biofilm resistance (R_{BF}) is practically constant which denotes a well-established acclimation procedure on the anodic electrode. In particular, in the case of the Gore-Tex cell, the R_s and the R_{CT} were 2.5 times higher (R_s increase: 125%, R_{CT} increase: 146%) with the initial condensate increase from 600 to 3000 mg COD/L whereas R_{BF} was in the range of 347 to 354 Ω. Additionally, in the case of the Mullite cell, the R_s and the R_{CT} increased by 59% with an initial condensate increase from 600 to 3000 mg COD/L, while R_{BF} was in the range of 31 to 34 Ω.

Furthermore, it is observed that the Mullite cell has significantly lower values of R_S, R_{BF} and R_{CT} in comparison with the Gore-Tex cell. This result is correlated with the nature of the cathodic electrode configuration since all the other parameters were kept the same. Specifically, in the case of the Mullite cell, the cathodic electrode exploits the mullite porosity as the exchange medium in which the anolyte infuses and reaches the dense area of the catalytic paste. The whole reaction is enhanced through the significant larger area of the electrode (inner area of the tube) and oxygen reduction is more favored in this electrode in comparison with the Gore-Tex cell. Thus, the lower performance of Gore-Tex cell is attributed to the perforated Plexiglas tubes, which inhibit the full contact of the anodic solution, in contrast to the mullite tubes. Under this consideration, all the values of the resistances are lower in the Mullite cell.

In particular, R_{CT} is correlated to the overall electron mobility and the enhanced surface area of the cathodic catalyst [173], [182]–[184] and in case of Gore-Tex electrodes a power blockage of the cathodic electrode itself is a restricting factor. In addition, the smaller R_{BF} of the Mullite cell is also attributed to the enhanced surface area of the cathodic catalyst which possibly resulted in the formation of more electrogenic bacteria on the anodic electrode, since microorganisms developed in a better environment. Moreover, the increase of condensate concentration caused a drop of the solution conductivity (Table 7). The measured resistance of the solution, R_s, (Table 25 and Table 26) was in accordance with that result, since it increased as the condensate concentration increased. As the initial condensate concentration was increased in the feed of the MFC, the pH and the conductivity were reduced. The reduction in the conductivity led to an increase in the resistance of the solution, inhibiting the performance of the MFC. The improvement in the electrochemical performance of the MFC, by increasing the electrolyte conductivity, has been observed before [75]. Moreover, the pH reduction affected the microorganisms which operate better at close to neutral pH (~ 6.5 - 7) [185]. The LSV and EIS experiments validated the observation regarding the MFC performance. Increasing the initial condensate concentration, led to a higher initial COD in the feed, which in the case of the Gore-Tex cell, resulted in longer operation cycles. In the case of the Mullite cell, no such increase was observed in the operation cycle duration, possibly attributing this to the better performance of the Mullite cell, due to the use of mullite electrodes.

6.3.5 Conclusions

The operation of two single-chamber MFCs, using different cathode assemblies (Gore-Tex assembly, mullite assembly) was assessed, when operating at different food waste condensate concentrations (400 – 4000 mg COD/L). The work demonstrated that condensate was successfully treated in all cases (COD removal efficiencies >86%). However, the highest values of maximum power output and maximum E_{yield} were obtained at lower concentrations with the Mullite cell outperforming the Gore-Tex cell. In particular, the maximum power density was obtained at 600 mg COD/L initial condensate concentration (Cell 1: 0.55 W/m^3, Cell 2: 2.4 W/m^3) whereas the maximum E_{yield} was achieved at 400 mg COD/L for the Mullite cell (25.9 mJ/g COD/L) and at 500 mg COD/L (1.51 mJ/g COD/L) for Cell 1. Moreover, the highest current output was 1.6 mA and 0.6 mA, for the Mullite and the Gore-Tex cell, respectively.

The results indicate that the mullite cathode assembly exploits the mullite porosity in which the anolyte infuses and reaches the dense area of the catalytic paste whereas, the perforated Plexiglas tube, found to deteriorate this contact. In addition, it is shown that although the decrease of the anolyte's pH and conductivity which occur with an initial condensate concentration increase, limits the cells' electrical performance, condensate is successfully treated in all cases. The Rin values, originated from EIS experiments corroborate the above results.

These findings indicate that the MFC technology, with further improvement, can be effectively used in the alternative proposed management scenario of HFW. Thus, the MFC can be used after drying and shredding of the HFW, for the treatment and exploitation of the condensate by-product originated from this procedure.

6.4 “Raw” condensate treatment in MFC operation

6.4.1 Introduction

In this chapter, the results of MFC operation with “raw” condensate as feedstock are presented. The performance of two single chamber MFCs with different cathode assemblies (ceramic and Gore-Tex) was examined, with a “raw” condensate solution as feedstock.

Experimental set – up: 4.4.2.3.2

Experiments conducted: Condensate originating from HFW was used as a MFC feedstock. In order to improve the low conductivity and pH, phosphate buffer was added in the raw condensate. The condensate feeding presented fluctuations because it originated from gathered HFW, which varied each batch.

6.4.2 MFC operation with “raw” condensate feedstock

Gore-Tex cell

The duration of the acclimation period of the Gore-Tex cell was 660 h. For the acclimation to be considered complete, there had to be repeatable current peaks and high COD removal, implying development of the electrogenic active biofilm. The maximum current output for the acclimation cycles was 0.5 mA.

Following the acclimation period, the glucose synthetic feed was replaced with raw condensate and the results are presented in Figure 57. Five cycles were carried out; the detailed results of each cycle are presented in Table 27. The current output was comparable to the maximum current achieved during the acclimation, approximately 0.5 mA. However, the maximum current output was decreased over time, 1st cycle 0.62 mA and 4th cycle 0.42 mA.

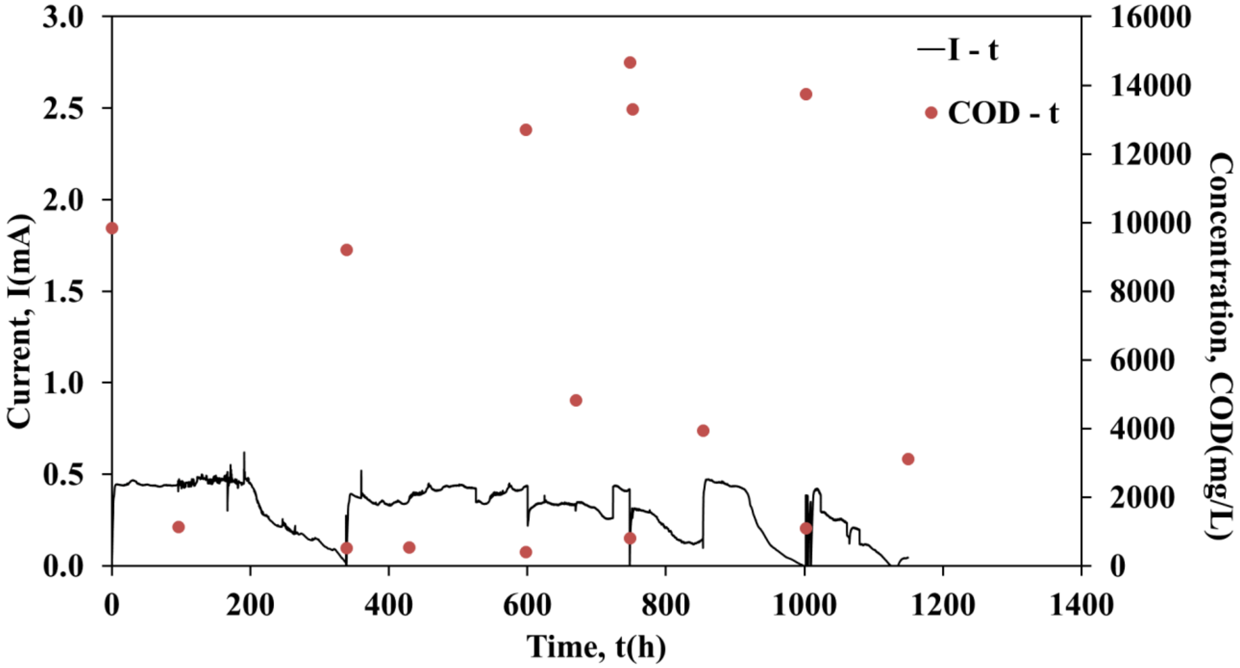

Figure 57. Current output and COD concentration versus time during "raw" condensate operation of the Gore-Tex cell.

Table 27. Measurements and calculations of the Gore-Tex cell operation.

Cycle #	CODin (g/L)	Inlet pH	I_{max} (mA)	COD Removal (%)
1st	9.9	5.9	0.62	95%
2nd	9.2	4.0	0.52	96%
3rd	12.7	4.9	0.44	94%
4th	14.7	3.8	0.47	92%
5th	13.8	4.3	0.42	77%

The Gore-Tex cell achieved high COD removal (>92%) in all five cycles, but a decrease was observed in the last cycle (77%). The inlet characteristics in terms of COD and pH have possibly affected the performance of the cell, as the inlet COD is increased and the pH is lowered through the cycles. The maximum current output (0.62 mA) was achieved in the first cycle, where both a low inlet COD (9.9 mg/L) and highest pH (5.9) were measured. Coulombic efficiencies calculated for the five cycles were very low, approximately 2%.

Mullite cell

The duration of the acclimation of the Mullite cell was 2010 h. The maximum current output for the acclimation cycles was 2.28 mA. Following the acclimation period, the synthetic glucose feed was replaced with raw condensate and the results are presented in Figure 58.

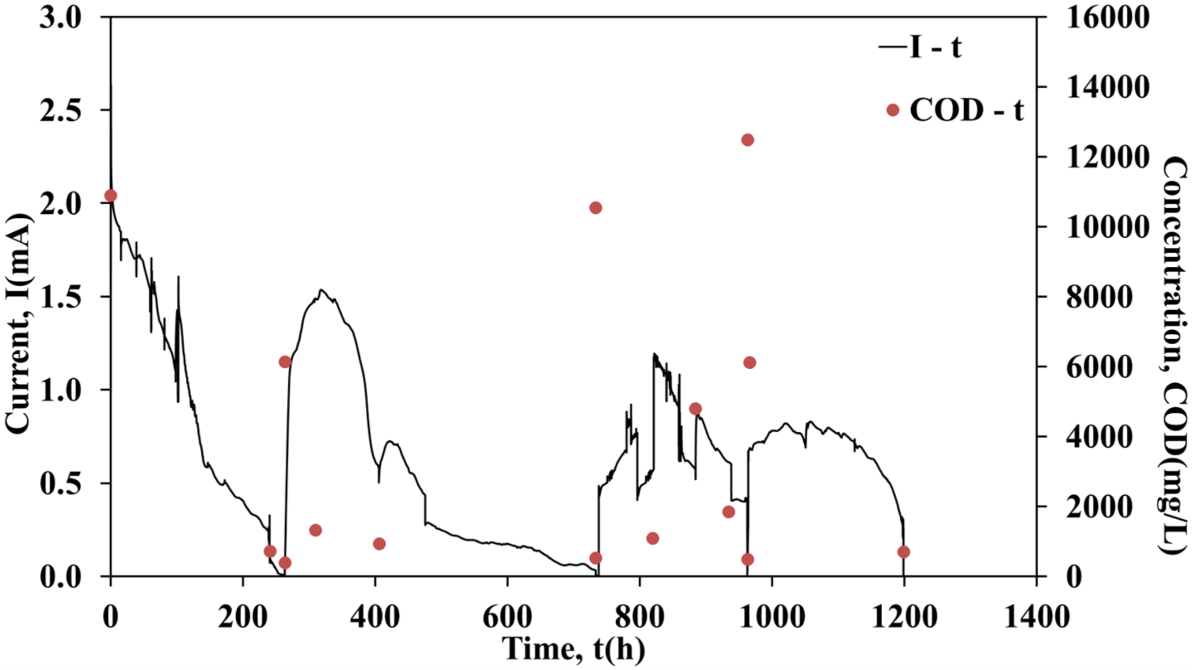

Figure 58. Current output and COD concentration versus time during "raw" condensate operation of the mullite cell.

Four cycles were carried out, the detailed results of each cycle being presented in Table 2. In particular, the maximum current output achieved was 2.02 mA, similar to the acclimation maximum current output (2.28 mA). However, the maximum current output decreased with time, as it can be seen in Figure 58 and Table 28 (current output for the 1st cycle 2.02 mA and 0.83 mA for the 4th cycle, respectively). As it can be seen from Figure 58, during the 3rd cycle the current output of the Mullite cell (red line) presented fluctuations which are attributed to the electrical connection issues.

Table 28. Measurements and calculations of the Mullite cell operation.

Cycle #	CODin (g/L)	Inlet pH	I_{max} (mA)	COD Removal (%)
1st	10.9	5.9	2.02	96%
2nd	6.2	6.1	1.54	91%
3rd	10.5	4.8	1.26	95%
4th	12.5	3.8	0.83	94%

The COD removal (>91%) was high for the Mullite cell. The maximum current output is affected by the low pH and the high COD of the raw condensate while a drop is observed in its maximum value during time (2.02 mA 1st cycle, 1.54 mA 2nd cycle, 1.26 mA 3rd cycle and 0.83 mA 4th cycle). Coulombic efficiencies calculated for the four cycles ranged between 4% - 9%.

The VFAs were almost completely consumed by the microorganisms, leading to an increase in the pH in both cells at the end of every cycle (e.g., Gore-Tex cell 1st cycle inlet pH=5.9, outlet pH=7.13, Mullite cell 4th cycle inlet pH 3.8, outlet pH=4.36).

6.4.3 Electrochemical Characterization

Figure 59 presents the polarization curves of the two cells.

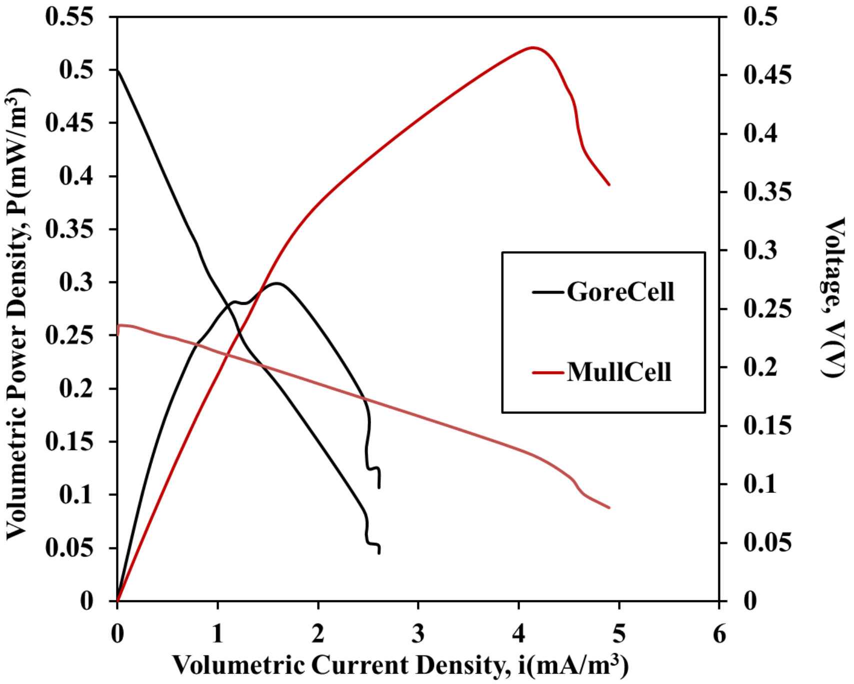

Figure 59. Volumetric power density versus volumetric current density versus voltage as extracted by LSV experiment on the two cells. (Black = Gore-Tex cell, Red = Mullite cell)

The maximum power output was achieved by the Gore-Tex cell P_{max} = 0.52 mW/m^3, while the Mullite cell achieved P_{max} = 0.3 mW/m^3. The OCVs (open circuit voltages) obtained were 0.23 V and 0.45 V for the Gore-Tex and Mullite cell, respectively. The voltage versus volumetric current density curves indicate that, in both cells, ohmic resistances dominated, but were greater for the Gore-Tex cell, due to a higher slope (698 Ω internal Gore-Tex cell resistance, 211 Ω internal Mullite cell resistance). Despite the facts that acclimation was not as fast and the OCV was not as high as for the Gore-Tex cell, the Mullite cell overall performed better in terms of power output, waste treatment efficiency and CE.

6.4.4 Conclusions

The liquid fraction of dried fermentable household waste was treated using two single chamber MFCs using different cathode assemblies (Gore-Tex and mullite assembly, respectively). The Mullite cell performed better than the Gore-Tex cell in terms of COD removal and power output. The results indicated that both cells had difficulty treating the raw condensate wastewater, because of its high COD 13 g/L and low pH 3.5 and conductivity 2.62 mS/cm.

6.5 Effluent, from PABR fed with condensate, as MFC feedstock

6.5.1 Introduction

The direct power production during the wastewater treatment using the MFC process could be a solution to the current issues that the conventional wastewater treatment practices face.

In particular, aerobic activated sludge requires large amounts of energy for aeration, recirculation and wastewater pumping. A MFC could be used in a treatment system as an alternative to the energy-demanding activated sludge system, resulting in net energy pro-duction rather than consumption. Moreover, the activated sludge process produces large amounts of sewage sludge, since it is an aerobic process, compared to the anaerobic MFC technology which generates only a small amount of microbial mass. Sludge handling drastically increases the operational and energy costs of the typical wastewater treatment plants [33], [186]. Currently, anaerobic digestion (AD) is widely applied as an alternative method for wastewater treatment since it saves energy sources and is highly effective in converting organic chemicals into methane (CH4) gas. However, the AD technology, un-like the MFC process, is not in general feasible when treating low-strength wastewater, such as municipal wastewater. Additionally, the use of AD as an electricity producing process is a two-step process (methane generation followed by burning in an internal combustion engine) in contrast to the MFC system, which directly produces electricity [187].

The aim of this work was to use a two-stage system consisting of a PABR and a single chamber MFC with fly ash as oxygen reduction catalyst.

Experimental set – up: 4.4.2.4

Experiments conducted: Condensate originating from HFW was used as PABR feedstock. In order to utilize the PABR effluent and "polish" it, taking advantage of the already treated effluent, while maximizing energy recovery, a MFC (SRMul) was used as the second stage of treatment. MFC current generation and wastewater treatment during operation with PABR effluent was examined aiming to utilize the treated wastewater for maximum energy recovery, while "polishing" it.

6.5.2 MFC operation with condensate fed PABR effluent as feedstock

The SRMul was operated with synthetic glucose wastewater (1.5 g COD/L) prior to the PABR effluent operation.

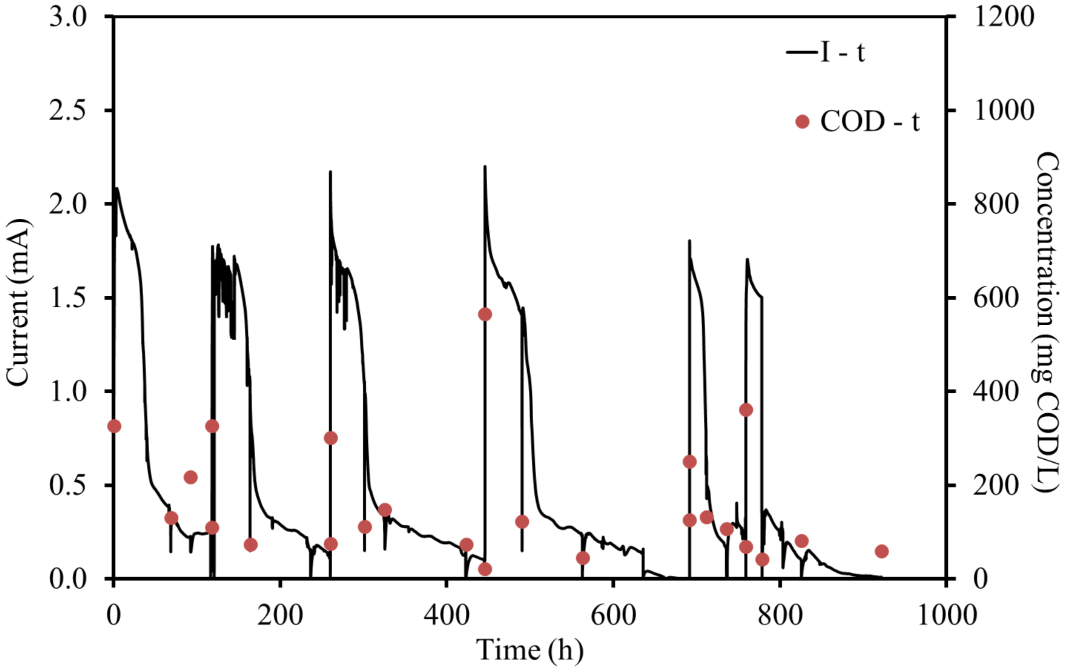

Figure 60. Current output and COD concentration versus time, during batch operation of MFC fed with PABR effluent.

In Figure 60, the current output of the SRMul operation with PABR effluent is presented. Despite the low initial COD concentration of the PABR effluent (0.36 ± 0.1 g COD/L, Table 8) SRMul achieved repeatable maximum current output 2 ± 0.2 mA, through the six operation cycles (Figure 60). The COD removal efficiency was high (78% ± 8%) across the experiments conducted. The SRMul performance was also characterized by high CE, indicating the efficient treatment of the wastewater. In particular, the highest CEs were achieved during the first operation cycles (43% – 1st cycle, 39% – 2nd cycle and 36% – 3rd cycle). The corresponding initial COD concentration of the PABR effluent was ~ 0.3 g COD/L, during the three first operation cycles, Figure 60. In the following cycles, the CEs presented a decrease (27% – 4th cycle, 23% – 5th cycle and 15% – 6th cycle), which was attributed to the fluctuations of the initial COD concentration for these cycles (0.5 g COD/L – 4th cycle, 0.25 g COD/L – 5th cycle and 0.36 g COD/L – 6th cycle).

The E_{yield} presented a similar pattern as the CE, achieving maximum values during the first three operation cycles (Figure 60), (40 mJ/gCOD/L – 1st cycle, 36 mJ/gCOD/L – 2nd cycle and 38 mJ/gCOD/L – 3rd cycle). The E_{yield} decreased in the following cycles (25 mJ/gCOD/L – 4th cycle, 20 mJ/gCOD/L – 5th cycle and 14 mJ/gCOD/L – 6th cycle). The values of CE and E_{yield} indicate the potential of the MFC technology to exploit even treated wastewaters for maximum energy recovery. Specifically, during the 1st operation cycle the CE was equal to 43%, indicating the percentage of the COD consumed that contributed to current generation, coupled with the highest E_{yield} value, gaining 40 mJ per treated gCOD/L. Similarly, the 2nd SRMul operation with PABR effluent as feedstock, achieved 39% CE, with a 36 mJ gained per gCOD/L.

The pH of the PABR effluent was 7.9 ± 0.1 (Table 8), while in the SRMul effluent a pH of 7.5 ± 0.1 was measured. The conductivity of the PABR effluent was 3 ± 0.7 mS/cm (Table 8), while an increased conductivity (4 ± 1.4 mS/cm) was measured in the SRMul effluent. The increase in the effluent conductivity, compared to the initial value, may be attributed to the salts retained in the graphite granules, which were washed out during the PABR effluent cycles. These salts originated from the synthetic glucose wastewater, with which the SRMul operated prior to the PABR effluent. Regarding the concentrations of total suspended solids (TSS) and volatile suspended solids (VSS), both presented a decrease (22% TSS and 44% VSS).

6.5.3 Electrochemical characterization during MFC operation with PABR effluent

To further examine the SRMul performance, while “polishing” the PABR effluent, linear sweep voltammetry (LSV) experiments were conducted. The results are presented in Figure 61.

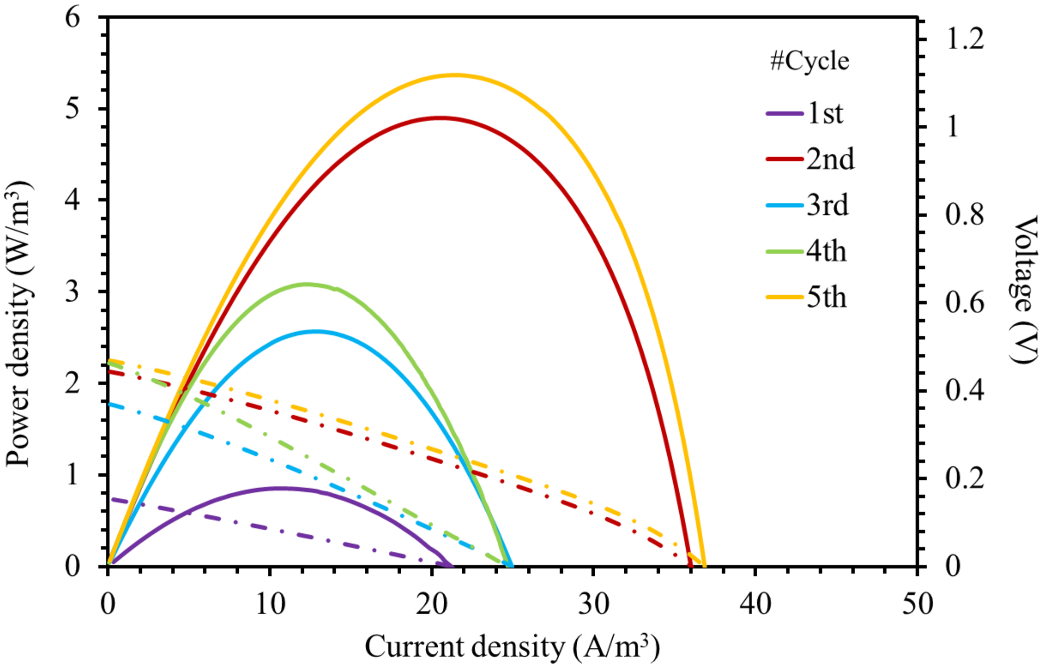

Figure 61. Volumetric power density (W/m^3) and voltage versus volumetric current density (A/m^3) versus voltage as extracted by LSV experiments on the MFC operating with PABR effluent as feedstock.

In Figure 61 the power density versus current density is depicted by continuous lines, while the voltage versus current density is depicted by dashed lines. The maximum power density was achieved during the 5th operation cycle, equal to 5.4 W/m^3, corresponding to a 0.25 g COD/L initial condensate concentration of the PABR effluent. The power density achieved during the 2nd operation cycle was equal to 5 W/m^3, with an initial COD concentration of 0.33 g COD/L. Lower power densities were achieved during the rest operation cycles (0.9 W/m^3 – 1st cycle, 2.6 W/m^3 – 3rd cycle and 3.1 W/m^3 – 4th cycle). Using the maximum power theorem, the internal resistance of the SRMul was calculated during the LSV experiments. For the 2nd and 4th operation cycle, the lowest $R_{Internal}$ were observed equal to 76 Ω and 78 Ω, respectively. The $R_{Internal}$ attained higher values during the rest of the LSV experiments (150 Ω – 1st cycle, 104 Ω – 3rd cycle and 136 Ω – 4th cycle), justifying the differences which were observed in the power densities. The voltage versus current density lines indicate the type of electrochemical losses present in the SRMul. The linearity of the dashed lines in Figure 61, corresponds to ohmic losses dominating during the SRMul operation.

6.5.4 Conclusions

The MFC technology was efficiently used to “polish” the treated effluent of a PABR. The PABR operated with HFW condensate as its feedstock, resulting in an effluent with low COD (0.36 ± 0.1 g COD/L, Table 8). The SRMul exploited the supplied effluent, resulting in a maximum current output of 2 mA and a maximum power density output of 5.4 W/m^3, during its operation. Additionally, the low initial COD concentration resulted in high CEs (43% – 15%) and high E_{yield} (40 mJ/gCOD/L – 14 mJ/gCOD/L), showcasing the capabilities of the MFC technology to take advantage of the wastewater despite its characteristics, recovering as much energy from waste as possible.

6.6 MFC technology combined with dark fermentation to efficiently treat cheese whey

6.6.1 Introduction

Cheese whey is the remains of the cheese – making process, containing carbohydrates, lactose, lactic acid and salts [52]. The cheese industry generates large quantities of this wastewater, estimated at 190 billion kg/y, which poses an environmental problem given its high quantity and high organic load. Various bioprocesses have been used in order to exploit CW, including anaerobic digestion (AD), dark fermentation (DF), Biopolymer production and BESs [188]. Additionally, combinations of the above technologies have been tested for CW treatment, the most promising being the combination of DF with AD, although DF has been combined with BES for maximum exploitation of the CW to produce H_2 or electricity, during its treatment. Regarding MFCs treating CW, both dual and single chamber configurations have been tested [188]. It was noted that treating CW with a single chamber MFC produced higher power output (439 mW/m^2), than the dual chamber MFC CW treatment (46 mW/m^2 – 6.7 gCOD/L initial concentration) [188].

The aim of this work was the utilization of the MFC technology as a second stage in cheese whey treatment, coupled with DF. Additionally, coal fly ash was examined as an oxygen reduction catalyst, used with mullite electrodes, aiming to increase the performance efficiency of the MFC treating CW.

Experimental set – up: 4.4.2.5

Experiments conducted: The SDF was used as the MFC feedstock for 4 operation cycles. Afterwards, the RDF was used as the feedstock at different concentrations (10%, 50% RDF) and with increased conductivity (10% RDF + KCl) with each concentration conducted in duplicate, in order to confirm the reproducibility of the results.

6.6.2 MFC operation with synthetic DF wastewater (SDF) as feedstock

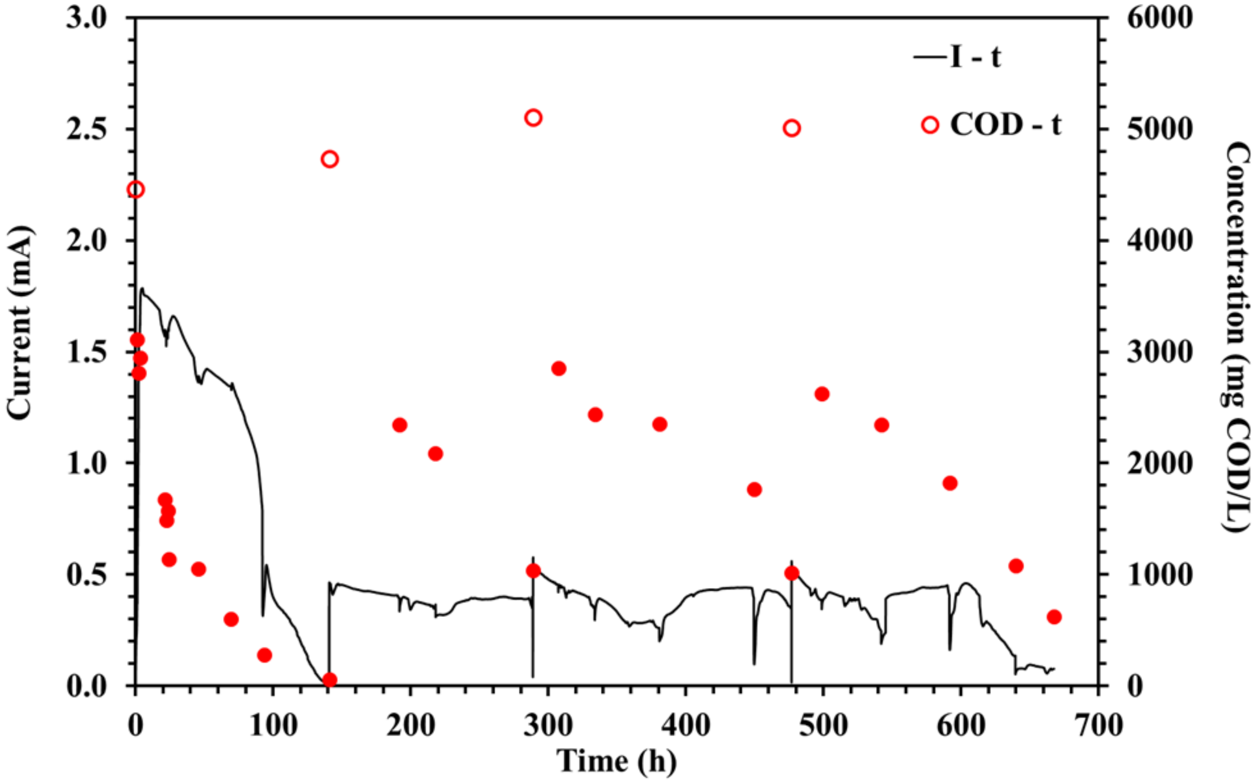

Figure 62. Current output and COD concentration versus time, during batch operation of MFC fed with SDF wastewater.

As it can be seen in Figure 62, a decrease of the maximum current output was observed from Cycle 1 to Cycle 2 (from 1.8 mA to 0.5 mA). Following this decrease, the maximum current output remained approximately constant for the next operation cycles (3rd Cycle: 0.6 mA, 4th Cycle: 0.6 mA). This drop is partially attributed to an acclimation period of the biofilm from the switch of the glucose medium to the SDF wastewater. The COD removal efficiency was high in all cases (86% ± 8%). The CE ranged from 1.4% to 3.2%, indicating that the MFC performance was hindered by parasitic activities, such as antagonistic microorganisms [33]. The pH of the MFC effluent was almost stable (6.3 ± 0.2).

Furthermore, the current generation was inhibited by the low initial conductivity of the SDF solution (1.6 ± 0.2 mS/cm, Table 9). The conductivity of the MFC effluent presented a decreasing trend from cycle 1 to cycle 4 (4.2 mS/cm 1st cycle, 1.6 mS/cm 2nd cycle, 1.4 3rd cycle and 1 mS/cm 4th cycle). The conductivity of the 1st cycle was influenced by the residual synthetic medium in the porous anode electrode. In cycles 2 through 4, the effect of the low conductivity SDF wastewater on the current generation of the MFC was observed, resulting in a maximum current output of 0.6 mA.

6.6.3 MFC operation with real DF wastewater (RDF) as feedstock

Afterwards, SDF was replaced with filter sterilized and diluted RDF (IBH_2S effluent). Initially, 10% RDF was used as feedstock, followed by 50% RDF. The effect of the RDF initial concentration was examined on the MFC performance. To further compare the two cases, the conductivity of the 10% RDF was adjusted from 3.9 mS/cm to 14 mS/cm (Table 9), by the addition of KCl. the experiments were conducted in duplicates, to test the repeatability of the results. The current output and COD concentration of the MFC are presented in Figure 63.

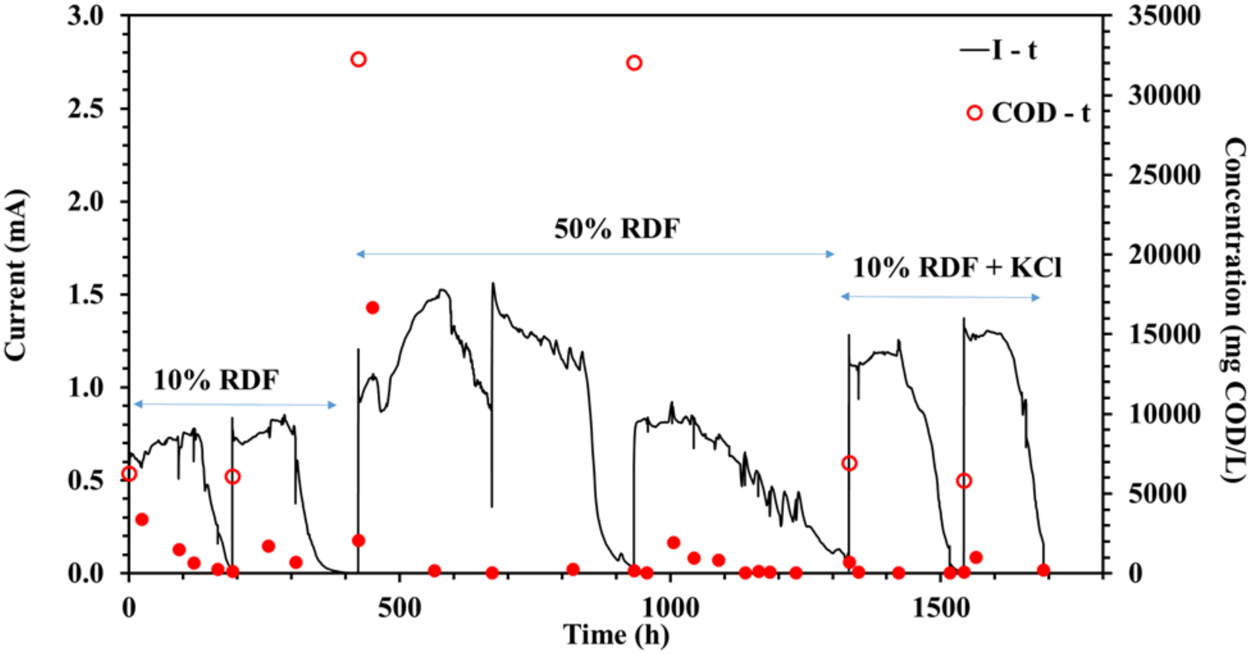

Figure 63. Current output and COD concentration versus time for the MFC operation with RDF (10% diluted RDF – left, 50% diluted RDF – middle, 10% diluted RDF with KCl – right).

During the MFC operation with 10% RDF as feedstock (1st and 2nd cycle – Figure 63), the current output increased (0.8 mA 1st cycle, 0.9 mA 2nd cycle – Figure 63) in comparison with the SDF cycles (0.6 mA 3rd and 4th cycles – Figure 62). The current output further increased to 1.6 mA (Figure 63) during the 3rd cycle with 50% RDF as MFC feed. During the 4th cycle, the maximum current was 0.9 mA (4th cycle – 50% RDF – Figure 63). In order to examine the effect of conductivity, after the 50% RDF the feedstock was switched to 10% RDF+KCl. The addition of KCl led to an initial conductivity similar to the 50% RDF (14 mS/cm). The maximum current output was 1.3 mA and 1.4 mA for the 5th and 6th cycle with 10% RDF+KCl as feedstock (Figure 63).

The duration of the MFC operation cycles averaged 212 ± 21 h, presenting an increase from the respective SDF duration (167 ± 21 h). The COD removal efficiency was high across all RDF cases, averaging 93% ± 12%. During the 50% RDF operation the COD concentration decreased by 48% in the first 24 h of the cycle (3rd cycle – Figure 63). Afterwards, the COD further decreased, achieving COD removal efficiency of 98% after 100 h of MFC operation. Although the organic matter was almost totally removed from the bulk solution, the current output became practically zero after 409 h of cell operation (Figure 63). This indicated that the chemical energy obtained from substrate decomposition (first 100 h) was stored, resulting in continuous current output for 509 h. It has been noted by [111], that in case of excess substrate the electrochemically active biofilm temporarily stores energy. The stored energy is then slowly released by the electrochemically active bacteria resulting in electricity generation. Furthermore, similar MFC behavior to a different substrate was documented by [62], presenting the rapid decomposition of the organic load and storage of the energy by the biofilm. The COD concentration of the 4th cycle presented a similar trend as the 3rd cycle, with 50% RDF feedstock. A rapid decrease (85%) during the first 50 h was observed, followed by a 98% COD removal efficiency over 300 h. The durations of the 3rd and 4th cycles with 50% RDF as feedstock, were 509 h and 397 h, respectively. The current output lasted in both cases for more than 350 h, showing the slow release of energy from the electrochemically active biofilm.

Additionally, the conductivity of 50% RDF (14 mS/cm – Table 9) was considerably higher than the respective 10% RDF (4 mS/cm – Table 9), contributing to the difference in current output (0.9 mA 10% RDF, 1.6 mA 50% RDF, respective maximum current output). In both cases the MFC effluent conductivity decreased, from 3.9 ± 0.1 mS/cm to 1.6 ± 0.2 mS/cm for the 10% RDF and from 14 ± 0.6 mS/cm to 1.7 ± 0.2 mS/cm for the 50% RDF.

The 10% RDF+KCl achieved similar conductivity values as 50% RDF, resulting in similar values to the current output (1.6 mA 50% RDF – 1.4 mA 10% RDF + KCl, Figure 63). The maximum current output for the 10% RDF was 0.9 mA (Figure 63) with an initial conductivity of 3.9 ± 0.1 mS/cm, in comparison to the respective output for the 10% RDF + KCl, which was 1.4 mA (Figure 63) with an initial conductivity of 14 mS/cm. Both the 10% RDF and 10% RDF+KCl had similar initial COD concentrations (6.4 g COD/L – 10% RDF, 6.2 g COD/L – 10% RDF+KCl) and high average COD removal efficiencies (82% – 10% RDF, 97% – 10% RDF+KCl). The pH of the MFC effluent was similar to the initial pH of the RDF solutions studied in all cases. The COD removal efficiency was high (>82%) for the whole of MFC operation whereas the CE ranged from 0.7% to 3.7%.

6.6.4 Electrochemical characterization of MFC operation with DF wastewater

LSV experiments were conducted at the beginning of each operation cycle when the current output of the cycle reached its maximum value.

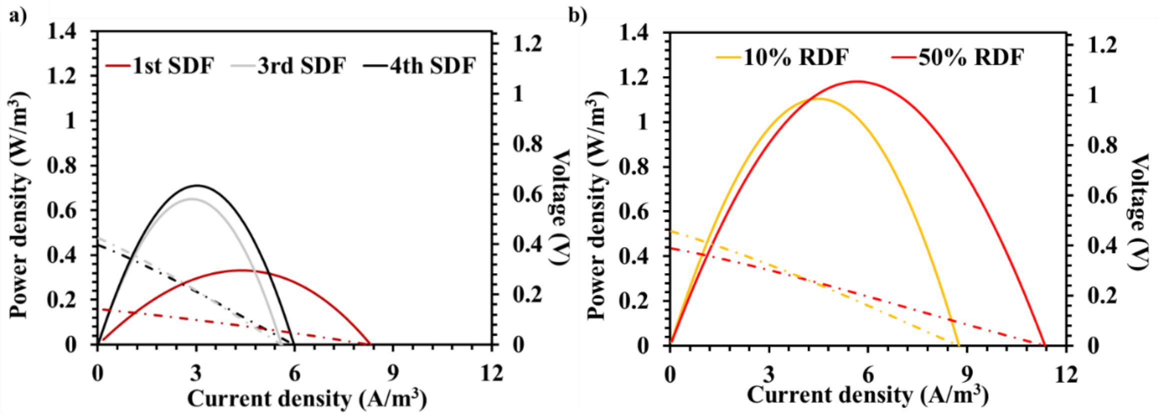

Figure 64. Power density and Voltage versus current density for three SDF cycles (1st - 3rd - 4th) (a) and the RDF (b) as feedstock for the MFC.

Figure 64 presents the power density versus current density curves with a straight line and the voltage versus current density curves with a dashed line. The maximum power density achieved for the SDF feedstock (Figure 64 – a) was 0.7 W/m^3 corresponding to a 5014 mg COD/L initial concentration and 1.8 mS/cm initial conductivity. The maximum power obtained for the RDF feedstock (Figure 64 – b) was 1.2 W/m^3, corresponding to 50% RDF case, with an initial concentration of 32 g COD/L and 14.4 mS/cm initial conductivity. During the 10% RDF operation the MFC achieved 1.1 W/m^3, with a 6.4 g COD/L and 3.9 mS/cm conductivity initially (Table 9). Despite the difference in the initial COD concentration and conductivity, the maximum power output was similar between the 10% RDF (1.1 W/m^3) and the 50% RDF (1.2 W/m^3). The internal resistance of the MFC was calculated using Jacobi’s law for the different experiments. The lowest internal resistance (202 Ω) was observed during the 1st SDF operation cycle, where the operation of the MFC was influenced by the residual glucose medium. The following cycles presented an increase in the internal resistance of the MFC (3rd SDF 645 Ω, 4th SDF 509 Ω). This was caused by the conductivity of the SDF (1.5 ± 0.3 mS/cm, Table 9). The switch of the SDF wastewater with the RDF diluted wastewater resulted in a reduced internal resistance (10% RDF 369 Ω, 50% RDF 248 Ω). The increased conductivity of the RDF solutions (Table 9) led to reduced internal resistance of the MFC, thus improving the power output (Figure 7 – b) and the current output (Figure 63) across all cases studied. Across both experiments the voltage versus current density lines indicated the ohmic losses dominating in the MFC.

6.6.5 Conclusions

The MFC technology was proposed as an addition to DF (IBH_2S) processing CW. High COD removal efficiencies were achieved (86% ± 8%) across all cases examined. Maximum current output (1.6 mA) was observed for the 50% RDF feedstock. Similarly, maximum power density (1.2 W/m^3) was obtained for 50% RDF feedstock. The temporary storage of energy by the biofilm, was detected for all RDF cases, due to the rapid (24 h) COD concentration decline accompanied with a long (>180 h) duration of current output. This result showed that high strength substrates such as IBH_2S effluent can be successfully treated by this type of MFC and opened up the possibility of attempting to apply directly the undiluted effluent in future investigations.

7 Dual – chamber MFC results

In this chapter the results of the dual – chamber MFCs operation is presented. The experiments were focused on the use of MFC technology for the recovery of heavy metals from the MFC cathode. The anode solution was kept the same glucose synthetic medium. The cathode solution was the focus of this study, in order to detect the heavy metals reduction. The heavy metal solution originated from the hydrometallurgical processing of PV panels (1^{st} and 2^{nd} generation). Two sets of experiments were conducted one was focused on silver recovery from a synthetic solution simulating the 1^{st} generation PV panel chemical extract and one on indium recovery using the 2^{nd} generation PV panel chemical extract. The performance of the dual – chamber MFCs was compared to the operation with oxygen as the electron acceptor

7.1 MFC operation with silver as electron acceptor – Silver recovery experiments

7.1.1 Introduction

In this chapter the results of the dual – chamber MFC operation for silver recovery are presented. The aim of this work is to examine the feasibility of using MFC technology to recover silver from a synthetic wastewater simulating PV hydrometallurgical process extract.

Experimental set – up: 4.5.1

A dual – chamber MFC was used with a PEM as the anode and cathode separator. Graphite based electrodes were used for both chambers. The anode solution was the synthetic glucose medium (Table 1). The cathode solution was a synthetic solution containing silver, simulating the characteristics (pH, conductivity and silver concentration) of the 1^{st} generation PV hydrometallurgical process extract.

Experiments conducted: Four cases of silver recovery were studied for four different synthetic solutions. The silver concentration (~ 50 mg/L) was kept the same across all cases, while the pH and the conductivity were altered to further examine the silver recovery process.

7.1.2 Current output and silver reduction during MFC operation

The maximum current output which was achieved during each experiment (R1, R2, R3 and R4) versus the number of the batch cycle is presented in Figure 65. Figure 66 presents the dissolved silver concentration versus time for each case. The dissolved silver in the synthetic wastewater was considered completely recovered once the dissolved silver concentration was reduced to approximately 0 mg/L.

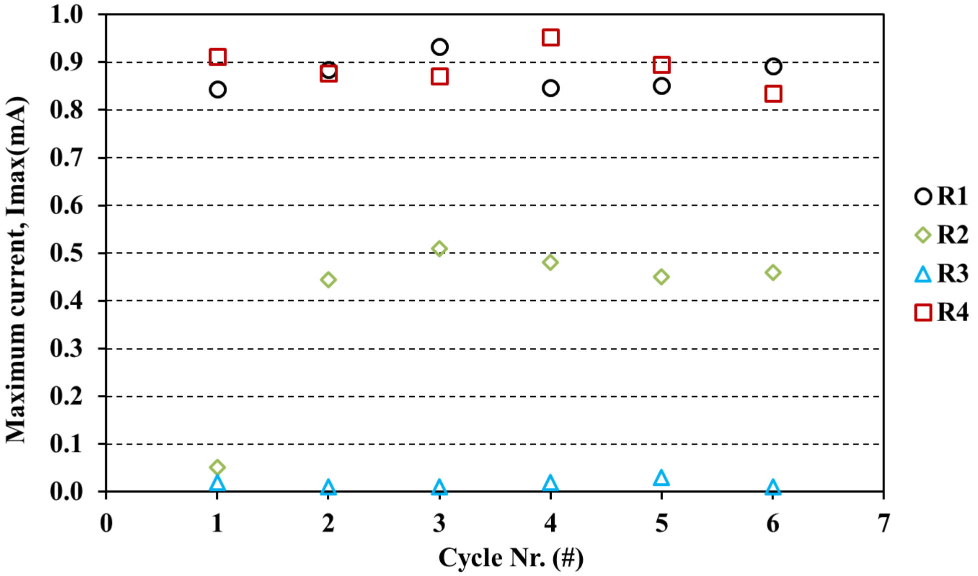

Figure 65. Maximum current output (mA) of the batch cycles of R1, R2, R3 and R4 experiments (cathodic solution for each case: R1: silver nitrate and sodium perchlorate at pH 7, R2: silver nitrate and potassium chloride at pH 7, R3: silver nitrate at pH 7 and R4: silver nitrate and sodium perchlorate at pH 2).

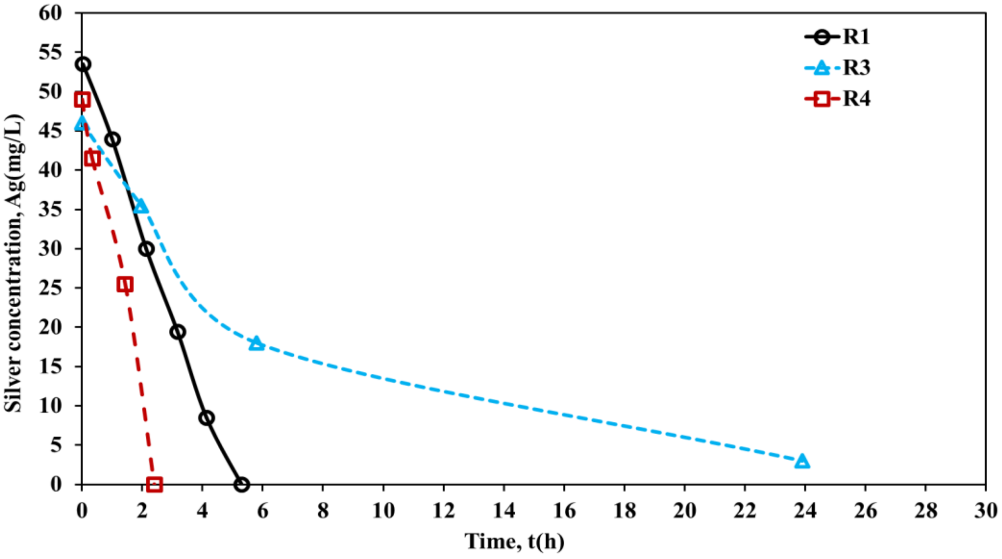

Figure 66. Silver concentration versus time for the R1, R2, R3 and R4 experiments, (cathodic solution for each case: R1: silver nitrate and sodium perchlorate at pH 7, R2: silver nitrate and potassium chloride at pH 7, R3: silver nitrate at pH 7 and R4: silver nitrate and sodium perchlorate at pH 2).

As it can be seen from Figure 65 the maximum current output (I_{max}) for the R1 batch cycles was equal to 0.93 mA. Moreover, the silver was almost completely recovered (silver recovery > 99%) (Figure 66). In the R1 case the dissolved ions formed silver perchlorate reacting as is presented in the following reaction:

$NaClO_4 + AgNO_3 \rightarrow AgClO_4 + Na^+ + NO_3^-$ Eq. 33

The anion of silver perchlorate being unstable, led to the formation of silver cations [189]. Subsequently, the reduction of the silver that occurred in the catholyte was the following:

$Ag^+ + e^- \rightarrow Ag_{(S)} \downarrow$ Eq. 34

As it can be seen from Figure 66 the silver reduction occurred within 5 h for the R1 case. The R1 cathodic solution had an average conductivity of 17.8 ± 2 mS/cm at the end of each cycle (initial conductivity 18.9 mS/cm). This may have been caused by the reacting substances of the cathodic solution and the formation of silver, resulting in the decreased conductivity of the cathodic solution.

Table 29. Equations of the silver reduction rates extracted from the dissolved silver concentrations for the four experiments (R1, R2, R3, and R4).

Experiment sets	R1	R2	R3	R4
Fitted equations of silver reduction	c=-10.451t+53.38 $R^2 = 0.9953$	-	c=41.839exp(-0.112t) $R^2 = 0.9887$	c=-19.65t+49.469 $R^2 = 0.9821$

During the R2 experiment, potassium chloride was used to increase the electrolyte's conductivity (Figure 66). No silver reduction took place since the silver ions reacted almost immediately with chloride ions forming silver chloride. This reaction led to low dissolved silver concentration at the beginning of the cycle (t = 0 h, 0.5 mg / L). In particular, the following reaction (Eq. 35) took place:

$KCl + AgNO_3 \rightarrow AgCl_{(S)} \downarrow + K^+ + NO_3^-$ Eq. 35

In the R2 experiment the synthetic wastewater was initially blurred due to the presence of silver chloride. However, at the end of the batch cycles, the catholyte was no longer blurred and deposits were visible on the cathodic electrode. The silver concentration at the end of the cycle was 0 mg/L. The maximum current output of all batch cycles was I_{max} = 0.51 mA (Figure 65). Due to the low initial silver concentration (0.5 mg/L) in the R2 case, the current peaks observed (Figure 65) were attributed to the reduction of an alternate electron acceptor.

The catholyte's pH at the end of the cycle increased to 10.3 ± 1.8, from the initial pH 7. The final cathodic conductivity presented a slight decrease (18.5 ± 0.4 mS/cm) when compared to the initial value (19.5 mS/cm, Table 11). This decrease was attributed to the formation of silver chloride. The dissolved silver was bound with the ions occurring from the supporting electrolyte.

In the case of R3 experiment, using silver nitrate and DI water, the maximum current output was I_{max} = 0.03 mA (Figure 65). This caused the slower reduction of silver, which occurred within 24 h. The silver recovery at the end of the batch cycle was approximately 93% (Figure 66). An increase in the pH of the cathodic solution was observed from 6.7 to 7.9. The conductivity of the R3 cathodic solution at the end of the batch cycle increased by (287%) (0.24 mS / cm) (Table 11).

The maximum current (I_{max}) which was obtained during the R4 experiment was 0.95 mA (Figure 65). Furthermore, a high percentage of silver recovery was achieved (> 99%) (Figure 66). The silver recovery was completed within 3 h (Figure 66). Moreover, an increase of the catholyte's pH was observed (initial pH 2, final pH 2.8). The increase in the pH is caused by the transfer of the hydrogen cations (migration) through the separator from the cathode to the anode [190]. The conductivity of the R4 cathodic solution decreased after the end of the batch cycles to 15 ± 2 mS/cm versus from the initial 18 mS/cm (Table 11). This change was attributed to the formation of silver perchlorate (similarly to R1 case, Eq. 33), from which subsequently the solid silver was formed, hence reducing the conductivity of the cathodic solution.

The silver reaction rates were extracted from the data of Figure 66 and are presented in Table 29. For the R1 and R4 cases, where the reduction was completed within 3 h and 5 h respectively, a linear equation ($c=at+b$) was the best fit. Since silver reduction was faster in the R4 case, a smaller "t" coefficient was calculated (R1 $a=-10.451$ versus R4 $a=-19.65$). For the R3 case an exponential equation ($c = 41.839\exp(-0.112t)$) fitted the data best. As mentioned above, silver reduction was not observed for the R2 case.

Overall, the addition of sodium perchlorate ($NaClO_4$) led to faster silver recoveries (R1 5 h, R4 3 h) by increasing the conductivity of the cathodic solution. When no supporting electrolyte was added in the catholyte (R3), silver was recovered within 24 h. Despite the absence of supporting electrolyte a high silver recovery (93%), was achieved in the R3 case (Figure 66). The addition of potassium chloride (R2) inhibited silver recovery by decreasing the initial dissolved silver concentration.

The maximum current output which was obtained for the R1 (I_{max} = 0.93 mA) and R4 (I_{max} = 0.95 mA) cases was higher than the R2 (I_{max} = 0.51 mA) and R3 (I_{max} = 0.03 mA) cases (Figure 65). This is attributed to the supporting electrolyte which was used in each case. The R3 case did not present a notable current output (I_{max} = 0.03 mA) due to its low initial conductivity ($\sigma_{initial}$ = 0.06 mS/cm). Consequently, the high initial conductivity ($\sigma_{initial}$ = 18 – 19.5 mS/cm, Table 11) affected the current output for the R1, R2 and R4 cases. The reduction of the initial cathodic pH to 2 for the R4 case (Table 11) did not affect the maximum current as it was similar to the R1 cases (Figure 65). However, the low pH value decreased the time required for the silver reduction to occur from 5 h (R1) to 3h (R4). No notable change in the anode pH for the R4 case at the end of the silver reduction (~ 3 h) was observed. The phosphate buffer used in the anode maintained the pH at the desired value for the microorganisms ~ 7 pH. Additionally, no proton back migration was noted from the low pH cathode (~ 2) to the higher pH anode (~ 7).

At the end of silver reduction, COD removal of the R1, R3 and R4 cases was approximately 50%. The assessment of the bio-anode performance was carried out by calculating the coulombic efficiencies (CE) for the batch cycles, using Eq. 20. The highest CEs were 8.8%, 7.6%, 0.04% and 16% for the R1, R2, R3 and R4 cases, respectively. The highest CEs were achieved for the R4 and the R1 cases. Similarly, during the R1 and the R4 experiments faster silver recoveries (5 h R1 case and 3 h R4 case) and higher current outputs (Figure 65) were obtained. The R3 case presented the lowest CE because of the absence of supporting electrolyte, resulting in the lowest current output overall (Figure 65).

7.1.3 SEM imaging and EDS analysis

After the silver recovery experiments the cathode electrodes were studied with SEM and EDS, to detect the silver depositions on the electrode surface.

R1 experiment

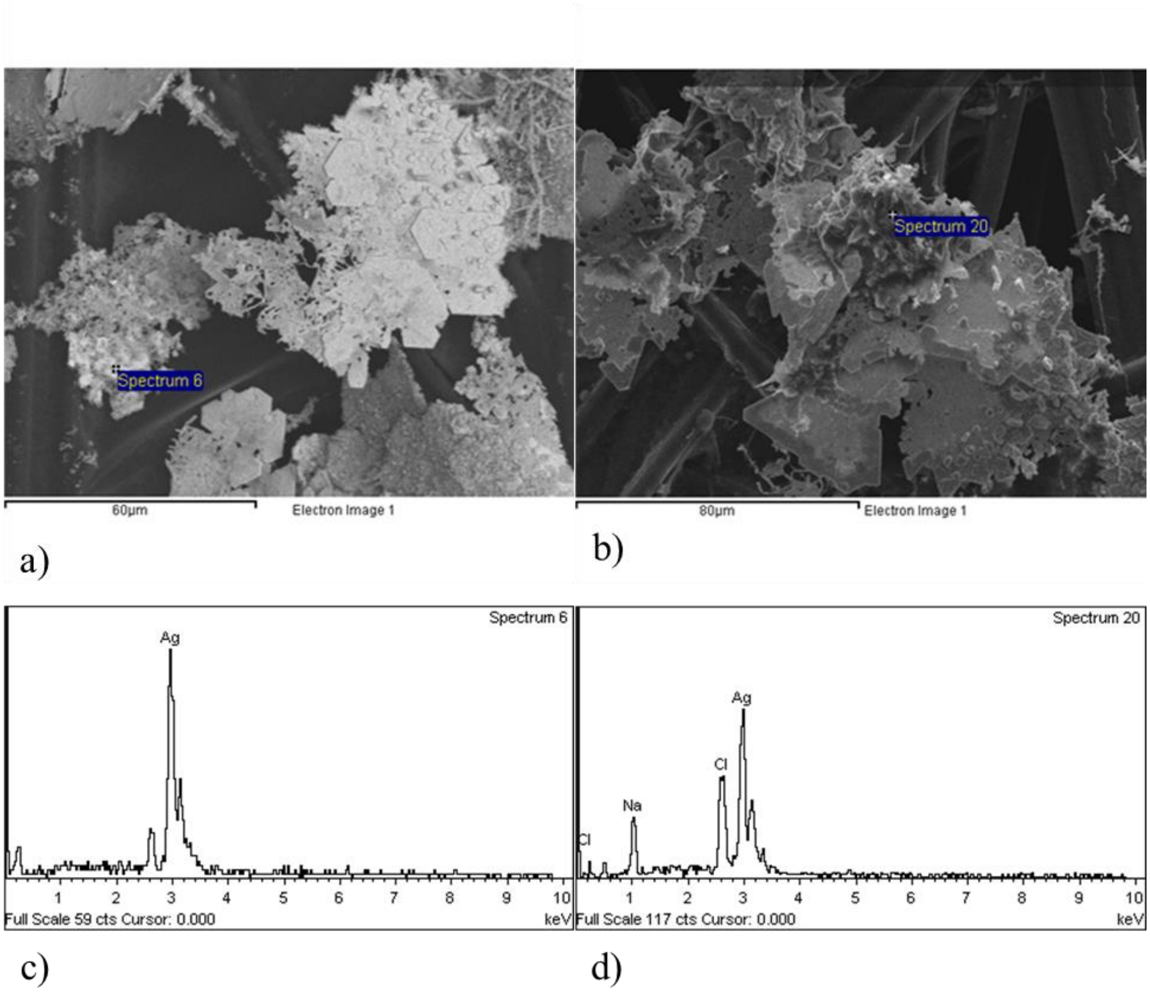

Figure 67. SEM micrograph (a, b) and EDS spectra (c, d) of the cathodic electrode surface for the R1 recovery. Pure silver crystals (a, c) and formed chloride salts (b, d).

In the SEM images of the R1 electrodes, silver deposits on the carbon paper surface were observed. Pure silver crystals were formed and in some cases chloride salts can be seen (Figure 67a and Figure 67b). The deposition of pure silver on the electrode is confirmed by the SEM images (Figure 67a and Figure 67b) and EDS spectra (Figure 67c and Figure 67d).

R2 experiment

During the R2 experiment, potassium chloride was used as the supporting electrolyte instead of sodium perchlorate. The cathodic solution was filtered and the solid phase was analyzed with

SEM and EDS. Figure 68a and Figure 68c present the SEM and EDS analysis on the electrode and Figure 68b and Figure 68d present the analysis on the filtered precipitate.

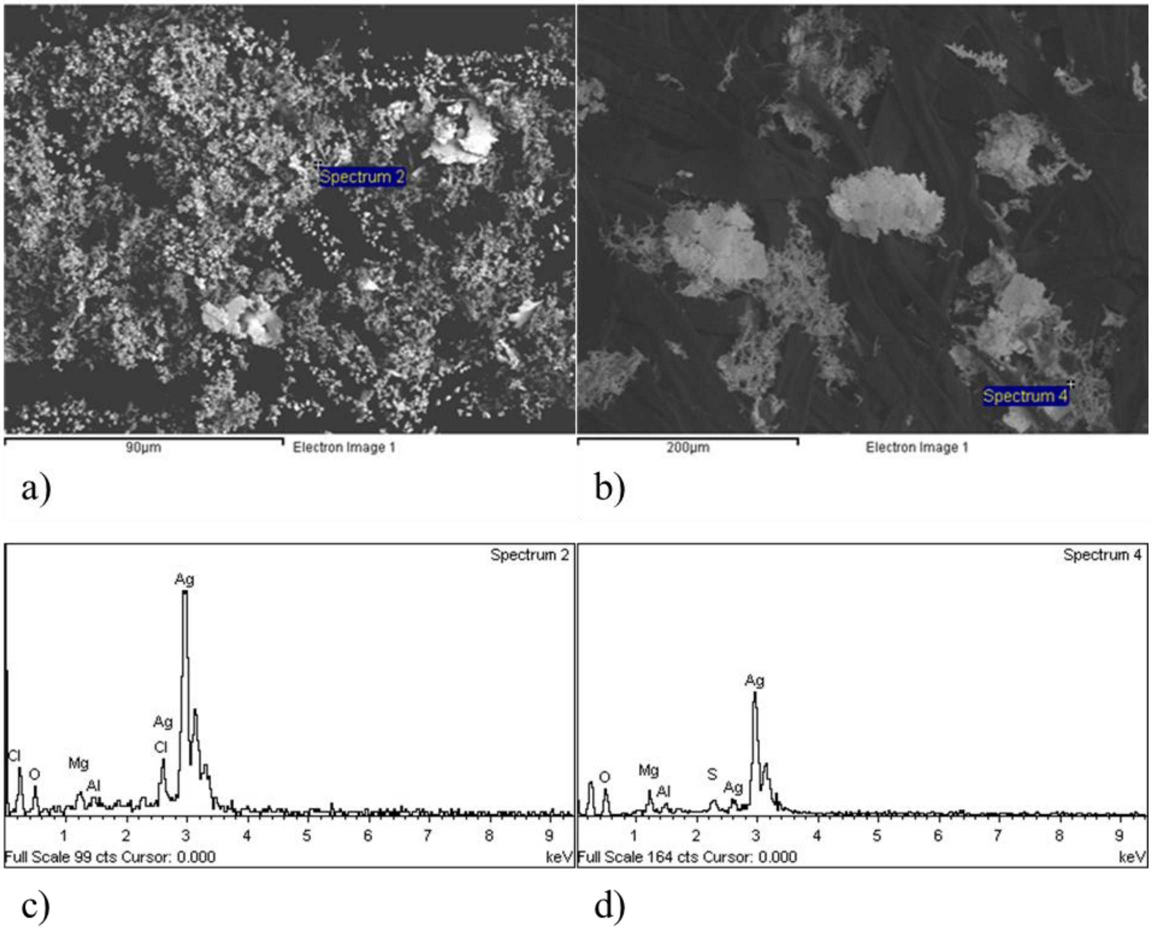

Figure 68. SEM micrograph (a, b) and EDS spectra (c, d) of the R2 cathodic electrode (a, c) and filtered solids of the catholyte (b, d).

The images of the SEM and the EDS spectra confirmed the formation of a silver chloride layer on the cathodic electrode (Figure 68a, Figure 68c), as well as the precipitation of silver chloride (Figure 68b).

R4 experiment

The R4 experiment was conducted with $NaClO_4$ (0.2 M, pH 2) as supporting electrolyte in the cathode. Silver crystals were observed on the graphite paper from SEM images. In Figure 69a and

Figure 69b pure silver crystals are observed between the graphite fibers. The EDS-EDX revealed the high purity of the silver crystals (Figure 69a and Figure 69d).

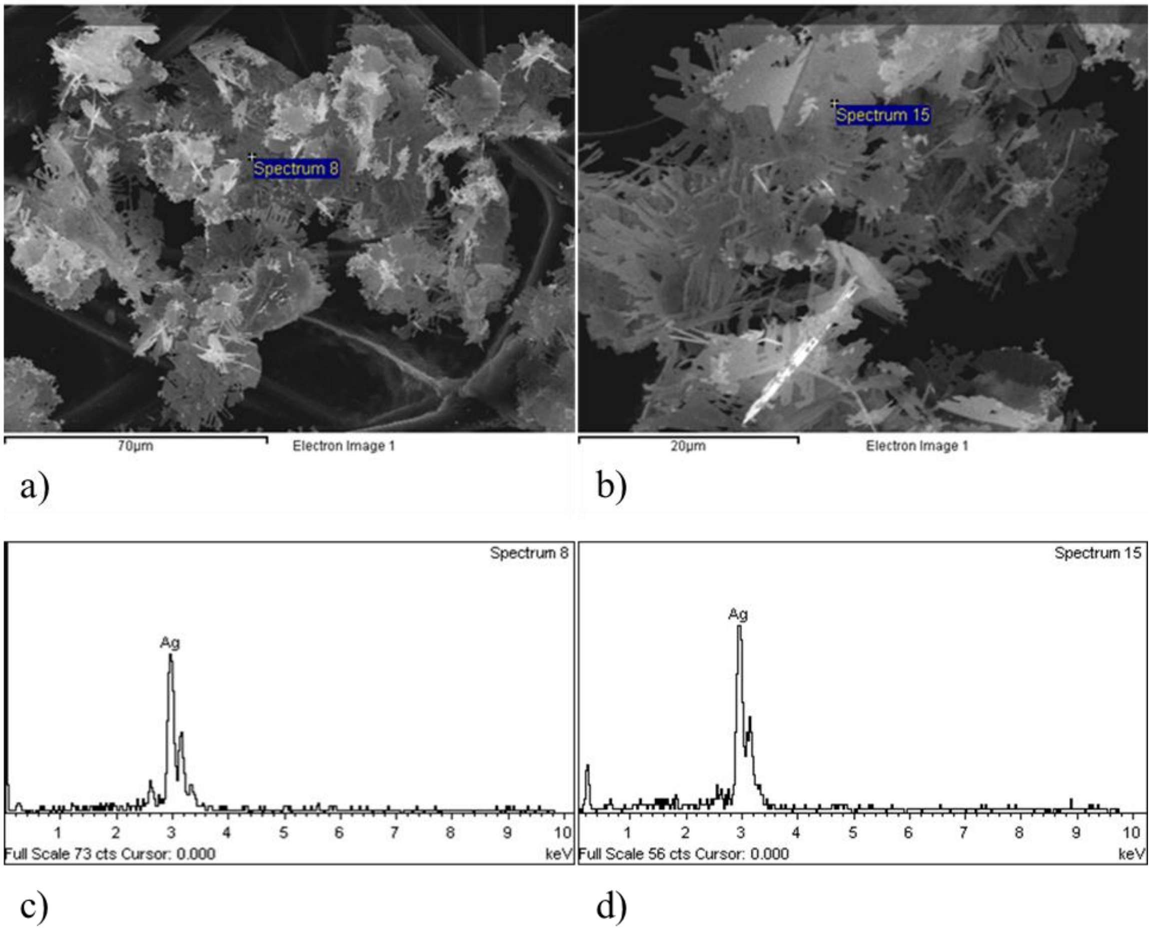

Figure 69. SEM micrograph (a, b) and EDS spectra (c, d) of the cathodic electrode surface for the R4 recovery.

In Figure 67c the presence of chloride salts was visible on the cathodic electrode. By comparison, in Figure 69c and Figure 69d no corresponding notable peaks are present, indicating the absence of chloride salts. This is caused by the decrease in the pH to 2 for the R4 case.

7.1.4 Polarization experiments during silver recovery experiments

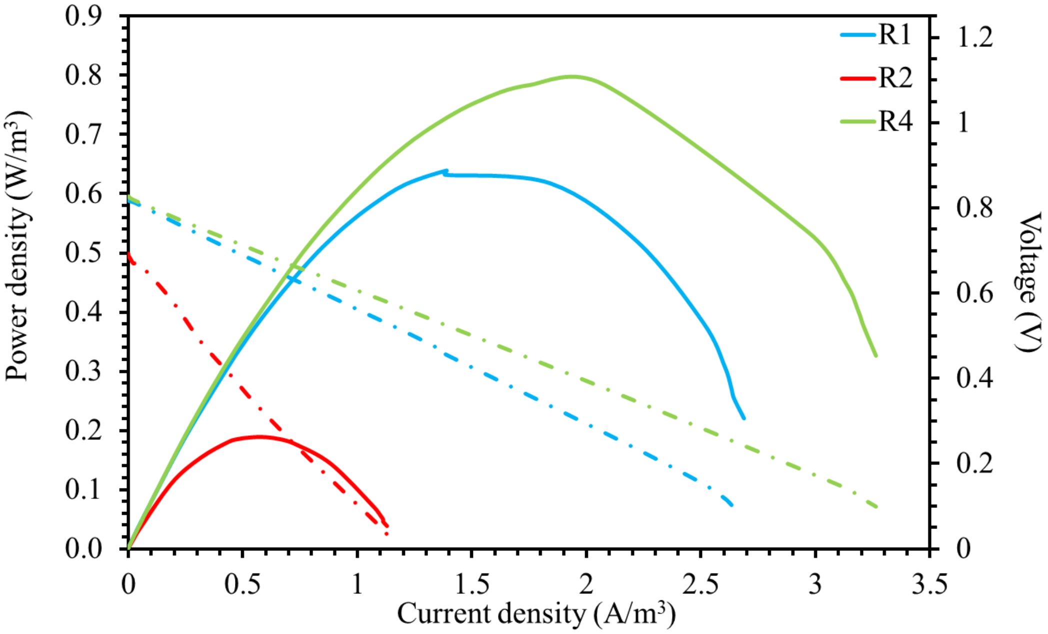

Figure 70. Polarization and power curves for the three silver recovery experiments (R1, R2 and R4)

Figure 70 presents the results of polarization experiments which were conducted at the beginning of the batch cycle (t = 0 h), for the three cases (R1, R2 and R4). No polarization curve was extracted for the R3 case, since the cell did not produce power, as presented in Figure 65. The maximum power (Pmax) was 0.64 W/m^3, 0.19 W/m^3 and 0.8 W/m^3, for the R1, R2 and R4 experiments, respectively. Furthermore, a lower internal resistance was calculated for the R4 case in comparison with the R1 and R2 experiments (R4 = 604 Ω, R1=1103 Ω and R2=2010 Ω). The R4 case presented higher power output and lower internal resistance, operating more efficiently when compared with the other cases. The operation of the MFC becomes better the greater the difference in the pH of the anode and the cathode (R4 case) [190]. The linear slope of the polarization curves (Figure 70) indicated that the ohmic losses dominated in all cases. The ohmic losses are attributed to the geometry of the H-type dual chamber MFC, as well as all the connections between the electrodes, the external resistance and the voltage recorder. In the R2 experiment where the potassium chloride was used as the supporting electrolyte the maximum power was Pmax = 0.19 W/m^3.

The current densities at maximum power were 1.39 A/m^3 and 2.08 A/m^3 for the R1 and R4 cases respectively (Figure 70). The maximum silver recovery rates were calculated using Faraday's law. For the R1 case it was 1.77 g Ag/h/m^2 and for the R4 case 2.65 g Ag/h/m^2. For the R2 case the silver recovery rate was 0 g Ag/h/m^2, due to the formation of silver chloride. In the R3 case the recovery rate was 0.05 g Ag/h/m^2, because of the absence of the supporting electrolyte slowing down the electron transfer.

7.1.5 Conclusions

For this work silver recovery using the MFC technology was studied. A synthetic silver wastewater was prepared simulating a PV panel chemical extract. The particular PV panel recycling process was proposed by the PHOTOREC project [116]. A dual chamber MFC was constructed and the pH and conductivity of the cathodic solution were examined in four cases (R1 – R4). Silver recovery was high (>93%) in all cases, except when potassium chloride was used a supporting electrolyte, where silver precipitated as silver chloride. Silver crystals were deposited on the cathodic electrodes in the R1, R3 and R4 cases. The best performance in terms of power output and internal resistance was achieved at pH 2 (0.8 W/m^3, 604 Ω) and sodium perchlorate as the supporting electrolyte. Moreover, at pH 2 (R4 case) the MFC completely recovered the silver in 3 h, when compared with the other cases (5h, 24 h for the R1 and R3 cases respectively). The maximum silver reaction rate, using the Faraday's law, was obtained during the R4 experiment and was equal to 2.65 g Ag/h/m^2. By using the MFC technology the heavy metal recovery is feasible, but parameters such as the conductivity and the pH of the wastewater should be further examined in order to improve the MFC performance.

7.2 MFC operation with indium as electron acceptor - Indium recovery experiments

7.2.1 Introduction

Indium (In) is a heavy metal broadly used in electrical applications such as solar cells for photovoltaic (PV) panels, liquid crystal display (LCD screens), transistors and microchips among others [191]. The recovery of indium from the various waste streams is essential due to its extended use and acquisition method (by-product of zinc refining). The aim of this work is to examine the feasibility of using MFC technology to recover indium from a synthetic indium wastewater and a 2nd generation PV panel chemical extract.

Experimental set – up: 4.5.2

Experiments conducted: Three cases of indium recovery were examined. In the first case, the synthetic indium wastewater (~170 mg/L) was used in the MFC cathode. Afterwards, potassium chloride was added in the synthetic indium wastewater, in order to simulate the high initial conductivity of the real PV panel chemical extract. In the third and final case, the real indium wastewater originating from the 2nd gen. PV panel chemical extract was used in the cathode. In all experiments the anode solution was kept the same synthetic glucose wastewater (1.5 gCOD/L)

7.2.2 Current output and indium reduction during MFC operation

In Figure 71a, the diluted indium concentration in the MFC cathode versus time is presented. During the MFC operation with the synthetic indium wastewater (Synth), the maximum current output was 0.09 mA (Synth – 1st cycle) and 0.14 mA (Synth – 2nd cycle). The duration of indium recovery was 45 h and 46 h for Synth – 1st and Synth – 2nd, respectively (Figure 71a). In both cases high indium recovery was achieved (96% Synth – 1st and 97% Synth – 2nd). The pH of the cathode solution presented an increase from ~2 (Table 12) (controlled by 2 M HCl addition) to ~6, indicating the decrease in the hydrogen cation ($[H^+]$) concentration. Additionally, the pH of the anode decreased from ~7 (due to buffer solution) to 6, because of the hydrogen cation migration from the cathode to the anode. The conductivity of the cathode solution (initially 2.5 mS/cm, Table 12) did not present a notable change, ~1.6 mS/cm at the end of the Synth MFC operation. The conductivity of the anode solution presented a drop in the Synth MFC operation from 11.6 mS/cm initially to 9.5 mS/cm at the end of the indium recovery. The COD removal efficiency in the anode was 75% and 60% for the Synth – 1st and Synth – 2nd operation cycles, respectively.

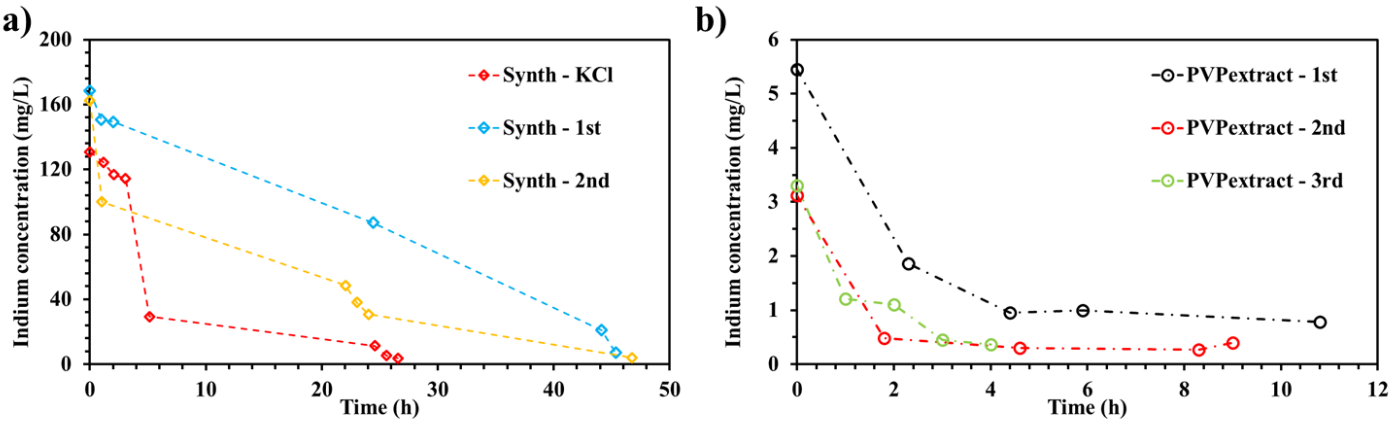

Figure 71. Indium concentration versus time in the cathode solution, during the indium recovery experiments, cathodic solution for a) Synth – synthetic indium wastewater and Synth – KCl synthetic indium wastewater with increased conductivity, b) Real – diluted PV panel chemical extract.

After the Synth MFC operation the cathode solution was switched with synthetic indium wastewater with increased conductivity, by KCl addition until ~15 mS/cm (Table 12). The increased conductivity was examined to determine its impact on the indium recovery. The maximum current output during the Synth – KCl experiments was 0.2 mA. The indium recovery was faster (~27 h, Figure 71a), when compared to the Synth experiments (~46 h, Figure 71a), due to the higher initial conductivity of the Synth – KCl solution (15 mS/cm, Table 12), than the Synth solution (2.5 mS/cm, Table 12). High indium recovery (97%, Figure 71a) was observed in the Synth – KCl case, as well. The COD removal efficiency in the anode during the Synth – KCl experiments was 53%. The conductivity of the cathode solution presented a decrease from the initial value (15 mS/cm, Table 12) to 9 mS/cm. The conductivity decrease observed during the Synth and Synth – KCl experiments was attributed to the reduction of the diluted indium in the cathode and the deposition of indium oxides on the electrode surface.

Following the MFC operation with synthetic indium wastewater, the PV panel chemical extract was used as the cathode. In particular the 2nd generation PV panel chemical extract was diluted (10%), due to the extremely low pH (out of detection limit, Table 12), in order to avoid possible damage on the MFC materials and pH imbalance between the anode and the cathode. Moreover the characteristics of the cathode solution were presented in Table 12. The diluted indium concentration during the PVPextract operation is presented in Figure 71b. The maximum current output during the PVPextract was 1.1 ± 0.1 mA. The duration of the indium recovery experiments was 11 h, 9 h and 4 h for the 1st, 2nd and 3rd PVPextract cycles (Figure 71b). The higher current output and faster indium reduction during the PVPextract experiments, when compared to the synthetic indium wastewater experiments, was attributed to the higher initial conductivity of the solution used (~84 mS/cm, Table 12) and the low initial indium concentration (Figure 71b). The COD removal efficiency during the PVPextract experiments was 46%, despite the fast depletion of diluted indium in the cathode solution (4 – 11 h, Figure 71b). The low initial pH of the PVPextract (1.2, Table 12) used in the cathode, affected the anode pH, regardless of the buffer solution used in the anode. The initial anode pH was ~7 (regulated by the buffer solution in the synthetic glucose wastewater) and the anode pH after the PVPextract experiments was reduced to ~2, indicating the hydrogen cation back migration from the cathode to the anode, resulting in the anode pH drop. Moreover, the cathode pH (initially 1.2, Table 12) presented a slight increase to ~2, after the indium recovery from the PVPextyract. The conductivity of the cathode solution was ~84 mS/cm (Table 12) initially and after the MFC operation the final conductivity of the cathode solution was 26 ± 2 mS/cm. The conductivity of the anode solution initially was 11.5 mS/cm and after the indium recovery with the PVPextract it was increased to 21 ± 2 mS/cm. The drop in the cathode conductivity was attributed to the reduction of the diluted indium in the cathode and the deposition of indium oxides on the electrode surface, similarly the Synth and Synth – KCl experiments. The MFC achieved a higher current output (~1.1 mA) during the PVPextract, than the Synth (0.14 mA) and Synth – KCl (0.2 mA). The indium recovery was faster across all PVPextract cases (4 – 11 h, Figure 71b), than the Synth and Synth – KCl experiments (46 h and 27 h, respectively Figure 71a).

7.2.3 SEM imaging and EDS analysis

After the indium recovery experiments the cathode electrodes were studied with SEM and EDS, in order to determine the depositions on the electrode surface.

Synthetic indium wastewater

In Figure 72a, the depositions on the electrode surface imaged by SEM are presented. In Figure 72b the respective EDS is presented. Indium deposits were detected, corresponding to indium hydroxides and indium oxides, based on the EDS analysis (Figure 72b). Furthermore, a small amount of crystalline indium was detected (< 4%, weight (%), Figure 72b). Similar results were obtained by [54], detecting indium hydroxides and achieving a high indium removal (91% - 93%) from synthetic indium wastewater used in a dual chamber MFC.

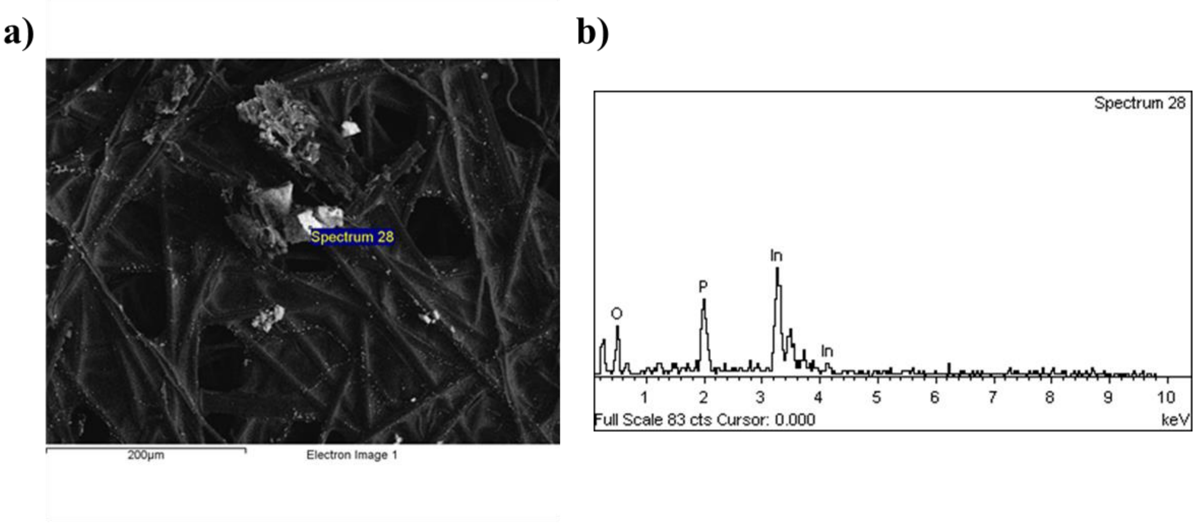

Figure 72. SEM micrograph (a) and EDS spectra (b) of the cathodic electrode surface for the Synth experiments.

Apart from the cathode electrode, the cathode solution after the MFC operation was filtered in order to collect possible sediments. The filter was then studied with SEM and EDS, extracting Figure 73a and Figure 73b, respectively. The deposits on the filter were similar to the deposits observed on the electrode surface (Figure 72). Indium oxides were observed with a small amount of crystalline indium (< 3%, Figure 73b). Impurities were detected in both cases Figure 72 and Figure 73.

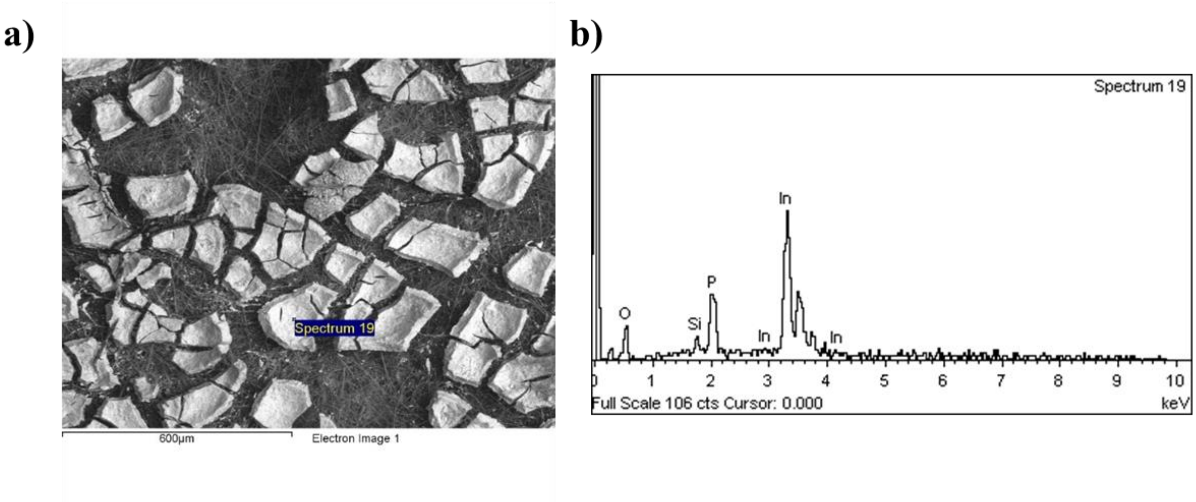

Figure 73. SEM micrograph (a) and EDS spectra (b) of the filter after the cathode solution solid – liquid separation for the Synth experiments.

<u>Real indium wastewater</u>

After the Synth and Synth – KCl operation the cathode solution was switched with the PVPextract. Following the indium recovery from PVPextract the cathode electrode was studied with SEM and EDS, presenting the results in Figure 74.

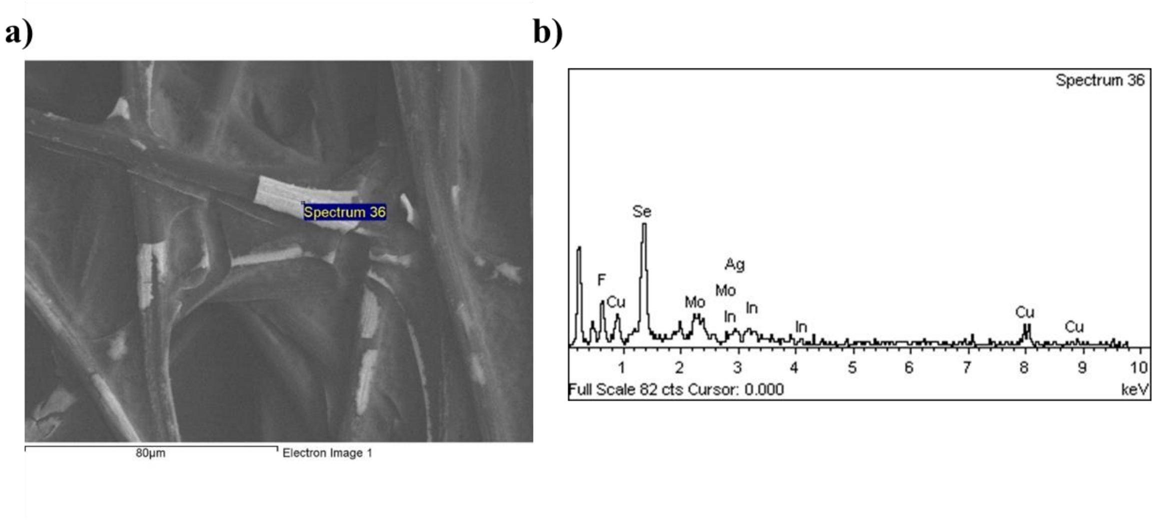

Figure 74. SEM micrograph (a) and EDS spectra (b) of the cathode electrode's surface after the PVPextract operation.

On the electrode surface multiple depositions were detected (Figure 74b), including selenium (Se), copper (Cu), molybdenum (Mo), indium (In) and silver (Ag). No gallium was detected since it cannot be recovered electrochemically. Selenium, copper, molybdenum and indium are all present on the thin film of the 2nd generation PV panel. Silver deposits were considered impurities, originating from the conductive epoxy damaged by the extremely low pH of the PVPextract (Table 12). Indium formed hydroxides similarly to the synthetic indium wastewater experiments. A small amount of crystalline indium (< 3%, Figure 74b) was detected in this case as well.

7.2.4 Polarization experiments during indium recovery experiments

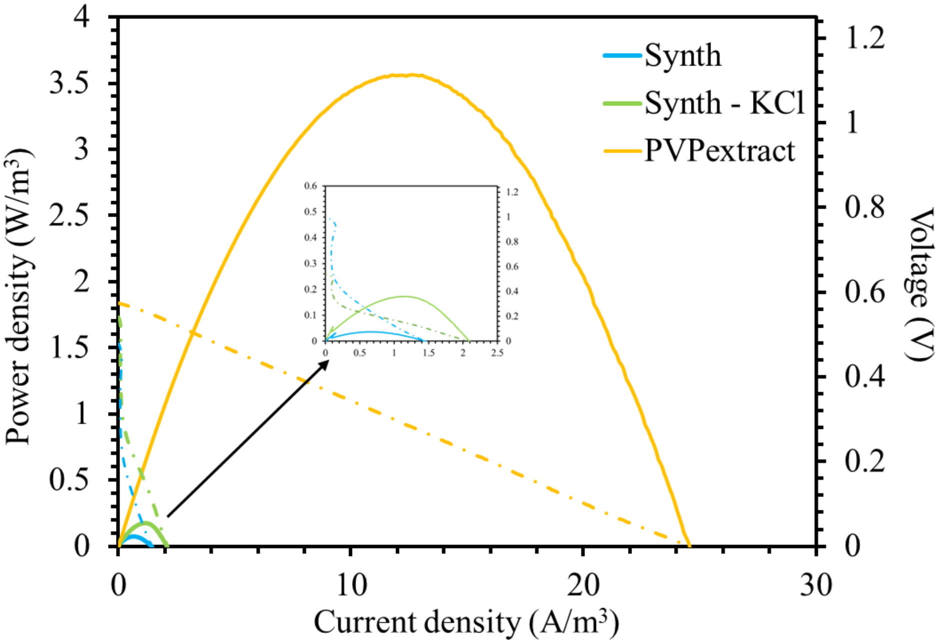

Figure 75. Polarization and power curves for the indium recovery experiments (Synth, Synth – KCl and PVPextract).

To further examine the MFC performance during indium recovery experiments, LSV experiments were conducted to measure the maximum power output of the MFC. The maximum power was normalized to the anode volume (70 ml). The maximum power density was achieved during the PVPextract experiments, peaking at 3.5 W/m^3 (orange lines - Figure 75). The power density during the Synth experiments was 0.08 W/m^3 (blue lines - Figure 75) and the addition of KCl led to a power density of 0.17 W/m^3 (green lines - Synth – KCl, Figure 75). The initial conductivities of the cathode solutions justify the power density obtained across the three different experiments (2.5 mS/cm – Synth, 15 mS/cm – Synth – KCl and 84 mS/cm – PVPextract Table 12). Using the maximum power theorem, the internal resistance of the MFC was calculated during the different indium recovery experiments. The lowest internal resistance was measured during the PVPextract equal to 320 Ω. The Synth – KCl achieved an internal resistance of 1800 Ω and the highest internal resistance was recorded during the Synth experiments equal to 2600 Ω. The lowest internal resistance corresponded to the highest power density output (PVPextract Figure 75) and the highest internal resistance corresponded to the lowest power density output (Synth Figure 75).

7.2.5 Conclusions

In this work indium was recovered using a dual chamber MFC, with synthetic and real PV panel chemical extract as the cathode. The highest current and power density output was detected during the PVPextract experiments (2 mA and 3.5 W/m^3, respectively). Indium was successfully recovered from the cathode solutions, with at least 85% removal efficiency, across all experiments. The deposits on the electrode surface indicated the deposition of indium in the form of oxides and hydroxides. The low pH of the PVPextract lowered the anode pH despite the usage of buffer solution in the synthetic glucose wastewater. The MFC technology has the ability to efficiently treat an organic wastewater in the anode, reduce the indium from the wastewater in the cathode and generate electricity at the same time. The usage of MFC technology in PV panel recycling has the potential of a clean and sustainable method for material recovery.

7.3 Comparison of dual – chamber MFC performance during operation with different electron acceptors

This study was conducted in order to examine the MFC technology as an addition to PV panel recycling, in particular for material recovery, through the cathode reduction of the MFC. The proposed process for PV panel recycling was carried out in the framework of the PHOTOREC project.

Regarding the synthetic silver wastewater, high recoveries were achieved (>93%) with a maximum current output of 0.9 mA. The indium synthetic experiments achieved a high recovery of indium (97%) with deposits of indium oxides on the electrode surface. The current output even with increased electrolyte conductivity (Synth – KCl) achieved a current output of 0.2 mA, which is lower than the respective current generated during silver reduction. The indium recovery from the PVP extract achieved a higher current output 1.1 mA and a fast recovery time (4 – 11 h).

By using the MFC technology the heavy metal recovery is feasible, but parameters such as the conductivity and the pH of the wastewater should be further examined in order to improve the MFC performance.

8 Model results

8.1 Introduction

The aim of this work was the development of a model simulating the operation of a dual chamber MFC.

MFC model and configuration brief description: 4.74.7

A time – dependent 2D model was developed in the COMSOL Multiphysics® software, containing mass and charge conservation and transfer phenomena. Electrochemical kinetics were incorporated through the combined Butler – Volmer – Monod equation. The model took into account the geometry and the materials used of the H – type MFC. The experimental set – up included a dual – chamber MFC, operating with a synthetic glucose medium (Table 1). The parameters used in the equations were estimated during an identical MFC operation and have been described elsewhere ([192]).

Phenomena studied: The model was used to simulate the glucose consumption, the voltage development and the power output of the dual – chamber MFC. The model was validated by comparing the simulation data with experimental results. Subsequently, the effect of different initial glucose concentrations on the MFC performance was examined and the effect of different initial electrolyte conductivities on the MFC performance.

8.2 Preliminary model result presentation and comparison with experimental data

The model presented quick convergence, in under one minute, simulating the consumption of glucose in the MFC and the simultaneous voltage output. Initially, the results from the model were compared with the operation of the two - chamber MFC, with an external resistance set at 100 Ω. Figure 76a presents the concentration of the organic substrate calculated during one batch cycle as this was extracted by the model, as well as the concentration obtained from the experiments. Figure 76b shows the voltage output of the cells as calculated by the model as well as the respective values originating from the experiment. Specifically, the concentration was normalized to the initial substrate concentration (1 g COD/L) while voltage recording started as soon as the MFC was fed with fresh glucose synthetic wastewater.

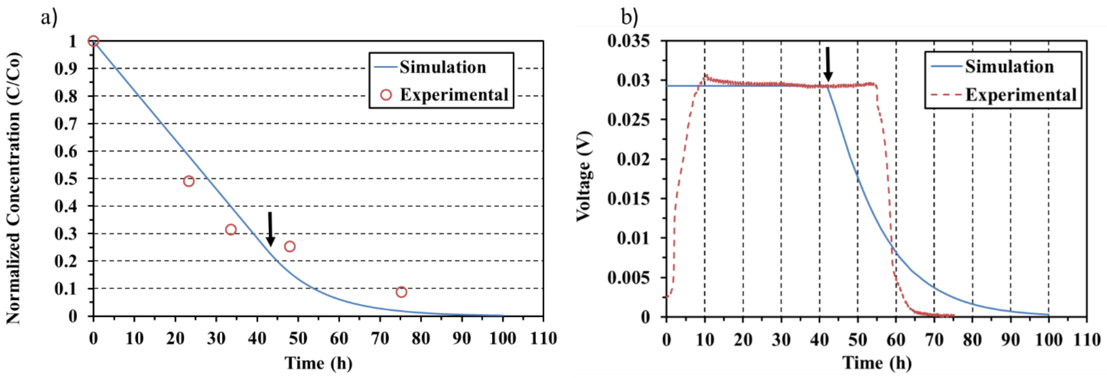

Figure 76. Comparison of simulated results (blue line) with experimental data (red circles and red dashed line) for the MFC with the external resistance set at 100 Ω. Glucose concentration versus time (left) and voltage output (right). The black arrows in both figures indicate the point when the voltage plateau drops.

As shown in Figure 76a, the concentration initially presents a linear drop and then tends asymptotically to zero (blue line Figure 76a). The COD removal achieved by the cell was 91% (Figure 76a). The simulation continued until the substrate concentration inside the cell reached 0 mol/m^3. The operation cycle lasted for 75 h, while the simulated time for the model was 100 h (Figure 76a). The model predicted a 98% substrate consumption at the 75 h mark. The experimental measurements of substrate concentration (red circles) were in agreement with the simulation data.

The voltage output originating from the model at 100 Ω case, was close to the experimental data (Figure 76b). In particular, the maximum voltage was 29 mV, while the respective voltage peak during the experiment was 31 mV. The voltage plateau was close and with the same duration for both experimental and computational results (~ 40 h). The difference between the experiment and the model was that the plateau formed immediately in the model (0 h) while in the experiment the maximum voltage was achieved after 10 h of cell operation. This was attributed to the glucose diffusion in the biofilm and the activation energy required to initiate the glucose oxidation. On the other hand, in the model, the reaction takes place on the electrode surface and it comes immediately in contact with the organic substrate, thus achieving the maximum value at the beginning of the cycle. The second difference between the results of the experimental data and the model prediction, is observed after the plateau and the voltage decrease trend. The experimental data show that it takes 19 h for the voltage to be reduced to 0 V, but the model requires 59 h to decrease this value to 0 V. This deviation is attributed to the ohmic losses which are present during the experiment, because of the electrical connections. In the case of the model (100 Ω), a slower and smoother voltage decline takes place. Overall, the model fitting regarding the voltage output of the units at 100 Ω external load, is considered to be satisfactory. The experimental data used in the modified Zeng model [104] were extracted from the operation of the cell with a 100 Ω external resistance. The voltage output and the substrate consumption were in good agreement with the experimental measurements in the MFC operation with 100 Ω, because these experimental data were used for the parameter calculation.

For better understanding of the organic substrate distribution, four different images are presented in Figure 77. The concentration of glucose was normalized to the initial value (C_0).

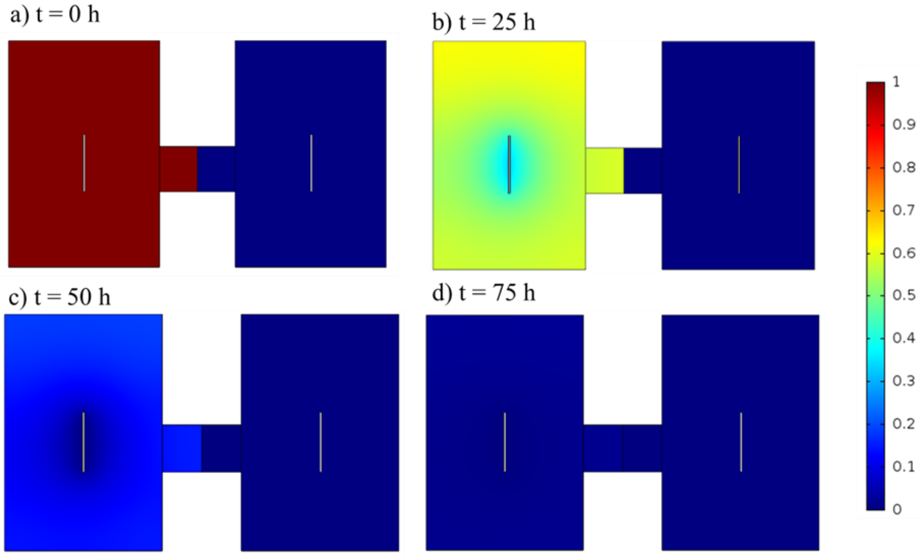

Figure 77. Organic substrate distribution (normalized concentration C/C_0) for 0, 25, 50 and 75 h, with 100 Ω external resistance.

The distribution of the substrate is presented in Figure 77a, when the oxidation had not started yet. At 25 h (Figure 77b) the substrate consumption was 45%, at 50 h (Figure 77c) it was 87% and at 75 h 98% (Figure 77d). The distribution of the substrate in the anodic chamber is uniform, with the exception of a gradient present at 25 h and 50 h. This was observed around the anodic electrode, as expected, since the reaction takes place on its surface. Moreover, in all four cases (Figure 78 a – d) the effect of the separator was observed, inhibiting the transfer of glucose from the anode to the cathode ($C_{cathode} = 0$, dark blue color).

In order to validate the model and test its ability to predict the MFC performance with R_{ext} 1000 Ω, more data were compared. Figure 78 presents the results of the simulation of glucose concentration and the voltage output during cell operation (at R_{ext} 1000 Ω), in comparison with the respective experimental data.

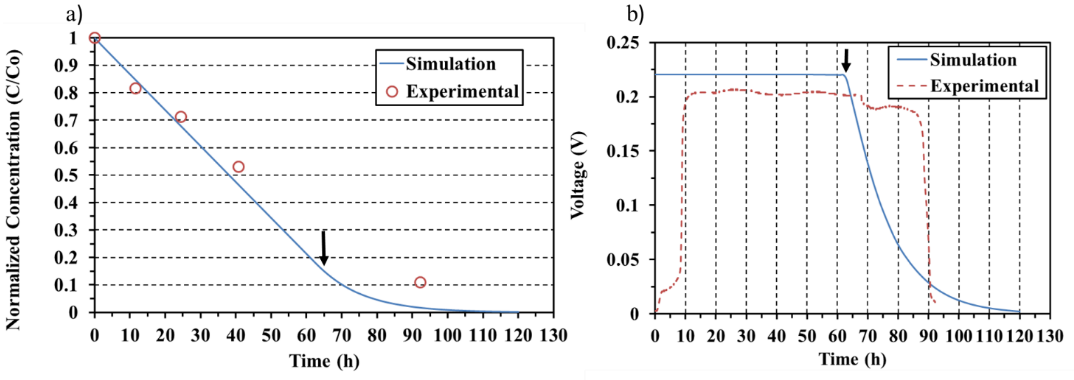

Figure 78. Comparison of simulated results (blue line) with experimental data (red circles and red dashed line) for the MFC with the external resistance set at 1000 Ω. Glucose concentration (left) and voltage output (right) versus time. The black arrows in both figures indicate the point when the voltage plateau drops.

By shifting the external resistance in the model to 1000 Ω, similar results were obtained with the respective experimental data (Figure 78). The experimental COD removal was 89% at the end of the batch cycle. The cycle duration for the 1000 Ω experiment was 92 h close to the simulated time (110 h), for the full depletion of substrate in the anode chamber. At 92 h the model calculated 98% substrate consumption (Figure 78a). A similar pattern is observed from the results originating from the system set at 100 Ω, as expected, since the consumption of glucose primarily depends on the Monod kinetics and not on the external resistance. The substrate concentration decreased similarly in the model and in the experiment. The voltage output peak was 220 mV for the model and 210 mV for the experiment (Figure 78b). The voltage plateau was maintained for 63 h in the simulation and 72 h in the experiment. The voltage output reached its maximum value (210 mV) after 10 h of cell operation, while the model predicted that the voltage reaches its maximum value (220 mV) at 0 h. The voltage decrease lasted for 52 h simulated time, but this decrease for the experiment was faster (7 h). Similarly, to Figure 76b, the time difference between the model and the experiment is attributed to glucose diffusion within the biofilm, to the voltage losses because of the electrical connections and the cell's geometry (H-type). Moreover, when the simulated voltage plateau ceased in both cases at 40 h and 63 h (see black arrows in Figure 76b and 17b), the organic substrate was reduced by 75% and 81%, respectively (see black arrows in Figure 76a and 17b). The prediction of the MFC operation with an external resistance set at 1000 Ω was considered successful, validating the developed model

After simulating the MFC operation with two different external resistances (100 Ω, 1000 Ω) and comparing the results with experimental data, the next step was the extraction of the polarization curve. A parametric study was carried out on the external resistance variable, testing a range of values (0.5 MΩ – 0 Ω).

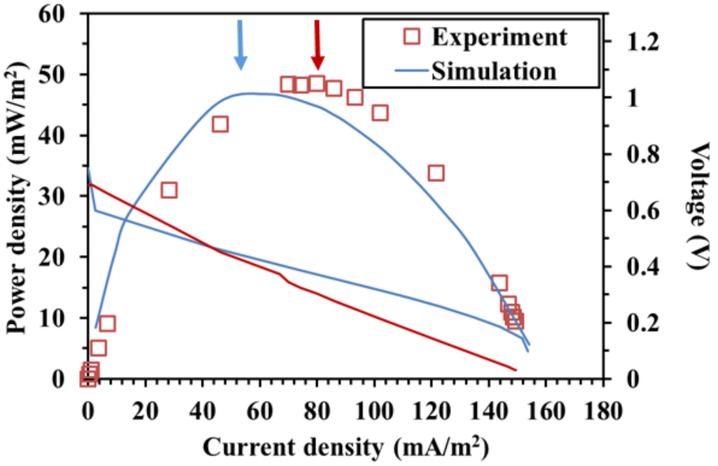

Figure 79. Comparison of polarization curves extracted by the model and experiments, for 1 g COD/L initial glucose concentration. The blue arrow indicated the maximum power density simulated and the red arrow indicated the maximum power density measured in experiments.

The polarization curve calculated by the model (blue line Figure 79) was in agreement with the respective curve resulting from the experiment. Both power and current values, were normalized to the surface of the anodic electrode (Table 14), in order for the results to be easily comparable with other cases. The model's maximum power density (47 mW/m^2) was obtained at external resistance equal to 5000 Ω and current density equal to 63 mA/m^2. The corresponding experimental power density (49 mW/m^2) was achieved at 1900 Ω and at 80 mA/m^2. Despite the apparent consistency of these results, the same maximum power was achieved for different external resistances (Simulation: 5000 Ω, Experiment: 1900 Ω) and consequently different current densities (see blue and red arrows in Figure 79). On the other hand, the model was able to predict the range of the current densities 2.6 – 154 mA/m^2 produced by the MFC (0 – 149 mA/m^2). The difference between the experimental and the computational polarization curves was observed in the 20 – 140 mA/m^2 range. In Figure 5 the I – V curves for both the experiment (red line) and the simulation (blue line) were also presented. The slope of the lines indicates in both cases the ohmic resistances as the main cause of electrochemical losses. The OCV of the model is 0.75 V and the respective value measured in the experiment was 0.7. In the simulated I – V curve, apart from the ohmic losses, the effect of substrate diffusion is also visible, for high current densities and low voltages. The experimental I – V line does not indicate other electrochemical losses apart from the ohmic.

8.3 Different initial substrate concentrations

The model was also validated in terms of its ability to predict the MFC performance when the initial glucose concentration is changed. The initial glucose concentration ranged between 0.125 – 4 g COD/L. In terms of Chemical Oxygen Demand removal (COD) 90% COD removal was considered adequate of a well performing MFC. The time required for the 90% COD removal, was defined as the time required for the MFC model to achieve a satisfying substrate treatment. Furthermore, the duration of the maximum voltage output was maintained for the different initial substrate concentrations. The results are presented in Figure 80.

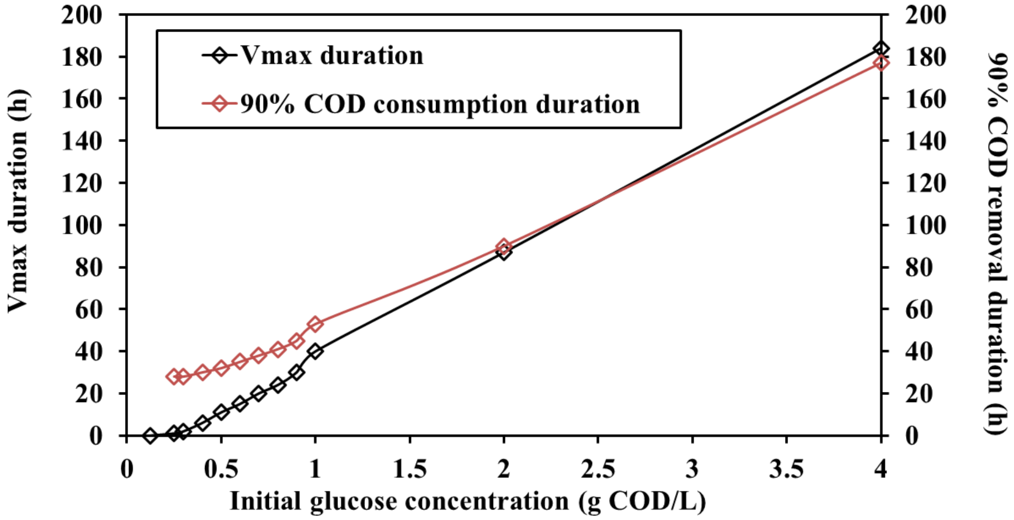

Figure 80. Duration of maximum voltage output (V_{max}) plateau (left) and duration until 90% COD removal (right) versus the initial glucose concentration in g COD/L.

The duration of the plateau, during which maximum voltage output was maintained, increased with increasing glucose concentration (Figure 80 black line). A similar increase was observed for the time to 90% COD removal corresponding to a glucose increase (Figure 80 red line). In the case of glucose concentration at 0.125 g COD/L the maximum voltage value was 15 mV, which was lower than the one achieved for the other concentrations (29 mV) and was maintained for less than 1 h. For 0.25, 0.3 g COD/L the maximum voltage (29 mV) was kept for 1 h, as well. As the initial glucose concentration increased, the duration of the maximum voltage increased as well, presenting a linear correlation between the two. For the 90% COD removal duration a similar pattern was extracted from the model. The time required for 90% COD consumption was higher than the respective duration of the maximum voltage required for lower initial concentrations (0.125 – 2 g COD/L). On the other hand, for values higher than 2 g COD/L the two lines intersected at approximately 2.5 g COD/L and the duration of the maximum voltage was higher than the corresponding time required for 90% COD removal. This result indicated that there may be an initial concentration which when fed to a MFC will achieve a more intensive and effective operation, in successive batch cycles. Moreover, for lower initial concentrations, the MFC underperforms in terms of voltage output as it did not achieve the maximum voltage value. The maximum voltage (29 mV) achieved did not depend on the increasing initial glucose concentration for the bigger part of the range examined (0.4 – 4 g COD/L).

8.4 Different initial electrolyte conductivities

In order to examine the model's capabilities, a parametric study was conducted on the effect of electrolyte conductivity, maintaining all other parameters at their respective initial values (Table 14) and the external resistance at 100 Ω. The electrolyte conductivity was adjusted in the experiments by the addition of potassium chloride, sodium hydroxide and the trace elements, all of them increased the conductivity of the synthetic glucose solution to 1.2 S/m. The range of the electrolyte values tested was 0.036 S/m – 100 S/m. The initial glucose concentration corresponded to 1 g COD/L.

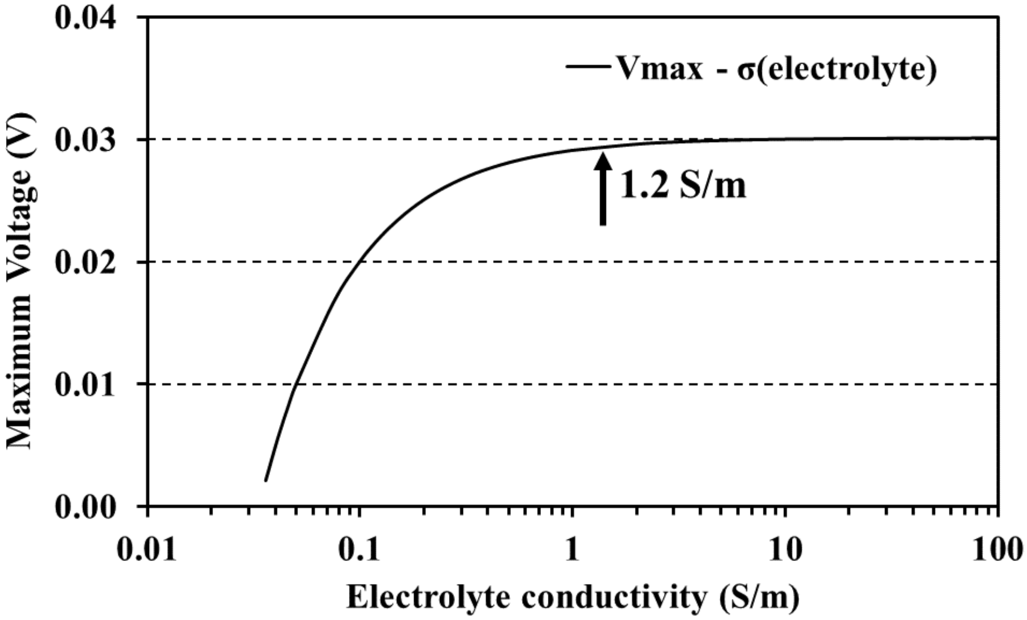

Figure 81. Maximum voltage output versus the corresponding electrolyte conductivity. The black arrow indicates the electrolyte conductivity value used in the experiments and in the initial model simulation.

Figure 81 presents the results from the electrolyte conductivity parametric study. The maximum voltage output was 30 mV and the lowest voltage was 2.1 mV. For a better presentation of the computational results a logarithmic scale was used for the x-axis, aiming to indicate the effect of the electrolyte conductivity on the voltage output. The point of the electrolyte value (1.2 S/m) used in the experiments and the initial runs (100 Ω, 1000 Ω) is highlighted in Figure 81 (black arrow). An increase in the maximum voltage output was observed as the electrolyte conductivity was increased. Furthermore, at higher conductivity values (> 2 S/m), the maximum voltage from each simulation converged to the same value (30 mV). The initial value of the electrolyte conductivity selected (1.2 S/m) achieved a similar maximum voltage (29 mV). These results indicated that by increasing the electrolyte conductivity up to 2 S/m, the maximum voltage output by the MFC increased as well. Further increasing the electrolyte conductivity (>2 S/m), did not have a similar effect on the voltage and the maximum value remained the same. Based on this conclusion, it was deduced that in order to increase the performance of a MFC, the addition of electrolyte salts was effective, up to a critical value, beyond which adding extra conductivity boosters has no effect on the maximum voltage.

The different electrolyte conductivities did not have an effect on the COD removal. This observation was expected as well, since the conductivity does not affect directly the substrate consumption, but affects the voltage which through the overpotential is implemented in the Monod – Butler – Volmer. The voltage was not high enough to have an impact on the glucose consumption, nor did it affect the transport of species due to migration since the electric field was weak.

8.5 Conclusions

In this work, a 2D MFC model was developed in order to simulate the complex operation of MFCs. Electrochemical kinetics along with mass and charge transfer equations were solved in the FEM software Comsol Multiphysics®. The results were compared with experimental data from the operation of the MFC on which the model was based on. The model predicted well the value of the maximum voltage output of the MFCs operated at R_{ext} 100Ω (simulation: 29 mV; experiment: 30 mV) and R_{ext} 1000 Ω (simulation: 220 mV; experiment: 210 mV), respectively. Moreover, by shifting the external resistance of the MFC, the polarization curve extracted from the model resulted in a similar maximum power (47 mW/m^2) as the corresponding experimental data (49 mW/m^2). By changing the initial organic substrate concentration, the maximum voltage output decreased for low initial concentrations (0.125 g COD/L) and for higher values (0.25 – 4 g COD/L) peaked at the same value (29 mV). Increasing the initial substrate concentration increases the duration of the maximum voltage. It was determined that an appropriate initial concentration for both high COD removal (90%) and lasting maximum voltage was approximately 2.5 g COD/L. Finally, examining the effect of the electrolyte conductivity, a maximum voltage was achieved (29 mV) by increasing the value beyond 2 S/m. These findings need to be validated with respective experiments conducted in the H-type MFC. This model despite the adequate MFC simulation, focuses on a specific MFC configuration with various assumptions. Further examination is needed in order to optimize and enrich the model with more electrochemical phenomena, aiming at a more complete MFC simulation.

9 Conclusions

In this chapter, the key findings of this work are summarized.

a. Single – chamber MFC

- Successful treatment (COD removal efficiency) of FORBI leachate, Condensate, Digestate, PABR effluent, Cheese whey (DF effluent) and synthetic glucose wastewater
- The conditions supplied through the synthetic glucose wastewater produced the highest power density achieved (14.2 W/m^3), from a single chamber MFC with four air cathode Gore-Tex electrodes (with MnO_2 as the oxygen reduction catalyst) and graphite granules with a graphite rod anode.
- At higher power densities, electrochemical losses due to mass diffusion were observed in the polarization curve.
- By creating an array consisting of 4 similar MFCs (4 Gore-Tex MnO_2 cathodes, graphite granule and graphite rod anode) continuous efficient treatment of FORBI leachate was achieved.
- Efficient implementation of single chamber MFC technology in various stages of a food waste valorization process.
- Coupling of MFC technology with other biological processes (anaerobic digestion, dark fermentation) to maximize wastewater treatment and energy from waste recovery.
- Detection of antagonistic microorganisms present in the anode biofilm, inhibiting the current production but contributing to the waste decomposition.
- Mullite was studied as a cathode material, combined with stainless steel mesh or copper wire for electron collection, achieving similar efficiency as the operation with Gore-Tex electrodes.
- Fly ash, biochar and activated carbon were studied as oxygen reduction catalysts in single chamber MFC cathodes, producing promising results in terms of current output, power output and COD removal efficiency.
- By increasing the number of cathode electrodes from 4 to 6 the current output and power output of the MFC presented an increase (1.7 to 3.9 W/m^3).

- During the condensate examination as a MFC feedstock, different initial concentrations were used at the feedstock, resulting in higher current and power output during lower concentrations.
- During the raw condensate feedstock, MFC performance presented unstable current output due to the high organic content of the feed, inhibiting the efficient MFC operation.
- The equivalent circuit used to simulate the EIS data presented convergence during the various wastewaters treatment in the single chamber MFCs.

b. Dual – chamber MFC

- Silver recovery from synthetic wastewater simulating PV panel chemical extract utilizing dual chamber MFC. High recoveries were detected (>93%), with visible silver depositions on the electrodes, confirmed by SEM and EDS-EDX analysis.
- Indium recovery from synthetic and real wastewater originating from PV panel chemical extract (>85%), with indium depositions on the cathode electrode which consisted of indium oxides, as revealed by the SEM and EDS-EDX analysis.
- Higher power output was achieved during the indium recovery from the PVP chemical extract (3.5 W/m^3)

c. Model

- After the validation of the proposed MFC model, the initial conductivity and initial substrate concentration effect on the MFC performance was investigated.
- By increasing the initial electrolyte conductivity above 1.2 S/m the current output did not correspond to a current output increase.

10 Future Prospects

Based on the work conducted and the conclusions extracted, the following ways are proposed for the continuation of the research:

a. Continuous operation of single chamber MFC units connected externally to form MFC arrays, in order to maximize the power generation.
b. Continuous operation of dual chamber MFCs treating simultaneously two wastewaters, one requiring oxidation and one reduction, in the anode and cathode respectively.
c. Further development and adaptation of the proposed MFC model to include single chamber MFCs, with focus on the simulation of the continuous operation of the four air cathode single chamber MFC.
d. Coupling of the MFC technology with different BESs to maximize bioelectricity and bioproducts generation.

The proposed work for continuation of the research aims at the better utilization of the MFC technology, in order to practically implement this method for wastewater treatment outside of the lab environment.

11 References

[1] “World Population Prospects 2022 World Population Prospects 2022 Summary of Results.”

[2] “Global electricity demand growth is slowing, weighed down by economic weakness and high prices - News - IEA.” https://www.iea.org/news/global-electricity-demand-growth-is-slowing-weighed-down-by-economic-weakness-and-high-prices (accessed Oct. 02, 2022).

[3] “Frequently Asked Questions (FAQs) - U.S. Energy Information Administration (EIA).” https://www.eia.gov/tools/faqs/faq.php?id=427&t=3 (accessed Oct. 13, 2022).

[4] “Where does our electricity come from? - World Nuclear Association.” https://world-nuclear.org/nuclear-essentials/where-does-our-electricity-come-from.aspx (accessed Oct. 12, 2022).

[5] B. Hoen *et al.*, “Attitudes of U.S. Wind Turbine Neighbors: Analysis of a Nationwide Survey,” *Energy Policy*, vol. 134, Nov. 2019, doi: 10.1016/j.enpol.2019.110981.

[6] “Facts About Hydropower | Wisconsin Valley Improvement Company.” http://www.wvic.com/content/facts_about_hydropower.cfm (accessed Oct. 13, 2022).

[7] “Geothermal Electricity Production Basics | NREL.” https://www.nrel.gov/research/re-geo-elec-production.html (accessed Oct. 13, 2022).

[8] “Biomass Energy Pros and Cons.” https://www.solarreviews.com/blog/biomass-energy-pros-and-cons (accessed Oct. 13, 2022).

[9] “www.iea.org/Textbase/techno/essentials.htm-Please send comments to giorgio.simbolotti@iea.org 1. IEA Energy Technology Essentials The IEA Energy Technology Essentials are regularly-updated briefs that draw together the best-available, consolidated information on energy technologies from the IEA network ETE03-Biomass for Power Generation and CHP *”, Accessed: Oct. 13, 2022. [Online]. Available: www.iea.org/Textbase/techno/essentials.htm

[10] “Global Waste Index 2019 | SENSONEO.” https://sensoneo.com/global-waste-index-2019/ (accessed Oct. 15, 2022).

[11] “Advantages and Disadvantages of Landfills - Conserve Energy Future.” https://www.conserve-energy-future.com/advantages-disadvantages-landfills.php (accessed Oct. 19, 2022).

[12] “Advantages and Disadvantages of Incineration - Macrotec Engineering.” https://macrotecengineering.com/advantages-and-disadvantages-of-incineration/ (accessed Oct. 19, 2022).

[13] “15 Benefits of Composting for the Environment, Economy, & Community.” https://growensemble.com/benefits-of-composting/ (accessed Oct. 19, 2022).

[14] C. Warwick, A. Guerreiro, and A. Soares, “Sensing and analysis of soluble phosphates in environmental samples: A review,” *Biosensors and Bioelectronics*, vol. 41, no. 1. pp. 1–11, Mar. 15, 2013. doi: 10.1016/j.bios.2012.07.012.

[15] H. Guven, M. E. Ersahin, H. Ozgun, I. Ozturk, and I. Koyuncu, “Energy and material refineries of future: Wastewater treatment plants,” *Journal of Environmental Management*, vol. 329. Academic Press, Mar. 01, 2023. doi: 10.1016/j.jenvman.2022.117130.

[16] J. Cantwell, B. Erickson, L. Fillmore, J. Kottwitz, M. Levy, and M. Rickert, “Energy Data Management Manual for the Wastewater Treatment Sector,” 2017.

[17] V. Parravicini, K. Svardal, and J. Krampe, “Greenhouse Gas Emissions from Wastewater Treatment Plants,” in *Energy Procedia*, Elsevier Ltd, 2016, pp. 246–253. doi: 10.1016/j.egypro.2016.10.067.

[18] S. Bajracharya *et al.*, “An overview on emerging bioelectrochemical systems (BESs): Technology for sustainable electricity, waste remediation, resource recovery, chemical production and beyond,” *Renew Energy*, vol. 98, pp. 153–170, 2016, doi: 10.1016/j.renene.2016.03.002.

[19] J. Annie Modestra, L. Matsakas, U. Rova, and P. Christakopoulos, “Prospects and trends in bioelectrochemical systems: Transitioning from CO2 towards a low-carbon circular bioeconomy,” *Bioresour Technol*, p. 128040, Nov. 2022, doi: 10.1016/j.biortech.2022.128040.

[20] B. E. Logan, “Exoelectrogenic bacteria that power microbial fuel cells,” *Nat Rev Microbiol*, vol. 7, no. 5, pp. 375–381, 2009, doi: 10.1038/nrmicro2113.

[21] M. A. Rosenbaum and A. W. Henrich, “Engineering microbial electrocatalysis for chemical and fuel production,” *Curr Opin Biotechnol*, vol. 29, no. 1, pp. 93–98, 2014, doi: 10.1016/j.copbio.2014.03.003.

[22] K. S. Madiraju, D. Lyew, R. Kok, and V. Raghavan, “Carbon neutral electricity production by Synechocystis sp. PCC6803 in a microbial fuel cell,” *Bioresour Technol*, vol. 110, pp. 214–218, 2012, doi: 10.1016/j.biortech.2012.01.065.

[23] G. Mohanakrishna, J. S. Seelam, K. Vanbroekhoven, and D. Pant, “An enriched electroactive homoacetogenic biocathode for the microbial electrosynthesis of acetate through carbon dioxide reduction,” *Faraday Discuss*, vol. 183, pp. 445–462, 2015, doi: 10.1039/c5fd00041f.

[24] A. Z. Imoro, M. Mensah, and R. Buamah, “Developments in the microbial desalination cell technology: A review,” *Water-Energy Nexus*, vol. 4, pp. 76–87, 2021, doi: 10.1016/j.wen.2021.04.002.

[25] S. D. Minteer, B. Y. Liaw, and M. J. Cooney, “Enzyme-based biofuel cells,” *Curr Opin Biotechnol*, vol. 18, no. 3, pp. 228–234, 2007, doi: 10.1016/j.copbio.2007.03.007.

[26] A. Kadier, Y. Simayi, P. Abdeshahian, N. F. Azman, K. Chandrasekhar, and M. S. Kalil, “A comprehensive review of microbial electrolysis cells (MEC) reactor designs and configurations for sustainable hydrogen gas

production," *Alexandria Engineering Journal*, vol. 55, no. 1, pp. 427–443, 2016, doi: 10.1016/j.aej.2015.10.008.

[27] Z. Du, H. Li, and T. Gu, "A state of the art review on microbial fuel cells: A promising technology for wastewater treatment and bioenergy," *Biotechnol Adv*, vol. 25, no. 5, pp. 464–482, 2007, doi: 10.1016/j.biotechadv.2007.05.004.

[28] S. Pandit, A. Sengupta, S. Kale, and D. Das, "Performance of electron acceptors in catholyte of a two-chambered microbial fuel cell using anion exchange membrane," *Bioresour Technol*, vol. 102, no. 3, pp. 2736–2744, Feb. 2011, doi: 10.1016/j.biortech.2010.11.038.

[29] S. Shiva Kumar and H. Lim, "An overview of water electrolysis technologies for green hydrogen production," *Energy Reports*, vol. 8. Elsevier Ltd, pp. 13793–13813, Nov. 01, 2022. doi: 10.1016/j.egyr.2022.10.127.

[30] E. B. Agyekum, C. Nutakor, A. M. Agwa, and S. Kamel, "A Critical Review of Renewable Hydrogen Production Methods: Factors Affecting Their Scale-Up and Its Role in Future Energy Generation," *Membranes*, vol. 12, no. 2. MDPI, Feb. 01, 2022. doi: 10.3390/membranes12020173.

[31] A. Kundu, J. N. Sahu, G. Redzwan, and M. A. Hashim, "An overview of cathode material and catalysts suitable for generating hydrogen in microbial electrolysis cell," *Int J Hydrogen Energy*, vol. 38, no. 4, pp. 1745–1757, 2013, doi: 10.1016/j.ijhydene.2012.11.031.

[32] A. A. Pawar, A. Karthic, S. Lee, S. Pandit, and S. P. Jung, "Microbial electrolysis cells for electromethanogenesis: Materials, configurations and operations," *Environmental Engineering Research*, vol. 27, no. 1. Korean Society of Environmental Engineers, Feb. 01, 2022. doi: 10.4491/eer.2020.484.

[33] B. E. Logan, *Microbial Fuel Cells*. John Wiley & Sons, Inc., Hoboken, New Jersey, 2008. doi: 10.1002/9780470258590.

[34] T. Fudge *et al.*, "Microbial electrolysis cells for decentralize dwastewater treatment: The next steps," *Water (Switzerland)*, vol. 13, no. 4, Feb. 2021, doi: 10.3390/w13040445.

[35] D. P. B. T. B. Strik, R. A. Timmers, M. Helder, K. J. J. Steinbusch, H. V. M. Hamelers, and C. J. N. Buisman, "Microbial solar cells: Applying photosynthetic and electrochemically active organisms," *Trends in Biotechnology*, vol. 29, no. 1. pp. 41–49, Jan. 2011. doi: 10.1016/j.tibtech.2010.10.001.

[36] L. Liu and S. Choi, "Miniature microbial solar cells to power wireless sensor networks," *Biosensors and Bioelectronics*, vol. 177. Elsevier Ltd, Apr. 01, 2021. doi: 10.1016/j.bios.2021.112970.

[37] Ahirwar, A., Das, S., Das, S., Yang, Y. H., Bhatia, S. K., Vinayak, V., & Ghangrekar, M. M. (2023). Photosynthetic microbial fuel cell for bioenergy and valuable production: A review of circular bio-economy approach. *Algal Research*, *70*. https://doi.org/10.1016/j.algal.2023.102973

[38] L. Barelli *et al.*, "Enzymatic fuel cell technology for energy production from bio-sources," in *AIP Conference Proceedings*, American Institute of Physics Inc., Dec. 2019. doi: 10.1063/1.5138747.

[39] S. Jariwala and B. Krishnamurthy, “Transport equations in an enzymatic glucose fuel cell,” *Chem Phys Lett*, vol. 692, pp. 7–13, Jan. 2018, doi: 10.1016/j.cplett.2017.11.055.

[40] K. Chandrasekhar, A. Naresh Kumar, G. Kumar, D. H. Kim, Y. C. Song, and S. H. Kim, “Electro-fermentation for biofuels and biochemicals production: Current status and future directions,” *Bioresource Technology*, vol. 323. Elsevier Ltd, Mar. 01, 2021. doi: 10.1016/j.biortech.2020.124598.

[41] O. Sarkar and S. Venkata Mohan, “Synergy of anoxic microenvironment and facultative anaerobes on acidogenic metabolism in a self-induced electrofermentation system,” *Bioresour Technol*, vol. 313, Oct. 2020, doi: 10.1016/j.biortech.2020.123604.

[42] S. Bajracharya, A. Krige, L. Matsakas, U. Rova, and P. Christakopoulos, “Advances in cathode designs and reactor configurations of microbial electrosynthesis systems to facilitate gas electro-fermentation,” *Bioresource Technology*, vol. 354. Elsevier Ltd, Jun. 01, 2022. doi: 10.1016/j.biortech.2022.127178.

[43] I. Vassilev, N. J. H. Averesch, P. Ledezma, and M. Kokko, “Anodic electro-fermentation: Empowering anaerobic production processes via anodic respiration,” *Biotechnology Advances*, vol. 48. Elsevier Inc., May 01, 2021. doi: 10.1016/j.biotechadv.2021.107728.

[44] Tremouli A. [2013]. Development of an innovative single chamber microbial fuel cell for wastewater treatment [Doctoral dissertation, University of Patras, School of Chemical Engineering, Patras, Greece.]

[45] K. Rabaey *et al.*, “Microbial ecology meets electrochemistry: Electricity-driven and driving communities,” *ISME Journal*, vol. 1, no. 1. pp. 9–18, May 2007. doi: 10.1038/ismej.2007.4.

[46] U. Schröder, “Anodic electron transfer mechanisms in microbial fuel cells and their energy efficiency,” *Physical Chemistry Chemical Physics*, vol. 9, no. 21, pp. 2619–2629, 2007, doi: 10.1039/b703627m.

[47] N. Sekar and R. P. Ramasamy, “Electrochemical impedance spectroscopy for microbial fuel cell characterization,” *Journal of Microbial and Biochemical Technology*, vol. 5, no. SPECIALISSUE.2. OMICS Publishing Group, 2013. doi: 10.4172/1948-5948.s6-004.

[48] Y. Ahn and B. E. Logan, “Effectiveness of domestic wastewater treatment using microbial fuel cells at ambient and mesophilic temperatures,” *Bioresour Technol*, vol. 101, no. 2, pp. 469–475, Jan. 2010, doi: 10.1016/j.biortech.2009.07.039.

[49] H. Liu and B. E. Logan, “Electricity generation using an air-cathode single chamber microbial fuel cell in the presence and absence of a proton exchange membrane,” *Environ Sci Technol*, vol. 38, no. 14, pp. 4040–4046, Jul. 2004, doi: 10.1021/es0499344.

[50] Y. Feng, X. Wang, B. E. Logan, and H. Lee, “Brewery wastewater treatment using air-cathode microbial fuel cells,” *Appl Microbiol Biotechnol*, vol. 78, no. 5, pp. 873–880, 2008, doi: 10.1007/s00253-008-1360-2.

[51] G. Antonopoulou, I. Ntaikou, C. Pastore, L. di Bitonto, S. Bebelis, and G. Lyberatos, “An overall perspective for the energetic valorization of household food waste using microbial fuel cell technology of its extract,

coupled with anaerobic digestion of the solid residue," *Appl Energy*, vol. 242, no. December 2018, pp. 1064–1073, 2019, doi: 10.1016/j.apenergy.2019.03.082.

[52] A. Tremouli, G. Antonopoulou, S. Bebelis, and G. Lyberatos, "Operation and characterization of a microbial fuel cell fed with pretreated cheese whey at different organic loads," *Bioresour Technol*, vol. 131, pp. 380–389, 2013, doi: 10.1016/j.biortech.2012.12.173.

[53] G. Wang, L. Huang, and Y. Zhang, "Cathodic reduction of hexavalent chromium [Cr(VI)] coupled with electricity generation in microbial fuel cells," *Biotechnol Lett*, vol. 30, no. 11, pp. 1959–1966, 2008, doi: 10.1007/s10529-008-9792-4.

[54] C. Kim *et al.*, "Spontaneous and applied potential driven indium recovery on carbon electrode and crystallization using a bioelectrochemical system," *Bioresour Technol*, vol. 258, no. February, pp. 203–207, 2018, doi: 10.1016/j.biortech.2018.02.103.

[55] A. Ter Heijne, F. Liu, R. Van Der Weijden, J. Weijma, C. J. N. Buisman, and H. V. M. Hamelers, "Copper recovery combined with electricity production in a microbial fuel cell," *Environ Sci Technol*, vol. 44, no. 11, pp. 4376–4381, 2010, doi: 10.1021/es100526g.

[56] C. Choi and Y. Cui, "Recovery of silver from wastewater coupled with power generation using a microbial fuel cell," *Bioresour Technol*, vol. 107, pp. 522–525, 2012, doi: 10.1016/j.biortech.2011.12.058.

[57] B. S. Lim, H. Lu, C. Choi, and Z. X. Liu, "Recovery of silver metal and electric power generation using a microbial fuel cell," *Desalination Water Treat*, vol. 54, no. 13, pp. 3675–3681, 2015, doi: 10.1080/19443994.2014.923191.

[58] J. Winfield, I. Gajda, J. Greenman, and I. Ieropoulos, "A review into the use of ceramics in microbial fuel cells," *Bioresour Technol*, vol. 215, pp. 296–303, 2016, doi: 10.1016/j.biortech.2016.03.135.

[59] V. Yousefi, D. Mohebbi-Kalhori, and A. Samimi, "Ceramic-based microbial fuel cells (MFCs): A review," *Int J Hydrogen Energy*, vol. 42, no. 3, pp. 1672–1690, 2017, doi: 10.1016/j.ijhydene.2016.06.054.

[60] T. Kouam Ida and B. Mandal, "Microbial fuel cell design, application and performance: A review," *Mater Today Proc*, 2022, doi: 10.1016/j.matpr.2022.10.131.

[61] C. Santoro, C. Arbizzani, B. Erable, and I. Ieropoulos, "Microbial fuel cells: From fundamentals to applications. A review," *J Power Sources*, vol. 356, pp. 225–244, 2017, doi: 10.1016/j.jpowsour.2017.03.109.

[62] A. Tremouli, T. Kamperidis, P. K. Pandis, C. Argirusis, and G. Lyberatos, "Exploitation of Digestate from Thermophilic and Mesophilic Anaerobic Digesters Fed with Fermentable Food Waste Using the MFC Technology," *Waste Biomass Valorization*, vol. 12, no. 10, pp. 5361–5370, 2021, doi: 10.1007/s12649-021-01414-0.

[63] P. Wang, B. Lai, H. Li, and Z. Du, “Deposition of Fe on graphite felt by thermal decomposition of Fe(CO)5 for effective cathodic preparation of microbial fuel cells,” *Bioresour Technol*, vol. 134, pp. 30–35, 2013, doi: 10.1016/j.biortech.2013.01.153.

[64] Y. F. Guan, F. Zhang, B. C. Huang, and H. Q. Yu, “Enhancing electricity generation of microbial fuel cell for wastewater treatment using nitrogen-doped carbon dots-supported carbon paper anode,” *J Clean Prod*, vol. 229, pp. 412–419, 2019, doi: 10.1016/j.jclepro.2019.05.040.

[65] E. T. Sayed, M. A. Abdelkareem, H. Alawadhi, K. Elsaid, T. Wilberforce, and A. G. Olabi, “Graphitic carbon nitride/carbon brush composite as a novel anode for yeast-based microbial fuel cells,” *Energy*, vol. 221, p. 119849, 2021, doi: 10.1016/j.energy.2021.119849.

[66] I. Das, M. T. Noori, G. D. Bhowmick, and M. M. Ghangrekar, “Application of low-cost transition metal based Co0.5Zn0.5Fe2O4 as oxygen reduction reaction catalyst for improving performance of microbial fuel cell,” *MRS Adv*, vol. 3, no. 53, pp. 3149–3154, 2018, doi: 10.1557/adv.2018.450.

[67] K. Rabaey *et al.*, “Cathodic oxygen reduction catalyzed by bacteria in microbial fuel cells,” *ISME Journal*, vol. 2, no. 5, pp. 519–527, 2008, doi: 10.1038/ismej.2008.1.

[68] C. Santoro, M. Kodali, S. Herrera, A. Serov, I. Ieropoulos, and P. Atanassov, “Power generation in microbial fuel cells using platinum group metal-free cathode catalyst: Effect of the catalyst loading on performance and costs,” *J Power Sources*, vol. 378, no. September 2017, pp. 169–175, 2018, doi: 10.1016/j.jpowsour.2017.12.017.

[69] R. A. Rozendal, H. V. M. Hamelers, K. Rabaey, J. Keller, and C. J. N. Buisman, “Towards practical implementation of bioelectrochemical wastewater treatment,” *Trends in Biotechnology*, vol. 26, no. 8. pp. 450–459, Aug. 2008. doi: 10.1016/j.tibtech.2008.04.008.

[70] W. W. Li, G. P. Sheng, X. W. Liu, and H. Q. Yu, “Recent advances in the separators for microbial fuel cells,” *Bioresour Technol*, vol. 102, no. 1, pp. 244–252, 2011, doi: 10.1016/j.biortech.2010.03.090.

[71] S. M. Daud, B. H. Kim, M. Ghasemi, and W. R. W. Daud, “Separators used in microbial electrochemical technologies: Current status and future prospects,” *Bioresour Technol*, vol. 195, pp. 170–179, 2015, doi: 10.1016/j.biortech.2015.06.105.

[72] A. Tremouli, P. K. Pandis, T. Kamperidis, V. N. Stathopoulos, C. Argirusis, and G. Lyberatos, “Performance assessment of a four-air cathode membraneless microbial fuel cell stack for wastewater treatment and energy extraction,” *E3S Web of Conferences*, vol. 116, 2019, doi: 10.1051/e3sconf/201911600093.

[73] A. Tremouli, J. Greenman, and I. Ieropoulos, “Investigation of ceramic MFC stacks for urine energy extraction,” *Bioelectrochemistry*, vol. 123, pp. 19–25, 2018, doi: 10.1016/j.bioelechem.2018.03.010.

[74] P. Chatterjee and M. M. Ghangrekar, "Preparation of a fouling-resistant sustainable cathode for a single-chambered microbial fuel cell," *Water Science and Technology*, vol. 69, no. 3, pp. 634–639, 2014, doi: 10.2166/wst.2013.760.

[75] C. Santoro *et al.*, "Ceramic Microbial Fuel Cells Stack: Power generation in standard and supercapacitive mode," *Sci Rep*, vol. 8, no. 1, pp. 1–12, 2018, doi: 10.1038/s41598-018-21404-y.

[76] K. Lv, H. Zhang, and S. Chen, "Nitrogen and phosphorus co-doped carbon modified activated carbon as an efficient oxygen reduction catalyst for microbial fuel cells," *RSC Adv*, vol. 8, no. 2, pp. 848–855, 2018, doi: 10.1039/c7ra12907f.

[77] M. L. Jiménez González *et al.*, "Study of the effect of activated carbon cathode configuration on the performance of a membrane-less microbial fuel cell," *Catalysts*, vol. 10, no. 6, 2020, doi: 10.3390/catal10060619.

[78] X. Zhang, X. Xia, I. Ivanov, X. Huang, and B. E. Logan, "Enhanced activated carbon cathode performance for microbial fuel cell by blending carbon black," *Environ Sci Technol*, vol. 48, no. 3, pp. 2075–2081, 2014, doi: 10.1021/es405029y.

[79] S. Cheng, D. Xing, and B. E. Logan, "Electricity generation of single-chamber microbial fuel cells at low temperatures," *Biosens Bioelectron*, vol. 26, no. 5, pp. 1913–1917, Jan. 2011, doi: 10.1016/j.bios.2010.05.016.

[80] R. Sarma, A. Tamuly, and B. K. Kakati, "Recent developments in electricity generation by Microbial Fuel Cell using different substrates," *Mater Today Proc*, no. xxxx, 2021, doi: 10.1016/j.matpr.2021.02.522.

[81] L. Zhuang, Y. Zheng, S. Zhou, Y. Yuan, H. Yuan, and Y. Chen, "Scalable microbial fuel cell (MFC) stack for continuous real wastewater treatment," *Bioresour Technol*, vol. 106, pp. 82–88, Feb. 2012, doi: 10.1016/j.biortech.2011.11.019.

[82] P. Ledezma, J. Greenman, and I. Ieropoulos, "MFC-cascade stacks maximise COD reduction and avoid voltage reversal under adverse conditions," *Bioresour Technol*, vol. 134, pp. 158–165, 2013, doi: 10.1016/j.biortech.2013.01.119.

[83] A. James, "Ceramic-microbial fuel cell (C-MFC) for waste water treatment: A mini review," *Environ Res*, vol. 210, Jul. 2022, doi: 10.1016/j.envres.2022.112963.

[84] W. Yang, K. K. Lee, and S. Choi, "A laminar-flow based microbial fuel cell array," *Sens Actuators B Chem*, vol. 243, pp. 292–297, May 2017, doi: 10.1016/j.snb.2016.11.155.

[85] C. A. Cid, A. Stinchcombe, I. Ieropoulos, and M. R. Hoffmann, "Urine microbial fuel cells in a semi-controlled environment for onsite urine pre-treatment and electricity production," *J Power Sources*, vol. 400, pp. 441–448, Oct. 2018, doi: 10.1016/j.jpowsour.2018.08.051.

[86] M. F. Simões *et al.*, “Microbial fuel cell-induced production of fungal laccase to degrade the anthraquinone dye Remazol Brilliant Blue R,” *Environ Chem Lett*, vol. 17, no. 3, pp. 1413–1420, Sep. 2019, doi: 10.1007/s10311-019-00876-y.

[87] P. Mani *et al.*, “Degradation of Azo Dye (Acid Orange 7) in a Microbial Fuel Cell: Comparison Between Anodic Microbial-Mediated Reduction and Cathodic Laccase-Mediated Oxidation,” *Front Energy Res*, vol. 7, Sep. 2019, doi: 10.3389/fenrg.2019.00101.

[88] C. Y. Lai, C. H. Wu, C. T. Meng, and C. W. Lin, “Decolorization of azo dye and generation of electricity by microbial fuel cell with laccase-producing white-rot fungus on cathode,” *Appl Energy*, vol. 188, pp. 392–398, Feb. 2017, doi: 10.1016/j.apenergy.2016.12.044.

[89] F. P. van der Zee and S. Villaverde, “Combined anaerobic-aerobic treatment of azo dyes - A short review of bioreactor studies,” *Water Research*, vol. 39, no. 8. Elsevier Ltd, pp. 1425–1440, 2005. doi: 10.1016/j.watres.2005.03.007.

[90] S. P, “Simultaneous Chromium Removal and Power Generation Using Algal Biomass in a Dual Chambered Salt Bridge Microbial Fuel Cell,” *J Bioremediat Biodegrad*, vol. 04, no. 05, 2013, doi: 10.4172/2155-6199.1000190.

[91] T. Zhou, H. Han, P. Liu, J. Xiong, F. Tian, and X. Li, “Microbial fuels cell-based biosensor for toxicity detection: A review,” *Sensors (Switzerland)*, vol. 17, no. 10. MDPI AG, Oct. 01, 2017. doi: 10.3390/s17102230.

[92] A. S. Mathuriya and J. V. Yakhmi, “Microbial fuel cells to recover heavy metals,” *Environ Chem Lett*, vol. 12, no. 4, pp. 483–494, 2014, doi: 10.1007/s10311-014-0474-2.

[93] L. Huang, J. Chen, X. Quan, and F. Yang, “Enhancement of hexavalent chromium reduction and electricity production from a biocathode microbial fuel cell,” *Bioprocess Biosyst Eng*, vol. 33, no. 8, pp. 937–945, 2010, doi: 10.1007/s00449-010-0417-7.

[94] M. Y. Mitov, I. O. Bardarov, E. Y. Chorbadzhiyska, and Y. V Hubenova, “Copper recovery combined with wastewater treatment in a microbial fuel cell,” vol. 50, pp. 136–140, 2018.

[95] T. Catal, H. Bermek, and H. Liu, “Removal of selenite from wastewater using microbial fuel cells,” *Biotechnol Lett*, vol. 31, no. 8, pp. 1211–1216, 2009, doi: 10.1007/s10529-009-9990-8.

[96] H. Wang and Z. J. Ren, “Bioelectrochemical metal recovery from wastewater: A review,” *Water Res*, vol. 66, pp. 219–232, 2014, doi: 10.1016/j.watres.2014.08.013.

[97] J. Prasad and R. K. Tripathi, “Review on improving microbial fuel cell power management systems for consumer applications,” *Energy Reports*, vol. 8. Elsevier Ltd, pp. 10418–10433, Nov. 01, 2022. doi: 10.1016/j.egyr.2022.08.192.

[98] A. Tremouli, T. Kamperidis, and G. Lyberatos, “Comparative study of different operation modes of microbial fuel cells treating food residue biomass,” *Molecules*, vol. 26, no. 13, Jul. 2021, doi: 10.3390/molecules26133987.

[99] C. Donovan, A. Dewan, D. Heo, Z. Lewandowski, and H. Beyenal, “Sediment microbial fuel cell powering a submersible ultrasonic receiver: New approach to remote monitoring,” *J Power Sources*, vol. 233, pp. 79–85, 2013, doi: 10.1016/j.jpowsour.2012.12.112.

[100] Rabaey, K., Angenent, L., Schröder, U., Keller, J., 2010. Bioelectrochemical systems: from extracellular electron transfer to biotechnological application. 1st ed. London, IWA Publishing, pp. 430, 401.

[101] D. A. Jadhav, A. A. Carmona-Martínez, A. D. Chendake, S. Pandit, and D. Pant, “Modeling and optimization strategies towards performance enhancement of microbial fuel cells,” *Bioresour Technol*, vol. 320, no. PA, p. 124256, 2021, doi: 10.1016/j.biortech.2020.124256.

[102] D. Recio-Garrido, M. Perrier, and B. Tartakovsky, “Modeling, optimization and control of bioelectrochemical systems,” *Chemical Engineering Journal*, vol. 289, pp. 180–190, 2016, doi: 10.1016/j.cej.2015.11.112.

[103] X. Zhang and A. Halme, “MODELLING OF A MICROBIAL FUEL CELL PROCESS Xia-Chang Zhang and Aarne Halme Automation Technology Laboratory, Helsinki University of Technology, 02150 ESPOO, FINLAND,” vol. 17, no. 8, pp. 809–814, 1995.

[104] Y. Zeng, Y. F. Choo, B. H. Kim, and P. Wu, “Modelling and simulation of two-chamber microbial fuel cell,” *J Power Sources*, vol. 195, no. 1, pp. 79–89, 2010, doi: 10.1016/j.jpowsour.2009.06.101.

[105] P. Belleville, G. Merlin, J. Ramousse, and J. Deseure, “Two-dimensional modelling of syntrophic glucose conversion in bioanodes for coulombic efficiency optimization,” *Bioresour Technol Rep*, vol. 6, no. February, pp. 15–25, 2019, doi: 10.1016/j.biteb.2019.02.002.

[106] P. M. D. Serra, A. Espírito-Santo, and M. Magrinho, “A steady-state electrical model of a microbial fuel cell through multiple-cycle polarization curves,” *Renewable and Sustainable Energy Reviews*, vol. 117, no. October 2019, p. 109439, 2020, doi: 10.1016/j.rser.2019.109439.

[107] J. R. Day, E. S. Heidrich, and T. S. Wood, “A scalable model of fluid flow, substrate removal and current production in microbial fuel cells,” *Chemosphere*, no. October, p. 132686, 2021, doi: 10.1016/j.chemosphere.2021.132686.

[108] M. T. Matsena and E. M. N. Chirwa, “Hexavalent chromium-reducing microbial fuel cell modeling using integrated Monod kinetics and Butler-Volmer equation,” *Fuel*, vol. 312, no. December 2021, p. 122834, 2022, doi: 10.1016/j.fuel.2021.122834.

[109] M. Sindhuja, N. S. Kumar, V. Sudha, and S. Harinipriya, “Equivalent circuit modeling of microbial fuel cells using impedance spectroscopy,” *J Energy Storage*, vol. 7, pp. 136–146, 2016, doi: 10.1016/j.est.2016.06.005.

[110] V. B. Oliveira, M. Simões, L. F. Melo, and A. M. F. R. Pinto, “A 1D mathematical model for a microbial fuel cell,” *Energy*, vol. 61, pp. 463–471, 2013, doi: 10.1016/j.energy.2013.08.055.

[111] S. Freguia, K. Rabaey, Z. Yuan, and J. Keller, “Non-catalyzed cathodic oxygen reduction at graphite granules in microbial fuel cells,” *Electrochim Acta*, vol. 53, no. 2, pp. 598–603, Dec. 2007, doi: 10.1016/j.electacta.2007.07.037.

[112] APHA/AWWA/WEF, “Standard Methods for the Examination of Water and Wastewater,” 2012, doi: https://doi.org/ISBN 9780875532356.

[113] G. Lytras, E. Koutroumanou, and G. Lyberatos, “Journal of Environmental Chemical Engineering Anaerobic co-digestion of condensate produced from drying of Household Food Waste and Waste Activated Sludge,” *J Environ Chem Eng*, vol. 8, no. 4, p. 103947, 2020, doi: 10.1016/j.jece.2020.103947.

[114] I. Ntaikou, N. Menis, M. Alexandropoulou, G. Antonopoulou, and G. Lyberatos, “Valorization of kitchen biowaste for ethanol production via simultaneous saccharification and fermentation using co-cultures of the yeasts Saccharomyces cerevisiae and Pichia stipitis,” *Bioresour Technol*, vol. 263, no. April, pp. 75–83, 2018, doi: 10.1016/j.biortech.2018.04.109.

[115] G. de Gioannis *et al.*, “Bio-electrochemical production of hydrogen and electricity from organic waste: preliminary assessment,” *Clean Technol Environ Policy*, vol. 25, no. 1, pp. 269–280, Jan. 2023, doi: 10.1007/s10098-022-02305-1.

[116] “PhotoRec.” http://photorec.chemeng.ntua.gr/ (accessed Oct. 15, 2022).

[117] M. Theocharis *et al.*, “An integrated thermal and hydrometallurgical process for the recovery of Silicon and Silver from end-of-life crystalline Si photovoltaic panels,” 2019.

[118] M. A. R. S. Al-Baghdadi, “Modelling of proton exchange membrane fuel cell performance based on semi-empirical equations,” *Renew Energy*, vol. 30, no. 10, pp. 1587–1599, 2005, doi: 10.1016/j.renene.2004.11.015.

[119] B. E. Logan, C. Murano, K. Scott, N. D. Gray, and I. M. Head, “Electricity generation from cysteine in a microbial fuel cell,” *Water Res*, vol. 39, no. 5, pp. 942–952, 2005, doi: 10.1016/j.watres.2004.11.019.

[120] Haynes, W.M. (Ed.). (2014). CRC Handbook of Chemistry and Physics (95th ed.). CRC Press. https://doi.org/10.1201/b17118

[121] D. J. Batstone *et al.*, “The IWA Anaerobic Digestion Model No 1 (ADM1).,” *Water Sci Technol*, vol. 45, no. 10, pp. 65–73, 2002, doi: 10.2166/wst.2002.0292.

[122] M. Ahmaruzzaman, “A review on the utilization of fly ash,” *Progress in Energy and Combustion Science*, vol. 36, no. 3. pp. 327–363, Jun. 2010. doi: 10.1016/j.pecs.2009.11.003.

[123] I. M. Berkgaut, “Cation Exchange Properties of Hydrothermally Treated Coal Fly Ash,” 1995.

[124] X. Zhang *et al.*, “Power generation by packed-bed air-cathode microbial fuel cells,” *Bioresour Technol*, vol. 142, pp. 109–114, 2013, doi: 10.1016/j.biortech.2013.05.014.

[125] M. H. Do *et al.*, “Challenges in the application of microbial fuel cells to wastewater treatment and energy production: A mini review,” *Science of the Total Environment*, vol. 639. Elsevier B.V., pp. 910–920, Oct. 15, 2018. doi: 10.1016/j.scitotenv.2018.05.136.

[126] T. Kamperidis, P. K. Pandis, C. Argirusis, G. Lyberatos, and A. Tremouli, “Effect of Food Waste Condensate Concentration on the Performance of Microbial Fuel Cells with Different Cathode Assemblies,” *Sustainability (Switzerland)*, vol. 14, no. 5, Mar. 2022, doi: 10.3390/su14052625.

[127] P. K. Pandis *et al.*, “Comparative Study of Different Production Methods of Activated Carbon Cathodic Electrodes in Single Chamber MFC Treating Municipal Landfill Leachate,” *Applied Sciences (Switzerland)*, vol. 12, no. 6, Mar. 2022, doi: 10.3390/app12062991.

[128] A. James, “Ceramic-microbial fuel cell (C-MFC) for waste water treatment: A mini review,” *Environ Res*, vol. 210, Jul. 2022, doi: 10.1016/j.envres.2022.112963.

[129] C. M. Jeong, J. Dal, R. Choi, Y. Ahn, and H. N. Chang, “Removal of volatile fatty acids (VFA) by microbial fuel cell with aluminum electrode and microbial community identification with 16S rRNA sequence,” 2008.

[130] I. Merino-Jimenez, O. Obata, G. Pasternak, I. Gajda, J. Greenman, and I. Ieropoulos, “Effect of microbial fuel cell operation time on the disinfection efficacy of electrochemically synthesised catholyte from urine,” *Process Biochemistry*, vol. 101, pp. 294–303, Feb. 2021, doi: 10.1016/j.procbio.2020.10.014.

[131] V. Yousefi, D. Mohebbi-Kalhori, and A. Samimi, “Start-up investigation of the self-assembled chitosan/montmorillonite nanocomposite over the ceramic support as a low-cost membrane for microbial fuel cell application,” *Int J Hydrogen Energy*, vol. 45, no. 7, pp. 4804–4820, Feb. 2020, doi: 10.1016/j.ijhydene.2019.11.216.

[132] A. Tremouli, J. Greenman, and I. Ieropoulos, “Effect of simple interventions on the performance of a miniature MFC fed with fresh urine,” *Int J Hydrogen Energy*, vol. 46, no. 67, pp. 33594–33600, Sep. 2021, doi: 10.1016/j.ijhydene.2021.07.171.

[133] Z. Wang, G. D. Mahadevan, Y. Wu, and F. Zhao, “Progress of air-breathing cathode in microbial fuel cells,” *J Power Sources*, vol. 356, pp. 245–255, 2017, doi: 10.1016/j.jpowsour.2017.02.004.

[134] W. da Silva Freitas, D. Gemma, B. Mecheri, and A. D’Epifanio, “Air-breathing cathodes for microbial fuel cells based on iron-nitrogen-carbon electrocatalysts,” *Bioelectrochemistry*, vol. 146, Aug. 2022, doi: 10.1016/j.bioelechem.2022.108103.

[135] Y. Yuan, T. Yuan, D. Wang, J. Tang, and S. Zhou, “Sewage sludge biochar as an efficient catalyst for oxygen reduction reaction in an microbial fuel cell,” *Bioresour Technol*, vol. 144, pp. 115–120, 2013, doi: 10.1016/j.biortech.2013.06.075.

[136] Q. Zhang and L. Liu, “A microbial fuel cell system with manganese dioxide/titanium dioxide/graphitic carbon nitride coated granular activated carbon cathode successfully treated organic acids industrial wastewater with residual nitric acid,” *Bioresour Technol*, vol. 304, May 2020, doi: 10.1016/j.biortech.2020.122992.

[137] T. Huggins, H. Wang, J. Kearns, P. Jenkins, and Z. J. Ren, “Biochar as a sustainable electrode material for electricity production in microbial fuel cells,” *Bioresour Technol*, vol. 157, pp. 114–119, 2014, doi: 10.1016/j.biortech.2014.01.058.

[138] H. C. Chang, W. Gustave, Z. F. Yuan, Y. Xiao, and Z. Chen, “One-step fabrication of binder-free air cathode for microbial fuel cells by using balsa wood biochar,” *Environ Technol Innov*, vol. 18, May 2020, doi: 10.1016/j.eti.2020.100615.

[139] A. Tremouli, P. K. Pandis, T. Kamperidis, V. N. Stathopoulos, C. Argirusis, and G. Lyberatos, “Performance assessment of a four-air cathode membraneless microbial fuel cell stack for wastewater treatment and energy extraction,” in *E3S Web of Conferences*, EDP Sciences, Sep. 2019. doi: 10.1051/e3sconf/201911600093.

[140] Y. Liu, S. Guo, J. Wang, and C. Li, “Fundamental development and research of cathodic compartment in microbial fuel cells: A review,” *J Environ Chem Eng*, vol. 10, no. 3, Jun. 2022, doi: 10.1016/j.jece.2022.107918.

[141] A. Tremouli, A. Intzes, P. Intzes, S. Bebelis, and G. Lyberatos, “Effect of periodic complete anolyte replacement on the long term performance of a four air cathodes single chamber microbial fuel cell,” *J Appl Electrochem*, vol. 45, no. 7, pp. 755–763, 2015, doi: 10.1007/s10800-015-0842-z.

[142] Z. He, S. D. Minteer, and L. T. Angenent, “Electricity generation from artificial wastewater using an upflow microbial fuel cell,” *Environ Sci Technol*, vol. 39, no. 14, pp. 5262–5267, Jul. 2005, doi: 10.1021/es0502876.

[143] A. K. Manohar and F. Mansfeld, “The internal resistance of a microbial fuel cell and its dependence on cell design and operating conditions,” *Electrochim Acta*, vol. 54, no. 6, pp. 1664–1670, Feb. 2009, doi: 10.1016/j.electacta.2008.06.047.

[144] D. Hidalgo, A. Sacco, S. Hernández, and T. Tommasi, “Electrochemical and impedance characterization of Microbial Fuel Cells based on 2D and 3D anodic electrodes working with seawater microorganisms under continuous operation,” *Bioresour Technol*, vol. 195, pp. 139–146, 2015, doi: 10.1016/j.biortech.2015.06.127.

[145] D. B. Xochitl, S. Sevda, K. Vanbroekhoven, and D. Pant, “The accurate use of impedance analysis for the study of microbial electrochemical systems,” *Chem Soc Rev*, vol. 41, no. 21, pp. 7228–7246, Oct. 2012, doi: 10.1039/c2cs35026b.

[146] E. Martin, O. Savadogo, S. R. Guiot, and B. Tartakovsky, “Electrochemical characterization of anodic biofilm development in a microbial fuel cell,” *J Appl Electrochem*, vol. 43, no. 5, pp. 533–540, May 2013, doi: 10.1007/s10800-013-0537-2.

[147] I. Gajda, J. Greenman, and I. Ieropoulos, “Microbial Fuel Cell stack performance enhancement through carbon veil anode modification with activated carbon powder,” *Appl Energy*, vol. 262, no. February, p. 114475, 2020, doi: 10.1016/j.apenergy.2019.114475.

[148] “Bio-waste in Europe — turning challenges into opportunities — European Environment Agency.” https://www.eea.europa.eu/publications/bio-waste-in-europe (accessed Nov. 02, 2022).

[149] A. Sridhar *et al.*, “Valorization of food waste as adsorbents for toxic dye removal from contaminated waters: A review,” *J Hazard Mater*, vol. 424, no. PB, p. 127432, 2022, doi: 10.1016/j.jhazmat.2021.127432.

[150] A. Talan, B. Tiwari, B. Yadav, R. D. Tyagi, J. W. C. Wong, and P. Drogui, “Food waste valorization: Energy production using novel integrated systems,” *Bioresour Technol*, vol. 322, no. December 2020, p. 124538, 2021, doi: 10.1016/j.biortech.2020.124538.

[151] FAO, “Food wastage footprint & Climate Change,” *Food wastage footprint & Climate Change*, no. 1, pp. 1–4, 2015, [Online]. Available: http://www.fao.org/3/a-bb144e.pdf

[152] P. Sharma, V. K. Gaur, S. H. Kim, and A. Pandey, “Microbial strategies for bio-transforming food waste into resources,” *Bioresour Technol*, vol. 299, no. October 2019, p. 122580, 2020, doi: 10.1016/j.biortech.2019.122580.

[153] J. Venus, S. Fiore, F. Demichelis, and D. Pleissner, “Centralized and decentralized utilization of organic residues for lactic acid production,” *J Clean Prod*, vol. 172, pp. 778–785, 2018, doi: 10.1016/j.jclepro.2017.10.259.

[154] Z. Zhang, P. Tsapekos, M. Alvarado-Morales, and I. Angelidaki, “Bio-augmentation to improve lactic acid production from source-sorted organic household waste,” *J Clean Prod*, vol. 279, p. 123714, 2021, doi: 10.1016/j.jclepro.2020.123714.

[155] K. Rousta and K. Bolton, *Sorting household waste at the source*. Elsevier B.V., 2019. doi: 10.1016/B978-0-444-64200-4.00008-6.

[156] G. Antonopoulou, M. Alexandropoulou, I. Ntaikou, and G. Lyberatos, “From waste to fuel: Energy recovery from household food waste via its bioconversion to energy carriers based on microbiological processes,” *Science of the Total Environment*, vol. 732, p. 139230, 2020, doi: 10.1016/j.scitotenv.2020.139230.

[157] “WASTE4think - Moving towards Life Cycle Thinking by integrating Advanced Waste Management Systems.” https://waste4think.eu/ (accessed Nov. 02, 2022).

[158] I. Michalopoulos *et al.*, “Hydrogen and Methane Production from Food Residue Biomass Product (FORBI),” *Waste Biomass Valorization*, vol. 11, no. 5, pp. 1647–1655, 2020, doi: 10.1007/s12649-018-00550-4.

[159] I. v. Skiadas and G. Lyberatos, “The periodic anaerobic baffled reactor,” *Water Science and Technology*, vol. 38, no. 8-9–9 pt 7, pp. 401–408, Jan. 1998, doi: 10.1016/S0273-1223(98)00717-3.

[160] A. Tremouli *et al.*, “Bioelectricity production from fermentable household waste extract using a single chamber microbial fuel cell,” *Energy Procedia*, vol. 161, pp. 2–9, 2019, doi: 10.1016/j.egypro.2019.02.051.

[161] J. Greenman, I. A. Ieropoulos, and C. Melhuish, *Microbial Fuel Cells – Scalability and their Use in Robotics*. 2011. doi: 10.1007/978-1-4614-0347-0_3.

[162] Q. Zhang, J. Hu, and D. J. Lee, “Biogas from anaerobic digestion processes: Research updates,” *Renew Energy*, vol. 98, pp. 108–119, 2016, doi: 10.1016/j.renene.2016.02.029.

[163] V. Diamantis, A. Eftaxias, K. Stamatelatou, C. Noutsopoulos, C. Vlachokostas, and A. Aivasidis, “Bioenergy in the era of circular economy: Anaerobic digestion technological solutions to produce biogas from lipid-rich wastes,” *Renew Energy*, vol. 168, pp. 438–447, May 2021, doi: 10.1016/j.renene.2020.12.034.

[164] F. Xu, Y. Li, X. Ge, L. Yang, and Y. Li, “Anaerobic digestion of food waste – Challenges and opportunities,” *Bioresource Technology*, vol. 247. Elsevier Ltd, pp. 1047–1058, Jan. 01, 2018. doi: 10.1016/j.biortech.2017.09.020.

[165] A. Slepetiene *et al.*, “The potential of digestate as a biofertilizer in eroded soils of Lithuania,” *Waste Management*, vol. 102, pp. 441–451, Feb. 2020, doi: 10.1016/j.wasman.2019.11.008.

[166] L. Ioannou-Ttofa, S. Foteinis, A. Seifelnasr Moustafa, E. Abdelsalam, M. Samer, and D. Fatta-Kassinos, “Life cycle assessment of household biogas production in Egypt: Influence of digester volume, biogas leakages, and digestate valorization as biofertilizer,” *J Clean Prod*, vol. 286, Mar. 2021, doi: 10.1016/j.jclepro.2020.125468.

[167] J. Liu, S. Huang, K. Chen, T. Wang, M. Mei, and J. Li, “Preparation of biochar from food waste digestate: Pyrolysis behavior and product properties,” *Bioresour Technol*, vol. 302, Apr. 2020, doi: 10.1016/j.biortech.2020.122841.

[168] J. P. Sheets, L. Yang, X. Ge, Z. Wang, and Y. Li, “Beyond land application: Emerging technologies for the treatment and reuse of anaerobically digested agricultural and food waste,” *Waste Management*, vol. 44. Elsevier Ltd, pp. 94–115, Oct. 01, 2015. doi: 10.1016/j.wasman.2015.07.037.

[169] S. M. Martinez and M. di Lorenzo, “Electricity generation from untreated fresh digestate with a cost-effective array of floating microbial fuel cells,” *Chem Eng Sci*, vol. 198, pp. 108–116, Apr. 2019, doi: 10.1016/j.ces.2018.12.039.

[170] T. Kim, J. An, J. K. Jang, and I. S. Chang, “Coupling of anaerobic digester and microbial fuel cell for COD removal and ammonia recovery,” *Bioresour Technol*, vol. 195, pp. 217–222, Aug. 2015, doi: 10.1016/j.biortech.2015.06.009.

[171] L. di Palma *et al.*, “Experimental assessment of a process including microbial fuel cell for nitrogen removal from digestate of anaerobic treatment of livestock manure and agricultural wastes,” *Chem Eng Trans*, vol. 43, pp. 2239–2244, 2015, doi: 10.3303/CET1543374.

[172] E. G. di Domenico, G. Petroni, D. Mancini, A. Geri, L. di Palma, and F. Ascenzioni, “Development of electroactive and anaerobic ammonium-oxidizing (Anammox) biofilms from digestate in microbial fuel cells,” *Biomed Res Int*, vol. 2015, 2015, doi: 10.1155/2015/351014.

[173] B. Wei, J. C. Tokash, F. Zhang, Y. Kim, and B. E. Logan, “Electrochemical analysis of separators used in single-chamber, air-cathode microbial fuel cells,” *Electrochim Acta*, vol. 89, pp. 45–51, 2013, doi: 10.1016/j.electacta.2012.11.004.

[174] D. Chuka-ogwude, J. Ogbonna, and N. R. Moheimani, “A review on microalgal culture to treat anaerobic digestate food waste effluent,” *Algal Research*, vol. 47. Elsevier B.V., May 01, 2020. doi: 10.1016/j.algal.2020.101841.

[175] B. Ruffino, A. Cerutti, G. Campo, G. Scibilia, E. Lorenzi, and M. Zanetti, “Thermophilic vs. mesophilic anaerobic digestion of waste activated sludge: Modelling and energy balance for its applicability at a full scale WWTP,” *Renew Energy*, vol. 156, pp. 235–248, Aug. 2020, doi: 10.1016/j.renene.2020.04.068.

[176] Q. Hou, Z. Yang, S. Chen, and H. Pei, “Using an anaerobic digestion tank as the anodic chamber of an algae-assisted microbial fuel cell to improve energy production from food waste,” *Water Res*, vol. 170, Mar. 2020, doi: 10.1016/j.watres.2019.115305.

[177] J. D. R. Choi, H. N. Chang, and J. I. Han, “Performance of microbial fuel cell with volatile fatty acids from food wastes,” *Biotechnol Lett*, vol. 33, no. 4, pp. 705–714, Apr. 2011, doi: 10.1007/s10529-010-0507-2.

[178] A. Tremouli, P. K. Pandis, I. Karydogiannis, V. N. Stathopoulos, C. Argirusis, and G. Lyberatos, “Operation and Electro(chemical) characterization of a microbial fuel cell stack fed with fermentable household waste extract,” *Global NEST Journal*, vol. 21, no. 2, pp. 253–257, 2019, doi: 10.30955/gnj.002996.

[179] K. Stamatelatou, G. Antonopoulou, A. Tremouli, and G. Lyberatos, “Production of gaseous biofuels and electricity from cheese whey,” *Ind Eng Chem Res*, vol. 50, no. 2, pp. 639–644, 2011, doi: 10.1021/ie1002262.

[180] M. Behera, P. S. Jana, T. T. More, and M. M. Ghangrekar, “Rice mill wastewater treatment in microbial fuel cells fabricated using proton exchange membrane and earthen pot at different pH,” *Bioelectrochemistry*, vol. 79, no. 2, pp. 228–233, 2010, doi: 10.1016/j.bioelechem.2010.06.002.

[181] S. Cheng and B. E. Logan, “Increasing power generation for scaling up single-chamber air cathode microbial fuel cells,” *Bioresour Technol*, vol. 102, no. 6, pp. 4468–4473, 2011, doi: 10.1016/j.biortech.2010.12.104.

[182] N. Sekar and R. P. Ramasamy, “Electrochemical impedance spectroscopy for microbial fuel cell characterization,” *J Microb Biochem Technol*, vol. 5, no. SPECIALISSUE.2, 2013, doi: 10.4172/1948-5948.s6-004.

[183] E. Martin, O. Savadogo, S. R. Guiot, and B. Tartakovsky, “Electrochemical characterization of anodic biofilm development in a microbial fuel cell,” *J Appl Electrochem*, vol. 43, no. 5, pp. 533–540, 2013, doi: 10.1007/s10800-013-0537-2.

[184] N. Uria, I. Ferrera, and J. Mas, “Electrochemical performance and microbial community profiles in microbial fuel cells in relation to electron transfer mechanisms,” *BMC Microbiol*, vol. 17, no. 1, pp. 1–12, 2017, doi: 10.1186/s12866-017-1115-2.

[185] G. S. Jadhav and M. M. Ghangrekar, “Performance of microbial fuel cell subjected to variation in pH, temperature, external load and substrate concentration,” *Bioresour Technol*, vol. 100, no. 2, pp. 717–723, 2009, doi: 10.1016/j.biortech.2008.07.041.

[186] Korneel Rabaey, Geert Lissens, and Willy Verstraete, “Microbial fuel cells: performances and perspectives,” in *Biofuels for fuel cells : renewable energy from biomass fermentation*, Lens Piet, Westermann Peter, Haberbauer Marianne, and Moreno Angelo, Eds., 1st ed.London, UK: IWA Publishing, 2005, pp. 377–399.

[187] O. Lefebvre, A. Uzabiaga, I. S. Chang, B. H. Kim, and H. Y. Ng, “Microbial fuel cells for energy self-sufficient domestic wastewater treatment-a review and discussion from energetic consideration,” *Applied Microbiology and Biotechnology*, vol. 89, no. 2. pp. 259–270, Jan. 2011. doi: 10.1007/s00253-010-2881-z.

[188] F. Asunis *et al.*, “The dairy biorefinery: Integrating treatment processes for cheese whey valorisation,” *Journal of Environmental Management*, vol. 276. Academic Press, Dec. 15, 2020. doi: 10.1016/j.jenvman.2020.111240.

[189] “Silver perchlorate Formula.” https://www.softschools.com/formulas/chemistry/silver_perchlorate_formula/393/ (accessed Oct. 24, 2022).

[190] L. Zhuang, S. Zhou, Y. Li, and Y. Yuan, “Enhanced performance of air-cathode two-chamber microbial fuel cells with high-pH anode and low-pH cathode,” *Bioresour Technol*, vol. 101, no. 10, pp. 3514–3519, 2010, doi: 10.1016/j.biortech.2009.12.105.

[191] C. Candelise, J. F. Spiers, and R. J. K. Gross, “Materials availability for thin film (TF) PV technologies development: A real concern?,” *Renewable and Sustainable Energy Reviews*, vol. 15, no. 9, pp. 4972–4981, 2011, doi: 10.1016/j.rser.2011.06.012.